Final Report

Resource Extraction Autonomous Vehicle for Environmental Recovery

AE3200 Design Synthesis

DSE Group 07

Delft University of Technology

TU Delft

This page is intentionally left blank.

Final Report

by

DSE Group 07

Student Name	Student Number
Absil, Lauke	6035434
Auffret, Jean-Baptiste	5924227
Dussaud, Raphael	5912326
Fortes Rincón, Jose	5915546
Niinivaara, Venla	5823447
Petek, Miron Oliver	5992729
Teeuwen, Jules	5786835
Witlox, Daan	5994071
Yanes Sanchez, Sofia	5908051
Ying, Diogo	5908361

Tutor: Steve Gehly
Coaches: Kherlen Jigjid, Wouter van Straalen
Course: AE3200 - Design Synthesis Exercise
Faculty: Faculty of Aerospace Engineering, Delft

Style: TU Delft Report Style, with modifications by Group 7: REAVER
Cover: Image background is generated by ChatGPT

Contents

Nomenclature

Abbreviations

ADN	Ammonium dinitramide
ADR	Active debris removal
AE3200	Design Synthesis Exercise course code
AEP	Apogee engine probe
AIAA	American Institute of Aeronautics and Astronautics
AIT	Assembly, Integration and Testing
AOCS	Attitude and Orbit Control System
BOL	Beginning of life
BPSK	Binary phase-shift keying
C&DH	Command and Data Handling
CAN	Controller Area Network
CBE	Current best estimate
CBS	Cost Breakdown Structure
CCSDS	Consultative Committee for Space Data Systems
CDR	Critical Design Review
CF	Cash flow
CFRP	Carbon-fibre-reinforced polymer
CG	Centre of gravity
CNA	Computer network architecture
COPV	Composite overwrapped pressure vessel
COTS	Commercial off-the-shelf
CW	Clohessy-Wiltshire
CTE	Coefficient of Thermal Expansion
DARPA	Defense Advanced Research Projects Agency
DISCOS	Database and Information System Characterising Objects in Space
DL	Downlink
DOD	Depth of discharge
DOF	Degree of freedom
DPU	Data processing unit
DSE	Design Synthesis Exercise
ECC	Error-correcting code
ECSS	European Cooperation for Space Standardization
EIRP	Equivalent isotropic radiated power
EMC	Electromagnetic compatibility
EOL	End of life
EP	Electric propulsion
EPS	Electrical Power System
EPS-X00	Safran low-power electric propulsion system
ESA	European Space Agency
ESD	Electrostatic discharge
ESTEC	European Space Research and Technology Centre
ETSI	European Telecommunications Standards Institute
EU	European Union
FBS	Functional Breakdown Structure
FCC	Federal Communications Commission
FDIR	Fault Detection, Isolation and Recovery
FFD	Functional Flow Diagram
FIT	Failures in time
FMS	Flow management system
FoS	Factor of safety
FRR	Flight Readiness Review
FSPL	Free-space path loss
GEO	Geostationary Earth orbit
GEVS	General Environmental Verification Standard
GMAT	General Mission Analysis Tool
GN&C	Guidance, Navigation and Control
GNC	Guidance, Navigation and Control
GNSS	Global Navigation Satellite System
GPS	Global Positioning System
GRMS	Root-mean-square acceleration
GS	Ground station / ground segment
GTO	Geostationary transfer orbit
HGA	High-gain antenna
HIL	Hardware-in-the-loop
HK	Housekeeping
HPGP	High Performance Green Propulsion
HPV	High-pressure vessel
IADC	Inter-Agency Space Debris Coordination Committee
IA&T	Integration, Assembly and Test
IDSS	International Docking System Standard
IMU	Inertial measurement unit
IR	Infrared
IRR	Internal rate of return
ISC	Independent Spacecraft
ITSO	International Telecommunications Satellite Organisation
ITU	International Telecommunication Union
KOS	Keep-out sphere
LAE	Liquid apogee engine
LCA	Life-cycle assessment
LCC	Life-cycle cost
LCSA	Life Cycle Sustainability Analysis
LEO	Low Earth orbit
LEOP	Launch and early orbit phase
LiDAR	Light Detection and Ranging
LMP-103S	ADN-based green monopropellant
LNA	Low-noise amplifier
MAI	Manufacturing, Assembly and Integration
MC&DH	Mothership C&DH
M&T	Mothership and Tugs
MEOP	Maximum expected operating pressure
MEV	Mission Extension Vehicle
MLI	Multilayer insulation
MPPT	Maximum power-point tracking
MRV	Mission Robotic Vehicle
MS	Mothership
MTBF	Mean time between failures
MTR	Multiple Target Retrieval
NASA	National Aeronautics and Space Administration
NFOV	Narrow field of view
NORAD	North American Aerospace Defense Command catalogue ID
NPV	Net present value
OASPL	Overall sound pressure level
OBC	On-board computer
OBDH	On-board data handling
OOS	On-orbit servicing
OST	Outer Space Treaty
PAF	Payload attach fitting
PCDU	Power conditioning and distribution unit
PD&D	Project Design and Development
PDR	Preliminary Design Review
PESTLE	Political, Economic, Social, Technological, Legal and Environmental
PGS	Pyrolytic graphite sheet
PL	Payload
PMD	Propellant management device
PMS	Project management system
PPU	Power processing unit
PPU-X00	Safran power processing unit
PPS-X00	Safran Hall-effect thruster class
PSW	Pusher Swarm
PV	Present value
QI	Quasi-isotropic
QA	Quality assurance
RAAN	Right Ascension of the Ascending Node
RAMS	Reliability, Availability, Maintainability and Safety
RCS	Reaction-control system
REAVER	Resource Extraction Autonomous Vehicle for Environmental Recovery
RF	Radio frequency
RH	Recycling hub
RHA	Radiation hardness assurance
ROI	Return on investment
RPD	Regulated power distribution
RPO	Rendezvous and proximity operations
RPOD	Rendezvous, Proximity Operations and Docking
RS-422	Serial communication standard
RS-485	Serial communication standard
RSGS	Robotic Servicing of Geosynchronous Satellites
RX	Receiver
S/C	Spacecraft
S-band	2-4 GHz radio-frequency band
SBC	Single-board computer
SDLS	Space Data Link Security
SEE	Single-event effects
SMA	Semi-major axis
SMAD	Space Mission Analysis and Design
SNR	Signal-to-noise ratio
SRP	Solar radiation pressure
SRR	System Requirements Review
SRS	Shock response spectrum
SS	Subsystems
SSPA	Solid-state power amplifier
SSR	Space Sustainability Rating (chapter 15); solid-state recorder (chapter 5)
STM	State transition matrix
STR	Single Target Retrieval
STC	Structures subsystem
STK	Stakeholder requirement prefix
SWOT	Strengths, Weaknesses, Opportunities and Threats
SYS	System-level function or requirement prefix
TBD	To be determined
TC	Telecommand
TCS	Thermal Control Subsystem
TID	Total ionising dose
TLE	Two-line element set
TM	Telemetry
TMR	Triple modular redundancy
TPM	Thruster pointing mechanism
TRL	Technology readiness level
TT&C	Telemetry, Tracking and Command
TUG	Tug spacecraft
TX	Transmitter
UL	Uplink
V&V	Verification and validation
VNB	Velocity-normal-binormal frame
WBS	Work Breakdown Structure
X-band	8-12 GHz radio-frequency band

Symbols

a	Semi-major axis (chapter 3) [m, km]
a_A, a_B	Initial and final orbit semi-major axes (chapter 3) [m, km]
a_t, a_{ph}	Transfer and phasing-orbit semi-major axes (chapter 3) [m, km]
a_{GEO}, a_{GTO}	GEO and GTO semi-major axes (chapter 3) [km]
a_{SRP}, a_{triax}	SRP and Earth-triaxiality accelerations (section 3.5) [m s^{-2}]
A	Area (chapters 9 and 10); generic aperture area (chapter 12) [m^2]
A_i	Insulated area of thermal zone i (chapter 10) [m^2]
A_m, A_{eq}	Member and equivalent structural area (chapter 9) [m^2]
A_{rad}, A_{sa}	Radiator area (chapter 10); solar-array area (chapter 11) [m^2]
$A_{t,X}$	X-band transmit aperture area (chapter 12) [m^2]
B_r	Information bit rate (chapters 5 and 12) [bit s^{-1}]
B_{point}	Payload size per LiDAR point (chapter 5) [bit]
b_i	Quantisation bit depth (chapter 5) [bit]
C	Colour channels (chapter 5); Coriolis matrix (chapter 7) [-]
C_R	Radiation-pressure coefficient (section 3.5) [-]
C_η	Antenna-gain efficiency constant (chapter 12) [dB]
C_{camp}	First campaign cost (chapter 15) [EUR]
C_{recur}	Recurring campaign cost (chapter 15) [EUR]
D	Bit depth (chapter 5) [bit]; antenna diameter (chapter 12) [m]; member diameter (chapter 9) [m]
D_i	Inner tank diameter (chapter 8) [m]
D_{req}	Required data storage (chapter 5) [byte]
d	Slant range (chapter 12); transfer chord length (section 3.5); member diameter (chapter 9) [m]
d_{thruster}	Distance between opposite RCS thrusters (chapter 3) [m]
$\mathbf{d} * k$	Offset vector of body k from reference point (section 3.5) [m]
E	Young's modulus (chapter 9) [Pa]; elevation angle (chapter 12) [deg]
$E * bat$	Required battery energy (chapter 11) [Wh, J]
E_b/N_0	Energy-per-bit to noise-density ratio (chapter 12) [dB]
F	Thrust (chapters 3 and 8) [N]; frame rate (chapter 5) [Hz]; applied force (chapter 9) [N]
F_{axial}, F_{lat}	Axial and lateral launch loads (chapter 9) [N]
F_N, F_V	Normal and velocity-direction thrust components (chapter 3) [N]
F_{REG}	Pressurant regulator factor (chapter 8) [-]
f	Frequency (chapter 12) [Hz, GHz]
f_i	Sampling frequency of group i (chapter 5) [Hz]
f_{ax}, f_{lat}	Axial and lateral natural frequencies (chapter 9) [Hz]
f_x, f_y, f_z	CW acceleration components per unit mass (section 3.5) [m s^{-2}]
G	Antenna gain (chapter 12) [dBi]; plant transfer function (chapter 6) [-]
G/T	Receiver figure of merit (chapter 12) [dB K^{-1}]
G_{strap}	Thermal-strap conductance (chapter 10) [W K^{-1}]
g_0	Standard gravity (chapters 3 and 8) [m s^{-2}]
H	Image height (chapter 5) [pixel]; arm mass matrix (chapter 7) [kg m^2]; wheel momentum (chapter 6) [N m s]
H_{req}	Required reaction-wheel momentum storage (chapter 6) [N m s]
h	Orbit altitude (chapter 3) [m]; structural height (chapter 9) [m]
h_{CG}	Height of centre of gravity above interface (chapter 9) [m]
I	Interface count (chapter 5) [-]; second moment of area (chapter 9) [m^4]; identity matrix (section 3.5 and chapter 7) [-]; inertia tensor [kg m^2] (chapter 6)
I_d	Inherent solar-array degradation factor (chapter 11) [-]
I_{eq}, I_m	Equivalent and member second moment of area (chapter 9) [m^4]
I_{max}	Maximum spacecraft moment of inertia (chapter 6) [kg m^2]
I_{sp}	Specific impulse (chapters 3 and 8) [s]
$I_{x,y,z}$	Principal moments of inertia (chapters 6 and 9) [kg m^2]
i	Inclination (chapter 3) [deg]; index notation [-]; discount rate (chapter 15) [-]
i^*	Internal-rate-of-return discount rate (chapter 15) [-]
$\mathbf{J} * comb$	Combined inertia tensor (section 3.5) [kg m^2]
$\mathbf{J} * k$	Inertia tensor of body k (section 3.5) [kg m^2]
K	Controller gain or matrix (chapters 6 and 7) [-]; effective-length factor (chapter 9) [-]
$K * inst$	MLI installation factor (chapter 10) [-]
$K * mass$	Debris removed per supplied or launched mass (chapter 15) [kg kg^{-1}]
K_{prop}	Propellant intensity per object (chapter 15) [kg object^{-1}]
$K_{prop,mass}$	Propellant per debris mass removed (chapter 15) [kg kg^{-1}]
K_{cost}	Cost intensity (chapter 15) [EUR kg^{-1}, EUR object^{-1}]
$K_{orbital}$	Avoided uncontrolled mass-time (chapter 15) [kg yr]
k_b	Boltzmann constant (chapter 12) [J K^{-1}]
L	Generic length (chapters 7 and 9) [m]; distance from thruster plane to CG (chapter 8) [m]
L_d	Solar-array lifetime degradation factor (chapter 11) [-]
L_e	Effective column length (chapter 9) [m]
L_{arm}, L_{tug}	Robotic-arm and tug length (chapter 7 and section 3.5) [m]
L_{panel}	Target solar-panel span (section 3.5) [m]
L_{tot}	Total structural member length (chapter 9) [m]
L_{FS}	Free-space path loss (chapter 12) [dB]
L_{TX}, L_x	Transmitter and lumped additional losses (chapter 12) [dB]
LM	Link margin (chapter 12) [dB]
M	Protocol margin (chapter 5) [-]; bending moment (chapter 9) [N m]; spacecraft mass matrix [kg] (chapter 6)
M_{base}	Bending moment at structure base (chapter 9) [N m]
M_{HDOP}	Helium mass at depletion of propellant (chapter 8) [kg]
M_{HPDOP}	Helium mass delivered to propellant tanks at depletion (chapter 8) [kg]
M_{margin}	Engineering margin factor in data-rate sizing (chapter 5) [-]
m	Mass (chapters 3, 8, 9, 11 and 13) [kg]
m_0, m_f	Initial and final mass (chapters 3 and 8) [kg]
m_{debris}	Captured debris mass (chapter 3) [kg]
m_{dry}	Dry mass (chapters 3 and 13) [kg]
m_h	Heater sizing margin (chapter 10) [-]
$m_i, \mathbf{r} * i$	Component mass and lateral position vector (chapters 8 and 9) [kg, m]
$m_p, m * prop$	Propellant mass (chapters 3 and 8) [kg]
$m_{launched}$	Mass launched to orbit (chapter 15) [kg]
m_{prim}, m_{sec}	Primary and secondary structure mass (chapter 9) [kg]
m_{rad}	Radiation-shielding panel mass (chapter 9) [kg]
m_s	Storage margin (chapter 5) [-]
$m_{tug,wet}$	Wet tug mass (chapters 3 and 8) [kg]
N	Number of subsystems or interfaces (chapter 5) [-]; number of targets or debris objects (chapter 3) [-]; number of arcs or samples (chapters 3 and 5) [-]
N_{arcs}	Number of half-orbit burn pairs (chapter 3) [-]
N_{cam}, N_{ir}	Number of optical and infrared cameras (chapters 5 and 12) [-]
N_{deb}	Number of debris objects (chapter 3) [-]
N_{ph}	Number of phasing revolutions (chapter 3) [-]
N_i	Number of parameters in sensor group i (chapter 5) [-]
n	Mean motion (section 3.5) [rad s^{-1}]; number of structural members (chapter 9) [-]
NPV	Net present value (chapter 15) [EUR]
P	Load (chapter 9) [N]; pressure (chapter 8) [Pa]; power (chapters 11 and 12) [W]; probability (chapters 4 and 15) [-]
P_{BOL}, P_{EOL}	BOL and EOL solar-array power density (chapter 11) [W m^{-2}]
P_d, P_e	Daylight and eclipse power demand (chapter 11) [W]
$P_{direct}, P_{bending}$	Direct and bending-induced member loads (chapter 9) [N]
P_{cr}, P_{member}	Critical and applied member buckling load (chapter 9) [N]
$P_{EP,in}$	Electric-propulsion input power (chapters 8 and 11) [W]
P_{HBOM}, P_{HDOP}	Helium pressure at begin of mission and depletion (chapter 8) [Pa]
P_{TP}	Regulated propellant tank pressure (chapter 8) [Pa]
P_{TX}	Transmit power (chapter 12) [dBW]
P_{sa}	Required solar-array power at EOL (chapter 11) [W]
$P_\odot$	Solar radiation pressure at 1 AU (section 3.5) [N m^{-2}]
PRF	LiDAR pulse repetition frequency (chapters 5 and 12) [Hz]
PV	Present value (chapter 15) [EUR]
p	Roll angle [rad] (chapter 6)
q	Heat flux (chapter 10) [W m^{-2}]; robotic-joint coordinate (chapter 7) [rad]; pitch angle [rad] (chapter 6)
$\dot{q}, \ddot{q}$	Joint velocity and acceleration (chapter 7) [rad s^{-1}, rad s^{-2}]
$q_{abs}, q_{out}, q_{net}$	Absorbed, gross rejected and net radiator heat flux (chapter 10) [W m^{-2}]
q_{ref}	Desired robotic-arm state (chapter 7) [rad]
Q	Heat rate (chapter 10) [W]
Q_{AOCS}, Q_{TTC}	AOCS and TTC heat loads (chapter 10) [W]
$Q_{EP,heat}$	EP waste heat (chapter 10) [W]
Q_{heater}	Installed heater capacity (chapter 10) [W]
$Q_{loss,i}$	Radiative heat loss from insulated zone i (chapter 10) [W]
Q_{out}	Gross radiator heat rejection (chapter 10) [W]
Q_{rad}	Heat load assigned to radiator (chapter 10) [W]
Q_{strap}	Heat transported by thermal strap (chapter 10) [W]
R	Reliability (chapter 15) [-]; structure circumradius (chapter 9) [m]; range or slant range (chapters 3 and 12) [m]
R_E	Earth radius (chapter 3) [m, km]
R_{HE}	Specific gas constant of helium (chapter 8) [J kg^{-1} K^{-1}]
R_i	Reliability of component i (chapter 15) [-]
R_t	Net cash flow in year t (chapter 15) [EUR]
$R_{cam}, R_{ir}, R_{lidar}$	Camera, IR and LiDAR data rates (chapters 5 and 12) [bit s^{-1}]
$R_{series}, R_{parallel}$	Series and parallel reliability (chapter 15) [-]
R_{total}	Total data rate (chapters 5 and 12) [bit s^{-1}]
r	Position radius or relative-position vector (chapter 3 and section 3.5) [m]; yaw angle [rad] (chapter 6)
r_0, r_f	Initial and final relative-position vectors (section 3.5) [m]
r_{apo}	GTO apogee radius (chapter 3) [km]
r_{KOS1}, r_{KOS2}	Keep-out sphere radii (section 3.5) [m]
S	Solar constant or solar irradiance (chapters 10 and 11) [W m^{-2}]

SE	Solar irradiance at Earth (chapter 11) [W m^{-2}]
T	Orbital period or transfer time (chapter 3) [s]; thrust (chapter 8) [N]; temperature (chapter 10) [K]; economic time horizon (chapter 15) [yr]
T_B	Final-target orbit period (chapter 3) [s]
T_d, T_e	Daylight and eclipse durations (chapter 11) [s, h]
T_{HP}	Hold-point duration (section 3.5) [s]
T_{leg}, T_{tr}, T_{ph}	Leg, transfer and phasing times (chapter 3) [s, d]
T_{rad}, T_{space}	Radiator and deep-space temperatures (chapter 10) [K]
$T_{set,i}$	Minimum controlled temperature of zone i (chapter 10) [K]
T_{sys}	Receiver system noise temperature (chapter 12) [K]
T_{THDOP}	Helium tank temperature at depletion (chapter 8) [K]
T_{tot}	Total thrust (chapter 8) [N]
t	Time (chapter 3) [s]; year index (chapter 15) [yr]; thickness (chapter 9) [m]
t_{burn}	Burn duration (chapters 3 and 8) [s, h]
t_d	Time between desaturation events (chapter 6) [s]
t_{HO}	Handover completion time (chapter 3) [d]
$t_{mission}$	Mission completion time (chapter 3) [d]
t_{ph}, t_{spiral}	Phasing and spiral-transfer time (chapter 3) [s, d]
$t_{risk,reduced}$	Time over which uncontrolled debris risk is reduced (chapter 15) [yr]
$t_{tug,start}$, $t_{tug,arrive}$	Tug spiral start and arrival times (chapter 3) [d]
t_w	Structural member wall thickness (chapter 9) [m]
u	Robotic-arm control input (chapter 7) [rad s^{-2}]
V	Volume (chapter 8) [m^3]; velocity component in local orbital frame (chapter 3) [m s^{-1}]
V_{He}	Required helium tank volume (chapter 8) [m^3, L]
V_{prop}	Propellant volume (chapter 8) [m^3, L]
V_{tank}	Xenon tank volume (chapter 8) [m^3, L]
V_{THDOP}	Propellant-tank gas volume at depletion (chapter 8) [m^3]
$V_{Xe,req}$	Required xenon storage volume (chapter 8) [L]
V_{max}	Maximum approach velocity (section 3.5) [m s^{-1}]
v	Orbital or relative velocity (chapter 3 and section 3.5) [m s^{-1}]
v_A, v_B	Circular velocities in initial and final orbits (chapter 3) [m s^{-1}]
v_c	Circular-orbit velocity (chapter 3) [m s^{-1}]
v_{ex}	Effective exhaust velocity (chapters 3 and 8) [m s^{-1}]
v_{GEO}, $v_{GTO,apo}$	GEO and GTO-apogee orbital velocities (chapter 3) [km s^{-1}]
$v_{t,A}$, $v_{t,B}$	Transfer-ellipse velocities at initial/final orbit (chapter 3) [m s^{-1}]
$\mathbf{v}*0$, $\mathbf{v}*0^+$	Initial and post-burn relative velocity (section 3.5) [m s^{-1}]
W	Image width (chapter 5) [pixel]
x, y, z	CW relative-position components (section 3.5) [m]
$\mathbf{x}$	Relative state vector [$\mathbf{r}$; $\dot{\mathbf{r}}$] (section 3.5) [m, m s^{-1}]
Z	Compressibility factor (chapter 8) [-]
z	Structural coordinate from base (chapter 9) [m]
α	Elevation angle (chapter 12) [deg]; thrust split angle (chapter 3) [deg]; solar absorptivity (chapter 10) [-]; angular acceleration [° s^{-1}] (chapter 6)
$\alpha*overhead$	Protocol overhead factor (chapter 5) [-]
$\alpha*rad$	Radiator solar absorptivity (chapter 10) [-]
β	Solar incidence angle on radiator (chapter 10) [deg]
Δr_{CG}	Lateral centre-of-gravity offset (chapter 8) [m]
ΔT_{allow}	Allowable thermal-strap temperature drop (chapter 10) [K]
ΔV	Velocity increment (chapters 3 and 8) [m s^{-1}]
ΔV_1, ΔV_2	First and second transfer burns (chapter 3) [m s^{-1}]
ΔV_E	Edelbaum low-thrust velocity increment (chapter 3) [m s^{-1}]
ΔV_{leg}	Total velocity increment per leg (chapter 3) [m s^{-1}]
ΔV_{ph}	Phasing velocity increment (chapter 3) [m s^{-1}]
ΔV_{RPO}	RPO velocity increment (section 3.5) [m s^{-1}]
ΔV_{SK}	Stationkeeping velocity increment (section 3.5) [m s^{-1}]
ϵ_{eff}	Effective MLI emissivity (chapter 10) [-]
ϵ_{rad}	Radiator infrared emissivity (chapter 10) [-]
η	Aperture efficiency (chapter 12) [-]; generic subsystem efficiency (chapters 8 and 11) [-]
η_{EP}	Electric-propulsion efficiency (chapters 8 and 11) [-]
η_{cell}	Solar-cell efficiency (chapter 11) [-]
η_d, η_e	Daylight and eclipse power-path efficiencies (chapter 11) [-]
η_{har}, η_{pcdu}, η_{bat}	Harness, PCDU and battery efficiencies (chapter 11) [-]
λ	Wavelength (chapter 12) [m]; failure rate (chapter 15) [h^{-1}]
μ_E	Earth gravitational parameter (chapter 3) [m^3 s^{-2}]
ν_{start}	Spiral-arc start true anomaly (chapter 3) [deg]
ρ	Material density (chapter 9) [kg m^{-3}]
ρ_{HBOM}	Helium density at begin of mission (chapter 8) [kg m^{-3}]
$\rho_{LMP-103S}$	LMP-103S density (chapter 8) [kg m^{-3}]
$\rho_{Xe,storage}$	Xenon storage density (chapter 8) [kg L^{-1}]
σ	Stefan-Boltzmann constant (chapter 10) [W m^{-2} K^{-4}]
σ_{max}	Maximum compressive stress (chapter 9) [Pa]
σ_{yield}	Yield stress (chapter 9) [Pa]
τ	Applied torque (chapters 6 and 8) [N m]
τ_d	Disturbance torque (chapter 6) [N m]
τ_{dist}	CG-offset disturbance torque (chapter 8) [N m]
τ_{req}	Required control torque (chapter 6) [N m]
$\tau_{x,y,z}$	Torque along principle axes (chapter 6) [Nm]
ω	Angular rate (chapter 6) [rad s^{-1}]; target tumble rate (section 3.5 and chapter 7) [rad s^{-1}]
ω_0	Orbital angular rate used for disturbance torques (chapter 6) [rad s^{-1}]
ω_{max}	Maximum commanded slew rate (chapter 6) [rad s^{-1}]
ϕ, θ	Roll/pitch angles (chapter 6) [rad]; plane-change angle (chapter 3) [deg]; gimbal or pointing angle (chapter 8) [deg]
ψ	Yaw angle [deg]
Ω	Right Ascension of the Ascending Node (chapter 3) [deg]; angular rate in spacecraft body frame (chapter 6) [deg/s]
Φ	State transition matrix (section 3.5) [-]
Φ_{rr}, Φ_{rv}	STM position-position and position-velocity blocks (section 3.5) [-, s]

1. Executive Overview

Mission Context and Objectives

The Resource Extraction Autonomous Vehicle for Environmental Recovery (REAVER) is a reusable active debris removal mission for the geostationary Earth orbit (GEO) graveyard region. GEO objects do not naturally de-orbit because atmospheric drag is negligible at this altitude [1]. This makes defunct GEO spacecraft a long-term collision and fragmentation risk for operational satellites. The Inter-Agency Space Debris Coordination Committee (IADC) guidelines identify debris mitigation as necessary to limit the long-term growth of the debris environment [2].

REAVER addresses this problem by capturing large non-cooperative[1] GEO debris and transporting it to a recycling hub. The mission is designed to remove five defunct GEO spacecraft within one operational year. The target objects are selected from a filtered GEO debris catalogue using orbital, mass, ownership and capture-interface constraints. The mission shall avoid the creation of additional debris during rendezvous, proximity operations, capture, transport and handover.

The mission is also shaped by legal, commercial and sustainability drivers. The Outer Space Treaty keeps space objects under the jurisdiction and control of their launching state [3]. The Liability Convention makes liability for damage caused by space objects an important concern for satellite operators and states [4]. REAVER therefore offers value by reducing long-term GEO risk, supporting compliance with debris-mitigation expectations, and enabling future circular-economy operations through delivery of debris to a recycling hub.

Mission Design and Concept of Operations

Five mission concepts were considered during the trade-off: Single Target Retrieval, Multiple Target Retrieval, Pusher Swarm, Mothership and Tugs, and Independent Spacecraft. The Mothership and Tugs architecture was selected because it gives the best balance between technical performance, launch mass, operational flexibility, reusability and feasibility.

The final REAVER architecture consists of one mothership and five reusable tugs, giving one tug per debris object. This updates the midterm four-tug concept and simplifies the mission sequence, since the mothership no longer needs to transport the fifth debris object itself. The mothership carries the tugs, performs the complex sensing, robotic and docking functions, and deploys one tug at each target. Each tug then captures its assigned debris object and transports it to the recycling hub. The capture processes can be seen in figure 1.1.

The mission uses six spacecraft modes: safe mode, commissioning, long-range rendezvous, proximity operations, capture and control, and standby. In a nominal cycle, the mothership transfers to the selected target, approaches using absolute navigation, and switches to relative navigation once close-range sensors are more accurate [5]. It then estimates the target motion and liquid apogee engine nozzle location, aligns a tug using the robotic arm, and brings the tug apogee engine probe to the capture position. After capture is confirmed, the tug carries the debris to the recycling hub, while the mothership continues the campaign.

The astrodynamics analysis supports the mission by filtering the GEO debris catalogue, selecting a feasible five-target sequence and sizing the transfers. Target filtering considers orbit, mass, ownership, Right Ascension of the Ascending Node and liquid apogee engine compatibility. The mothership trajectory is modelled with impulsive chemical manoeuvres, including Hohmann transfers, circularisation and phasing, using standard orbital-mechanics relations [6]. The tug transfers are modelled as low-thrust electric-propulsion spirals, with the tug (ΔV) estimated using Edelbaum's method for combined altitude and plane changes [7]. A Python optimiser is used to minimise propellant use across possible five-target sequences, while GMAT (General Mission Analysis Tool) simulations provide a higher-fidelity check of the analytical (ΔV), propellant and timeline results. The final mission duration is 292 d, leaving 73 d of margin against the one-year requirement.

[1] Non-cooperative objects in space are objects that cannot actively support rendezvous, docking, or capture.

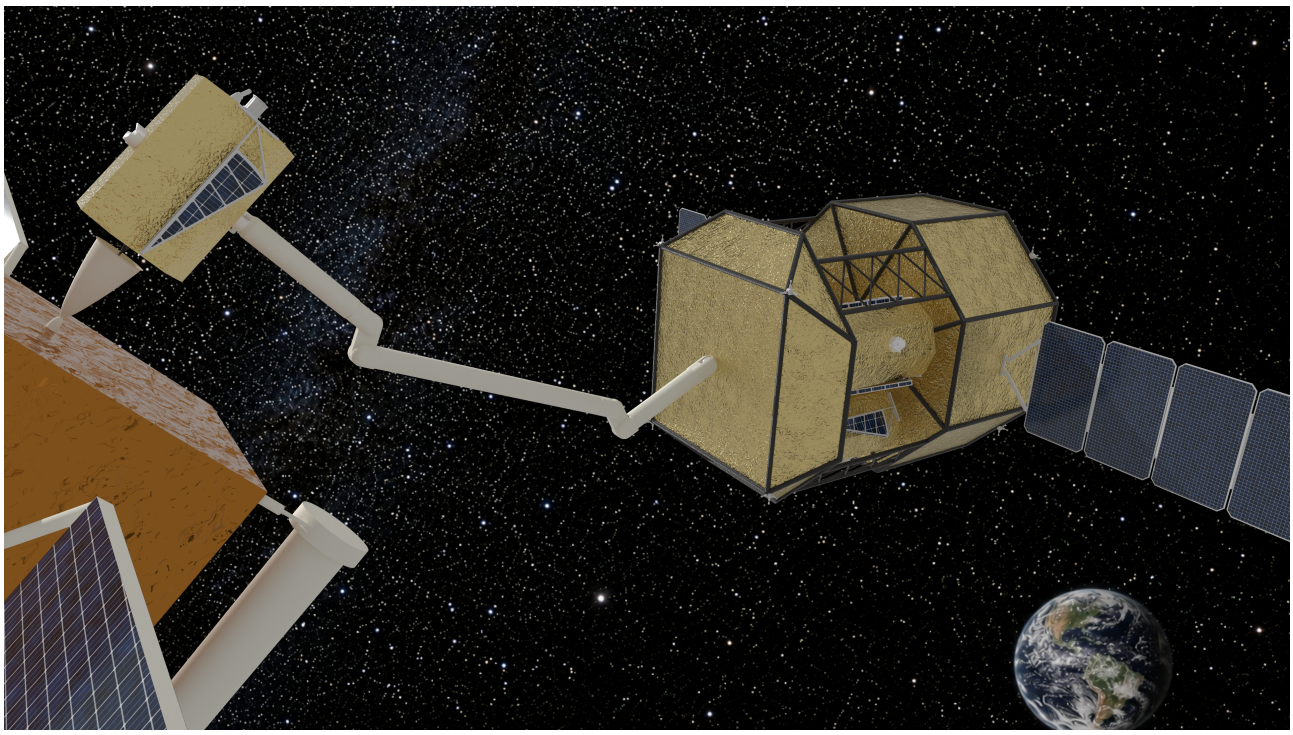

Figure 1.1: Mothership positioning tug with robotic arm prior to capture sequence (background generated with ChatGPT)

Subsystem Design

Command and Data Handling

The command and data handling (C&DH) subsystem manages commands, telemetry, onboard storage, data routing and onboard computing. The architecture keeps the main command hierarchy centralised, while high-rate processing is assigned to dedicated subsystem computers. This is required for target detection, relative navigation and pose estimation during close-range debris operations [8]. SpaceWire is used for high-rate payload data paths [9], while lower-rate housekeeping data use simpler buses such as CAN (Controller Area Network and RS-422. CCSDS (Consultative Committee for Space Data Systems) packet standards support command and telemetry handling [10], and CCSDS security standards protect critical command links [11].

Attitude and Orbit Control System

The attitude and orbit control subsystem (AOCS) provides orbit control, attitude control, pointing, stabilisation and proximity-manoeuvre support. It follows standard spacecraft attitude and orbit control requirements [12]. During debris operations, it uses relative-navigation data to hold position, align the tug, synchronise with target rotation and support detumbling. The main design choice is to keep the complex guidance and control functions on the mothership, while the tugs remain simpler and only require control authority for capture confirmation, departure and debris transport.

Capture Subsystem

The capture subsystem is split between the mothership and the tugs. The mothership uses a seven-degree-of-freedom robotic manipulator to position each tug, since robotic systems provide flexibility for non-cooperative spacecraft with uncertain geometry [13]. The tug uses an apogee engine probe mechanism inspired by GEO servicing heritage [14]. This allows capture through the liquid apogee engine nozzle, avoiding the need for a pre-installed docking interface. Robust closed-loop control is required because target motion, sensor noise and contact loads are uncertain during capture [15]. This makes capture one of the main technologies requiring later hardware-in-the-loop testing.

Propulsion

The mothership uses an LMP-103S green monopropellant system, selected for its lower toxicity compared with hydrazine and its flight heritage in high-performance green propulsion systems [16]. The system includes four 22 N main thrusters, twenty-four 5 N reaction-control thrusters, four propellant tanks and helium pressurisation. The feed system follows conventional monopropellant design practice [17], and the tanks are arranged symmetrically to reduce centre-of-gravity shifts. The tugs use xenon electric propulsion because Hall thrusters provide high specific impulse for long-duration debris transport [18]. The selected electric thruster is the PPS-X00 Hall thruster [19]. A small xenon cold-gas branch provides tug reaction-control capability.

Structures
The structural design is driven by launch loads, tug accommodation, propellant tank support, the robotic arm and the docking interface. The primary structure follows ECSS (European Cooperation for Space Standardization) structural design logic [20]. A stiff central structure carries the main tanks, tug deployment rail, robotic arm and docking port, while external truss elements support the radial tug layout. Preliminary checks show positive margins for static strength, buckling and natural frequency, indicating that the structure is feasible at preliminary design level.

Thermal Control Subsystem
The thermal control subsystem (TCS) keeps batteries, avionics, propulsion components, payload sensors and tug electric-propulsion hardware within their allowable temperature limits. The design uses a passive-first approach with radiators, multilayer insulation, coatings, thermal straps and thermal isolation, consistent with ECSS thermal-control practice [21]. The mothership uses 5.0 m^2 of radiator area, 25 m^2 of multilayer insulation and 100 W of installed heater capacity. Each tug uses 1.6 m^2 of radiator area, 2.5 m^2 of multilayer insulation and 20 W of heater capacity. The main tug thermal drivers are electric-propulsion waste heat and battery survival in low-power modes.

Electrical Power System
The electrical power subsystem (EPS) generates, stores, conditions and distributes power. The mothership is sized by proximity operations, while the tug is sized by electric-propulsion thrusting. Solar-array sizing includes beginning-of-life and end-of-life performance to account for degradation. The tug solar array uses an UltraFlex-style concept inspired by the Mars InSight solar array [22], providing high deployed area while remaining compact during storage. Tug thrusting is stopped during eclipse to limit battery size. The main EPS concern is the small tug end-of-life power margin, which should be protected in later design iterations.

Telemetry, Tracking and Command
The telemetry, tracking and command (TT&C) subsystem provides communication with ground operations. S-band is used for housekeeping telemetry and telecommand because it is a standard spacecraft communication band [23]. The mothership also uses X-band for high-rate payload data during proximity operations and capture. Redu is the primary ground station, with Kourou as secondary support. The S-band links close with large margins, while the X-band payload link has a thinner margin of 3.64 dB. Data compression, onboard storage and careful downlink scheduling are therefore required to protect this link.

Risk, Sustainability and Verification

The final risk assessment updates the midterm risk register using a likelihood–consequence method. This approach follows ECSS risk-management practice [24]. Most risks are reduced to low or medium severity after mitigation. Three residual high risks remain: collision or critical-system damage, GNC (Guidance, Navigation, and Control Subsystem)/autonomy failure, and target fragmentation during capture. These risks remain high because their consequences are severe even when their likelihood is reduced.

A new detailed-design risk is added for the robotic arm. The robotic arm is essential for tug deployment, alignment, capture support and handover. If its technology readiness is too low, the full mission architecture is affected. The mitigation is to mature the arm through breadboard testing, representative capture tests and hardware-in-the-loop demonstrations. This follows standard TRL (Technology Readiness Level) maturation logic [25].

The sustainability assessment is performed as a design-level Life Cycle Sustainability Analysis. ESA's space-system LCA (Life-Cycle Assessment) approach is used as the main reference for environmental assessment [26]. The main benefit is the removal of 10 050 kg of uncontrolled GEO debris in one campaign. This gives approximately 2.52 kg of debris removed per kilogram launched. The main environmental burdens are manufacturing, launch, propellant use, high-reliability testing and the risk of creating debris during capture. These are mitigated through reuse, non-toxic mothership propellant, electric propulsion on the tugs and conservative capture operations.

The economic assessment shows that the original 200M€ cost target is not met if treated as a strict requirement, with the updated investment cost estimated at approximately 250M€. At a service price of 60M€ per removal, the first campaign generates 300M€ in revenue and gives a nominal surplus of 50M€. However, the base mission alone is not attractive on a discounted basis, with a negative net present value and an internal rate of return of only 3.63 %. The investment case becomes viable when the mothership and tugs are reused for extension campaigns after refuelling at the recycling hub. In the extended case, the internal rate of return increases to 26.49 %, showing that REAVER's financial value depends strongly on reuse, follow-on contracts and keeping extension costs close to 10M€ per year.

Verification and validation are planned through inspection, analysis, test and demonstration. This follows ECSS verification practice [27]. Environmental and functional testing follow ECSS testing logic [28]. Some requirements remain open because they need higher-fidelity simulation, hardware-in-the-loop testing or final interface definition. The most important open verification items are capture-interface alignment, closed-loop fine velocity control and full RPOD (Rendezvous, Proximity Operations & Docking Subsystem) /capture demonstration.

Future Development and Final Status

The post-DSE development plan follows a V-model. The next phase should close the remaining TBD values, freeze interfaces, update the target list, confirm ownership and recycling-hub assumptions, and mature the highest-risk technologies. This is consistent with standard space-project development logic [29]. The schedule includes the System Requirements Review, the Preliminary Design Review, the Critical Design Review, manufacturing, Assembly–Integration–Testing, the acceptance review, the flight-readiness review, and launch-site integration. Schedule planning should include margin before the Critical Design Review and before environmental acceptance testing, because late design changes at those stages would be costly [30].

The manufacturing, assembly and integration plan follows a make-buy strategy. Mature components are bought where possible, while REAVER-specific hardware such as the primary structure, capture system, tug interfaces, propulsion integration and harnessing is developed separately. One qualification tug is built before the five flight tugs to reduce integration risk. The most important mission-specific test is a hardware-in-the-loop RPOD and capture rehearsal, combining the RPOD sensors, C&DH, AOCS, robotic arm, tug interface and representative tumbling target.

Overall, the final REAVER design demonstrates that reusable geostationary Earth orbit debris removal is technically feasible at preliminary system level. The architecture removes five non-cooperative spacecraft, with a combined debris mass of more than 10 t, within one operational year while closing the main mass, power, propulsion, communication and structural budgets. Its strongest value is not only the first removal campaign, but the creation of reusable infrastructure that can support repeated debris-recovery missions and future orbital recycling. The main work after the DSE is to mature the autonomous rendezvous and capture sequence, complete detailed structural and thermal analyses, protect the thin power and communication margins, refine the cost model, and demonstrate safe capture through representative ground testing.

2. Market Analysis

The commercial feasibility of REAVER depends on a clear customer base, a credible competitive position, and a financially viable service model. This model rests not only on the removal of defunct spacecraft but also on the recovery and reuse of orbital assets through in-situ remanufacturing, which opens an additional revenue stream and underpins the wider circular space economy that REAVER seeks to enable. This chapter analyses the market for active debris removal (ADR) in the geostationary orbit (GEO) region, with a focus on defunct GEO spacecraft that remain in orbit and create long-term operational and legal risks.

First, section 2.1 defines the GEO debris market context and section 2.2 identifies the main customer segments for REAVER. Section 2.3 compares REAVER with adjacent active debris removal and in-orbit servicing systems to establish its competitive position. After this, section 2.4, sizes the market opportunity using REAVER's mission capacity and expected removal price. Section 2.5 also discusses the added value of the service; future market development is discussed in section 2.6, and the role of regulation in creating demand. Finally, the market environment is assessed through a Political, Economic, Social, Technological, Legal and Environmental (PESTLE) analysis (section 2.7), followed by a Strengths, Weaknesses, Opportunities and Threats (SWOT) analysis (section 2.8).

2.1. Market Context

The GEO, which sits at approximately 35786 km altitude, hosts the most commercially valuable orbital real estate above Earth. Slots in this band are fixed relative to the Earth's surface and allocated by the International Telecommunication Union (ITU); once a satellite ceases operation, it occupies that slot without performing any useful function. The ITU radio regulations require operators to move end-of-life spacecraft to a graveyard orbit at least 300 km above GEO [31].

Unlike low Earth orbit (LEO), where atmospheric drag eventually removes debris over years to decades, objects in GEO experience no significant drag. Without active removal, each defunct spacecraft remains in orbit indefinitely, accumulating collision risk that threatens operational assets. The Inter-Agency Space Debris Coordination Committee (IADC) has warned since 2002 that failure to actively manage the GEO population will produce an unrecoverable growth in fragmentation debris [32]. This creates a clear market driver: satellite operators and their insurers face a growing liability that can only be resolved through ADR. A second driver is economic: because launching mass to GEO is so costly, the material in defunct satellites retains real value, and recovering and remanufacturing it in situ turns debris into a reusable resource [33].

The United States Federal Communications Commission introduced a five-year de-orbit rule for new LEO satellites in 2022 and has signalled interest in extending similar logic to GEO [31]. The European Union's Space Programme Regulation and ESA's Zero Debris Charter, adopted in 2023, commit member-state agencies and operators to debris-neutral operations by 2030 [1]. These regulations convert a voluntary sustainability ambition into an anticipated obligation, and it is this obligation that justifies the demand for REAVER.

2.2. Target Market Segmentation

Three customer segments are identified, differentiated by procurement authority, primary motivation, and contractual form. Table 2.1 summarises the segmentation matrix.

Table 2.1: Customer segmentation matrix for REAVER removal services.

Segment	Primary motivation	Procurement path	Contract type
Commercial satellite operators	Insurer pressure; regulatory compliance	Direct service contract with REAVER	Fixed-price removal per object
Space agencies (ESA, NASA, JAXA)	Policy compliance; heritage asset management	Government procurement or co-funding agreement	Cost-plus or milestone payment
Recycling hub operator	Supply for on-orbit materials	Offtake agreement for delivered hardware	Mass-based payment (secondary revenue stream)

[1] https://www.esa.int/Space_Safety/Clean_Space/The_Zero_Debris_Charter [accessed 12 June 2026]

Commercial satellite operators represent the primary and highest-volume segment. Large fleet operators such as SES, Eutelsat, Intelsat, and Telesat each maintain dozens of GEO spacecraft and are responsible for the corresponding number of end-of-life spacecraft. Each defunct satellite represents an unresolved liability under the 1972 Liability Convention [4] and a potential interference risk to adjacent spacecraft. Operators have both regulatory and reputational incentives to contract removal services before mandated compliance deadlines take effect.

Space agencies constitute the secondary segment. ESA's ClearSpace-1 contract and NASA's ongoing investment in on-orbit servicing, assembly, and manufacturing (OSAM) demonstrate that agencies will fund commercial ADR providers as part of their technology development policy [34]. Agency procurement is typically slower and more process-intensive than commercial contracting, but fixed contracts from this segment provide revenue certainty during the early market phase.

The recycling hub operator is an alternative revenue channel. REAVER delivers derelict spacecraft to a pre-existing hub facility for component reclamation. The operator of that hub, which is outside the scope of the REAVER mission design, may generate some income from the delivered mass of recoverable materials.

2.3. Comparable Products and Competitive Landscape

No commercially available system performs multi-target, uncooperative active debris removal in the GEO regime. REAVER has no direct commercial competitors as of mid-2026. The competitive landscape, therefore, consists of systems that are either different orbit regimes (LEO ADR) or functionally adjacent (GEO servicing of cooperative targets).

Three systems serve as the primary benchmarks. Northrop Grumman's Mission Robotic Vehicle (MRV), developed under the DARPA Robotic Servicing of Geosynchronous Satellites (RSGS) programme, is the closest system by orbital regime [35]. It targets GEO, operates a robotic arm capable of grasping non-standard interfaces, and is scheduled for launch in summer 2026. However, MRV is a government programme that serves pre-approved US government satellite operators; it does not offer commercial removal services on the open market, and its primary mission is inspection and life extension rather than end-of-life removal, recycling and reuse[2]. Astroscale's ELSA-m (End-of-Life Services by Astroscale) is the leading commercial ADR concept in LEO [3]. ELSA-m requires a docking plate to be pre-installed on client satellites at manufacture, restricting its capture envelope to new spacecraft and excluding the legacy GEO abandoned population entirely. ClearSpace-1, contracted by ESA, is a single-target LEO demonstration mission targeting Vespa debris at approximately 800 km altitude [4]. Table 2.3 presents an eight-parameter comparison across the three benchmark systems.

Table 2.3: Competitive Comparison Matrix

Parameter	REAVER	MRV / DARPA RSGS	Astroscale ELSA-m	ClearSpace-1
System architecture	1 mothership + 5 (reusable) autonomous tugs	Single robotic servicer + mission extension pods	Single servicer (multi-client)	Single multi-arm servicer
Target orbit	GEO	GEO	LEO	LEO
Capture approach	Robotic arm + Apogee Engine Probe mechanism	Cooperative docking arm (RSGS interface)	Passive docking plate (pre-installed at manufacture)	Multi-arm active capture
Target type	Uncooperative defunct satellites	Cooperative (mainly) - has some non-cooperative target handling	Semi-cooperative (docking plate required)	Uncooperative
Targets per mission	5 (base, 1 yr); 20 (possible extension, 4 yr via hub refuelling)	3 initially (designed for multiple GEO servicing operations)	Multiple sequential captures	1
Propulsion heritage	HPGP LMP-103S mothership; PPS-X00 Hall-effect tugs	Chemical bipropellant	Electric propulsion	Chemical
Mission status (mid-2026)	Design phase; launch date prior to Janurary 1st 2035	Launch summer 2026 [2]	Target launch ~2028 [3]	Target launch ~2029 [4]
Commercial scalability	Fleet expandable; hub refuelling enables multi-year operations without re-launch	Government access only; single vehicle	Fleet concept planned; legacy satellites excluded by design	Single vehicle; single target per mission

The comparison confirms that REAVER's GEO coverage, uncooperative capture architecture, and multi-target fleet design are not replicated by any current or near-term commercial entrant. The primary competitive tension is not direct product rivalry but market inertia: the current status for satellite operators is to absorb the liability risk of derelict spacecraft. REAVER must therefore prove its value against this do-nothing baseline as much as against any direct competitor.

The value proposition REAVER offers begins with it being the only system capable of addressing the existing legacy GEO derelict population, requiring no client hardware, no docking plate, and no prior operator engagement beyond a signed removal contract. Second, the fleet architecture distributes mission cost across five removals per base mission, yielding €40 M per removal. Third, hub-based refuelling enables an extended four-year mission, driving the cost per removal down to €12 M.

2.4. Market Sizing

REAVER's addressable market is the supply of intact abandoned spacecraft currently occupying the GEO regime. ESA's DISCOS catalogue records 807 payload objects in the GEO belt as of 2026, of which the majority are non-operational.[5]. This population grows in the absence of active removal, since no natural decay mechanism exists at GEO altitude.

REAVER's reach to this population is constrained by the tug's orbital regime (where the tug can go), its Δv budget, and the capture mechanism's mass rating. The exact object count satisfying all constraints simultaneously requires a targeted literature study of the ESA DISCOS orbital catalogue[6] and is not expressed here as a fixed percentage, as it would require assumptions on the mass and attitude distribution of the GEO derelict population that are not established in public literature. For revenue modelling, the sizing is therefore driven directly by REAVER's own mission capacity: five removals in the base year and up to 20 removals over a four-year extended mission enabled by hub refuelling.

The target service price of €60 M per removal is set above the unit cost floor of €50 M, which is derived from the re-iterated €250 M total programme cost distributed across five base-mission captures, and below the implied cost of any single-target GEO mission, for which no publicly contracted comparable yet exists. Table 2.5 presents the revenue scenarios at this price point.

Table 2.5: REAVER market sizing: revenue scenarios by mission duration. Net is calculated against the €250 M base programme cost; the extended mission incurs additional propellant and operations expenditure not captured in this table.

Scenario	Duration	Removals	Service price	Revenue	Net
Break-even (base)	1 yr	5	€50 M	€250 M	€0 M
Base case	1 yr	5	€60 M	€300 M	+€50 M
Extended mission	4 yr	20	€60 M	€1160 M	+€910 M

The extended mission scenario shows that REAVER's economic case improves with duration. The €250 M fixed development and launch cost is sunk at mission start; each additional year of hub-refuelled operations adds removal revenue at near-zero incremental fixed cost, since propellant is the only material variable. The €10 M annual operating charge covers ground operations and mission control (€4-5 M), propellant resupply and hub-interface fees (€3-4 M), and an insurance and contingency reserve (€1-2 M). This estimate includes a conservative margin to absorb uncertainty in propellant prices and early-phase operational inefficiencies at GEO altitude. The €50 M break-even price also establishes the floor for commercial contracting: any operator negotiation below this level converts the base mission from a marginal surplus into a loss, providing a principled lower bound for pricing discussions.

2.5. Added Value

REAVER creates value at three levels: operational cost reduction per removal, extinction of satellite operator liability, and contribution to a circular economy in orbit.

The most direct value dimension is cost per removal. Any single-target mission must recover all development,

[2] https://www.northropgrumman.com/wp-content/uploads/Mission-Robotic-Vehicle-MRV-fact-sheet.pdf [accessed 12 June 2026]

[3] https://www.astroscale.com/en/missions/elsa-m [accessed 12 June 2026]

[4] https://clearspace.today/ [accessed 12 June 2026]

[5] https://sdup.esoc.esa.int/discosweb/statistics/ [accessed 14 June 2026]

[6] https://discosweb.esoc.esa.int [accessed 12 June 2026]

launch, and operations costs from one revenue event. REAVER spreads those same fixed costs across five removals in the base mission, yielding €40 M per removal. In the extended scenario, hub-based refuelling adds only incremental propellant cost for 15 additional removals, reducing the cost per removal to €12 M. This unit-cost advantage is structural and cannot be replicated by single-vehicle architectures, regardless of how they are optimised.

The second value dimension is legal liability extinction. Under the 1967 Outer Space Treaty and the 1972 Liability Convention, the state of registration retains permanent legal responsibility for its space objects [3, 4]. A satellite operator whose derelict spacecraft collides with a third-party asset may face indemnification claims that are uncapped in principle. A removal service transfers the logistical burden of decommissioning to REAVER, while the operator retains a record of compliance with applicable regulations. This liability transfer has a measurable monetary value and is directly linked to insurance reductions for operators maintaining active spacecraft in GEO.

The third value dimension arises from material reclamation at the hub. A retired GEO satellite contains aluminium structural members, titanium propellant tanks, solar panel substrates, and, in some cases, residual xenon propellant. Delivery of this hardware to the recycling hub enables component-level reclamation, reducing the cost of future on-orbit manufacturing. Although hub offtake pricing is not yet established in the base case, the circular economy pathway reduces long-run material costs across the in-orbit services sector.

2.6. Future Market Prediction and New Market Establishment

The active debris removal market was valued at approximately $452 M in 2024 and is projected to reach $2.52 B by 2032, representing a compound annual growth rate of 29.9% [7]. Three structural factors will drive growth in the GEO ADR market over the next decade. First, the regulatory environment is tightening across all major spacefaring jurisdictions. The FCC five-year de-orbit rule for LEO satellites, adopted in 2022, has established a precedent for mandatory decommissioning timelines that is expected to propagate to GEO [31]. Second, the GEO derelict population continues to grow at 15-25 objects per year, increasing the aggregate liability exposure of operators who have not yet contracted removal services. Third, the maturation of commercial in-orbit servicing capabilities, evidenced by Northrop Grumman's Mission Extension Vehicle (MEV) operations and the imminent launch of MRV, is normalising the concept of third-party satellite intervention and reducing the perceived reputational risk for operators who engage external service providers[8].

REAVER participates in establishing the market rather than merely entering it. As of mid-2026, no commercial provider has successfully removed a GEO derelict object. A successful REAVER base mission would constitute a first-of-kind operational demonstration that validates the commercial model and creates reference pricing for the GEO segment. This pioneer advantage is substantial: the first operator to demonstrate GEO multi-target ADR sets the technical and contractual norms that subsequent entrants must conform to, and accumulates mission heritage that cannot be replicated without completing actual removals.

The long-run market structure is expected to converge on a small number of specialised providers serving different orbital regimes and customer types. In the GEO segment, REAVER's fleet architecture and hub-based refuelling capability present structural barriers to entry, specifically, the capital requirement for the operational complexity of multi-vehicle autonomous rendezvous at GEO altitude. Entrants arriving after REAVER's operational window will face a market in which REAVER has already demonstrated operational capability and established contractual relationships with the primary customer segment.

2.7. PESTLE Analysis

Table 2.7 summarises the macro-environmental factors affecting REAVER's market position across the six PESTLE dimensions.

Table 2.7: PESTLE analysis for REAVER's GEO active debris removal market.

Dimension	Key factors	Market implication
Political	OST Article VIII (permanent state ownership of space objects); Liability Convention 1972; ITU frequency coordination obligations; ESA Zero Debris Charter (2023);	Regulatory trajectory favours mandatory decommissioning; ownership ambiguity creates contracting friction that must be resolved through operator consent agreements before each removal

[8] https://www.northropgrumman.com/wp-content/uploads/Mission-Extension-Vehicle-MEV-fact-sheet.pdf [accessed 12 June 2026]

Table 2.7 – Continued from previous page

Dimension	Key factors	Market implication
Economic	ADR market CAGR 29.9 % through 2032 [8]; GEO operators collectively operate over $100 B in satellite assets; €250 M REAVER total mission cost	Strong market growth provides revenue certainty over the mission horizon; structural cost-per-removal advantage supports competitive pricing against single-target analogues
Social	Growing institutional and public awareness of orbital sustainability; increasing media coverage of conjunction events; EU discussions beginning to address space sustainability	Operator reputational incentive to demonstrate proactive debris management; sustainability narrative supports contract negotiations with space agencies
Technological	GEO autonomous rendezvous at TRL 5-6; uncooperative capture at TRL 4-5; HPGP and Hall-effect propulsion with flight heritage; autonomous guidance, navigation, and control maturing	Propulsion subsystems carry low technical risk; rendezvous and capture represent the primary development risk; programme schedule is driven by capture mechanism maturation
Legal	No binding international ADR licensing framework	Compliance adds complexity; absence of an international framework requires an operator-by-operator contractual approach to each removal
Environmental	Kessler cascade risk in GEO without active management [32]; ITU frequency spectrum at risk from uncontrolled GEO population growth; circular economy benefits through on-orbit material reclamation	Cascade and spectrum risk drive a demand for removal services; in addition to debris removal, material reclamation is monetisable as-well.

2.8. Market SWOT Analysis

The following SWOT analysis is framed at the market level, addressing REAVER's competitive position and commercial environment.

Table 2.8: Market SWOT analysis for REAVER.

Strengths	**Weaknesses**
• Only multi-target uncooperative GEO ADR architecture in development • Fleet design drives cost per removal to €40 M (base) and €12 M (extended) • Hub-based refuelling enables multi-year revenue without a second launch campaign • No client hardware requirement expands the addressable debris pool	• High TRL risk at GEO for autonomous uncooperative rendezvous and capture • €200 M upfront cost requires financing before the first revenue event • Hub operator is a third-party dependency outside REAVER's design control • Single launch vehicle (Falcon 9) creates schedule concentration risk
Opportunities	**Threats**
• ADR market growing at 29.9 % CAGR through 2032 [8] • Tightening regulation converting voluntary sustainability commitments to compliance obligations • Potential ESA or national agency anchor contract to de-risk the early commercial phase • Recycling revenue upside if hub offtake market matures beyond the base case	• No binding international legal framework creates per-removal contracting uncertainty • Government ADR programmes (MRV/RSGS) could absorb institutional budgets without opening a commercial market • Future commercial entrants could decrease GEO ADR pricing once the market has been demonstrated • A single mission failure eliminates base-case revenue, while all fixed programme costs are already paid

[8] https://www.intelmarketresearch.com/active-debris-removal-market-6340 [accessed 12 June 2026]

3. Mission Design & Concept of Operations

This chapter defines the mission design and concept of operations for REAVER. It first summarises the design heritage and explains how the selected Mothership and Tugs (M&T) architecture was chosen from the previous concept trade-off. The chapter then describes the overall system architecture, including the mothership, the tugs, the deployment ring, the docking interfaces, and the main internal subsystem layout.

The operational concept is then presented through the main spacecraft modes, from safe mode and commissioning to long-range rendezvous, proximity operations, capture, tug release, and standby. The chapter also updates the functional breakdown structure (FBS) and functional flow diagram (FFD), linking the system functions to the mission sequence. Finally, the astrodynamics analysis is described, including target filtering, transfer modelling, capture-sequence optimisation, recycling hub orbit selection, General Mission Analysis Tool (GMAT) validation, and rendezvous and proximity operations (RPO) modelling.

3.1. Design Heritage

This section summarises the concept trade-off process that resulted in the selected REAVER mission architecture.

Five feasible high-level mission concepts were considered: Single Target Retrieval (STR), Multiple Target Retrieval (MTR), Pusher Swarm (PSW), Mothership and Tugs (M&T), and Independent Spacecraft (ISC). Each concept was analysed in terms of mission profile, concept-specific (ΔV), propulsion system compatibility, capture, AOCS architecture, mass, and schedule. The concepts are summarised in table 3.1.

Concept	Main description	Main trade implication
STR	One spacecraft captures and returns one debris object at a time, refuelling between captures.	Low system complexity, but inefficient due to repeated back-and-forth transfers and a single point of failure.
MTR	One spacecraft visits all five debris objects sequentially and stores them before returning to the recycling hub.	Efficient trajectory, but very high dry mass and propellant mass due to carrying multiple debris objects.
PSW	Multiple small spacecraft form a distributed pusher swarm around the debris object.	High redundancy and scalability, but strong coordination complexity and high dependence on control algorithms.
M&T	One mothership performs complex operations and deploys tugs that transport debris back to the hub.	Balanced architecture with low equivalent launch mass, parallel tug operations, and reusable elements, but with higher system complexity.
ISC	Five independent spacecraft each capture and return one debris object.	High redundancy and parallel operations, but high launch mass, duplicated subsystems, and increased operational burden.

The mission and subsystem trade-offs were performed using weighted decision matrices, supported by sensitivity analyses to assess the robustness of the selected architecture. At mission level, the M&T concept achieved the highest total score, mainly due to its strong Technical Performance and Innovation scores, its low equivalent launch mass, and its ability to remain within the debris retrieval schedule. In parallel, subsystem-level trades supported this architecture by selecting LMP-103S for the mothership chemical propulsion system, the PPS-5000 Hall thruster for the tugs, the robotic manipulator as the mothership capture system, and the Apogee Engine Probe (AEP) mechanism as the tug capture system. The sensitivity analysis confirmed that the M&T architecture remained the most balanced and frequently winning concept under changing weight assumptions.

3.2. System Architecture

This section outlines the REAVER system architecture. The mission consists of 2 types of spacecraft; the mothership and the tug. The role of the mothership is to transport and attach the tugs to the debris. The role of the tugs is to simply transport the debris to a hold point close to the recycling hub. Since REAVER will capture 5 debris in 1 year the mothership will carry 5 tugs.

As can be seen in figure 3.1a the 5 tugs are radially attached to a central structure on the mothership. On top there is a robotic manipulator used to move the tugs from the mothership to a point where they can capture the debris. On the sides of the mothership 2 foldable solar arrays are attached to provide electrical power.

On the bottom (see figure 3.2a) an International Docking System Standard (IDSS) docking port enables the mothership to dock to the recycling hub. Since the tugs take up significant space 4 external trusses are added to the mothership to strengthen the structure as seen in figure 3.1b. On the propulsion side the mothership features 4 main thrusters and 8 reaction control thruster blocks with 3 orthogonal thrusters per block (see figure 3.3c. The tugs are equipped with 2 foldable, circular solar arrays to minimize volume during storage and a PPS-5000 electric thruster. The tug in the unfolded configuration can be seen in figure 3.1c.

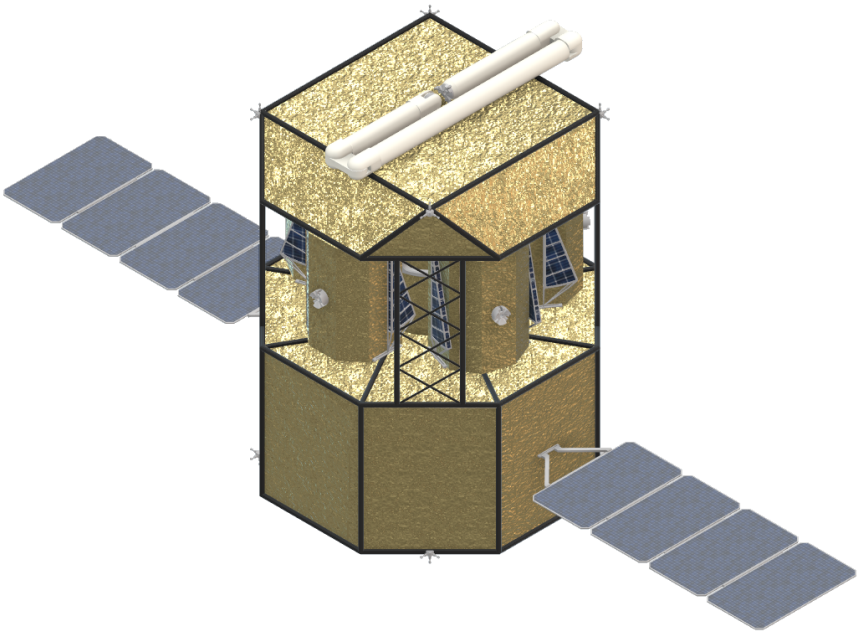

(a) Mothership carrying 5 tugs

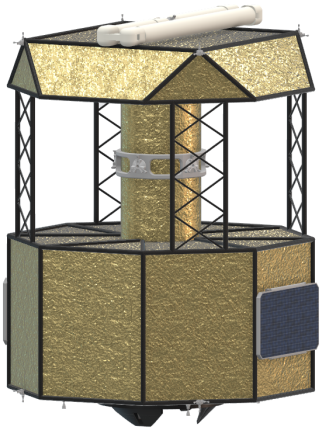

(b) Mothership only

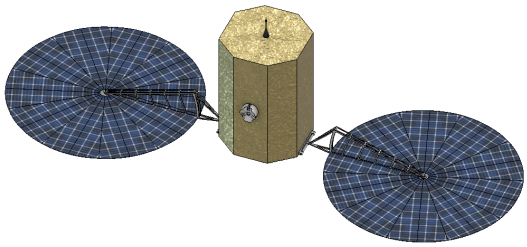

(c) Tug only

Figure 3.1: Mothership and tug spacecraft renders made with 3DEXPERIENCE Catia

The following overview presents the most important components of the REAVER mission. Figure 3.2b shows a cross section of the vehicles. As can be seen, most of the volume of the lower mothership structure is taken up by the four spherical LMP-103S propellant tanks and the propulsion feed system. The limited volume of the central structure is largely occupied by the cylindrical helium composite overwrapped pressure vessel (COPV). A detailed view of the mothership propulsion system is shown in figure 3.3b. Around the COPV the tug deployment ring (also seen in figure 3.3a) is placed. Its purpose is to rotate the tugs to a position where the robotic manipulator can attach itself to the tugs via the mechanical interface (further discussed in chapter 7). The same mechanical interface is present on the tug deployment ring to hold and release the tugs when required. The tug deployment sequence enabled by the tug deployment ring is shown in figure 3.6.

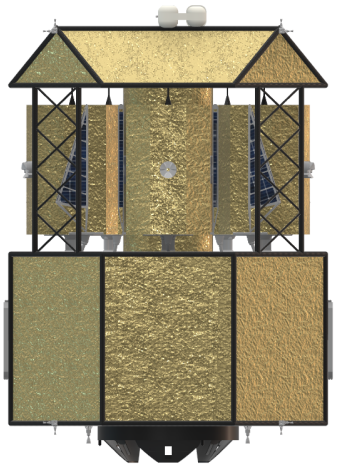

(a) Mothership with tugs - side view

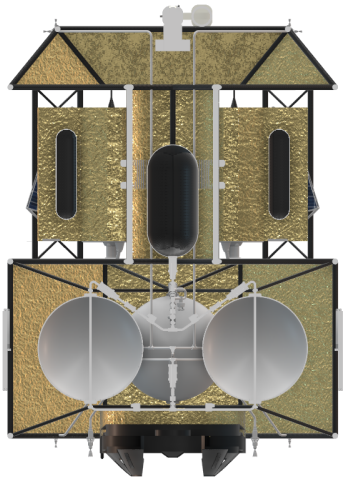

(b) Mothership with tugs - side cross section view

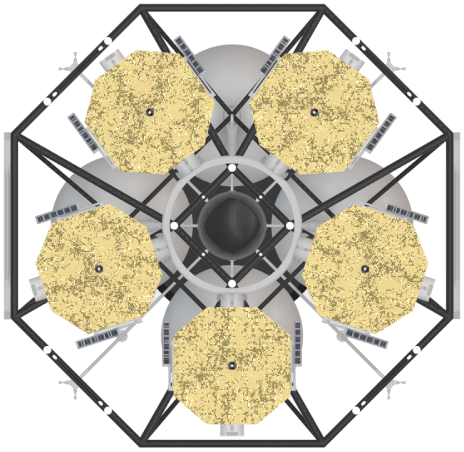

(c) Tug radial placement and deployment ring

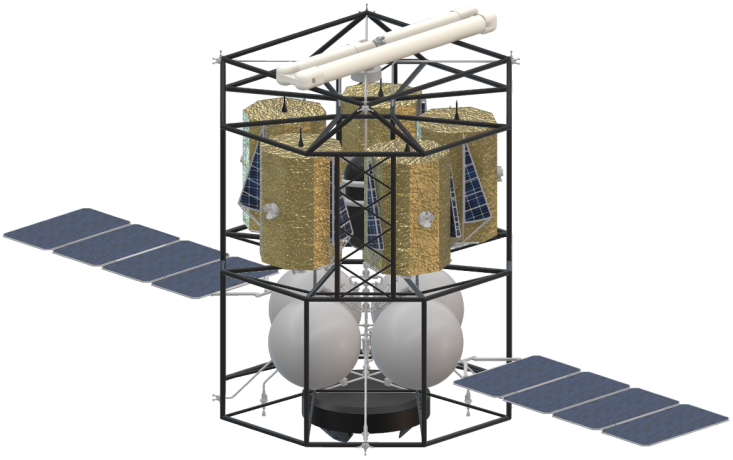

(d) Mothership with tugs - internal components

Figure 3.2: REAVER configuration overview made with 3DEXPERIENCE Catia

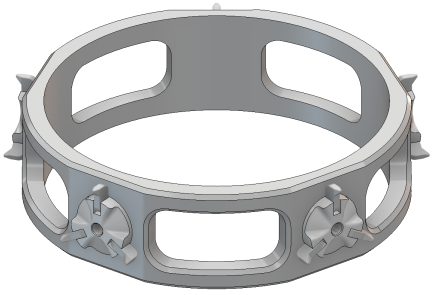

(a) Tug deployment ring

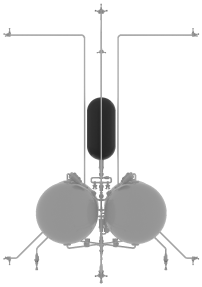

(b) Mothership propulsion system

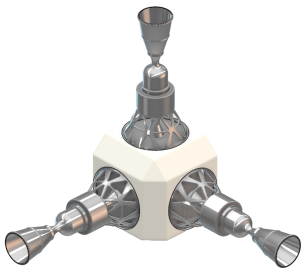

(c) Mothership RCS block

Figure 3.3: Detailed views of small or hard to see components made with 3DEXPERIENCE Catia

The tug architecture is extremely simple by design. Since the mothership has to carry 5 tugs, minimizing dry mass is absolutely crucial. As can be seen in figure 3.4b the tug internal volume is almost entirely occupied by the two xenon propellant tanks and the AEP mechanism. The tugs feature 2 female mechanical interfaces used to attach the tugs to the mothership and for robotic arm manipulation. An octogonal structure enables higher radial packing density (see figure 3.2c). The bottom of the tug volume is reserved for the PPS-5000 hall effect thruster and the battery. Small AOCS and electronics components are not shown and are discussed in detail in their respective subsystem chapters.

(a) Tug (stowed configuration)

(b) Tug cross section view

Figure 3.4: Overview of tug architecture made with 3DEXPERIENCE Catia

3.3. Concept of Operations

The REAVER mission is split into multiple spacecraft modes presented in table 3.2: safe mode, commissioning mode, long-range rendezvous mode, proximity operations mode, capture and control mode and standby mode. The RPOD sequence is presented in figure 3.6, while the complete concept of operations (CONOPS) diagram is provided in figure 3.7.

Table 3.2: Spacecraft modes

ID	Name	Spacecraft	Description
MD-MS-SAF, MD-TUG-SAF	Safe mode	Both	Fallback state, only essential systems active and waiting for ground control
MD-MS-COM, MD-TUG-COM	Commissioning mode	Both	Initialising systems, after MS separation from kick-stage or after Tug separation from mothership
MD-MS-LRR, MD-TUG-LRR	Long-range rendezvous mode	Both	Inter-debris transfer for mothership, transporting debris to recycling-hub for tugs
MD-MS-PRX	Proximity operations mode	Mothership	Approaching and synchronising with the debris
MD-TUG-CAP	Capture and control mode	Tug	Capturing and controlling the target debris
MD-MS-SBY, MD-TUG-SBY	Standby mode	Both	Spacecraft holding for further operations to proceed

CONOPS Overview

Once the mothership has detached from the kick-stage, the mothership enters commissioning mode; where all subsystems are initialised and functionalities verified. The mothership then begins its journey to the first debris, performing all necessary orbital manoeuvres to reach the first debris. Upon arrival, control will transition to Proximity Operations mode to enable a controlled approach to the target. Subsequently, during Capture and Control mode, the debris is secured and the tug proceeds back to the RH, while the mothership proceeds to the next debris target. Once the mothership has dropped off all tugs, it too returns to the RH and awaits the arrival of the tugs. The mothership then performs the proximity operations required to transfer the tug and debris assembly to either the recycling infrastructure or an allocated storage system using the compatible docking port.

Safe Mode

The safe mode is the fallback state of both the mothership and the tugs. This mode is entered when an anomaly is detected, when the spacecraft state becomes uncertain, or when the current operation can no longer be continued safely. Only the essential systems remain active. The spacecraft maintains a stable attitude, basic pointing, housekeeping, thermal survival, and communication with GS when available. Mission-specific systems, such as propulsion, capture hardware, and RPOD sensors, are kept inactive unless required for spacecraft survival. Safe mode ends once the spacecraft health has been assessed and GS commands the spacecraft back to commissioning, standby, or another valid mission mode.

Commissioning Mode

The commissioning mode is used after mothership separation from the kick-stage, or after tug separation from the mothership. The purpose of this mode is to initialise the spacecraft and verify that the required subsystems are functioning correctly before nominal operations are started. During commissioning, the C&DH activates the required onboard computers and data links, TT&C establishes communication with GS, and EPS and TCS confirm that the spacecraft is within its power and thermal limits. The AOCS then initialises and verifies its sensors, actuators, estimation filters, and control loops. Propulsion and capture-related interfaces are checked, but no mission-critical manoeuvres or capture operations are performed. Once the health checks are completed and confirmed by GS, the spacecraft transitions to standby mode or to the next operational mode.

Long-range Rendezvous Mode

The long-range rendezvous mode begins either at the recycling hub (start of operations) or at the just-captured debris. Information of the subsequent target current best estimate (CBE) location is sent by the GS to the mothership's C&DH (MC&DH) via the TT&C subsystem. This is sent to the AOCS computer (chapter 6). The mothership then proceeds using absolute navigation (GPS) to the target. This mode ends at a predefined cut-off distance, where relative navigation sensors (RF, camera-based, LiDAR) become more accurate (see figure 3.5).

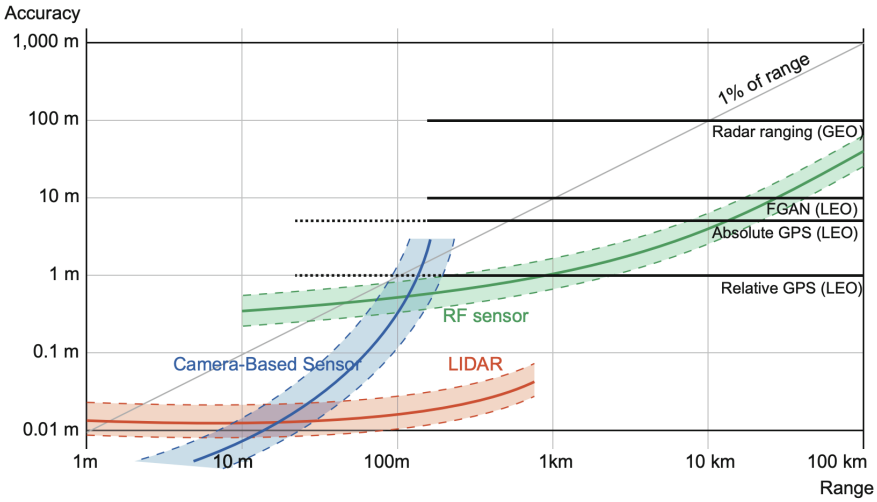

Figure 3.5: Operational ranges and measurement accuracies of different rendezvous sensors [5]. Coloured lines show onboard sensor performance, while horizontal lines are reference accuracies for external navigation systems. In LEO, the accuracies are provided for relative GPS which measures inter-spacecraft separation, absolute GPS which determines spacecraft orbital position, and FGAN which provides ground-based imaging radar tracking of LEO objects. Radar ranging in GEO indicates ground-based tracking accuracy for GEO spacecraft.

For the tug, once the debris is captured and a rigid connection with the AEP has been formed, the long-range rendezvous starts after separation from the robotic arm and the commissioning mode of the tug. During this commissioning mode, the tug unfolds its solar panel and starts up critical systems. The tug then begins the transfer to a hold point in the recycling hub orbit near the recycling hub.

Proximity Operations Mode

The proximity operations mode consists of three phases; approach, inspection, and final approach. Approach begins at the cut-off distance (100 m), which is also when the RPOD sensor suite is activated, and ends once the mothership reaches the inspection standoff point (20 m from the target along the V-bar), discussed in more depth in section 3.5.

Once the mothership has reached this point, the inspection phase begins. The debris is analysed to identify the rotation axis (for the purpose of this report, the target rotation is assumed about the greatest moment of inertia), rotational velocity, and LAE nozzle location using computer vision algorithms (see section 5.3). Subsequently, the raw images and debris characteristics processed by C&DH are sent to GS via TT&C. Once GS has transmitted a confirmation to the mothership, the final approach phase begins: the manoeuvres discussed in section 3.5 are conducted to bring the mothership to the target in preparation for capture. Using the identified debris rotation axis, the C&DH sends the desired position of the centre of mass of the mothership-tug assembly to the AOCS. The AOCS sends control commands to the RCS thrusters such that the mothership repositions itself to align its rotational axis with that of the debris. Thereafter, the AOCS commands the mothership-tug assembly to begin to synchronise its rotational velocity with that of the target. Once the debris is stationary in the frame of reference of the mothership, the robotic arm brings the tug towards the liquid apogee engine (LAE) nozzle. The

tug's RPOD sensor suite is activated to closely monitor the LAE nozzle approach, sending the data via a wired connection in the robotic arm to the mothership C&DH. The final approach phase terminates when the tug's AEP is within reach of the LAE nozzle: the ready position.

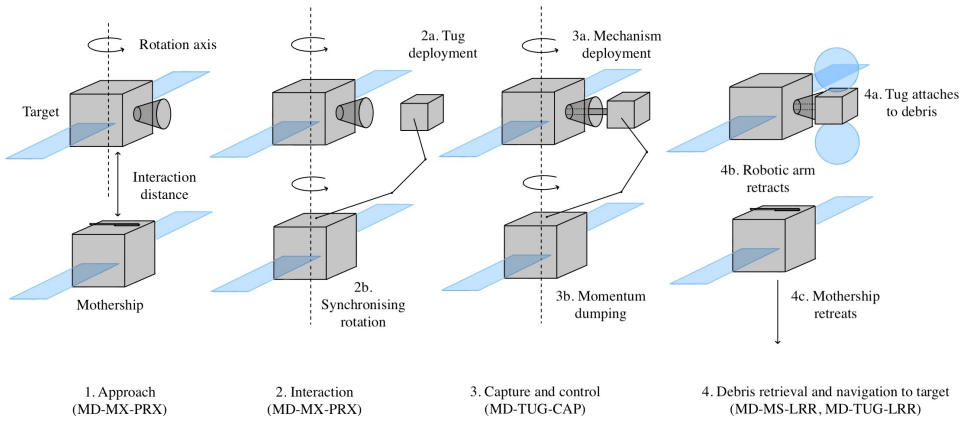

Figure 3.6: RPOD sequence

Capture and Control Mode

The capture and control mode begins at the ready position, where the AEP mechanism of the tug attaches to the target's LAE. The tug proceeds to send docking confirmation to the mothership via a physical link within the robotic arm. Upon confirmation, the mothership performs momentum dumping to eliminate the rotational velocity of the mothership-tug-debris assembly. The tug will then confirm its own communications with the GS, whereupon the robotic arm detaches from the tug and returns to nominal position (stowed). This phase ends with the tug rigidly connected to the target and the mothership in its nominal position.

Standby Mode

The standby mode is used when either the mothership or a tug is holding for further operations to proceed. This can occur while waiting for GS confirmation, target information, a handover opportunity, or the start of the next mission phase. During standby, the spacecraft remains in a stable and controlled configuration, while high-power and mission-specific systems are not continuously active. The C&DH continues housekeeping and command monitoring, TT&C maintains scheduled communication with GS, EPS maintains the required power state, and TCS maintains the spacecraft within its allowable thermal limits. The AOCS keeps the spacecraft in a stable waiting configuration until the next mission operation is commanded.

3.4. Updated FBS and FFD

The final functional flow diagram and functional breakdown structure are provided in figure 3.8 and figure 3.9.

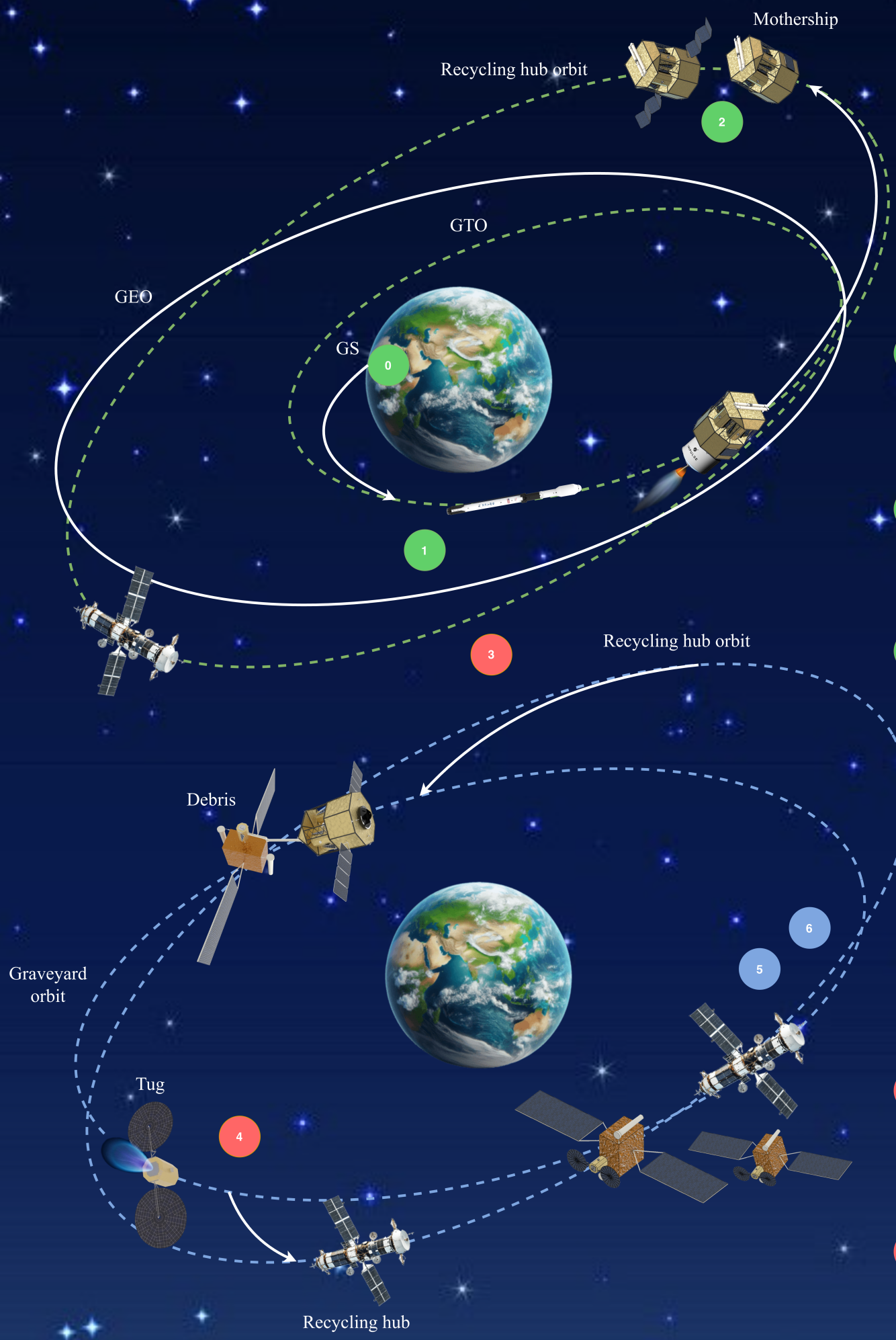

0 Pre-launch
Manufacturing and AIT is conducted. The GS prepares for launch by staffing personnel and developing necessary software. Preliminary target selection and trajectory optimisation is performed. The launch services prepare the launcher in time for the launch and the M&T is integrated into the launcher.

1 Launch
REAVER will launch from the Guiana Space centre before 2035. The selected launch vehicle, Falcon 9, will insert the M&T into Geostationary Transfer Orbit (GTO). A kick stage will then perform a burn to transfer the M&T to the RHO located in the graveyard orbit at: 36500km altitude, 7° inclination and 10° RAAN.

2 Comissioning
After separation from the kick stage, the M&T enters commissioning mode; transitioning into a mission ready state, having all functionalities verified by GS.

Legend

GS = Ground segment
RH = Recycling hub
M&T = mothership and tugs
AIT = Assembly Integration and Testing
GTO = Geosynchronous transfer orbit
GEO = Geostationary earth orbit

3 Debris rendezvous and capture
The mothership performs all necessary orbital manoeuvres to reach a debris target of interest. Upon arrival, control will transition to Proximity Operations mode to enable a controlled approach to the target. Subsequently, during Capture and Control mode, the debris is secured and the tug is dispatched back to the recycling hub, while the mothership proceeds to the next designated debris target.

4 Debris capture
The deployed tug transports the captured debris to the RH. Once the mothership has dropped off all tugs, it returns to the RH and awaits the arrival of the remaining tugs.

5 Recycling hub docking
The mothership performs proximity operations necessary to transfer the tug and debris assembly to either the recycling infrastructure or an allocated storage system

6 End of life
GS determines whether REAVER concludes its primary mission and transitions into the disposal phase; the overall health and status of subsystems are evaluated, after which the appropriate decommissioning procedures may be initiated. Once decommissioning operations have been completed, for instance by returning the spacecraft itself to the recycling hub for processing and recycling, all mission data is archived and the mission performance is assessed.

Figure 3.7: REAVER ConOps diagram, with additional images sourced from[1][2][3][4][5]

[1] https://pngtree.com/so/earth-cartoon-sketch/4 [accessed 17 June 2026]
[2] https://in.pinterest.com/pin/night-starry-sky-vertical-background-vector--675188169168813970/ [accessed 17 June 2026]
[3] https://buildamoc.com/products/falcon-9 [accessed 17 June 2026]
[4] https://www.satellitetoday.com/launch/2024/01/18/tom-mueller-details-kick-stage-helios-designed-to-disrupt-launch-to-geo/ [accessed 17 June 2026]
[5] https://www.vecteezy.com/free-png/space-station [accessed 17 June 2026]

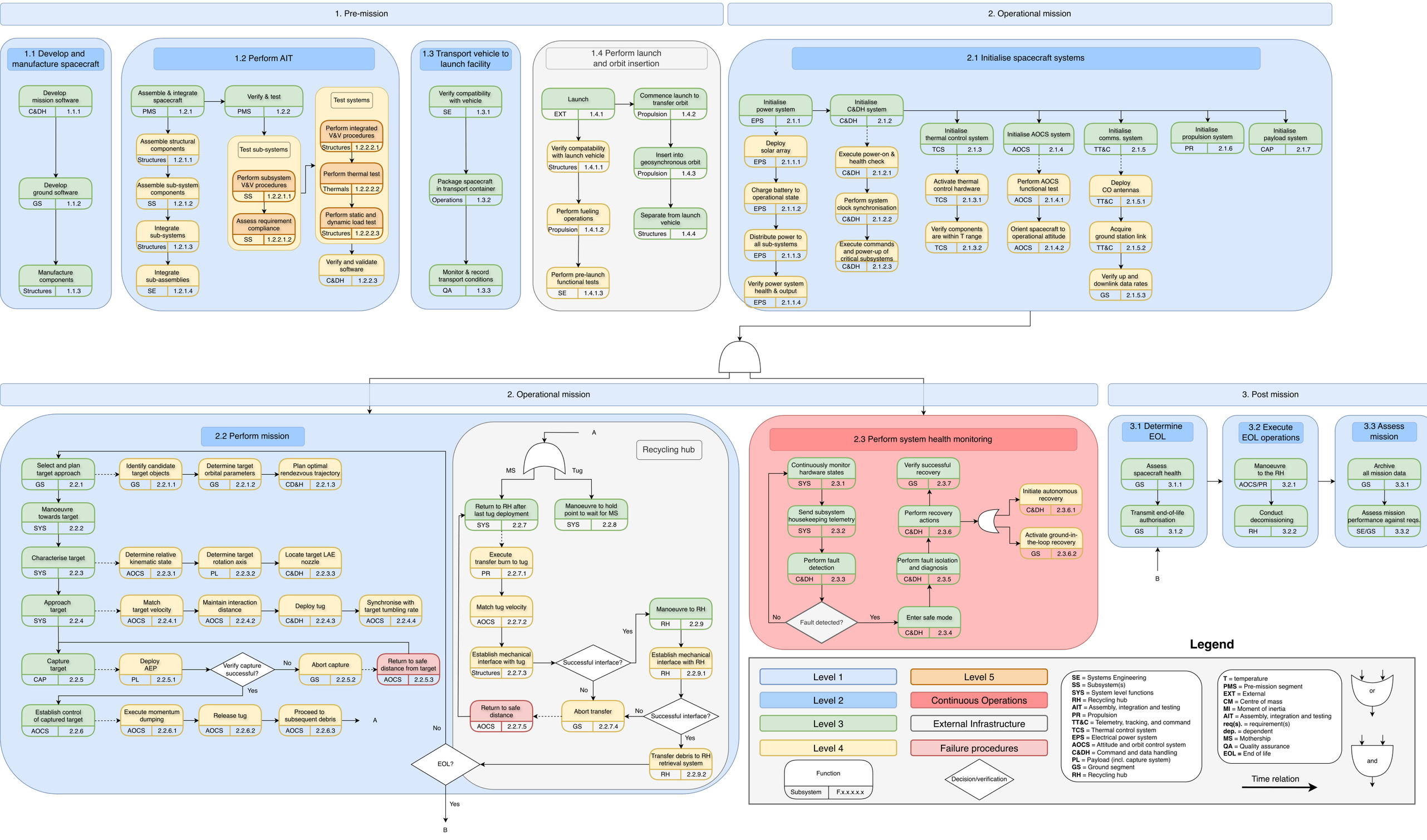

Figure 3.8: Functional Flow Diagram

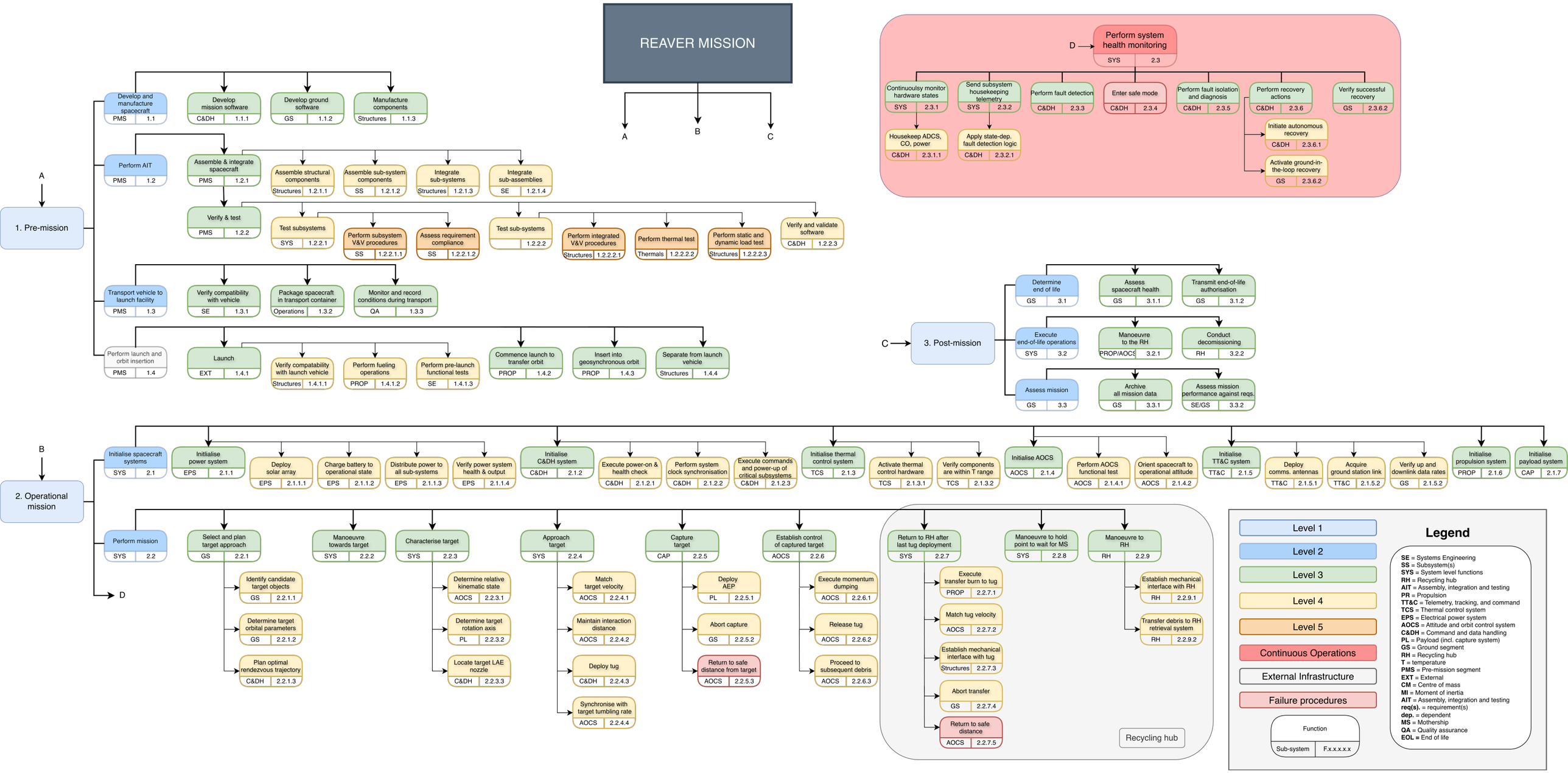

Figure 3.9: Functional Breakdown Structure

3.5. Astrodynamics Characteristics

This section details the astrodynamics methodology supporting the design of the REAVER mission. The analysis addressed looks at four coupled problems: (1) filtering the GEO debris down to a mission-compatible candidate list; (2) defining the orbital mechanics methods used to measure all the mothership manoeuvres and low-thrust tug spirals; (3) optimising the five-target sequence and the RH orbital plane in a simultaneous manner; (4) validating the analytical calculations with NASA's General Mission Analysis Tool (GMAT); and (5) analysing the rendezvous proximity operations required throughout the whole mission.

Target Filtering

In order for the trajectory analysis to be built, it is necessary to start with a catalogue of potential debris to be captured. For that, DISCOSweb[1] (ESA's Debris Information System) and Space-Track[2] (US 18th Space Control Squadron TLE catalogue) are consulted. Checking both sources acts as the first filter. In fact, only objects present in the two datasets are kept. Filtering is then applied in two sequential stages.

Stage 1: Orbital and Physical Pre-filtering

The initial data gathered from Space-Track is filtered using orbital constraints. This helps to reduce the downloaded dataset to only spacecraft that are considered physically compatible with the mission. Three criteria are applied for this:

1. **Altitude:** Objects are restricted to their perigee above 35 700 km and apogee below 36 500 km, fitting inside the nominal GEO ring in which REAVER is required to operate.
2. **Inclination:** The filtering restricts objects with inclination between 0° and 15°. This angle window excludes objects whose plane-change cost would make capture and therefore mission infeasible within the propellant budget.
3. **Mass:** After combining the Space-Track and DISCOSweb datasets, objects are kept only if their wet mass fell within the range 1429 kg to 2857 kg. This range given by the SMAD statistical dry-to-wet mass ratio of 0.7 for GEO satellites, makes the debris fit within the dry mass requirement of 1000 kg to 2000 kg.

Stage 2: Post-merge Compatibility Filtering

Following the first filtering stage, a second stage is applied to the resulting dataset to make sure the objects fit in the REAVER mission constraints. The following filters are applied:

1. **Country and Operator:** A defined set of approved owners of objects is decided upon to not cause political conflicts: Germany (GER), the Netherlands (NETH), Sweden (SWED), Norway (NOR), Eutelsat (EUTE), EUMETSAT (EUME), the United States (US), SES (SES), the International Telecommunications Satellite Organisation (ITSO), and finally the United Kingdom (UK). Notably, this excludes objects owned by China and Russia, which together account for well over 100 objects in the GEO graveyard region and represent the largest share of debris removed by this filter. This filter lowers the number of debris to capture significantly.
2. **Right Ascension of Ascending Node (RAAN):** The next filter is the RAAN; a window of 60°-90° is agreed upon. This choice is made to reduce the ΔV required to perform a plane change and to account for the high density of objects within that range. Later on, in section 3.5, an optimization of the RH RAAN within this window helps to minimise the worst-case plane-change ΔV.
3. **Engine compatibility:** Finally, only four objects are removed from the filtered list because their liquid apogee engine throat diameter is incompatible with the tug's capture mechanism.

After implementing all filters to the original database, the available debris for this mission are given as a list of 21 candidate targets presented in table 3.3 below.

Orbital Mechanics

For the analysis described in the next subsections, every orbit is represented using three parameters: the semi-major axis a, the inclination i, and the RAAN Ω. For simplification, all orbits are treated as circular, allowing for straight-forward Hohmann and Edelbaum transfer calculations. Additionally, as REAVER operates as an Earth satellite, the following constants are used for calculations: Earth's gravitational parameter $\mu_E = 3.986004418 \times 10^{14}$ $m^3\,s^{-2}$ and Earth's radius 6 378 137 m. For a circular orbit of semi-major axis a, the orbital velocity and period are computed using equation (3.1).

[1] https://discosweb.esoc.esa.int/

[2] https://www.space-track.org/documentation

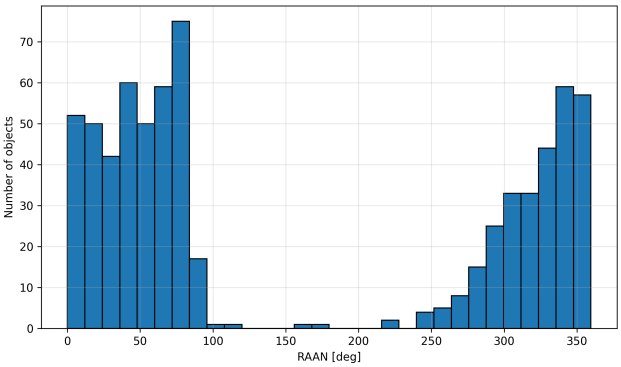

Figure 3.10: Distribution of RAAN

Table 3.3: Candidate debris list

NORAD	Name	Mass [kg]	a [km]	i [°]	Ω [°]
443	EchoStar 1	1902.9	42 544.8	8.57	63.16
488	AMC-3 (GE-3)	1585.7	42 165.1	8.09	64.35
505	NSS 806	2135.8	42 502.0	7.07	70.00
513	INTELSAT 805	1932.6	42 388.1	7.83	66.06
579	AMC-7 (GE-7)	1935.0	42 487.0	6.86	70.53
590	AMC-8 (GE-8)	2015.0	42 482.1	6.06	72.83
628	EUTE 12 West A	2700.0	42 728.2	7.23	68.79
640	Galaxy 12	1760.0	42 528.6	6.93	69.54
663	AMC-10 (GE-10)	2315.0	42 490.1	6.64	69.28
672	AMC-11 (GE-11)	2315.0	42 499.6	0.23	80.25
697	Galaxy 14	2087.0	42 549.0	4.98	75.34
699	Galaxy 15	2033.0	42 542.7	3.48	77.50
731	AMC-18	2081.0	42 565.5	2.56	84.39
748	INTELSAT 11	2450.0	42 510.9	3.51	78.93
755	Horizons 2	2304.0	42 164.6	2.55	80.89
774	AMC-21	2473.0	42 522.0	2.90	80.32
786	NSS 9	2290.0	42 164.9	1.21	82.85
804	COMSATBW-1	2440.0	42 164.2	0.07	89.69
834	Hylas 1	2570.0	42 164.3	5.59	73.29
884	Meteosat 10 (MSG 3)	2035.0	42 164.2	4.62	61.12
967	Meteosat 11 (MSG 4)	2043.0	42 164.3	3.15	71.23

$$v_c = \sqrt{\frac{\mu_E}{a}}, \qquad T = 2\pi\sqrt{\frac{a^3}{\mu_E}}. \tag{3.1}$$

Regarding the mothership manoeuvres, they are all treated as impulsive given the chemical propulsion system ($I_{sp} = 253\,\text{s}$, $F = 64\,\text{N}$). On the other hand, tug manoeuvres are treated as continuous low-thrust spirals, since they are to use an electric propulsion system ($I_{sp} = 1600\,\text{s}$, $F = 0.07\,\text{N}$).

Mothership Manoeuvres

Between each target, the mothership trajectory is made of three sequential impulsive manoeuvres: (1) the Hohmann departure, (2) the circularization of the orbit, and (3) the double-Hohmann phasing. It is important to note that the plane-change manoeuvre can be implemented either in the first or second manoeuvre depending on whether the mothership needs to undergo a descending or ascending orbit transfer. For the sake of the explanation, the plane-change manoeuvre is mentioned in both parts.

Burn 1: Hohmann Departure

The mothership starts its burn sequence with a Hohmann transfer ellipse with semi-major axis given by equation (3.2), where a is the semi-major axis, and the subscripts A and B denote the initial and final orbit respectively.

$$a_t = \frac{a_A + a_B}{2}. \tag{3.2}$$

The velocity at the departure point on the transfer ellipse comes from the vis-viva equation shown in equation (3.3).

$$v_{t,A} = \sqrt{\mu_E\left(\frac{2}{a_A} - \frac{1}{a_t}\right)}, \tag{3.3}$$

where subscript t denotes transfer orbit. The combined plane-change angle between any two orbital planes can be then measured via the spherical law of cosines (equation (3.4).

$$\cos\theta = \cos i_A \cos i_B + \sin i_A \sin i_B \cos(\Omega_B - \Omega_A), \tag{3.4}$$

where i is the inclination and Ω is the RAAN. To minimize ΔV, the plane change is always performed the slowest orbital velocity. When $a_B > a_A$ (ascending transfer), the departure burn is purely in-plane as per equation (3.5).

Whereas, when $a_B < a_A$ (descending transfer), the departure burn combines the altitude change with the full plane change (RAAN and inclination) shown in equation (3.6).

$$\Delta V_1 = |v_{t,A} - v_A|\,, \tag{3.5}$$

$$\Delta V_1 = \sqrt{v_{t,A}^2 + v_A^2 - 2\,v_{t,A}\,v_A \cos\theta}. \tag{3.6}$$

Burn 2: Circularisation
At the apogee of the transfer orbit, another burn is necessary to match the orbital velocity of the final target orbit. The velocity on the ellipse from the transfer is using equation (3.3) with a_B replacing a_A.

For an ascending transfer, the plane change is combined with circularisation using the same equation (3.6) with index B instead of A. Similarily, for a descending transfer, only a match in velocity is necessary (circularization) as per equation (3.5).

Burn 3: Double-Hohmann Phasing
Once the target orbit is reached, the mothership needs to meet with the target spacecraft and therefore shall phase towards it. The mothership hence performs a double-Hohmann phasing manoeuvre to operate on a slightly lower or higher orbit for $N_{ph} = 18$ revolutions. This number is chosen for the mission to be accomplished on time with a considerably low propellant consumption. The phasing manoeuvre shall close an assumed average phase gap of 90°. The phasing orbit period and phasing orbit semi-major axis is then determined using equation (3.7), with $T_B = 2\pi\sqrt{a_B^3/\mu_E}$.

$$T_{ph} = T_B\left(1 - \frac{1}{4\,N_{ph}}\right), \quad a_{ph} = \left(\frac{\mu_E T_{ph}^2}{4\pi^2}\right)^{1/3}, \tag{3.7}$$

where the subscript ph stands for phasing. The total phasing ΔV is the sum of the entry and exit burns given by equation (3.8), and the phasing time hence is $t_{ph} = N_{ph}\,T_{ph}$.

$$\Delta V_{ph} = 2\left|\sqrt{\frac{\mu_E}{a_B}} - \sqrt{\mu_E\left(\frac{2}{a_B} - \frac{1}{a_{ph}}\right)}\right|. \tag{3.8}$$

Leg totals and finite-burn time correction
The total ΔV and ballistic flight time per leg are given by equation (3.9), and equation (3.10), respectively.

$$\Delta V_{leg} = \Delta V_1 + \Delta V_2 + \Delta V_{ph} \tag{3.9}$$

$$T_{leg} = T_t + T_{ph} \tag{3.10}$$

An important fact to take into account when analysing the mothership orbital mechanics is the mothership thruster that delivers 64 N of thrust with a maximum firing duration of 38 min. Consequently, burn durations are not negligible relative to the orbital period and a proper burn sequence must be designed .

The number of firings required to reach a ΔV at mass m is $n_{fire} = \lceil \Delta V/(F_t \cdot \frac{t_{burn}}{m}) \rceil$, operate twice per orbit, once at perigee and the next at apogee. F_t represents the thrust and t_{burn} is the burn time of the thrusters. It is essential to note that performing two burns per orbit simplifies manoeuvres at the cost of time. On the good side, the elapsed time between firings allows for proper cooling down of the mothership thrusters and hence keeps their thrusting capacity at the desired level.

This correction is applied to the three types of burn describe earlier for timeline calculations. The impulsive ΔV values, however, are kept for propellant mass budgeting as these do not depend on the number of firings.

Tsiolkovsky Rocket Equation
Regarding propellant mass calculations, the Tsiolkovsky rocket equation can be used. The propellant used for a velocity increment ΔV at initial wet mass m_0 is given by equation (3.11).

$$m_p = m_0\left(1 - e^{-\Delta V/v_{ex}}\right), \tag{3.11}$$

where $v_{ex} = I_{sp}\,g_0$ with $g_0 = 9.806\,65\,\mathrm{m\,s^{-2}}$. For the mothership, $v_{ex_{MS}} = 253 \times 9.80665 = 2481.1\,\mathrm{m\,s^{-1}}$.

Tug Manoeuvres

Regarding the tug manoeuvres, they each perform a single low-thrust transfer once they have locked onto the debris. They each need to transfer from the debris orbit to the RH orbit, while carrying the captured debris as an extra payload. As the tugs use electric propulsion, the Edelbaum continuous-thrust model is the most fit for orbital transfer calculations.

The Edelbaum model helps to measure the ΔV for a combined plane change and altitude change for low-thrust spirals. For a transfer from a circular orbit with velocity v_1 and plane orientation (i_1, Ω_1) to a second circular orbit with velocity v_2 and plane orientation (i_2, Ω_2), the total plane-change angle θ is calculated using equation (3.4) by adapting the subscripts from A and B to 1 and 2 respectively.

$$\Delta V_E = \sqrt{v_1^2 + v_2^2 - 2\, v_1\, v_2 \cos\left(\frac{\pi}{2}\,\theta\right)}. \tag{3.12}$$

Tug Propellant Mass

The propellant required for each tug spiral is derived directly from the Tsiolkovsky rocket equation equation (3.11). The tug's initial wet mass is the sum of its dry mass, the captured debris mass, and the propellant itself: $m_0 = m_p + m_{debris} + m_{dry}$.

Spiral Time

The duration of the electric propulsion spiral transfer under an assumed constant thrust of $F = 0.07\,\text{N}$ can be measured with equation (3.13) below.

$$t_{spiral} = \frac{m_p\, v_{ex_{tug}}}{F} \tag{3.13}$$

From the large debris masses (1600 kg to 2700 kg) to the low tug dry mass (221.4 kg), spiral times range from approximately 100 d to 300 d depending on the debris that has been captured.

Capture Sequence Optimisation

The capture sequence optimisation is aimed at selecting five debris targets from the list given in table 3.3 and determining the order of visit that minimises propellant consumption and mission duration per combination. This optimization is built so as to make sure that the REAVER mission is able to operate and capture all five debris in the span of one year.

Combinatorial Space

The number of distinct ordered five target missions out of the 21 candidate list is as follows:

$$\binom{21}{5} \times 5! = 20\,349 \times 120 = 2\,441\,880$$

For a given combination of five targets, there are up to 120 different visit sequences which are potentially feasible or unfeasible. Therefore, to avoid having sub-optimal sequences, the result space is narrowed down by retaining only those that result in the lowest propellant mass out of the 120 sequences possible for each five-target combination. This reduces the combinations to 20349, significantly lowering the computational cost required in the following optimisation.

All legs between each debris' ΔV are pre-computed once and stored in $(N+1) \times (N+1)$ matrices, where $N = N_{deb}$ and node $N+1$ represents the RH. The five matrices are: $\mathbf{DV}_1$, $\mathbf{DV}_2$, $\mathbf{DV}_{ph}$ (from equations (3.5) to (3.8)), and the corresponding time matrices $\mathbf{T}_{tr}$ and $\mathbf{T}_{ph}$. The total combinations of sequences are calculated as equation (3.14).

$$\mathbf{DV}_{leg} = \mathbf{DV}_1 + \mathbf{DV}_2 + \mathbf{DV}_{ph} \qquad \mathbf{T}_{leg} = \mathbf{T}_t + \mathbf{T}_{ph} \tag{3.14}$$

Backward Mass Propagation

In order to measure the propellant mass for each candidate sequence $(d_1, d_2, d_3, d_4, d_5)$, the required initial wet mass needs to be determined by propagating the Tsiolkovsky rocket equation backwards from the final mass the mothership must have at the end of the mission. In fact, it must return to the RH with a final mass that is equal to its dry mass $m_{dry_{MS}} = 898.52\,\text{kg}$. The propagation should work with the following method outlined in equation (3.15), where the tug wet mass is then added back at each debris node.

$$
\begin{aligned}
m^{(6)} &= m_{dry_{MS}} \\
m^{(5)} &= m^{(6)} \times e^{\Delta V_5 / v_{ex_{MS}}} \\
m^{(\ell)} &= \left(m^{(\ell+1)} + m_{wet_{tug}}\right) \times e^{\Delta V_\ell / v_{ex_{MS}}} \quad \ell = 4, 3, 2, 1, 0.
\end{aligned} \tag{3.15}
$$

When applying a 10 % RCS margin, the orbital propellant mass required is then given by equation (3.16), and the initial wet mass of the mothership at launch is therefore shown in equation (3.17).

$$
m_{p_{total}} = 1.10 \cdot (m^{(0)} - m_{dry_{MS}} - 5\, m_{wet_{tug}}), \tag{3.16}
$$

$$
m_{wet_0} = m_{dry_{MS}} + 5\, m_{wet_{tug}} + m_{p_{total}}. \tag{3.17}
$$

Forward Mission Timeline Propagation
Then, it is needed to have a forward pass propagating mass and time simultaneously. After each leg manoeuvre, the mothership loses mass as per equation (3.11). Once the phasing manoeuvre is finished, a proximity operations period $T_{ops} = 5\,\mathrm{d}$ is added to the mission timeline. This period covers all the phases of the RPOD sequence described in section 3.5 and includes a high margin for aborting debris approach. Once this manoeuvre is performed, the tug is released and starts its transfer towards the RH. The time at which tug n starts its spiral is shown in equation (3.18) and the arrival at the RH as equation (3.19).

$$
t_{tug_{start}}(n) = \sum_{\ell=0}^{n-1} \left(T_{leg,\ell} + T_{ops}\right), \tag{3.18}
$$

$$
t_{tug_{arrive}}(n) = t_{tug_{start}}(n) + t_{spiral}(n). \tag{3.19}
$$

It is important to note that the RPOD ΔV is also added during the forward pass to account for the propellant mass used and deducted from the 10 % RCS margin (equation (3.20)). At each debris capture the combined RPOD cost, and at the RH orbit for each debris handover.

$$
\begin{aligned}
\Delta V_{RPO_{debris}} &= \Delta V_{inspect+capture} + \Delta V_{detumble}, \\
\Delta V_{RPO_{RH}} &= \Delta V_{tug-meet} + \Delta V_{dock}.
\end{aligned} \tag{3.20}
$$

The calculations are further described in the RPOD subsection.

Sequential RH Handovers
Once the mothership has captured all five debris and has returned to the RH, it then performs sequential proximity operations handovers (HO) with each tug once they have arrived. The tugs and their debris are each captured back by the mothership in order of arrival time. With $t_{RH_{free}}$ being the time at which the RH is available for the next handover, the completion time for each handover and mission completion is then given by the last tug handover, $n = 5$. This is shown in equation (3.21).

$$
t_{HO}(n) = \max\left(t_{RH_{free}},\ t_{tug_{arrive}}(n)\right) + T_{ops} \quad n = 1, 2, 3, 4, 5. \tag{3.21}
$$

A sequence can then be considered feasible if and only if $t_{mission} = \max(t_{HO}(n)) \leq 365\,\mathrm{d}$.

Recycling Hub RAAN Optimisation

In contrast to the altitude and the inclination, the RAAN of the RH orbit is a free design variable. Consequently, a proper optimisation is required as the plane-change cost described in equation (3.4) becomes larger as the angular separation between the RH and the debris increases. The optimal RAAN value can then be determined inside the reduced combinatorial sequence space.

The capture sequence optimisation method from section 3.5 is reused and takes the same best 20349 orderings. Only the 42 RH↔debris rows and columns of $\mathbf{DV}_{leg}$ and the 21 tug transfers are recomputed for each RAAN value. The optimisation of the RAAN is then performed over $60° \leq \Omega_{RH} \leq 90°$ in $1°$ steps. This is done so as

to be consistent with the RAAN distribution of the list of targets. The purpose of the optimization is then to identify the optimal RH RAAN that minimises the propellant mass by the worst combination out of the 20349 feasible ones.

The RAAN optimisation result is shown below in figure 3.11. On this figure, the relationship between the Mothership propellant mass and the RH RAAN is plotted. It can be seen that the optimal RAAN is $\Omega^*_{RH} = 64°$. This value is now adopted as a fixed RH orbit parameter for the next analyses.

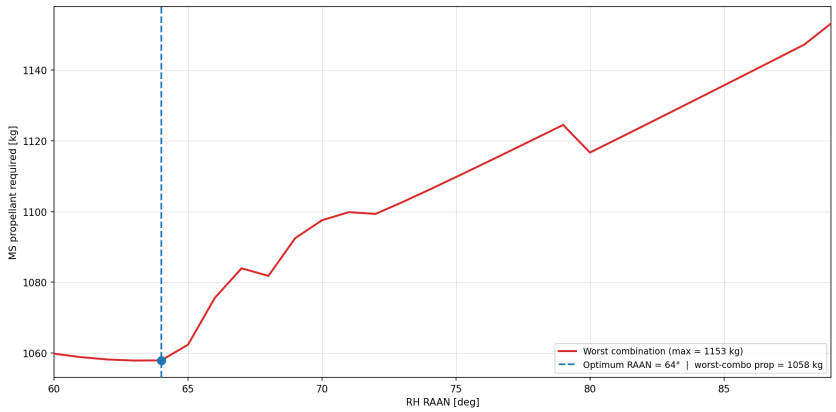

Figure 3.11: RH RAAN sweep result

Worst-Case Sequence Selection

Since the RH RAAN is now known, the sequence optimisation can be run again in order to identify the design-driving mission, referred to as the worst-case sequence. The objective of this analysis is to identify the five target combination whose best visit order has the highest propellant mass.

The reason behind this optimisation is REAVER being a commercially active debris removal service. The customer is asked to choose five targets out of the list of candidates and REAVER must be able to execute any feasible combination. Sizing the system with worst-case propellant allows this requirement to happen. The worst-case sequence and its key parameters are given in table 3.4 below.

Table 3.4: Summary of the worst-case design sequence ($\Omega^*_{RH} = 64°$).

Leg	**To**	ΔV_1 [m s^{-1}]	ΔV_2 [m s^{-1}]	ΔV_{ph} [m s^{-1}]	**Transfer** [d]	**Phase** [d]
1	*COMSATBW-1*	368.4	12.9	28.9	6.5	17.7
2	*METEOSAT 10*	244.7	0.0[1]	28.9	4.5	17.7
3	*GALAXY 14*	7.0	66.4	28.7	2.5	17.9
4	*AMC-3*	178.6	7.0	28.9	3.5	17.7
5	*ECHOSTAR-1*	6.9	27.8	28.7	2.5	17.9
R	Recycling Hub	6.0	83.8	28.6	2.5	18.2

Tug	**Debris**	ΔV [m s^{-1}]	M_{prop}[2] [kg]	**Spiral time** [d]	**Start day** [d]	**Arrival day** [d]	**Handover** [d]
1	*COMSATBW-1*	582.0	114.5	258.2	28.3	286.4	291.4
2	*METEOSAT 10*	202.7	114.5	75.2	55.5	130.6	162.3
3	*GALAXY 14*	195.9	33.3	74.3	81.9	156.3	172.3
4	*AMC-3*	95.3	33.3	28.1	109.1	137.2	167.3
5	*ECHOSTAR-1*	132.1	33.3	46.0	135.6	181.6	186.6

Parameter	**Value**
Mothership ΔV total	1182.0 m s^{-1}
Mothership orbital propellant mass	1019.3kg
RCS and reserve margin (15 %)	152.9kg
Mothership total propellant mass	1172.2 kg
Tug propellant (5 tugs)	329.0kg
Mothership return to RH	157.3 day
Mission completion	291.4 day

High-Fidelity GMAT Validation

In order to validate the ΔV, propellant mass and mission timeline obtained form the Python script, the final mission sequence was implemented in NASA's General Mission Analysis Tool (GMAT version R2026a). GMAT operates as a numerical propagator with configurable force models and burn sequencing, making it a suitable reference for verifying the closed-form analytical expressions derived in section 3.5. Two separate GMAT scripts were developed: one for the mothership grand-tour sequence and one for the tug low-thrust spiral transfer. The GMAT simulation optimises the specific mission sequence, and thus allows flexible allocation so each script is usable for all tugs and targets by changing the target conditions.

Mothership Script

The mothership is initialised in the recycling hub orbit, the tug wet mass is decremented from the spacecraft dry mass upon each tug deployment event, correctly reducing the inert mass carried into subsequent legs. Each transfer leg is structured identically, following the three-burn architecture described in section 3.5. A `DifferentialCorrector` (Newton-Raphson algorithm, limited to 50 iterations) is used as the targeter for both the Hohmann transfer and the phasing manoeuvre. For the Hohmann transfer segment, four conditions are simultaneously achieved: semi-major axis matching the target to within ±1 km, inclination to within ±0.01°, RAAN to within ±0.1°, and eccentricity driven to near-zero ($e < 0.01$). The manoeuvre is executed via two impulsive burns (ΔV_1 and ΔV_2) decomposed into velocity (V) and normal (N) components in the local VNB frame. The simulation would ideally use finite burns, however GMAT does not allow varying the thruster direction during optimisation. This means it is not possible to correctly choose the orientation of the finite burn. The impulsive burn optimises V and N components separately, enabling the optimiser to correctly choose the right burn.

For the phasing segment, the actual phase angle between the mothership and the target at orbit insertion is computed from their mean longitudes and divided by $N_{ph} = 18$ revolutions. The required phasing orbit semi-major axis is derived analytically within the GMAT script and achieved via a separate differential correction loop, after which N_{ph} full revolutions are propagated and the phasing orbit is exited symmetrically. This implementation closely mirrors equations (3.7) and (3.8), but uses the true phase gap at each leg rather than the 90° average assumed in the Python model.

Following phasing completion, a proximity operations hold of 10 d is propagated to represent the time allocated to RPOD and capture. The tug dry mass is then decremented to simulate tug deployment and separation. A mission event log records the epoch, orbital state, and event code at each key milestone: leg start, Hohmann completion, phasing completion, tug deployment, and RPOD end.

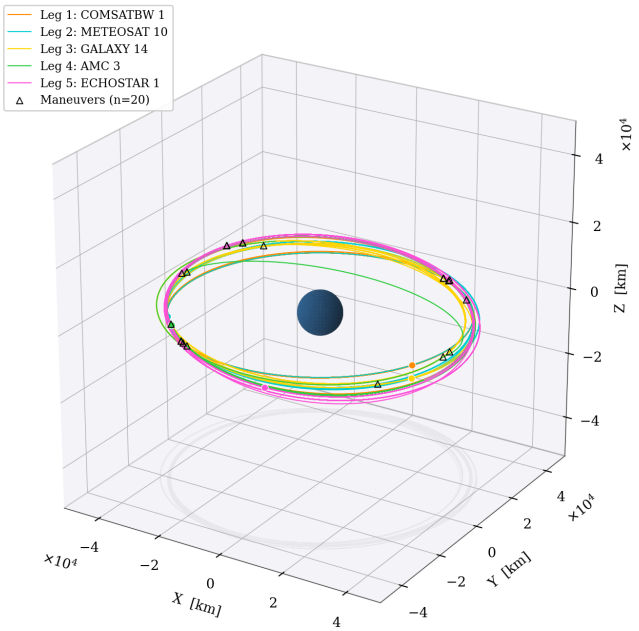

Figure 3.12: Mothership orbital mission visualisation in Python, using data generated by NASA's General Mission Analysis Tool (GMAT)

[1]The altitude change between COMSATBW-1 and METEOSAT 10 is ≈ 19m, justifying the 0.0 ΔV.

[2]The propellant loading strategy for the tugs is such that at least one tug acts as a redundant option in case one fails to perform its allocated manoeuvre.

Tug Script

The tug GMAT script simulates a single low-thrust spiral transfer from a specified debris orbit to the recycling hub orbit ($a = 42\,875$ km, $i = 7.00°$, $\Omega = 64.00°$). The script is parametrised such that the initial orbital state (semi-major axis, inclination, and RAAN) can be set to match any of the five selected debris targets, allowing the spiral transfer of each individual tug to be simulated and verified independently. In the present validation, the script is configured for the most demanding transfer, that from the COMSATBW-1 debris orbit ($a = 42\,164.2$ km, $i = 0.070°$, $\Omega = 89.69°$), which requires the largest combined altitude gain and plane change among all five debris and therefore represents the propellant mass and spiral time upper bound for tug sizing.

The tug carries a single electric thruster with a maximum thrust of $F = 0.07$ N and specific impulse $I_{sp} = 1600$ s. In operation, the thruster is gimballed to point in the direction that optimally balances altitude raising and plane change at each point in the spiral. To model this in GMAT, the single physical thruster is represented by three virtual thruster components aligned with the local VNB axes, prograde ($+\hat{V}$), out-of-plane ($+\hat{N}$), and anti-normal ($-\hat{N}$), whose thrust magnitudes are determined by the optimiser. The thrust split angle α partitions the total thrust between the prograde and out-of-plane directions as $F_V = F\cos\alpha$ and $F_N = F\sin\alpha$, such that the vector magnitude is always conserved.

The optimiser therefore determines the V and N components of the thruster pointing direction; the resulting values physically represent the gimbal angle of the single flight thruster and never exceed the 0.07 N thrust limit.

The spiral is executed via alternating half-orbit finite burns. On the first half-orbit of each pair, the prograde and $+\hat{N}$ virtual thrusters fire simultaneously; on the second half-orbit, the prograde and $-\hat{N}$ virtual thrusters fire simultaneously. This alternating-normal scheme accumulates inclination change in the same sense on each half-orbit, doubling the plane-change efficiency relative to a unidirectional normal burn. The half-period for each arc is recomputed from the current semi-major axis after each burn segment, correctly capturing the changing orbital period as altitude increases throughout the spiral.

The differential corrector simultaneously varies three free parameters to achieve the target orbit:

1. the thrust split angle $\alpha \in [1°, 89°]$, controlling the trade-off between altitude gain and plane change per arc;
2. the total number of half-orbit burn pairs N_{ARCS}, which determines the total spiral duration and drives the magnitude of the inclination change;
3. the true anomaly at arc start ν_{start}, which sets the orientation of the out-of-plane burn arcs relative to the line of nodes and thereby steers the direction of RAAN change.

Convergence tolerances are ±1 km on SMA, ±0.05° on inclination, and ±0.1° on RAAN. The converged solution yields $N_{\text{ARCS}} \approx 263$ half-orbit pairs, a thrust split angle $\alpha \approx 87.5°$ (predominantly out-of-plane), and an arc start anomaly $\nu_{\text{start}} \approx 279°$.

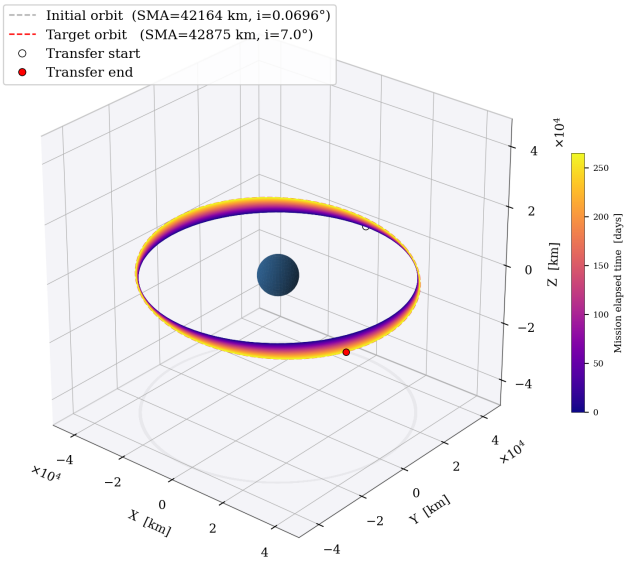

Figure 3.13: Tug orbital mission visualisation in Pythonusing data generated by NASA's General Mission Analysis Tool (GMAT)

Comparison with Analytical Results

The GMAT results are compared against the Python analytical outputs for each mothership leg and for the tug spiral in table 3.5. For the mothership legs, the principal sources of expected discrepancy are the use of the true phase gap at each leg rather than the 90° average assumed in the Python model, and the finite number of phasing revolutions ($N_{ph} = 18$) used in GMAT compared to the idealised continuous-phase assumption. For the tug, the main difference is that GMAT propagates a true finite-burn low-thrust spiral with time-varying orbital elements, whereas the Edelbaum formula of equation (3.12) provides a scalar ΔV estimate that does not account for the continuously evolving orbit geometry. Agreement within approximately 5% confirms that the analytical model is of sufficient accuracy for preliminary design sizing; deviations on individual mothership legs are expected to reflect phase gap variability rather than modelling error.

Table 3.5: Comparison of Python analytical and GMAT results

Parameter	Python	GMAT	Difference %	Unit
Mothership, Total (all 5 legs)				
m_{prop}	1172.2	1234.0	+5.3%	kg
$T_{\text{mothership}}$	291.4	289.0	-0.8%	d
Tug, COMSATBW-1 to RH (worst case)				
m_{prop}	114.5	109.33	-4.5%	kg
t_{spiral}	258.2	263.0	+1.9%	d

Rendezvous, Proximity Operations, and Docking (RPOD)

Moving on to capture operations, the mothership shall transition at least once per debris from a far-range orbital rendezvous to a close-range approach. Once the mothership transitions from absolute to relative navigation, it must continue to cover final approach, inspection, capture, detumbling and also tug handover to the RH. The RPOD simulation implemented for this astrodynamics analysis follows from the method used by Conings and Mooij [36]. It must be noted that this method is adapted from LEO to GEO.

Translational Dynamics

The linearised Clohessy-Wiltshire (CW) equations model close-range relative navigation and can be applied to this analysis (equation (3.22)).

$$\begin{aligned} \ddot{x} - 2n\dot{y} - 3n^2 x &= f_x \\ \ddot{y} + 2n\dot{x} &= f_y \\ \ddot{z} + n^2 z &= f_z, \end{aligned} \tag{3.22}$$

with mean motion $n = \sqrt{\frac{\mu_E}{a^3}}$; x, y, and z are the position components of the mothership relative to the debris or tug; and f_x, f_y and f_z are the force components per unit mass acting on the mothership.

The closed-form State Transition Matrix (STM) $\mathbf{\Phi}(t)$ propagates the relative state $\mathbf{x} = [\mathbf{r}; \dot{\mathbf{r}}] \in \mathbb{R}^6$. Two-impulse targeting between rest-to-rest positions $\mathbf{r}_0$ and $\mathbf{r}_f$ in transfer time t is solved using the STM (equation (3.23)).

$$\mathbf{v}_0^+ = \mathbf{\Phi}_{rv}^{-1}\left(\mathbf{r}_f - \mathbf{\Phi}_{rr}\,\mathbf{r}_0\right), \qquad \Delta\mathbf{v}_1 = \mathbf{v}_0^+ - \mathbf{v}_0, \tag{3.23}$$

where $\mathbf{\Phi}_{rr}$ and $\mathbf{\Phi}_{rv}$ are the 3×3 position–position and position–velocity partitions of $\mathbf{\Phi}(t)$; $\mathbf{v}_0^+$ is the required velocity immediately after the first burn; and $\Delta\mathbf{v}_1$ is the first impulse vector. For all rest-to-rest transfers in this analysis, $\mathbf{v}_0 = \mathbf{v}_f = \mathbf{0}$. The transfer time is then measured using the chord length $d = \|\mathbf{r}_f - \mathbf{r}_0\|$ and the maximum approach velocity constraint set at $V_{max} = 0.05\,\mathrm{m\,s^{-1}}$ with equation (3.24).

$$t = \frac{d}{0.5\,V_{max}} \tag{3.24}$$

GEO Perturbations During Hold-Point Phases

When the mothership is in a hold position, to inspect the debris or awaiting ground commands, the mothership needs to perform continuous attitude control to reject disturbance perturbations from solar radiation pressure and Earth's triaxility (J_{22} tesseral harmonic) contributions.

The solar radiation pressure acceleration is calculated using equation (3.25), with $C_R = 1.5$, $A/m = 0.020\,\mathrm{m^2\,kg^{-1}}$, and $P_\odot = 4.56 \times 10^{-6}\,\mathrm{N\,m^{-2}}$. Note that these values are derived from the component data and a spacecraft-Sun distance assumed at 1AU. The Earth's triaxility contributes $a_{triax} \approx 3 \times 10^{-8}\mathrm{m\,s^{-2}}$ to the acceleration.

$$a_{SRP} = C_R \cdot \frac{A}{m} \cdot P_\odot \approx 1.03 \times 10^{-7}\,\mathrm{m\,s^{-2}} \tag{3.25}$$

The combined station-keeping ΔV for a hold-point of duration T_{HP} is estimated as a worst-case bound using equation (3.26):

$$\Delta V_{SK} = (a_{SRP} + a_{triax})\, T_{HP} \tag{3.26}$$

The ΔV calculated is conservative for two reasons. First, the Earth triaxiality acceleration a_{triax} acts on both spacecraft since they are at the same orbital position, so its relative contribution to station-keeping can be considered negligible; including it overestimates the ΔV_{SK} the cost by ≈30%. Second, the SRP term uses the mothership area-to-mass ratio $A/m = 0.020\,\mathrm{m^2\,kg^{-1}}$; the target debris, being a much heavier satellite bus, has a lower A/m and thus smaller SRP acceleration in the same direction. The net relative SRP disturbance is therefore smaller than a_{SRP} of the mothership alone. Only using the mothership value gives again a conservative upper bound on the stationkeeping cost. For an 8 h hold-point, $\Delta V_{SK} \approx 0.004\,\mathrm{m\,s^{-1}}$, which can be considered negligible relative to the total RPOD budget.

Phase 1: Approach

When the mothership arrives at approximately 100 m from the debris, it transitions to relative navigation and the RPOD sensor suite is activated. Hill's frame coordinates are used to describe the relative position of both the mothership and target, visualised in figure 3.14. At this point, the mothership will position itself along the negative the V-bar. This is the axis along the targets orbital motion and is the only one that provides a fixed CW hold point. In fact, it can be said that a spacecraft placed at a fixed along-track offset remains stationary relative to the target. Whereas an equivalent offset along the cross-track H-bar axis naturally results in oscillatory motion. The mothership therefore autonomously translates along the V-bar to a 20 m inspection standoff point using a two-impulse CW solver.

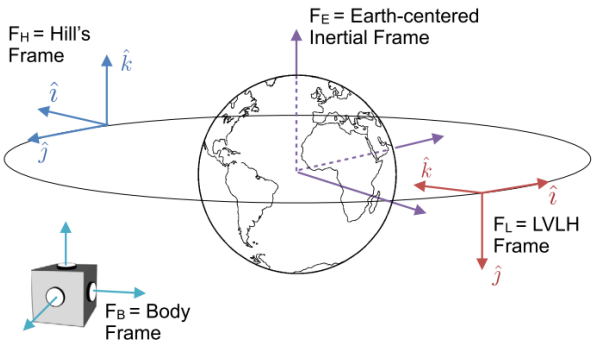

Figure 3.14: Hill's frame [37]

Phase 2: Inspection and Ground Relay

The mothership first remains at the mentioned inspection point that can be seen in figure 3.15 for approximately 8 h. This hold-point covers inspection data processing (≈30 min), telemetry downlink and ground analysis of the debris parameters (6–7 h), and finally go/no-go uplink (≈15 min). From this last uplink, the solar-panel span of the target is confirmed, establishing the inner keep-out sphere radius $r_{KOS1} = \frac{L_{panel}}{2} \times 1.20$ The factor 1.20 is a 20% safety margin on the solar panel span so as to ensure no collision with the debris.

An important note: the RPOD analysis is based on the worst-case reference target COMSATBW-1 which has a solar panel span of $L_{panel} = 17.2\,\mathrm{m}$. This leads to keep-out-sphere 1 (KOS1) radius of $r_{KOS1} = 10.3\,\mathrm{m}$. After go/no-go command, the mothership shall move on to the H-bar as per phase 3.

Phase 3: Transition to H-bar

Here, the mothership transitions from the negative V-bar to H-bar as can be seen by the green dotted line in figure 3.15, while maintaining a minimum distance of r_{KOS1} from the target. If the direct chord between the start and final point passes inside the KOS1 sphere, the manoeuvre is instead routed through a midpoint placed on the KOS1 surface. This increases the total transfer time, as the single direct transfer is replaced by two consecutive two-impulse CW transfers.

Phase 4: Arm Extension
During phase 4, the mothership remains at r_{KOS1} from the target along the H-bar. The robotic arm is deployed, attached to the tug and prepares it for capture. The change in inertia due to this arm extension is a significant contributor to the RPOD ΔV.

Phase 5: Spin Synchronisation
During phase 5, the mothership spins to match the tumble rate ω_{debris} of the target. The worst-case tumbling rate considered is $\omega = 6^\circ\,\mathrm{s}^{-1}$, i.e. 1 rpm, as per REQ-MIS-06.

Phase 6: Final Approach, Capture, and Detumble
During this phase, the mothership manoeuvres from KOS1 to KOS2 ($r_{KOS2} = L_{arm} + L_{tug}/2$) along the H-bar via a two-impulse CW transfer. This is the distance between the orange and blue spheres in figure 3.15. At the KOS2 hold-point, the tug's capture mechanism moves on to approach the debris LAE nozzle and secures itself to it. The mothership then needs to dump the momentum of the combined assembly (mothership, arm, tug, and debris) in order to establish control of the full stack. The combined inertia tensor $\mathbf{J}_{comb}$ is computed using the parallel-axis theorem in equation (3.27).

$$\mathbf{J}_{comb} = \sum_{k} \left[\mathbf{J}_k + m_k \left(|\mathbf{d}_k|^2 \mathbf{I} - \mathbf{d}_k \mathbf{d}_k^{\mathsf{T}} \right) \right], \tag{3.27}$$

where k indexes each body in the combined stack (mothership, robotic arm, tug, and debris); $\mathbf{J}_k$ and m_k are the inertia tensor and mass of body k about its own centre of mass; $\mathbf{d}_k$ is the offset vector from the reference point to the centre of mass of body k; and $\mathbf{I}$ is the 3×3 identity matrix.

Phase 7: Retreat and Tug Release
After succesfully establishing control, the mothership releases the tug, and thus the debris, and retreats to a safe standoff of 20 m through a two-impulse CW transfer along H-bar. Finally, the mothership communicates the RPOD operations to the ground station and awaits for command to navigate to the next target.

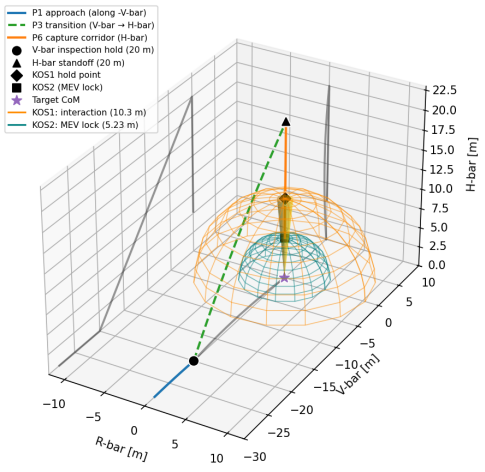

Figure 3.15: RPOD debris trajectory

RH Handover Proximity Operations
Once the mothership has captured all five targets and returned to the RH orbit, two RPOD phases are modelled per tug handover:

1. **Tug-meet**: a phase allocated to the mothership operating a cooperative close approach from 30 m to $r_{KOS2_{meet}} = L_{arm}$, where the arm engages the arriving tug. Figure 3.16(a) shows the trajectory of the tug meet manoeuvre.
2. **RH docking**: a second phase where the mothership navigates the combined body to the RH docking port through the RH keep-out sphere hierarchy ($r_{KOS1_{dock}}$, $r_{KOS2_{dock}}$), with the arm extended holding the tug and debris assembly. Note that the RH KOS radii are set to 11 and 5 m respectively. Figure 3.16(b) shows the trajectory of the RH docking manoeuvre.

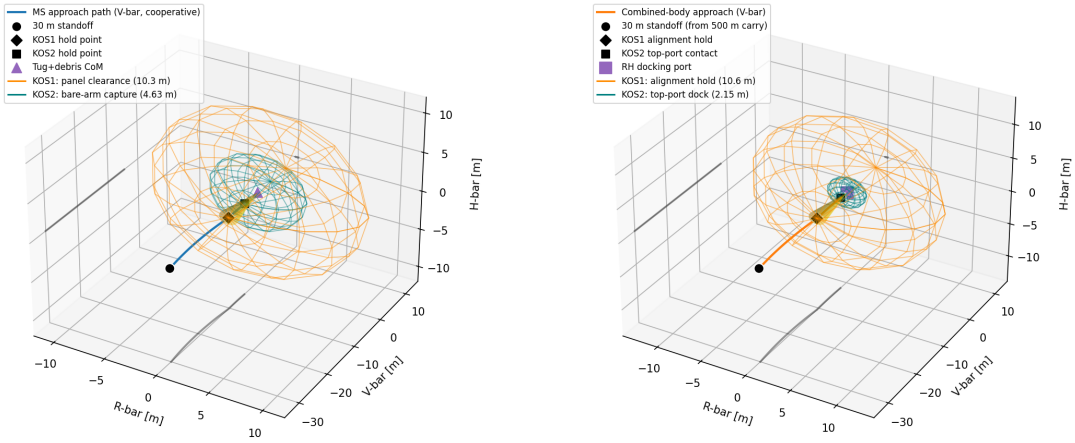

(a) Mothership meets tug

(b) Mothership docks to RH

Figure 3.16: RPOD RH trajectories

Abort Margin and Safety Constraints

A 100 % abort margin is applied to the debris RPOD ΔV so that it covers events such as unexpected debris attitude changes and failed capture attempts. The mothership shall go back to the V-bar holdpoint of 20 m and wait for ground command to attempt capturing the debris again. Additional safety constraints are applied for RPO:

- **Approach cone:** a 5° half-angle approach cone to the debris LAE nozzle is maintained, consistent with MEV heritage (MEV-1/Intelsat-901). A lateral offset exceeding $r_{KOS2} \tan 5° \approx 0.49$ m leads to an abort.
- **KOS hierarchy:** $r_{KOS1} > r_{KOS2}$. This ensures that the inner capture sphere always lies inside the debris tumble-exclusion zone.

Table 3.6 summarises the RPOD ΔV contributions per capture event. The values in the table are included in the mothership propellant mass as an RCS margin of 10 %. More details on the margin follow in chapter 8.

Table 3.6: RPOD ΔV budget per capture, derived from the close-range simulation.

Phase / Manoeuvre	ΔV [m s^{-1}]	**Margin applied**
Approach + inspection SK (P1-P2)	0.055	100%
Transition + spin sync + final app (P3-P7)	0.595	100%
Total debris RPO ($\Delta V_{RPO,debris}$)	**0.65**	-
Momentum dump / detumble (P6b)	1.33	100%
Tug-meet at RH	0.14	100%
RH docking	0.27	100%
Total RH RPOD per cycle ($\Delta V_{RPO,RH}$)	**0.41**	-

The total RPOD ΔV for all manoeuvres after a conservative margin of 100% is applied is 23.4 m s^{-1}. This is computed by multiplying the ΔV from table 3.6 by the number of times each is conducted within the mission. The margin is applied in order to account for an abortion per RPOD manoeuvre/phase.

4. Technical Risk Assessment

This chapter will discuss and assess the technical risks identified in the midterm report [38]. The analysis focuses on risks that may affect mission success, safety, cost, schedule, or the requirement to remove five GEO debris targets per year. Section 4.1 discusses all the risks identified together with their updated mitigation and contingency measures; section 4.2 will show the pre- and post-mitigation risk maps and discusses the high risks identified.

4.1. Technical Risks

The risk management approach follows the same likelihood-consequence scoring method used in the midterm report [38]. This is consistent with ECSS-M-ST-80C [24], which treats risk management as an integrated and iterative process across all project phases. The risk assessment is built upon the same risks established on the previous design phase and only one new main risk was identified (TR-M-07). The risk analysis is conducted on a general system level and identifies corresponding subsystems to which the risks apply, see the footnote of table 4.1. Mitigation measures are updated and reinforced from the midterm report [38] corresponding to the detailed design.

The risk analysis identified weak spots of the design and helped improve these weak spots throughout the design phase. For this reason, the risk analysis was conducted parallel to the detailed design phase and updated throughout, see table 4.1.

Table 4.1: Technical risk register for the Mothership and Tugs architecture

ID	Risk Description	Pre L	Pre C	Pre Score	Pre Sev.	Mitigation (preventive)	Contingency (reactive)	Post L	Post C	Post Score	Post Sev.
TR-U-01	Critical technologies lack development for final detailed design.	2	4	**8**	**Med.**	Start early TRL development; breadboards, qualification models, backup technologies [24, 25].	Select fallback; extend design phase.	1	3	**3**	**Low**
TR-U-02	V&V, ground testing, and simulation do not represent GEO RPO/capture/other operations.	4	2	**8**	**Med.**	Detailed V&V plan; assign test facilities, availability, cost [39, 27].	Extend the schedule; use analysis where testing is not possible.	2	2	**4**	**Low**
TR-U-03	Launch anomaly, delay, or injection error prevents operational-region arrival on time.	3	3	**9**	**Med.**	Proven GTO launcher; ΔV accuracy/injection margin; verified interfaces; backup window [40, 41].	Correct with onboard propulsion if possible; delay commissioning; replan campaign.	2	2	**4**	**Low**
TR-U-04	Transfer/phasing to GEO graveyard or RH needs more time/ΔV than budgeted.	4	3	**12**	**High**	Fixed target sequence; GMAT verification of required ΔV [42, 43].	Rephase sequence; reduce targets; prioritise closest/highest-value targets.	2	3	**6**	**Med.**
TR-U-05	Target identity/properties/ownership data incorrect or incomplete before approach.	3	4	**12**	**High**	Use DISCOSweb/SpaceTrack; manual check; verify ownership [44][1].	Abort approach; safe hold; re-characterise; skip target if uncertain.	2	3	**6**	**Med.**
TR-U-06	Communication blackout during critical autonomy; no abort authority/telemetry.	3	3	**9**	**Med.**	Size memory for command/payload data; preloaded abort logic [41, 45].	Safe hold; backup ground station/link; resume after telemetry review.	2	3	**6**	**Med.**
TR-U-07	Collision with active GEO S/C, inactive object, or micrometeoroid damages critical system.	3	5	**15**	**High**	GMAT-verified trajectory; track active/inactive objects; avoidance manoeuvre when collision probability high; margin and redundancy on affected subsystems. [46, 47].	Suspend operations; notify operators; replan path; isolate damage.	2	5	**10**	**High**

[1] `https://www.unoosa.org/oosa/en/ourwork/spacelaw/treaties/outerspacetreaty.html` [cited 22 May 2026]

ID	Risk Description	Pre L	Pre C	Pre Sc.	Pre Sv.	Mitigation	Contingency	Post L	Post C	Post Sc.	Post Sv.
TR-U-08	Failed approach/capture/handover/docking/tug transport attempts delay yearly campaign.	4	3	**12**	**High**	Campaign schedule reserve; sensor imaging for target characteristics [30].	Skip/postpone target; reduce scope; reassign tugs/propellant.	3	3	**9**	**Med.**
TR-U-09	GEO radiation, ESD, eclipses, and thermal cycling degrade spacecraft systems.	5	4	**20**	**Crit.**	Radiation-tolerant avionics; shielding where needed; heaters/radiators; qualified parts [48, 46].	Switch to redundancy; safe mode; shed loads; EOL if unstable.	2	4	**8**	**Med.**
TR-U-10	GNC/autonomy failure, hold-point, or disposal transfer.	3	5	**15**	**High**	Fault detection; autonomous recovery; safe-hold states; reserved ΔV [41, 46].	Transfer to nearest safe state; passivate; wait for ground input.	2	5	**10**	**High**
TR-M-01	Mothership chemical propellant depleted before all operations and return.	3	5	**15**	**High**	20% AOCS failed-RPOD margin; 2% residual propellant margin [42, 43].	Reprioritise targets; skip low priority; save propellant for return/disposal.	1	5	**5**	**Med.**
TR-M-02	Capture mechanism fails due to navigation sensor failure/degradation/poor calibration.	3	4	**12**	**High**	Redundant GEO-qualified sensors; calibration; pre-capture characterisation [49, 50, 41].	Abort; retreat to keep-out sphere 2; re-characterise; retry or abandon.	2	4	**8**	**Med.**
TR-M-03	Target fragments during capture due to excessive loads.	4	5	**20**	**Crit.**	Pre-capture inspection; load analysis; material study; compliant arm [46, 49].	Stop capture; retreat; track fragments; abandon if debris risk high.	2	5	**10**	**High**
TR-M-04	Residual propellant, pressurant, batteries, or stored energy cause rupture/leak/explosion/contamination.	4	5	**20**	**Crit.**	Review target history/operator data; visual inspection; avoid tanks/batteries [46].	Stop operation; retreat to keep-out sphere 2; wait; revise or abandon.	1	5	**5**	**Med.**
TR-M-05	Mothership fails to stabilise/align/position debris for safe tug coupling/handover.	4	4	**16**	**High**	Keep-out spheres; approach cone; cameras/IR/lidar for inspection/characterisation [51, 41].	Delay coupling; restabilise/reorient; mothership transports or releases target.	2	4	**8**	**Med.**
TR-M-06	Mothership arrays, antennas, sensors, thermal surfaces, or capture hardware damaged.	4	4	**16**	**High**	Retractable arrays; redundant sensors; keep-out spheres 1 and 2 [41].	Reconfigure power/comms; switch sensors; reduce scope; use power margin.	1	4	**4**	**Low**
TR-M-07	Robotic arm TRL too low; arm fails capture/detumbling/handover.	4	5	**20**	**Crit.**	Minimum TRL before launch; representative capture/detumbling/handover tests [52].	Add budget/schedule; replace by mature heritage/off-the-shelf arm; reduce capability.	2	4	**8**	**Med.**
TR-T-01	Tug EP/power insufficient for required operations within timeline.	3	4	**12**	**High**	Thruster sized for thrust + margin; PPU/solar arrays sized accordingly [18, 43].	Extend transfer; raise duty cycle; redirect to hold/disposal; use power margin.	2	3	**6**	**Med.**
TR-T-02	Tug deployment, activation, checkout, or separation fails after target capture.	3	4	**12**	**High**	Multi-start thrusters; predictable separation; visual/physical confirmation; ground relay [27].	Retry deployment; assign another tug; reduce campaign scope.	2	3	**6**	**Med.**
TR-T-03	Tug fails to couple; unstable tug + debris transport system.	3	4	**12**	**High**	Two-camera AEP confirmation; mothership relay/processing [41, 13].	Retry with alignment correction; return tug; assign another tug/mothership.	2	4	**8**	**Med.**
TR-T-04	One tug lost/degraded; campaign below five targets/year.	3	4	**12**	**High**	Tug redundancy; common spares; one-tug-loss replanning [29].	Reassign remaining tugs; reduce targets; prioritise closest/highest-value targets.	2	4	**8**	**Med.**
TR-T-05	Tug docking or debris handover at hub fails.	3	3	**9**	**Med.**	Redundant docking sensors; soft/hard capture; alignment checks [41, 53].	Retry to limit; hold at stand-off; redirect debris to disposal orbit.	2	3	**6**	**Med.**
TR-T-06	Tug coupling mechanism/structure fails under large-debris transport loads.	4	4	**16**	**High**	AEP sized for worst-case loads; safety factors; mothership connection confirmation [54, 55].	Reduce thrust/rates; stop transport; release debris safely if limits reached.	2	4	**8**	**Med.**

Legend: **Low (1–4)** **Medium (5–9)** **High (10–16)** **Critical (20–25)**

ID	Risk Description	Pre L	Pre C	Pre Sc.	Pre Sv.	Mitigation	Contingency	Post L	Post C	Post Sc.	Post Sv.
Subsystem Reference TR-U-01 Organisation; TR-U-02 Organisation; TR-U-03 Organisation, Astrodynamics; TR-U-04 Astrodynamics, AOCS, Structures, Propulsion; TR-U-05 Astrodynamics; TR-U-06 TT&C; TR-U-07 Astrodynamics, AOCS, Propulsion; TR-U-08 AOCS; TR-U-09 EPS; TR-U-10 C&DH; TR-M-01 Propulsion; TR-M-02 AOCS; TR-M-03 Capture; TR-M-04 Propulsion; TR-M-05 C&DH, AOCS; TR-M-06 AOCS, Structures, TT&C; TR-M-07 Capture; TR-T-01 Propulsion, EPS; TR-T-02 C&DH; TR-T-03 Capture; TR-T-04 Organisation; TR-T-05 AOCS, Structures; TR-T-06 Capture.										

4.2. Risk Maps

The pre- and post-mitigation risk maps shown in figure 4.1 visually depict risk exposure based on table 4.1. As stated in the midterm report [38], three residual high risks remain: collision or critical-system damage, AOCS and autonomy failure preventing safe disposal, and target fragmentation during capture. These keep a high consequence score because, while mitigation can reduce their probability of occurrence, it cannot fully eliminate their severity. Note that the risk ID's are shortened for image readability.

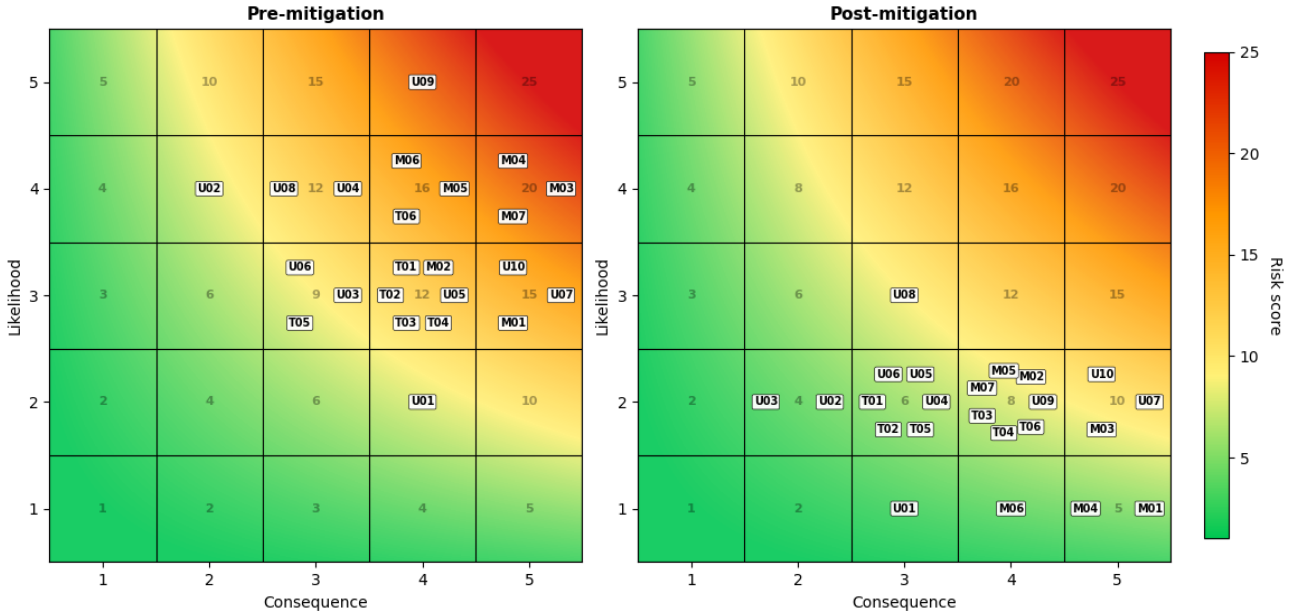

Figure 4.1: Pre- and post-mitigation technical risk maps (TR- is omitted for readability)

5. Command and Data Handling

The command and data handling (C&DH) subsystem acts as the brain of the spacecraft, managing the data flow within the vehicle, and performing on-board operations.[1] Sizing of the C&DH subsystem is done on a hardware basis by defining a computer architecture and selecting relevant components. The software development aspect of C&DH is not delved into in detail as it is considered to be outside the scope of this project.

5.1. Computer Network Architecture

The design of the computer network architecture is split into topology selection, ADR-specific considerations, subsystem interface definition, and software. This is followed by the selection of suitable components.

CNA Topology

Multiple computer network architectures (CNA) or topologies are considered, the most common of which are provided in figure 5.1. The choice of a particular architecture depends on factors derived from subsystem requirements. These include coverage requirements, data throughput (data rate), mass, and cost. [2]

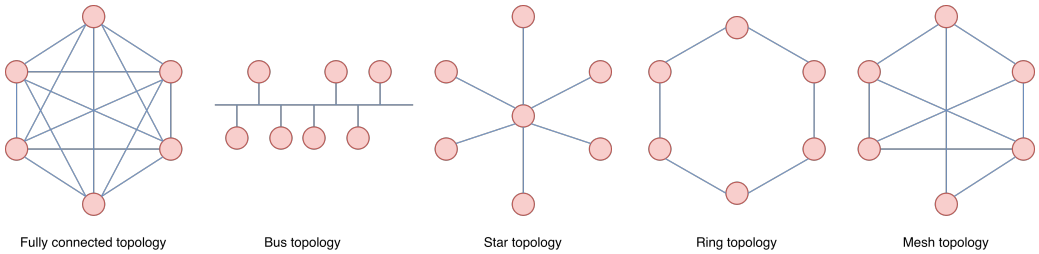

Figure 5.1: Computer network topologies

Each mission presents unique requirements and applications that demand specific architectural solutions, thereby influencing the selection of the CNA. Although papers specifically on active debris removal (ADR) missions focus on their mission architecture rather than the specific computer network topology, some conclusions on their CNA can nonetheless be made.

ADR and OOS spacecraft typically have a guidance, navigation, and control (GN&C) system (considered in this paper as part of AOCS), vision based navigation, and robotic manipulation (notable examples being RSGS, DEOS, e.Deorbit, and ClearSpace-1). [3] All of these functions feed into a centralised computer (the OBC) ultimately favouring a star topology. Whether or not subsystems require communication with one-another depends on whether they need (fast) closed-loop interaction. The fully connected topology can thus be ruled out, since subsystems such as TCS and PL, among others are unlikely to require direct communication and a connected topology would be overly redundant and expensive without offering significant advantages.

From the remaining topologies, an analysis can be made of the interface count. For N subsystems, the number of interfaces is computed using equation (5.1). For the 8 subsystems of the REAVER mission, the ring and star topologies have the lowest required interfaces ($I = 8$), followed by the bus topology, which requires a backbone cable and N drop-lines ($I = 9$). The mesh (similar to the fully connected topology), depending on whether a full or partial one is created results in much higher interface counts ($I_{max} = 28$). Since certain subsystems are likely to require direct interaction, a hybrid CNA between star, mesh, and bus topologies is chosen (see figure 5.2 and figure 5.3).

$$I_{star} = I_{ring} = N, I_{bus} = N + 1, I_{mesh} = N\frac{N-1}{2} \tag{5.1}$$

One thing to note, however, in the consideration of a hybrid approach is that a pure centralised network (one where all data and low-level control loops pass through the OBC) is not favoured. The command hierarchy might be centralised, but control execution should be distributed to subsystem computers / processors. This split is discussed further in subsequent sections.

[1] https://ocw.tudelft.nl/wp-content/uploads/1.0-Command-and-Data-Handling-Lecture-Notes.pdf [accessed 4 June 2026]
[2] https://spacerepublic.eu/satcom-architecture/ [accessed 9 June 2026]
[3] https://www.frontiersin.org/journals/robotics-and-ai/articles/10.3389/frobt.2021.686723/full [accessed 9 June 2026]

ADR-specific CNA

Active debris removal (ADR) missions present significant challenges for the design of the C&DH subsystem, particularly with respect to target detection and tracking prior to rendezvous, proximity operations, and docking (RPOD). These activities require the processing of high-rate data streams from multiple sensors, while vision-based navigation and pose estimation impose additional computational demands [8]. To accommodate these requirements, dedicated processing units are incorporated within the AOCS and payload subsystems, responsible for relative navigation, and image processing and robotic arm control algorithms, respectively. This distributed architecture fulfils the functions of a dedicated rendezvous on-board computer (OBC) for non-cooperative target tracking, as described by Juillard et al. [8]

Additional considerations of ADR missions, specifically in GEO, include radiation, and significant signal latency. Components must be selected to ensure that the radiation environment does not compromise functionality or performance of the C&DH subsystem during the mission lifetime. A multi-step methodology similar to that described by Poivey (2002) can be implemented, which covers part selection, testing, and shielding to ensure a radiation tolerant design [56]. Shielding is further discussed within the design of the structures subsystem (section 9.3). In addition to hardware selection, software workarounds can also be implemented in the form of Error-Correcting Code (ECC) memory or Triple Modular Redundancy (TMR). These software considerations are accounted for within standardised algorithms defined by the Consultative Committee for Space Data Systems (CCSDS) used by agencies such as NASA and ESA and are often already incorporated into commercial off-the-shelf (COTS) components. The second consideration of latency, which for satellites in geostationary orbit, is approximately 500 ms (including ground processing) is further discussed in chapter 12 [57].

Subsystem Interfaces

System-level data-handling diagrams of the mothership and tugs, outlining the data flow of the subsystems within each spacecraft are presented in figure 5.2, and figure 5.3. The C&DH subsystem communicates with all subsystems, receiving information on subsystem health, and transferring telecommands. The C&DH also receives and executes commands from GS and conversely sends housekeeping (HK) data back through the TT&C subsystem to provide ground with information on spacecraft and subsystem health. These basic operations are essentially comparable for both the mothership and each tug. The CAN bus connecting the mothership and tugs is intended solely for housekeeping and maintenance functions while the tugs are docked. High-volume software uploads are performed infrequently and are therefore not considered a driver for bus sizing. For this reason a CAN bus is considered appropriate, instead of a higher-data rate options, such as SpaceWire.

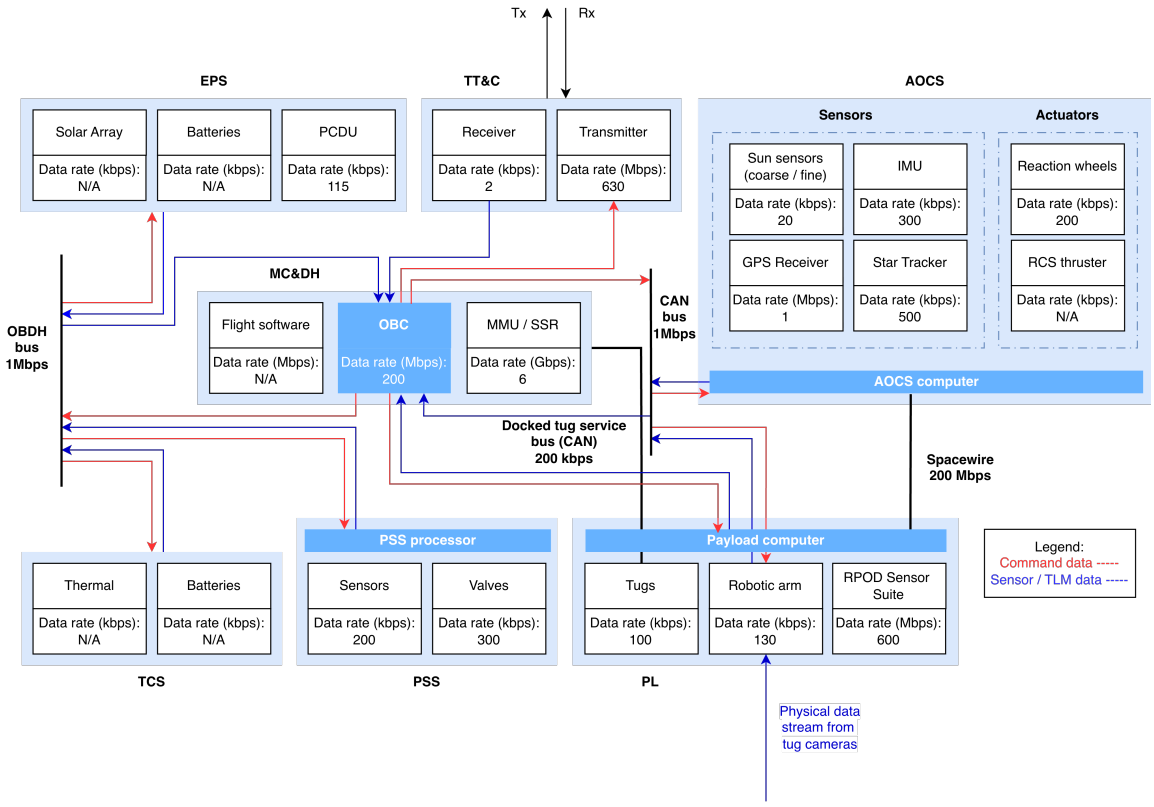

Figure 5.2: Mothership data handling block diagram (MMU = memory management unit)

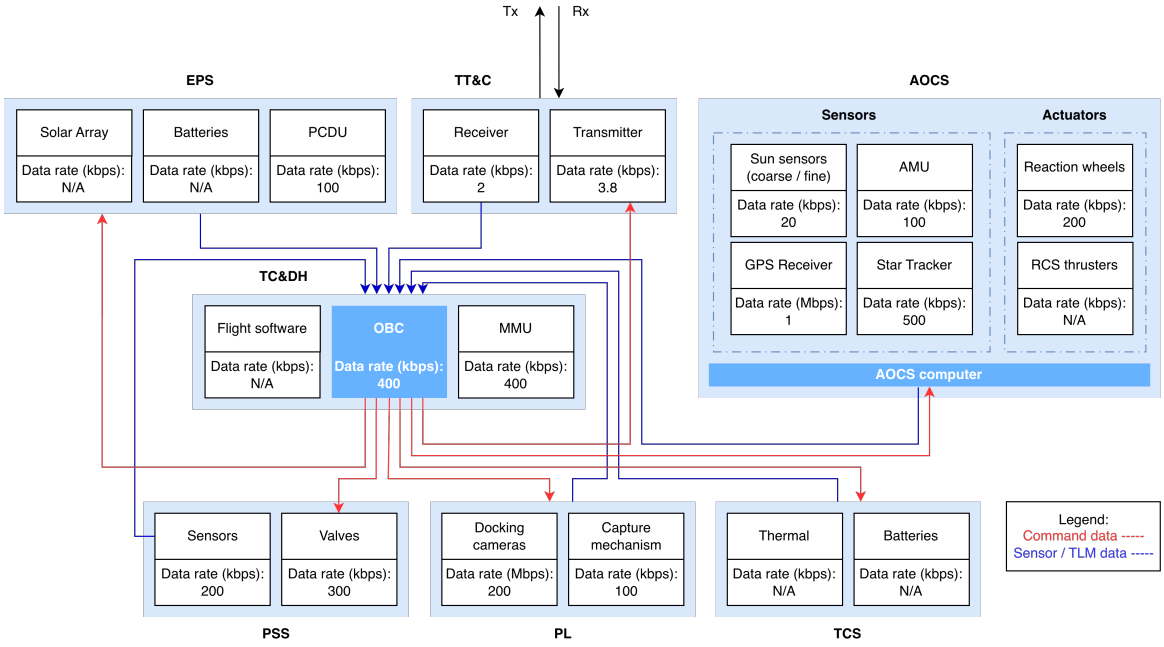

Figure 5.3: Tug data handling block diagram

Software

The C&DH system relies strictly on standard CCSDS (Consultative Committee for Space Data Systems) packet routing [11] and space data link security (SDLS) protocols (CCSDS 335.0-B-2) are used for encryption preventing interception, spoofing, and unauthorised command execution. This is particularly important for the REAVER mission with potential military applications. The computer vision software to address REQ-CDH-M1 is discussed in section 5.3.

5.2. Component Selection

For the C&DH subsystem, components for the on-board computers (OBCs), data buses, and memory are selected and sourced on the basis of heritage and technology readiness level (TRL). Multiple components need to be selected for the mothership and tugs, considering their different operational requirements. In addition to component selection, redundancy requirements for each component are evaluated based on consequence of failure.

Data Bus

For the bus, multiple TRL 9 options are considered. To choose the right data buses, reliability, data rate requirements, and heritage are evaluated. Table 5.1 presents the bus selection for each subsystem interaction based on estimated data rates. Compatibility with subsystem components is also considered. The SpaceWire communication network is selected for high data throughput connections (Payload, and TT&C) as it is designed to connect high data-rate sensors, processing units, large solid-state memories, and the downlink telemetry subsystem. Links support data rates of 2 Mbps to 400 Mbps [9]. Despite the high data rate of the RPOD suite as found in section 12.4, the payload can be divided into multiple parallel streams across multiple SpaceWire ports to avoid compatibility issues arising from the implementation of SpaceFibre (data rate of 6.25 Gbps). This choice is further substantiated by the fact that the selected RPOD sensors all possess SpaceWire interfaces.

Other buses are similarly selected based on the estimated data rates of the connections. One large consideration, however, is the wiring harness mass (consisting of the power cables of the EPS subsystem, and the C&DH signal data lines), which accounts for 5% of the S/C nominal dry mass [42, 58]. Since little information on cable harnesses is readily available, this figure is directly included in the mass budget. In large geostationary satellites replacing conventional point-to-point wiring (such as the RS-485 or MIL-STD-1553) with the two-wire CAN bus alternative provides a significant reduction to cable mass, saving between 10-18% of the total cabling mass. [4] This is presented in figure 5.4. Thus CAN buses are selected for multiple connections. In addition to this an on-board data handling (OBDH) centralised bus alternative is also considered, where a single, redundant OBDH bus loop is run across the spacecraft instead of separate distinct links. According to ESA, the harness

[4] `https://www.renesas.com/en/document/whp/using-can-bus-serial-communications-space-flight-applications` [accessed 11 June 2026]

mass consists of 30% power cables, with the rest (70%) being split between data (telemetry, Spacewire), and high-voltage RF or instrument cables [59]. The 10-18% reduction is thus not negligible.

Table 5.1: Data bus selection

Link / bus location	Estimated data rate	Appropriate bus	Alternative	Source
Payload/RPOD Suite → C&DH	474.62 Mbps	SpaceFibre	SpaceWire	[5]
C&DH → AOCS Computer	< 1 Mbps	MIL-STD-1553B	CAN bus	[6]
Payload → AOCS	200 Mbps	SpaceWire	-	[5] [6]
Tug → C&DH	1 kbps - 100 kbps	RS-485	CAN bus	[7] [8]
Robotic arm → C&DH	130 kbps	EtherCAT	CAN bus	[6] [60, 61]
PSS / TCS Control → C&DH	1 kbps - 100 kbps	RS-422 or CAN	OBDH bus	[9]
TT&C (Rx) → C&DH	> 1kbps	RS-422	-	[8]
C&DH → TT&C (Tx)	10 Mbps - 100Mbps	SpaceWire	-	[4] [10]
EPS → C&DH	< 100kbps	CAN bus (or I^2C/SPI)	OBDH bus	[6]
TCS → C&DH	< 10kbps	RS-422 or CAN bus	OBDH bus	[6] [8]

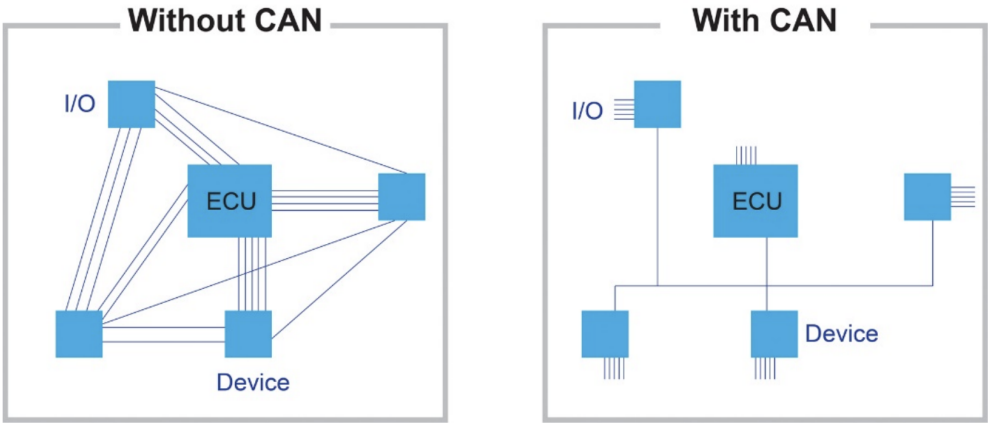

Figure 5.4: CAN bus effect on wiring, ECU = electronic control unit, I/O = input/output [4]

For the tugs, since there is no LiDAR, only 2 cameras are in use, and less data is to be transmitted to ground, no high-speed links are required. SpaceWire is thus not needed, and lower data-rate options like CAN or RS-422 lines can be relied on. The AOCS and payload of the tugs are also simpler, thus a simpler AOCS computer can be used, and no payload computer is required. This difference is reflected in figure 5.3

A final note about data bus selection is that multiple data streams from subsystems can be fed into the same bus simultaneously. The bus must carry both data streams concurrently, which may lead to buffering, and delays unless the total data rate is met. The bus selection alternatives in table 5.1 reflect this requirement. Additionally, the SpaceWire selection between the AOCS computer and payload computer is justified since the full RPOD sensor data is not being directly sent to the AOCS. This data is processed within the payload computer and the target characteristics are sent to the AOCS computer. Thus the 200Mbps SpaceWire does not need to carry 600Mbps of data from the RPOD sensor suite.

On-board Computer

The architecture of the on-board computer (OBC) integrates processors, memory resources, communication interfaces, and fault management. Commercial off-the-shelf (COTS) OBCs and single-board computers (SBCs) are considered to avoid assembling a custom computer out of the scope of a conceptual design project. COTS components are, however, limited as the GEO altitude exposes electronics to severe Total Ionizing Dose (TID) and Single Event Effects (SEEs). For short duration missions such as REAVER, studies assess commercial

[5] https://www.star-dundee.com/spacewire/getting-started/an-overview-of-the-spacewire-standard/ [accessed 9 June 2026]
[6] https://www.esa.int/Enabling_Support/Space_Engineering_Technology/Onboard_Computers_and_Data_Handling/Mil-STD-1553 [accessed 9 June 2026]
[7] https://www.renesas.com/en/document/whp/using-can-bus-serial-communications-space-flight-applications [accessed 9 June 2026]
[8] https://science.nasa.gov/earth-science/csda/vendor-vantor/ [accessed 9 June 2026]
[9] https://fi.pcm-cable.com/info/what-is-rs-422-cable-17265526381618176.html [accessed 9 June 2026]
[10] https://safran-navigation-timing.com/wp-content/uploads/2021/07/A_Guide_for_Testers_of_GPS_Devices_and_Systems__TN15-101_revB_v3-02-04-19-1.pdf [accessed 23 June 2026]

off-the-shelf electronics for a TID of 100krad [62]. However, according to NASA [63], an acceptable TID for the C&DH subsystem is 15krad since the system is not directly exposed. A safety factor of 2 is applied to this and components are thus selected to be able to withstand such doses.

The three computing blocks within the mothership, and those within the tugs have vastly different requirements regarding computation power, fault tolerance, and deterministic behaviour. All selected components must, however, feature radiation hardening or radiation tolerance combined with fault-mitigation. The selection criteria for the OBC are thus; TRL / heritage, radiation tolerance, interfaces, processing performance, power, and mass. A list of the chosen COTS components is provided in table 5.4.

Table 5.2: OBC component selection from COTS options

Component	**Selection**	**Quantity**	**Unit mass** [kg]	**Power consumption** [W]	**TID** [krad]
OBC	cOBC	1 (MS)	5.4	26 (nominal)	> 30
AOCS	TMS570-SEP	1 (MS)	≈ 0.4	1.5 (nominal)	30
Payload	SCFE6933	2 (MS)	≈ 1.5	25-40	> 30
OBC / AOCS	TMS570-SEP	5 (Tug)	≈ 0.4	1.5 (nominal)	30

Redundancy

The advantage of selecting COTS components is that they often already have built-in redundancy, fault mitigation, and radiation tolerance. This redundancy, however, falls under internal (or component-level redundancy), whereas system (vehicle-level) redundancy can not necessarily be ensured. Consequence of failure is thus identified to select an appropriate number of components. High-consequence boxes get vehicle-level redundancy unless they're already internally redundant. A summary is provided in table 5.3.

Table 5.3: Consequence of OBC failure and required redundancy (applicable to both mothership and tugs)

Computer	**Consequence**	**Required level of redundancy**
Main OBC	Potential loss of spacecraft, mission critical	**High**
AOCS computer	Potential loss of attitude and orbit control	**High**
Payload computer	Loss of ADR mission, but spacecraft survives	**Moderate**

Internal Redundancy

The main OBC, the cOBC, is a fully redundant product, offering flight proven FDIR and radiation mitigation. [11] Similarly, both the TMS570-SEP and SCFE6933 achieve fault tolerance through built-in hardware redundancy to protect the systems from single-event effects, and data corruption. The TMS570-SEP features two CPUs running in parallel, error correction code (ECC) for both single- and double-bit errors, built-in self-test (hardware for checking CPU and RAM integrity), cyclic redundancy checks (hardware ensuring memory and message integrity), and system integrity monitoring. [12] The SCFE6933 similarly features ECC, integrated hardware redundancy, and high-bandwidth data distillation (pre-processing large sensor data steams to save power and downlink bandwidth). [13]

System Redundancy

In addition to these built-in redundancies, some vehicle-level redundancy must be implemented as per table 5.3. Despite the built-in redundancy of the TMS570-SEP only protecting the internal processor logic, the reliability of the product is 99% and considered fully reliable so system-level redundancy is not implemented. [14] Similarly, the cOBC does not need additional redundancy since it already contains two independent computer boards, dual power supply, and cross-strapped routing and is proven 99% reliable over a 10-year period. The payload computer (SCFE6933) is, however, duplicated with both boards powered on (warm redundancy) as reliability values are not available. This is additionally justified due to the two simultaneously complex processing tasks involved in the REAVER mission; processing LiDAR point clouds, and optical camera frames for pose estimation, and generation of subsequent actuator commands for the 7 degree-of-freedom (DOF) robotic arm. One board hence acts as the *primary vision engine*, whereas the second board acts as the *primary robotics controller*. Since they are identical COTS boards, the two computers effectively act as system backups for one another. If the *primary robotics controller* suffers catastrophic failure, the *primary vision engine* is capable of loading an emergency robotics control package, completing the docking sequence safely.

[11] `https://satsearch.co/products/beyond-gravity-constellation-on-board-computer-c-obc` [accessed 12 June 2026]

[12] `https://www.ti.com/product/TMS570LC4357-SEP?utm_source=google&utm_medium=cpc&utm_campaign=epd-null-null-GPN_EN-cpc-pf-google-eu_en_cons&utm_content=TMS570LC4357-SEP&ds_k=TMS570LC4357-SEP&DCM=yes&gclsrc=aw.ds&gad_source=1&gad_campaignid=8752534513&gbraid=0AAAAAC068F3BgCRvK92IBJP70KNh872Dv` [accessed 12 June 2026]

[13] `https://www.mrcy.com/application/files/5716/9340/1271/Datasheet-SCFE6933-6U-VPX-fpga-processor-board.pdf` [accessed 12 June 2026]

[14] `https://www.ti.com/quality/docs/estimator.tsp` [accessed 12 June 2026]

Main Memory

All of the chosen OBCs contain built-in memory. The cOBC features 1GB processing memory and 4GB non-volatile memory, both with error correcting code (ECC). TMS570-SEP, and SCFE6933 also have built-in volatile and non-volatile memories. The 4 Mbit of internal storage of the TMS570-SEP is adequate for algorithm storage, inadequate, however, to store data logs. The required storage capacity is approximately 409GB (incl. 20% margin) as estimated in section 13.8. This exceeds the internal memory resources available on the OBC, necessitating an external solid state recorder. A radiation-tolerant SpaceVPX flash memory board is selected to provide the required storage while supporting payload data rates and offering fault-tolerance through ECC. At 10Tb (1.25TB), this satisfies the storage needs with adequate margin.

Table 5.4: Memory component selection

Component	**Selection**	**Quantity**	**Unit mass** [kg]	**Power consumption** [W]	**TID** [krad]
SSR	Flash SpaceVPX Memory Board	1	≈ 0.6	10	50

Budgets

The consolidated mass and power budgets of the C&DH subsystem are summarised in table 5.5. The 5% dry mass taken up by the cable harness dominates the C&DH mass budget, making up 77% of the mothership C&DH mass, and 95% of the tug C&DH. The potential mass reductions introduced from the bus architecture are thus significant, bringing down the total C&DH mass from 82 kg (without contingency) to 66.34 kg.

Table 5.5: C&DH component selection budgets and margins

Component	**MS CBE** [kg]	**Tug/Unit CBE** [kg]	**Power (nominal)** [W]	**Power (peak)** [W]
cOBC	5.4	-	26	26
TMS570-SEP (AOCS)	0.4	-	1.5	1.5
SCFE6933	3	-	0 (off/idle)	40
TMS570-SEP (tug OBC)	-	0.4	1.5	-
SpaceVPX SSR	0.6	-	5 (idle)	10
Wiring Harness (data)	32	7	-	-
Total	41.4	7.4	34	77.5
10% mass contingency	45.5	8.14	-	-
Potential reduction	35.64	6.14	-	-

5.3. Computer Vision

Autonomous spacecraft operations, including on-orbit servicing (OOS) and active debris removal (ADR), require precise relative navigation of the target spacecraft using cameras and LiDAR. The RPOD sensor suite consists of instruments to aid in pose estimation of the target debris.

LiDAR

Pose estimation of the target spacecraft can be achieved using SpaceSense Bench; a multi-modal (RGB, Depth, LiDAR) benchmark for spacecraft perception in autonomous operations such as OOS and ADR. [64][15] The dataset contains 136 satellite models, with each frame providing 1024x1024 RGB images, millimeter-precision depth maps, 256-beam LiDAR point clouds, and 6DOF pose. The algorithm is run on ACRIMsat, producing depth estimation and a LiDAR point cloud, provided in figure 5.5.

(a) Depth estimation **(b)** Lidar point cloud

Figure 5.5: Outputs of the SpaceSense Bench algorithm

[15] `https://github.com/wuaodi/SpaceSense-Bench` [accessed 8 June 2026]

The chosen RVS 3000-3D LiDAR (section 7.4) can estimate 6D pose of non-cooperative targets and can produce results analogous to those from SpaceSense Bench. Such an algorithm would thus be implemented into the LiDAR data processing unit (DPU) to generate 3D maps and analyse the debris characteristics within the payload computer (refer back to figure 5.2).

Optical Flow

Lucas Canade optical flow in OpenCV can be applied to estimate the rotation of the object. This is a simple application to track points from a video. The rotational rate can then be extracted. This rate, however is the rotation between the current and the previous frame or the best-fit 2D rotation explaining how the tracked image features move within the consecutive frames. If the rotation axis is known, then this rotation axis can be corrected. LiDAR and satellite laser ranging (SLR) algorithms can estimate the central line (vector) around which the object rotates [65]. These two tools can thus provide the mothership with knowledge of the debris shape, size, attitude, and tumbling rate, as per REQ-CDH-M1.

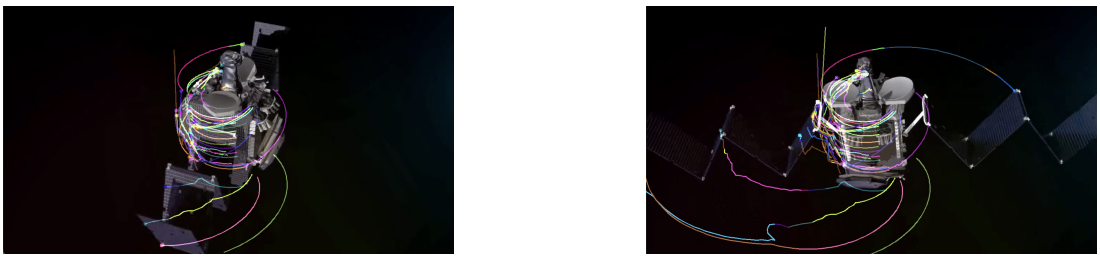

(a) Optical flow initial frame

(b) Optical flow subsequent frames

Figure 5.6: Optical flow applied to rotating Intelsat

5.4. Verification of C&DH Subsystem Requirements

Subsystem requirement **TBDs** (to be determined) from the midterm report are hereupon revisited and amended. REQ-CDH-M1 distance is sourced from figure 3.5, REQ-CDH-M2, M3, and REQ-CDH-T1, T2, are based on the capabilities of the data buses and estimated data rates. REQ-CDH-U10 is based on the NASA studies of C&DH box ionising dose requirements. Table 5.6 presents the subsystem requirements, along with parent requirements, verification method, and compliance. Verification can be performed using either test, analysis, inspection, or demonstration, and specific tests are provided where test is chosen as the verification method. Compliance is split into three categories; compliant, TBD, and non-compliant. The verification and compliance methodologies are applied throughout all subsystems.

Table 5.6: C&DH subsystem requirements, and requirement IDs [66]

ID	C&DH Subsystem Requirement	Parent Requirement	Method	Check
Mothership				
REQ-CDH-M1	The mothership C&DH shall be able to autonomously estimate the debris size, shape, attitude, and tumbling rate at a distance of < 120 m.	REQ-MIS-01, REQ-STK-20	A	TBD
REQ-CDH-M2	The MC&DH subsystem shall support a command and telemetry data rate of at least 100 Mbps.	REQ-SYS-14, REQ-SYS-15	D	Yes
REQ-CDH-M3	The MC&DH subsystem shall support an internal command and data handling throughput of at least 200 Mbps.	REQ-SYS-14	D	Yes
Tugs				
REQ-CDH-T1	The MC&DH subsystem shall support a command and telemetry data rate of at least 50 Mbps.	REQ-SYS-14, REQ-SYS-15	D	Yes
REQ-CDH-T2	The MC&DH subsystem shall support an internal command and data handling throughput of at least 100 Mbps.	REQ-SYS-14	D	Yes
Universal				
REQ-CDH-U1	The C&DH systems of the mothership and tugs shall support bidirectional communication via a physical data link.	REQ-SYS-13	D	Yes
REQ-CDH-U2	The C&DH subsystem shall provide computational capability for spacecraft command, control, and on-board data handling.	REQ-SYS-13	D	Yes
REQ-CDH-U3	The C&DH subsystem shall facilitate autonomous mission operations.	REQ-SYS-01, REQ-SYS-18	T	TBD
REQ-CDH-U4	The C&DH subsystem shall validate, and execute command sequences from Ground Operations.	REQ-SYS-13, REQ-SYS-18	T, A	TBD

Continued on next page

Table 5.6 – continued from previous page

ID	C&DH Subsystem Requirement	Parent Requirement	Verification	
REQ-CDH-U9	The C&DH subsystem shall support inter-vehicle command communication at a data rate of at least 100 kbps.	REQ-SYS-13	D	Yes
REQ-CDH-U11	The C&DH subsystem shall adhere to CCSDS protocols.	-	I	Yes

REQ-CDH-M1 can be verified using a hardware-in-the-loop (HIL) simulation, running the autonomous estimation algorithm against simulated or recorded debris. This requirement can further be validated through integration testing with the RPOD sensor suite, where the C&DH processes the sensor data in a controlled environment. REQ-CDH-U3 can be verified by executing autonomous mission sequences (orbit adjustments, targeting, manoeuvres) in a simulation and by ensuring that each autonomous function operates as expected. REQ-CDH-U4 verification consists of testing the execution of command sequences. This is done during end-to-end compatibility testing, where the C&DH unit is physically connected to the TT&C subsystem and relevant software. The uplink and downlink command sequence can then be tested for the entire assembly

6. Attitude and Orbit Control System

The Attitude and Orbit Control System (AOCS) provides the navigation, stabilisation, pointing, and manoeuvre control functions required throughout the REAVER mission. The AOCS plays a critical role in active debris removal missions, supporting proximity operations with uncooperative targets, synchronising tumbling motion, and detumbling the debris after capture. This chapter defines the AOCS functional architecture, then selects the sensor and actuator hardware, defines the software and control logic, summarises the budgets, and finally verifies the AOCS subsystem requirements.

6.1. AOCS Architecture

The AOCS architecture is defined from the operational functions required in each mission mode. At the system level, the AOCS converts mission commands and navigation information into actuator commands to achieve the desired dynamics. The baseline architecture is shared by the mothership and the tugs for safe mode, commissioning, standby, and long-range rendezvous. The mothership then extends this baseline with additional relative navigation and capture control functions required for proximity operations around uncooperative targets.

Functions and Operational Modes

The AOCS determines and controls the kinematic state of the spacecraft. The kinematic state of the spacecraft describes its position and motion with respect to the Earth, consisting of the instantaneous position, velocity, attitude, and angular rate. The determination of these properties consists of two steps: measurement and estimation. Measurements are the direct outputs of the onboard sensors, however these observations can be noisy and sometimes incomplete. Estimation is the subsequent processing step in which these measurements are filtered and combined with a spacecraft dynamics model to obtain the best available state estimate for control and navigation. Control then compares this estimated state to the commanded state in a closed feedback loop to compute the required correction and generate actuator commands. Through this hardware-software chain, the AOCS regulates the spacecraft orientation and trajectory throughout the mission.

The AOCS performs a set of core functions continuously, independent of the active spacecraft mode. These include monitoring sensors and actuators, estimating the current kinematic state, maintaining the control loop status, and checking attitude and angular rate errors to detect faults. The active spacecraft mode then determines which sensors, actuators, reference states, and control objectives are used by this basic hardware-software control chain. The functions specific to each mission mode are summarised in table 6.1.

Table 6.1: Summary of AOCS functions in each mission mode

Mode	Spacecraft	AOCS function
Safe mode	MS + tugs	Maintain stable attitude, fulfil basic pointing needs
Standby mode	MS + tugs	Maintain stable waiting configuration until the next mission operation is commanded
Commissioning mode	MS + tugs	Initialise and verify sensors, actuators, estimation filters, and control loops
Long range rendezvous	MS + tugs	Absolute navigation: process trajectory commands, slew to required burn attitude, maintain thrust vector pointing during orbit control manoeuvres
Proximity operations	MS	Relative navigation: command motion with RPOD sensor data, maintain hold points for debris analysis, synchronise angular rate with the target tumbling rate
Capture and control	MS	Maintain the capture interface alignment, monitor and match target motion, command and execute post-capture momentum dump to detumble the debris

Closed Loop Functional Architecture

The baseline AOCS architecture is common to both the mothership and the tugs, corresponding to the functions active during safe, standby, commissioning, and long-range rendezvous modes. It is organised as a closed loop functional chain, shown in figure 6.1, in which spacecraft commands are converted into reference states, compared with the estimated spacecraft state, and translated into actuator commands. This chain combines the hardware required to measure and change the spacecraft motion with the software required to estimate the current state and compute the required control action.

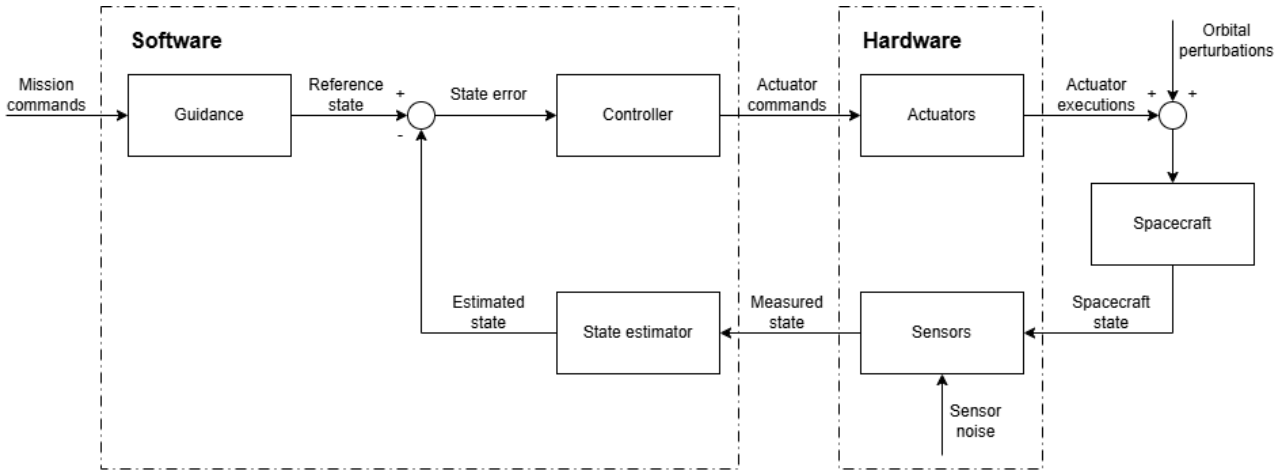

Figure 6.1: AOCS architecture visualised as a control loop

The baseline AOCS hardware consists of sensors that measure the spacecraft's motion and actuators that control its dynamic behaviour. Orbital determination during transfer and debris transport is supported by absolute navigation sensors, while attitude determination uses coarse sun sensors for rough orientation, and fine sensors and star trackers for high precision operations. Inertial sensors detect the dynamic behaviour of the spacecraft, tracking rotation and accelerations. Reaction wheels provide fine three-axis attitude control, while the propulsion and RCS thrusters provide orbit control, desaturation, and high rate manoeuvre control authority.

The mothership extends the baseline AOCS architecture with relative navigation, and capture and control functions required for operations around uncooperative targets. During proximity operations, the mothership AOCS receives relative position, relative velocity, target attitude, target angular rate, target rotational axis, and capture interface location from the C&DH. These quantities are combined with the mothership state estimate and used to command the relative motion, rotational synchronisation, and capture interface alignment. This functionality imposes stricter accuracy requirements on the mothership's sensors. Furthermore, the detumbling sequence requires the actuators to generate sufficient torque to reduce the angular momentum of the combined spacecraft-debris system.

Subsystem Interfaces

Most operational data from external subsystems is routed through C&DH, which validates and processes the data to be sent to AOCS. Through the C&DH, the AOCS receives reference trajectories, mode commands, abort commands, EPS solar array pointing requests, TT&C antenna pointing requests, and processed RPOD navigation data. In return, the AOCS provides estimated kinematic state, control loop status, actuator commands, and manoeuvre execution status for health and system monitoring. Figure 6.2 defines all the software and hardware interactions of the AOCS with the other subsystems.

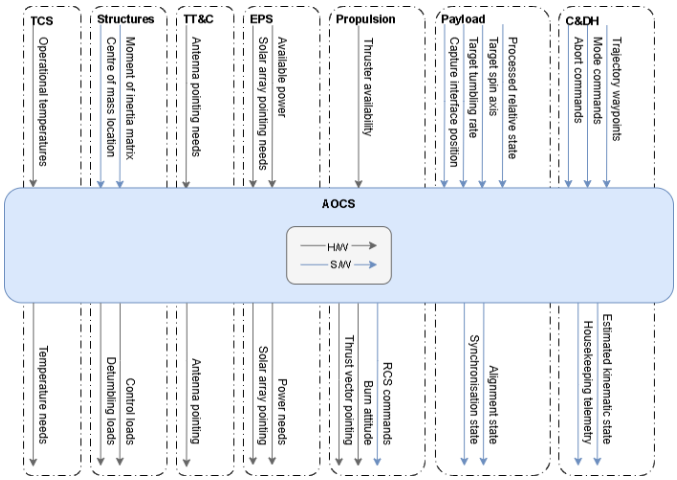

Figure 6.2: Inputs and outputs of AOCS interactions with other subsystems

6.2. Component Selection

The AOCS hardware is selected to satisfy the functional needs and accuracy requirements. Sensors are selected to provide absolute orbit, attitude, and dynamic state determination, while actuators are selected to provide three-axis attitude stabilisation, disturbance rejection, slew capability, and reaction wheel desaturation. Since REAVER operates in the GEO region, additional considerations must be taken into account: the radiation environment is significantly harsher than in LEO, Earth's magnetic field is too weak to use magnetic attitude sensing or actuation, and the available Global Navigation Satellite System (GNSS) signals are weak side-lobe and spillover signals, as illustrated in figure 6.3.

The AOCS component selection is therefore based on accuracy, GEO compatibility, radiation tolerance, redundancy, heritage, mass, power consumption, and interface compatibility with the C&DH architecture. For the mothership, additional emphasis is placed on high accuracy to successfully perform the proximity operations, tumbling synchronisation, capture alignment, and detumbling in accordance with the subsystem requirements. For the tugs, the same sensor classes are used to allow autonomous operation after separation, but lower mass components are selected since the accuracy requirements are less demanding. All components are COTS to reduce development costs and increase mission reliability.

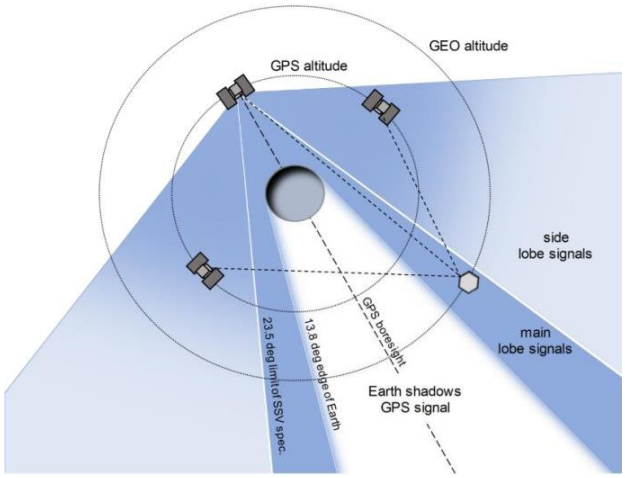

Figure 6.3: GNSS signal lobes in GEO [67]

Table 6.3: Representative AOCS sensor suite for active debris removal missions, adapted from ESA GNC design guidance [68]

Sensor	Quantity
GNSS receiver	2
Inertial measurement unit	2
Sun sensor	6
Star tracker	2

The AOCS sensor suite provides the measurements required for absolute navigation and attitude determination. A representative sensor set for active debris removal spacecraft is adopted from ESA GNC design guidance, as summarised in table 6.3 [68]. Since these sensor types are widely used on geostationary satellites, a variety of COTS components are available for detailed selection. Relative navigation during proximity operations is supported by the RPOD sensor suite, which is part of the payload subsystem and described in section 7.4.

Mothership Attitude and Orbit Determination Sensors

For absolute navigation, two Viceroy-4 GPS Spaceborne receivers are selected. Global Navigation Satellite System (GNSS) is used because it provides an onboard measurement of the spacecraft position and velocity with respect to an Earth-centred reference frame. Although GNSS reception at GEO is more challenging than in LEO because the spacecraft receives weaker main lobe and side lobe signals as shown in figure 6.3, the dedicated high altitude spaceborne receivers are designed for this application.

Spacecraft orientation and dynamic state determination requires a complementary sensor suite because no single sensor provides robust, high accuracy orientation and rate knowledge across all mission modes. The inertial measurement unit (IMU) provides high rate angular rate and acceleration measurements, allowing the estimator to propagate attitude and rate between slower external sensor updates. Since inertial measurements drift over time, they are fused with GNSS, Sun sensor, and star tracker measurements rather than used as standalone navigation source. The Sun sensors provide a robust attitude profile: four coarse Sun sensors give a broad field of view for Sun acquisition, while two fine Sun sensors are used for subsequent high precision attitude determination. Complementarily, the star trackers provide the primary high accuracy attitude reference during nominal operations. The components selected for the mothership AOCS are summarised in table 6.4.

Table 6.4: Selected AOCS components for the mothership

Type	Component	Accuracy requirements	Accuracy performance
GNSS receiver	Viceroy-4 GPS Spaceborne Receiver[1]	Position < 100 m, velocity < 1 m s^{-1}	Position 15 m, velocity 0.05 m s^{-1}
IMU	ASTRIX 120[2]	Angular rate < 0.1 °/s	Angular rate 2.78×10^{-6} °/s
Coarse sun sensor	Bradford Cosine Sun Sensor Redundant[3]	Attitude < 5°	Attitude 3°
Fine sun sensor	Redwire Space Fine Pointing Sun Sensor[4]	Attitude < 1°	Attitude 5.56×10^{-3}°
Star tracker	Sodern AURIGA-CP[5]	Attitude < 1°, slew rate > 0.5 ° s^{-1}	Attitude 0.017°, slew rate 3 ° s^{-1}

Tug Attitude and Orbit Determination Sensors

The tug AOCS uses the same sensor classes as the mothership, but with lighter components where the accuracy requirement is less demanding. Hence, its sensor suite is only sized to handle debris transport and thrust vector pointing. Table 6.5 shows a summary of the selected components for the tug. Although the tug AOCS is simpler than the mothership's, redundancy is still required because each tug operates autonomously after separation, hence the same quantity of sensors is selected.

Table 6.5: Selected AOCS components per tug

Type	Component	Accuracy requirements	Accuracy performance
GNSS receiver	Viceroy-4 GPS Spaceborne Receiver[1]	Position < 100 m, velocity < 1 m s^{-1}	Position 15 m, velocity 0.05 m s^{-1}
IMU	Bradford Accleration Measurement Unit[6]	Angular rate < 0.5 °/s	Angular rate 0.253 °/s
Coarse sun sensor	Bradford Cosine Sun Sensor Redundant[3]	Attitude < 5°	Attitude 3°
Fine sun sensor	Bradford Fine Sun Sensor[7]	Attitude < 2°	Attitude 0.3°
Star tracker	Sodern AURIGA-CP[5]	Attitude < 1°, slew rate > 0.5 ° s^{-1}	Attitude 0.017°, slew rate 3 ° s^{-1}

Attitude Control Actuators

The AOCS actuators are selected to provide three-axis attitude control, disturbance rejection, and commanded slew capability. Reaction wheels are chosen as the primary actuator because they provide a propellantless control torque and are effective in GEO, as opposed to magnetorquers. Although highly effective, RCS thrusters increase the propellant required for the mission, hence their use is limited for large momentum changes in the capture sequence, and reaction wheel desaturation. The RCS sizing is considered part of the propulsion system and detailed later in chapter 8.

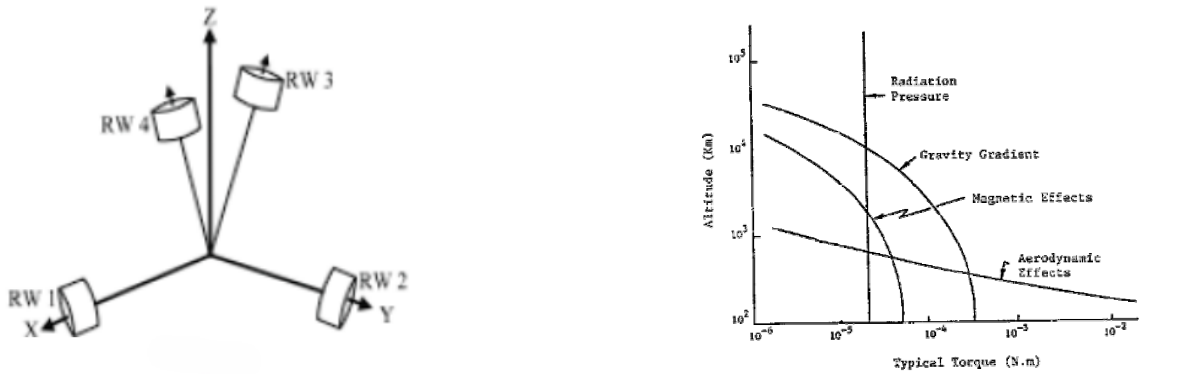

(a) Reaction wheel configuration [69]

(b) Typical torque perturbations at different orbital altitudes [70]

Figure 6.4: Sizing reaction wheels

Reaction wheels work by taking advantage of conservation of momentum. Since they are placed inside the spacecraft, the angular momentum of the entire spacecraft system must remain constant. If the spacecraft is

[1] https://satsearch.co/products/general-dynamics-viceroy-4-gps-spaceborne-receiver [accessed 17 June 2026]
[2] https://satsearch.co/products/airbus-defence-and-space-astrix-120 [accessed 17 June 2026]
[3] https://satsearch.co/products/bradford-redundant-cosine-sun-sensor [accessed 17 June 2026]
[4] https://satsearch.co/products/redwirespace-fine-pointing-sun-sensor [accessed 17 June 2026]
[5] https://satsearch.co/products/sodern-auriga [accessed 17 June 2026]
[6] https://satsearch.co/products/bradford-acceleration-measurement-unit [accessed 17 June 2026]
[7] https://satsearch.co/products/bradford-fine-sun-sensor [accessed 17 June 2026]

rotating, then this angular momentum can be transferred to the reaction wheels, reducing the angular rate of the spacecraft, but increasing that of the wheel. In principle, three orthogonal wheels are needed for full three-axis attitude control since each wheel can spin in either direction. However, to ensure full attitude control can be maintained in the case of a reaction wheel failure, four reaction wheels can be used in a skewed configuration. Figure 6.4a demonstrates the optimal configuration for the best balance in the case of any wheel failing, where the angular momentum is shared across all three spacecraft body axes [69]. Both the mothership and tug spacecraft use this configuration because it supports all required attitude control functions, while reducing the probability that a single reaction-wheel failure results in loss of attitude control.

The reaction wheels are selected as COTS components for each spacecraft using both torque and angular momentum storage requirements for sizing. The torque requirement is driven by the maximum commanded angular acceleration during attitude manoeuvres. The momentum storage requirement is driven by the greater of the angular momentum required during the maximum commanded slew and the angular momentum accumulated in the reaction wheels while counteracting the maximum expected external disturbance torques between desaturation events. During desaturation, the RCS thrusters generate an external torque while the reaction wheels reduce their speed to decrease the stored angular momentum without disturbing the spacecraft attitude. The required control torque can be simply estimated with equation (6.1), using the largest moment of inertia of the spacecraft I_{max}, and the worst case required angular acceleration α which is given by the subsystem requirements.

$$\tau_{req} = I_{max}\alpha \tag{6.1}$$

The required wheel momentum storage is estimated by equation (6.2), which finds the larger of the momentum required during a slew with a commanded angular rate ω_{max}, and the accumulated disturbance momentum from worst case external disturbance torques τ_d and the longest time between the attitude actuations t_d.

$$H_{req} = \max\left(I_{max}\omega_{max},\ \tau_d t_d\right) \tag{6.2}$$

The selected reaction wheels must provide sufficient torque and momentum capacity with margin, taking the worst case disturbances acting in one axis, and including the case where one wheel is unavailable. While disturbance torques in GEO remain small, with radiation pressure and gravity gradient having the largest contributions, although still on the scale of 10×10^{-5} N m, their cumulative effect can be driving. For geostationary satellites, a preliminary level estimation model for solar radiation pressure and gravity gradient torque can be used [70], these are summarised in table 6.6.

Table 6.6: Equations to model the primary external disturbance torques for geostationary satellites [70]

Torque	Solar Radiation Pressure	Gravity Gradient
τ_x	$= 2\cdot10^{-5}[1-2sin(\omega_0 t)]$	$= -3\omega_0^2(I_y - I_z)\phi$
τ_y	$= 10^{-4}cos(\omega_0 t)$	$= -3\omega_0^2(I_x - I_z)\theta$
τ_z	$= -5\cdot10^{-5}cos(\omega_o t)$	$= 0$

Since the solar radiation pressure equations are time varying, the disturbance time to analyse the torque accumulation was half an orbit [71], which in geostationary orbit corresponds to half a day. On the other hand, the gravity gradient equations are orientation specific, hence the trajectory over the same time period was exported from the GMAT calculation tool described in section 3.5. It is important to note that these calculations were done with many assumptions, including a preliminary estimate of the spacecraft maximum moment of inertia, and a highly simplified disturbance model. For this reason, a 2× safety factor was applied on top of these minimums to define the requirement for selecting the components [71]. The resulting driving sizing factors are listed in table 6.7. Momentum storage was a more limiting factor when selecting COTS components. This value was calculated assuming desaturation is only performed every half orbit.

Table 6.7: Reaction wheel selection and preliminary sizing, including required momentum storage and torque parameters with safety factor

Spacecraft	Component	H_{req} [N m s]	H [N m s]	τ_{req} [mN m]	τ [mN m]
Mothership	SSTL GEO Wheel[8]	5.8	12	42	200
Tug	Astrofein VRW-D-4 Reaction Wheel[9]	0.9	4	63	90

[8] `https://satsearch.co/products/sstl-sstl-geo-wheel` [accessed 17 June 2026]
[9] `https://satsearch.co/products/vectronic-aerospace-vrw-d-4-reaction-wheel` [accessed 17 June 2026]

For the mothership, the selected actuator is the SSTL GEO Wheel. This wheel is selected because it is designed for geostationary spacecraft applications and provides a suitable momentum storage range for the mothership. The preliminary sizing gives a required momentum storage of 5.8 N m s, which is below the selected wheel capacity. The mothership wheel set is therefore suitable for fine attitude control, slew manoeuvres, and disturbance rejection during long-range rendezvous and proximity operations. During capture and detumbling, the reaction wheels are not used as the primary high authority actuator. They are only used to maintain attitude control while the RCS provides the larger control torques required for momentum unloading and detumbling since sizing for reaction wheels for the maximum momentum detumbling case resulted in extremely large and heavy wheels, so using RCS thrusters is more efficient despite the propellant mass consumption.

For the tugs, a smaller reaction wheel is selected because the tug inertia and control requirements are lower than those of the mothership. Since the tugs do not perform independent debris inspection or capture interface alignment after release, their actuator sizing is driven by disturbance torques throughout transport. The preliminary sizing gives a required momentum storage of 0.9 N m s, based on the tug disturbance environment with a representative debris configuration. The selected tug reaction wheel is the Astrofein VRW-D-4 Reaction Wheel, as its momentum storage capacity exceeds this preliminary minimum requirement.

RCS and Orbit Control Interface

The RCS and orbit control propulsion hardware are part of the propulsion subsystem. AOCS determines when and how they are fired, while the propulsion subsystem provides thrust and propellant capabilities. The mothership AOCS commands RCS firings for wheel desaturation and post-capture detumbling. During orbit control manoeuvres, the AOCS maintains thrust vector pointing. This makes the RCS interface a key part of AOCS performance even though the thrusters themselves are part of propulsion.

6.3. Software and Control Logic

The AOCS software encompasses the state estimation, guidance, and control processes. To demonstrate the attitude control capacity of the AOCS, a simple spacecraft model is designed in Simulink. The rotational dynamics of the spacecraft are defined by equation (6.3) [72]. Here, M represents the net moment acting about the spacecraft centre of mass, $\Omega = [p \quad q \quad r]^T$ is the angular velocity vector in the spacecraft body frame, with $\dot{\Omega}$ corresponding to the angular acceleration vector, and $\mathbf{I}$ is the spacecraft inertia tensor, consisting of the moments and products of inertia along each axis of the spacecraft. The spacecraft attitude is described by the Euler angle vector $[\phi \quad \theta \quad \psi]^T$. For this preliminary linear model, small attitude deviations are approximated such that the body axis angular rates Ω are approximately equal to the derivative of the Euler angle vector.

$$M = \mathbf{I} \cdot \dot{\Omega} + \Omega \times \mathbf{I} \cdot \Omega \tag{6.3}$$

The spacecraft rotational dynamics are modelled as a state-space system, where actuator torques τ and modelled disturbance torques τ_d are inputted, and the resulting dynamic rotational state, with the Euler angles and angular rates, is outputted as a state vector $x = [\phi \quad \theta \quad \psi \quad p \quad q \quad r]^T$. The spacecraft inertia tensor $\mathbf{I}$ is a time-invariant preliminary model, sized from a representative medium geostationary satellite [70].

A closed loop control system is designed around this spacecraft model to simulate how the controller reacts to disturbance torques, presented in figure 6.5. A reference signal of a fixed rotational state is fed into the controller. The disturbance signal model follows from the torque model of solar radiation pressure and gravity gradient presented in table 6.6, as shown in figure 6.5b. The error between the reference state and the state of the satellite undergoing the continuous disturbance torques is fed into a simple proportional gain controller. This controller determines the necessary torque actuations sent into the satellite model to reduce the error between the reference signal and the instantaneous dynamic attitude state of the satellite. Essentially, the control algorithm receives a commanded state from C&DH and computes the satellite torque actuations to dampen disturbances.

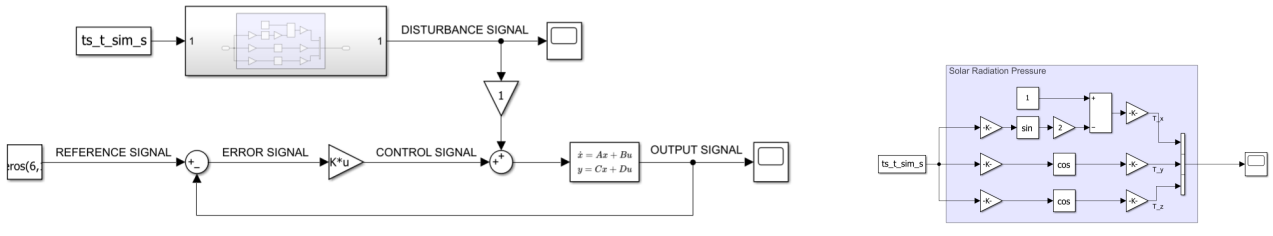

(a) Proportional gain control loop

(b) Disturbance model

Figure 6.5: AOCS spacecraft control loop model responding to orbital perturbation torques

The output signal of this control loop is visualised in figure 6.6. The disturbance torque τ_y is applied on spacecraft, and consequently, the spacecraft responds with a dramatic increase in pitch θ (State-Space 1:2). Since the spacecraft system is coupled, an increase in the corresponding angular rate q (State-Space 1:5) is also observed, however, since the disturbance torques are very low in magnitude, the increase is not as prominent. The controller action is initially observed by the sharp decrease in angular rate, however, the pitch angle takes longer to restore, beginning to decrease after 50 s in the simulation. This simulation demonstrates the AOCS controller capacity to dampen external torques.

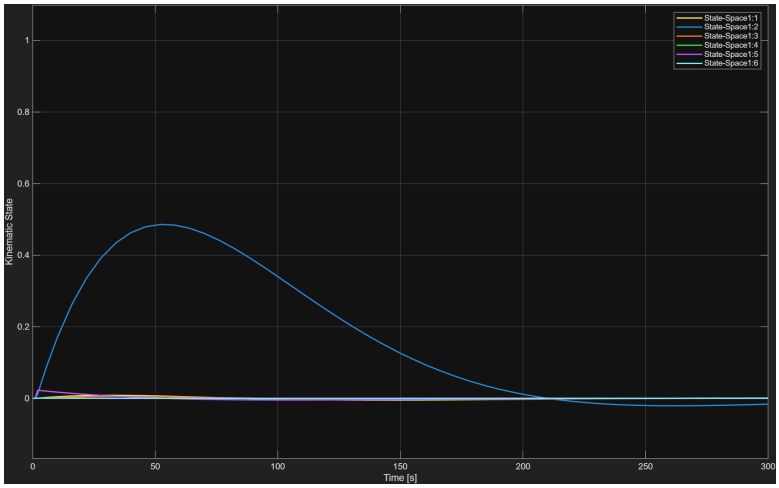

Figure 6.6: Controller response to a single axis disturbance torque

For absolute navigation, the AOCS relies on mission level trajectory planning from the C&DH, and command execution from the propulsion subsystems. The high level control architecture is described in figure 6.7. Given the target information provided to C&DH by the ground segment, C&DH proceeds to calculate the optimal trajectory to reach the debris. This trajectory is sent as a set of discrete points to the AOCS and serve as the reference signal. The AOCS continuously estimates the instantaneous state, comparing it with the provided guidance, to generate the control commands for the main thruster in the propulsion system. Importantly, this system updates continuously, where executed thruster commands change the instantaneous state, meaning the controller will send new thruster commands.

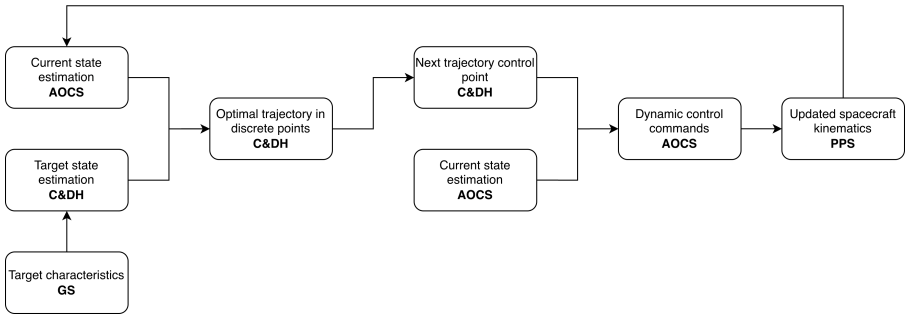

Figure 6.7: Absolute navigation control loop

During proximity operations, the AOCS must do relative navigation. The control architecture differs slightly, where instead of internally processing the current state from sensors, the AOCS is sent the processed relative state from the C&DH, since that is where the RPOD sensors send their data. This processing chain is outlined in figure 6.8, where raw RPOD sensor data from cameras, LiDAR, and infrared sensors is processed outside the AOCS by the payload and C&DH. The AOCS uses the resulting processed relative navigation data to command holding operations, synchronisation, capture alignment, and abort manoeuvres.

6.4. Mass and Power Budget

The mass and power budget for the AOCS system is detailed as a component wise breakdown in table 6.8. The AOCS budget includes sensors and reaction wheels for the mothership and tugs. RCS thrusters and main propulsion hardware are excluded from the AOCS hardware because they are budgeted in the propulsion subsystem, and AOCS electronics are included in the C&DH subsystem, although their commanded use is included in the AOCS control logic. Both the average and peak power budgets are presented as totals to provide

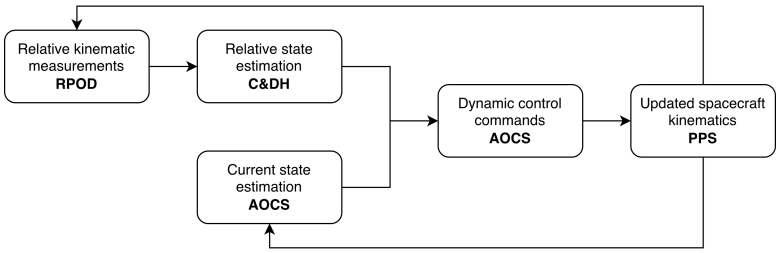

Figure 6.8: Relative navigation control loop

an overview of the power consumption across all mission phases.

Table 6.8: Mothership and tug selected component list including mass and power.

Component	Quantity	Mass [kg]	Power [W]
Mothership			
Viceroy-4 GPS Spaceborne Receiver	2	1.10	7
ASTRIX 120	2	6.5	6
Bradford Cosine Sun Sensor Redundant	4	0.017	0
Redwire Space Fine Pointing Sun Sensor	2	2.030	0.4
Sodern AURIGA-CP	2	0.225	6
SSTL GEO Wheel[6]	4	5.6	30
Total	-	42	Average 50, peak 773
Tug (per spacecraft)			
Viceroy-4 GPS Spaceborne Receiver	2	1.10	7
Bradford Acceleration Measurement Unit	2	2.035	1.6
Bradford Cosine Sun Sensor Redundant	4	0.017	0
Bradford Fine Sun Sensor	2	0.375	0.25
Sodern AURIGA-CP	2	0.225	6
VRW-D-4 Reaction Wheel[9]	4	2.5	9
Total	-	17.5	Average 54, peak 290

6.5. Verification of AOCS Subsystem Requirements

The AOCS subsystem requirements define the hardware and software capabilities required to perform the AOCS functions throughout the mission. Nominal operations are defined as all mission modes in which the spacecraft is actively carrying out the mission: commissioning mode, long-range rendezvous mode, proximity operations mode, and capture and control mode. The accuracies defined in the requirements are based on accuracy requirements of previous missions with similar functional and operational requirements. The main reference case is ESA's e.Deorbit mission, which defines representative performance requirements for absolute navigation, rendezvous closing, synchronisation and capture, stabilisation, and deorbiting for an active debris removal mission [73]. The target refers to either the debris or recycling hub since proximity operations have the same requirements for capture and docking.

Table 6.9: AOCS subsystem requirements, and requirement IDs

ID	AOCS Subsystem Requirement	Parent Requirement	Method	Check
Mothership				
REQ-ACS-M1	The mothership AOCS shall determine the kinematic state with respect to the ECI frame with an error less than the specifications in table 6.10 during nominal mission operations.	REQ-MIS-11	T	TBD
REQ-ACS-M2	The mothership AOCS shall control the commanded kinematic state with an error less than the specifications in table 6.10 during nominal mission operations.	REQ-MIS-11	T	TBD
REQ-ACS-M3	The mothership AOCS shall damp undesired angular rates to below $0.5\,^\circ\,s^{-1}$ within 300 s after disturbance events.	REQ-SYS-23	A	TBD
REQ-ACS-M4	The mothership AOCS shall execute commanded attitude manoeuvres with a slew rate greater than $0.5\,^\circ\,s^{-1}$.	REQ-MIS-11	A	TBD
REQ-ACS-M5	The mothership AOCS shall command orbit control manoeuvres with a ΔV execution error less than $0.3\,m\,s^{-1}$.	REQ-MIS-11	A	TBD

Continued on next page

Table 6.9 – continued from previous page

ID	AOCS Subsystem Requirement	Parent Requirement	Method	Check
REQ-ACS-M6	The mothership AOCS shall command thrust vector pointing during orbit control manoeuvres with an error less than 1°.	REQ-MIS-11	A	TBD
REQ-ACS-M7	The mothership AOCS shall determine the kinematic state relative to the target with an error less than the specifications in table 6.10 during proximity operations, capture, and control modes.	REQ-MIS-04, REQ-MIS-06, REQ-SYS-01	T	TBD
REQ-ACS-M8	The mothership AOCS shall command manoeuvres to match the target kinematic state with an error less than the specifications in table 6.10 during proximity operations, capture, and control modes.	REQ-MIS-04, REQ-MIS-06, REQ-SYS-01	T	TBD
REQ-ACS-M9	The mothership AOCS shall maintain the commanded kinematic state relative to the target with an error less than the specifications in table 6.10 during hold operations.	REQ-MIS-04, REQ-SYS-01	T	TBD
REQ-ACS-M10	The mothership AOCS shall command the capture interface alignment with the target with an angular error less than 2° during capture operations.	REQ-SYS-01	D	TBD
REQ-ACS-M11	The mothership AOCS shall be capable of detumbling the combined spacecraft-target system from an initial angular momentum of at least 3000 N m s.	REQ-MIS-06, REQ-MIS-08	A	TBD
REQ-ACS-M12	The mothership AOCS shall command a retreat manoeuvre during rendezvous or capture operations if onboard monitoring detects that performance requirements have been exceeded, or if commanded by C&DH.	REQ-MIS-05	D	TBD
REQ-ACS-M13	The mothership AOCS shall command a retreat manoeuvre that achieves a safe separation distance of ≥ 20 m within 120 s after abort initiation.	REQ-MIS-05	A	TBD
Tugs				
REQ-ACS-T1	The tug AOCS shall determine the spacecraft kinematic state with respect to the ECI frame with an error less than the specifications in table 6.10 during nominal mission operations.	REQ-SYS-06	T	TBD
REQ-ACS-T2	The tug AOCS shall control the commanded spacecraft kinematic state with an error less than the specifications in table 6.10 during nominal mission operations.	REQ-SYS-06	T	TBD
REQ-ACS-T3	The tug AOCS shall damp undesired spacecraft angular rates to below 0.5 ° s^{-1} within 120 s after disturbance events.	REQ-SYS-23	A	TBD
REQ-ACS-T4	The tug AOCS shall execute commanded attitude manoeuvres with a slew rate greater than 0.25 ° s^{-1}.	REQ-SYS-06	A	TBD
REQ-ACS-T5	The tug AOCS shall command thrust-vector pointing during orbit control manoeuvres with an error less than 2°.	REQ-SYS-06	A	TBD
REQ-ACS-T6	The tug AOCS shall command orbit control manoeuvres with a ΔV execution error less than 0.1 m s^{-1}.	REQ-SYS-06	A	TBD
Universal				
REQ-ACS-U1	The AOCS shall provide pointing control toward commanded directions as required by the active mission mode.	-	D	Yes
REQ-ACS-U2	The AOCS shall provide housekeeping telemetry of the sensor status, estimated kinematic state, actuator commands, and control loop status.	-	I	Yes

Table 6.10: Kinematic state accuracy requirements per spacecraft and operational mode

Function	Position [m]	Velocity [m s^{-1}]	Attitude [°]	Angular rate [° s^{-1}]
Mothership				
Determine absolute state	100	1	5	0.5
Control absolute state	-	0.3	1	0.1
Determine relative state	0.05	0.01	2	0.5
Control relative state	0.05	0.01	2	0.5
Tug				
Determine absolute state	100	1	5	0.5
Control absolute state	-	0.1	2	0.5

Table 6.10 provides the kinematic state accuracy requirements, distinguishing between state determination and closed loop control performance. The spacecraft kinematic state consists of a complete description of the instantaneous position, velocity, attitude, and angular rate. The accuracy of determining the state considers measurement uncertainties introduced by the sensors, as well as estimations in the data processing. Similarly, the accuracy of controlling the state considers both the errors introduced by the control algorithms, and the

uncertainties from the actuators. The absolute state accuracy requirements are applied to long range rendezvous and orbit control manoeuvres, while the relative state requirements are applied to proximity operations, hold points, synchronisation, and capture alignment. Since the controller commands the spacecraft attitude, thrust vector direction, and velocity increment, the resulting position determined by the executed trajectory. As a result, the instantaneous absolute position parameter is excluded from the control requirements. During proximity operations, however, the spacecraft position relative to the target is directly commanded by the relative motion controller, hence it is included in the relative state control requirements.

Verification & Validation Methods

The verification approach of AOCS relies largely on detailed analysis models and conducting hardware-in-the-loop tests where possible. The determination functions involve both hardware and software capabilities of the AOCS. All selected sensors provide accuracy higher than those specified in table 6.10, ensuring the measurement aspect of determining the kinematic state is complied. However, the final state estimate also depends on sensor fusion, filtering, and measurement update rates. Therefore, the state estimation algorithms are verified through analysis, using representative sensor noise, bias, and drift as documented by the manufacturers.

To verify the navigational capabilities of the AOCS, control algorithms can be simulated. Employing the same modelling approach presented in section 6.3, the spacecraft model response to disturbances, commanded slews, and orbit control manoeuvres can be verified. Importantly, a detailed dynamic model of the spacecraft must be defined, encompassing the time-varying centre of mass and inertial properties, actuator limitations and sensor delays.

The AOCS performance for all proximity operations, encompassing the requirements REQ-ACS-M7 to -M10, can be tested at the European Proximity Operations Simulator 2.0, shown in figure 6.9. This simulator allows for hardware-in-the-loop testing of control algorithms by simulating docking operations between two spacecraft. The RPOD sensors can be mounted on the model, and the control arguments generated by the AOCS are connected to a simulator which actuates the robotic arm. This facility allows for extensive verification of the state estimation and control command algorithms.

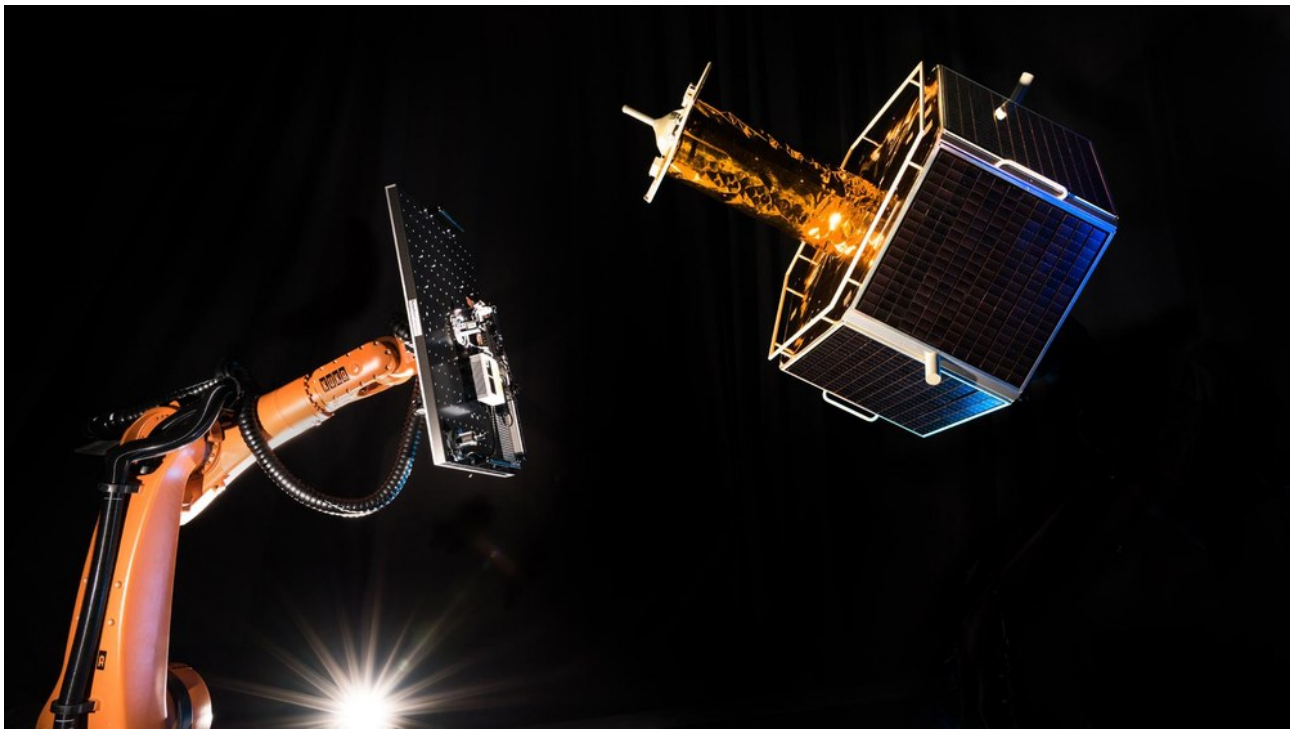

Figure 6.9: European Proximity Operations Simulator 2.0[1]

[1] https://www.dlr.de/en/research-and-transfer/research-infrastructure/european-proximity-operations-simulator-epos [accessed 17 June 2026]

7. Capture Subsystem

The capture subsystem enables REAVER to establish controlled mechanical contact with non-cooperative geostationary debris and prepare each target for transport to the recycling hub. Since capture is performed through cooperation between the mothership and the tugs, both vehicles use different capture hardware. The mothership characterises the debris, positions the tug, aligns it with the target liquid apogee engine (LAE), and supports detumbling. The tug then uses an apogee engine probe (AEP) mechanism to create a rigid connection with the debris. The tug's role is to achieve a rigid mechanical connection with the target debris as well as debris transport to the recycling hub. The capture processes can be seen in figure 7.1.

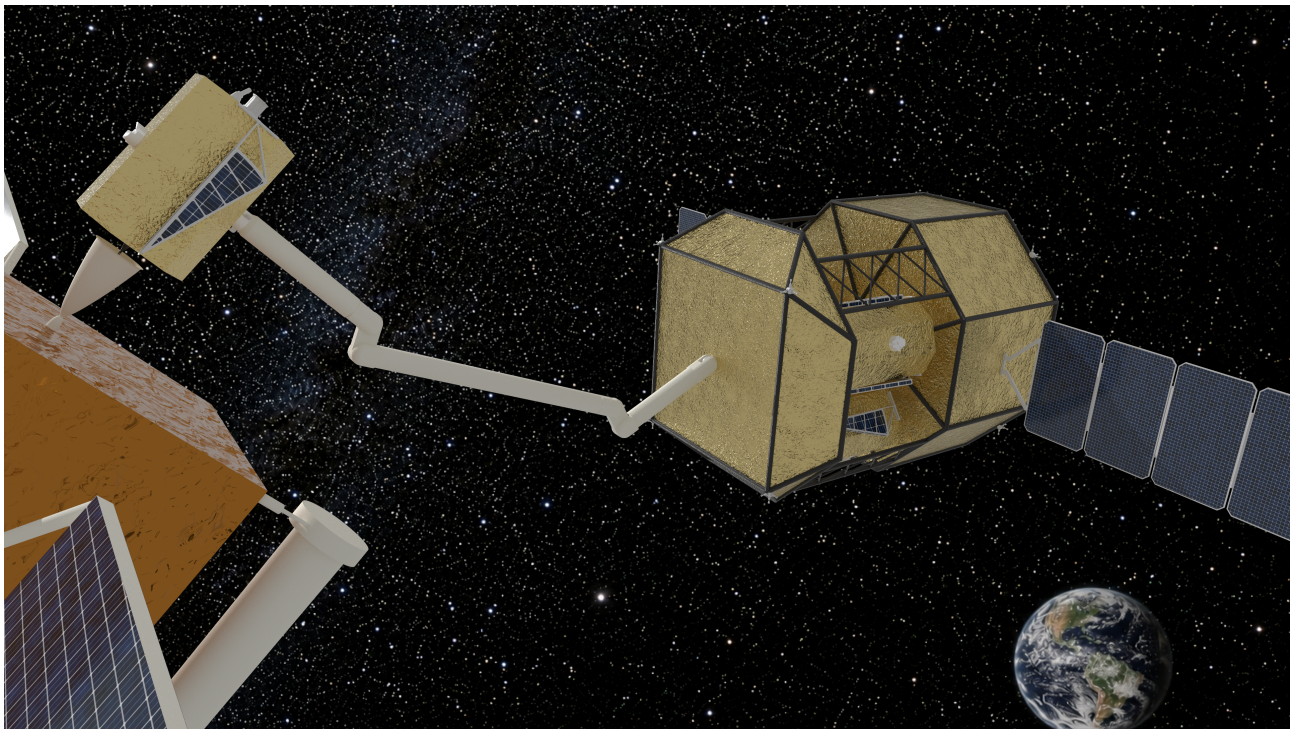

Figure 7.1: Mothership positioning tug with robotic arm prior to capture sequence (background generated with ChatGPT)

This chapter first describes the mothership capture system, including the robotic manipulator and its mechanical interface with the tugs. It then presents the tug capture system and explains the AEP mechanism used to interface with the target LAE nozzle. After this, the robotic manipulator control approach is discussed, followed by the rendezvous, proximity operations and docking (RPOD) sensor suite required for debris characterisation and alignment. Finally, the capture subsystem requirements are verified against the selected design.

7.1. Mothership Capture System

The mothership capture system consists of the robotic manipulator and the Jena Optronik ASTROhead cameras, the ASTROhead controller, Malin ECAM-IR3A, and the RVS 3000-3D LiDAR. The robotic arm moves the tugs from their stowed position into alignment with the target's apogee engine nozzle. It is designed to provide 7DOF manipulation (3 hinge joints, and 4 rotational joints) to reach any coordinate in space with any desired orientation. To attach the arm to the tugs a self aligning mechanical interface is used. The arm features a male interface with three claws, ensuring a rigid connection to the female interface on the tugs. An overview of the robotic arm and the mechanical interface can be seen in figure 7.2.

The total length of the robotic arm is 4.627 m. This specific length was selected to ensure the robotic arm could reach the tugs as well as have enough reach to move the tugs past any obstacles on the target debris such as antennas, solar arrays or other protruding components. After the tug has achieved a rigid connection with the debris the robotic arm is also used to transmit the forces during detumbling after which the tug is released and allowed to return to the recycling hub.

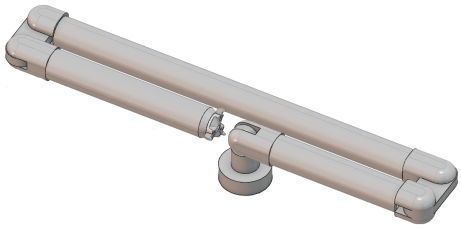

(a) Robotic arm in the stowed position

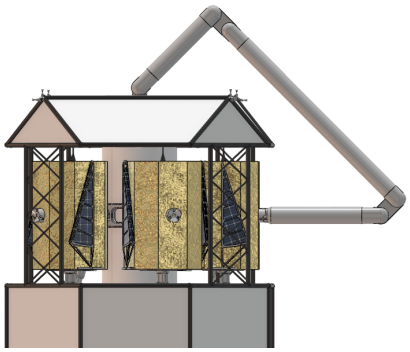

(b) Robotic arm grabbing a stowed tug

(c) Extended robotic arm (mothership on the bottom of the figure)

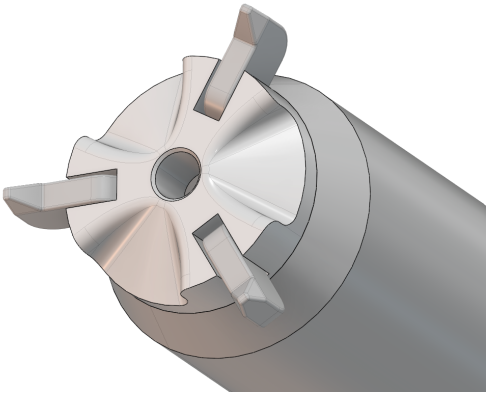

(d) Robotic arm male mechanical interface

Figure 7.2: Robotic arm configuration (3D model made with 3DEXPERIENCE Catia)

7.2. Tug Capture System

The tug capture system consists of the apogee engine probe (AEP), and two ASTROhead docking cameras. The apogee engine probe is a mechanism designed to insert a probe into the throat of the target's liquid apogee engine (LAE). After the probe clears the throat of the nozzle it expands such that when the mechanism is retracted the debris is pulled towards the tug. The mechanism retracts until the bottom of the LAE nozzle makes contact with a rigid plate on the tug, completing the mechanical connection.

According to [74] over 80% of geostationary satellites have a liquid apogee engine. Furthermore, a vast majority of the liquid apogee engines are made by just a few manufacturers. An overview of the most common LAEs and their key dimensions is provided in table 7.1. To ensure the AEP mechanism is compatible with these engines a 15mm probe diameter is selected.

Table 7.1: Common GEO satellite liquid apogee engines and throat diameters

Engine Model	Throat Diameter (mm)
Aerojet R-4D	18.8
IHI BT-4	17
ArianeGroup S400	16.45

A conical head aids with insertion and self aligning since extreme precision is needed to position the shaft in the throat. To extend the mechanism and pull the debris in a lead screw is used. Lead screws are optimal for this application because they offer high torque and resist back driving which would be catastrophic since constant pressure on the engine nozzle is required for a secure connection. The conical head also acts as a passive actuator for the hook extension. Once the head hits the injector plate of the LAE it expands and locks the hooks. Since the actuation is passive and simple it is very reliable and only a single actuator is needed to drive the entire capture. A cross section view of the hook extension and an overview of the AEP mechanism components can be seen in figure 7.3.

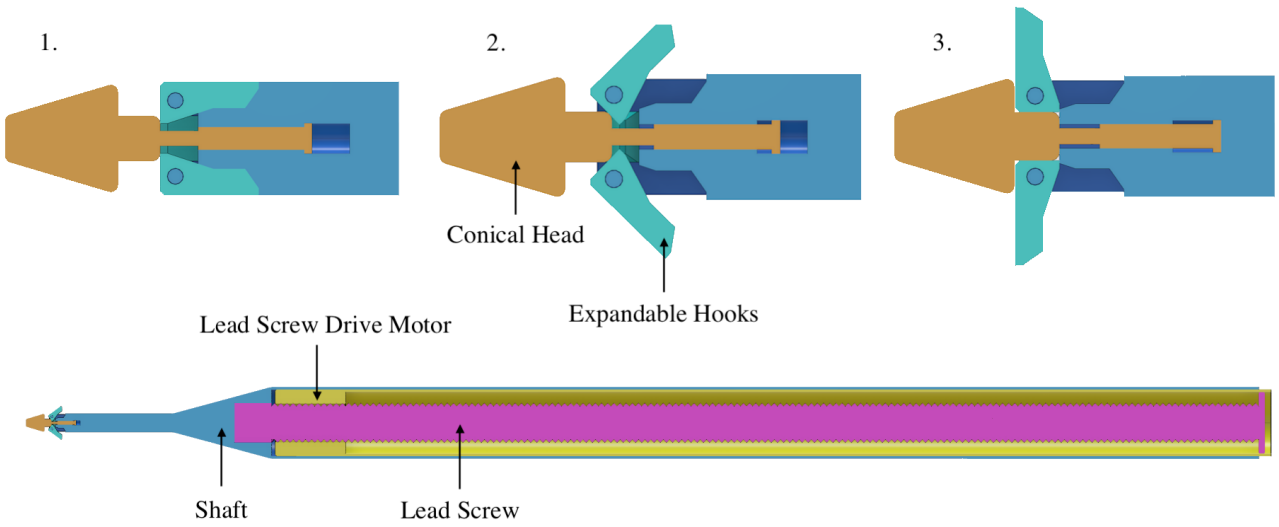

Figure 7.3: Apogee Engine Probe mechanism components

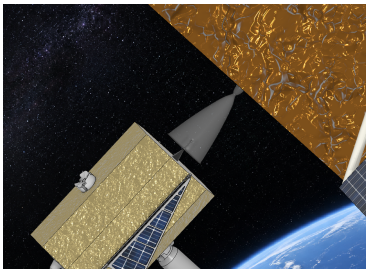

(a) Step 1: The AEP mechanism is aligned with the LAE throat (tug on bottom left)

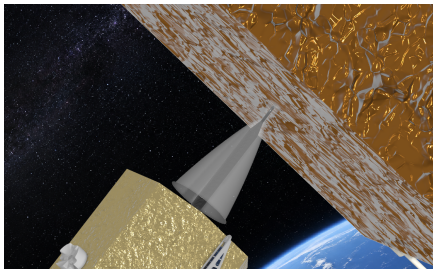

(b) Step 2: The AEP mechanism expands past the LAE throat

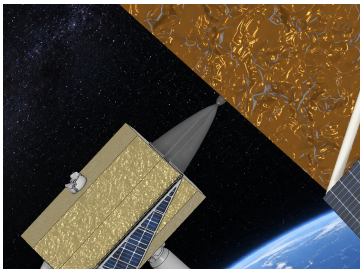

(c) Step 3: The AEP mechanism is retracted until the LAE nozzle is in contact with the tug

Figure 7.4: Debris capture sequence using AEP Mechanism (background generated with ChatGPT)

The AEP mechanism structure provides a multitude of advantages. The biggest advantage is that by virtue of the mechanism the tug will always be perfectly aligned with the target centre of mass. By using the LAE as the reference point during capture the AEP mechanism bypasses arguably the biggest challenge of capture mechanism design; C.G. misalignment. Furthermore, the apogee engine is one of the most structurally robust components on a spacecraft designed to withstand propulsion loads. This allows the tugs to perform manoeuvres while attached to the debris without overstressing weaker structures such as solar panels or antennas. Another advantage is that the LAE nozzle is radially symmetric making for a relatively forgiving target compared to trying to grasp an arbitrary spacecraft structure.

The main drawbacks of the AEP mechanism are high precision requirements and mechanism size. Since the 15 mm diameter probe needs to fit through LAE throats as tight as 16.45 mm, positional tolerances are very low, and angular tolerances are stricter yet because the mechanism can extend over 800 mm. The small size of the mechanism also provides structural challenges when pulling the debris towards the tug. Since the mechanism is only designed to withstand tension loads, all shear and bending loads must be kept to an absolute minimum, which is operationally restrictive. A visualisation of the tug transporting a captured debris can be seen in figure 7.5.

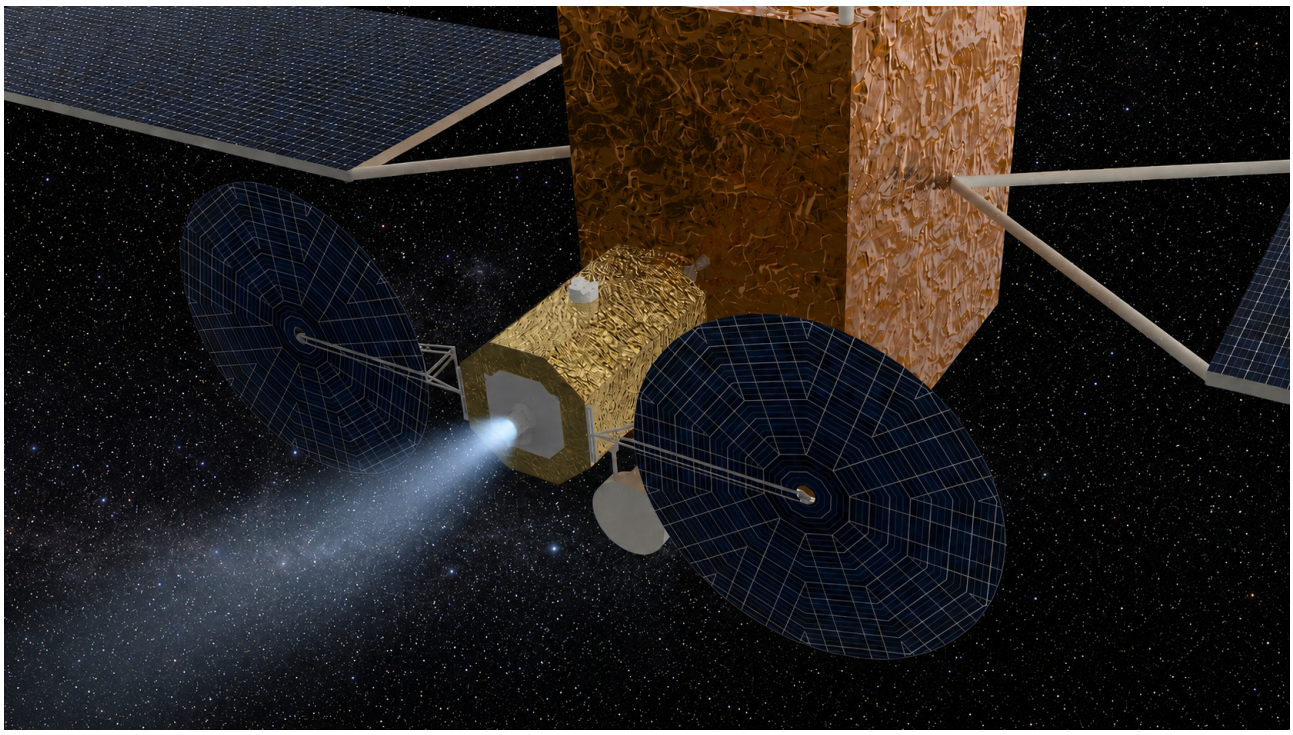

Figure 7.5: Tug transporting the COMSATBw-1 debris (background and engine plume generated by ChatGPT

7.3. Robotic Manipulator Control Algorithm

To successfully align the tug's AEP mechanism with the throat of the debris' liquid apogee engine, the mothership's robotic manipulator must have precise and robust control capabilities. By consolidating the sensor data from the RPOD sensor suite, the relative position between the tug and debris is estimated. During the capture and control sequence, both the mothership's kinematic state relative to the debris and the robotic manipulator's movement must be continuously controlled.

To model the dynamics of the robotic manipulator system, equation (7.1) describes how the applied torques τ and any disturbance torques τ_d acting on the robotic manipulator joints, affect the 7-DOFs of the robotic arm, described by the vector q [15]. H is the global mass matrix of the robotic arm, hence $H\ddot{q}$ describes the inertial torque from joint acceleration. Similarly, C is a matrix of the centrifugal and Coriolis terms contributing to the robotic arm accelerations, such that $C\dot{q}$ describes the inertial torque from the current motion. The matrix H is a function of q, while the matrix C is a function of both $\dot{q}$ and q, meaning these matrices are dependent on the current dynamic state of the robotic arm. As a result, the system is non-linear.

$$\mathbf{H}(q)\ddot{q} + \mathbf{C}(\dot{q}, q)\dot{q} = \tau + \tau_d \tag{7.1}$$

Equation (7.1) can be described as a block diagram, as detailed in figure 7.6. This block diagram characterises how an applied torque τ required to achieve a dynamic state q of the robotic arm is calculated. Variables that are passed into blocks vertically are inputs of the function, while variables passed horizontally are multiplied by the function. For example, to calculate the instantaneous matrix C, q and $\dot{q}$ are required as inputs, and then to calculate the inertial torques from the instantaneous motion $C\dot{q}$, the calculated matrix C is multiplied by $\dot{q}$. Essentially, a complete dynamic model of the current state q, $\dot{q}$, and $\ddot{q}$ is inputted, and the corresponding applied torque τ to reach that state is outputted.

Taking this block diagram model of the robotic manipulator dynamics, a closed-loop control system can be designed as detailed in figure 7.7 [15]. The non-linear system presented in figure 7.6 is effectively linearised as the plant $G(s)$, where s indicates that variables are transformed into the Laplace domain. The plant has seven independent control inputs u and system outputs q corresponding to the seven degrees of freedom of the robotic manipulator. Hence, the controller K must be designed to allow the robotic arm to move to a desired dynamic state q_{ref} can be a linear controller [15]. By comparing the control loop in figure 7.7 to the block diagram defining the robotic manipulator dynamic state in figure 7.6, it is clear that the control input $u = \ddot{q}$. Hence, the plant is simply a system of double integrators that take the input $\ddot{q}$ and output the state of the robotic arm q. The controller K calculates what acceleration command u needs to be inputted into the system such that the error between the measured system behaviour q, and the desired behaviour q_{ref} is reduced. The

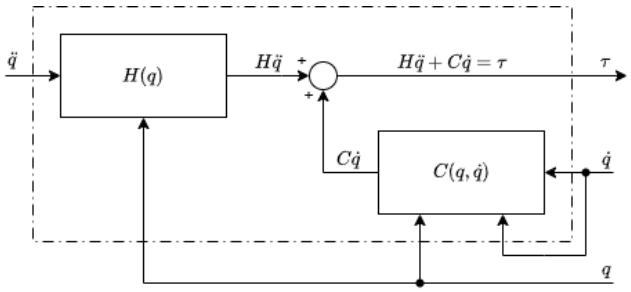

Figure 7.6: Modelling the robotic manipulator dynamics equation as a block diagram

computed-torque block in the plant $G(s)$ converts this acceleration command u into a torque command τ that is physically actuated in the robotic manipulator, causing its dynamic state to change, reflected by the resulting motion q.

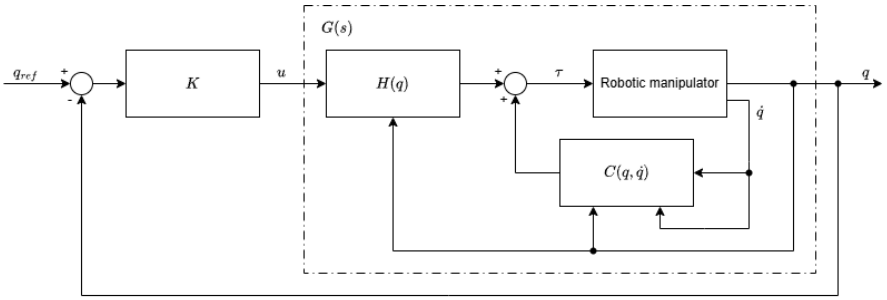

Figure 7.7: Control loop of the robotic manipulator

The robotic manipulator plant requires an acceleration command u provided by the controller K, but also the current dynamic state of the system q and $\dot{q}$ as inputs. Hence, the robotic arm is equipped with position and torque sensors at each joint to measure both the current position and velocity of each DOF of the robotic arm. However, it is important to note that measurements of a state always introduce uncertainty since sensors inevitably introduce noise, the robotic arm state is estimated from joint sensor data using numerical analysis, and data processing creates time delays meaning the measured state will always lag behind the true state. Furthermore, the exact characteristics of the robotic manipulator used to the model the system will also have uncertainties. Finally, disturbance torques τ_d can also act on the robotic arm, affecting its dynamic state unpredictably. Therefore, the controller K must be robust to modelling errors, sensor noise, actuator uncertainty, and external disturbance torques τ_d, all of which can cause the actual robotic manipulator response to deviate from the model. While H_∞ control methods are highly complex, they are well established in robust control, applied to robotics, and particularly suitable for multivariable systems with strong cross-coupling and uncertainties, as is the case for this robotic manipulator system [15].

The control algorithm for the robotic arm follows the closed-loop architecture shown in figure 7.7. First, the RPOD sensor suite estimates the relative position between the tug and debris, which is used to calculate the desired robotic arm reference motion. The actual state of the manipulator is then measured using joint sensors along the arm, providing feedback of the joint positions and velocities. By comparing this measured state with the reference state, the controller calculates the required action to match the reference. The controller will be designed with an H_∞ method to minimise the error between the desired and measured robotic arm behaviour since it is robust against all the uncertainties in the system.

7.4. Capture Subsystem Sensors

REAVER requires relative navigation data to enable RPOD capabilities. The RPOD sensor suite spans thus both the mothership and tugs. Use is made of the MEV-1 sensing hardware [14]. For the mothership the Jena Optronik ASTROhead visible stereo camera package is selected, consisting of two narrow field of view (NFOV), two wide field of view (WFOV), and two docking cameras (WFOV) providing both far- and near-range relative position and attitude data during RPOD. Images from these cameras as used on the MEV-1 are presented in figure 7.8. The mothership is additionally equipped with a long wavelength infrared (IR) stereo camera suite with both narrow and wide FOV. For the tugs only the two docking cameras are required for knowledge of alignment of the AEP mechanism with the target's liquid apogee engine.

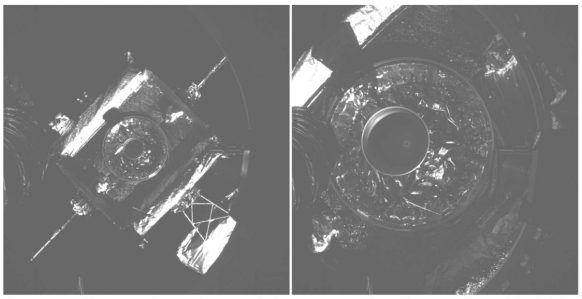

(a) Docking camera images of the MEV mission

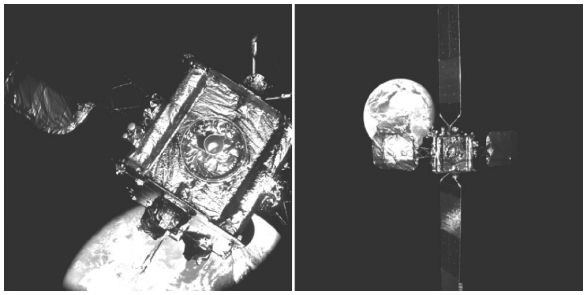

(b) Near- (left) and Wide- (right) field of view images from the MEV mission

Figure 7.8: Images from the MEV-1 sensor suite [74]

Table 7.2 presents the chosen payload sensor components. The chosen RPOD sensors are all compatible with the SpaceWire databus to handle the high data throughput.

Table 7.2: RPOD sensor selection

Sensor	Quantity	Data Interface	Data Rate	Mass	Source
Jena Optronik ASTROhead Cam (including 85 deg SEA baffle)	8	SpaceWire	80 Mbps	1 kg	[75]
Jena Optronik ASTROhead Controller	2	SpaceWire	-	4.3 kg	[75]
Malin ECAM-IR3A	4	SpaceWire (Single Port)	100 Mbps	525 g	[76]
Jena Optronik RVS 3000-3D (for non-cooperative targets)	2	SpaceWire (for X-variant)	Unavailable	13.9 kg	[77, 78]

7.5. Verification of Capture Subsystem Requirements

This section presents the capture subsystem requirements. The main drivers of the design are accuracy of the robotic arm and the range of throat diameters. A 0.5 mm positional error was required based on the minimum distance between the throat and AEP shaft. A 300 mrad angular tolerance was calculated as the maximum angle that still allows for the fully extended boom to clear the throat when combined with the aforementioned positional error. The range of 16 – 30 mm ensure the mechanism can capture the vast majority of geostationary satellites. Spacecraft with a throat diameter greater than 30 mm usually have much higher dry masses which means that the tugs could not transport them because of propellant limitations so there was no need to design past this point.

Table 7.3: CAP subsystem requirements, and requirement IDs

ID	Capture Subsystem Requirement	Parent Requirement	Method	Check
Mothership				
REQ-CAP-M1	The mothership capture system shall be able to position the tug with a positional error < 0.5 mm and a pointing error < 300 mrad relative to the debris.	REQ-MIS-03, REQ-MIS-11	T	TBD
Tugs				
REQ-CAP-T1	The tug capture system shall achieve a fully rigid connection with the debris.	REQ-STK-03	T	TBD
REQ-CAP-T2	The tug capture system shall be able to interface with debris liquid apogee engines with a throat diameter between 16 mm and 30 mm.	REQ-STK-03	I	Yes
Universal				
REQ-CAP-U1	The capture mechanism shall be capable of aborting a capture attempt and retracting to a stowed configuration.	REQ-STK-05	T	TBD
REQ-CAP-U2	The capture system shall not cause structural or other damage to debris components intended for reuse.	REQ-SYS-23	D	TBD
REQ-CAP-U3	The capture system shall not create any additional debris during capture operations.	REQ-SYS-24	D	TBD

8. Propulsion

In this chapter, the propulsion architecture of the REAVER mission is introduced. An overview is provided of the mothership propulsion design and thruster selection, tankage, pressurisation, feed architecture and centre-of-gravity management. The tug propulsion system is subsequently discussed, followed by the propulsion mass, power and cost budget. The chapter concludes with a requirement compliance matrix with associated verification methods.

8.1. Mothership Propulsion System

The mothership propulsion system is sized to perform the main campaign manoeuvres between the recycling hub and the GEO debris targets. This section presents the subsystem requirements, propellant and thruster selection, propellant tank sizing, pressurisation system, feed-system architecture and centre of gravity management approach.

Propellant and Thruster Selection

The mothership propulsion system must provide high total impulse within the one-year campaign schedule while avoiding toxic propellants. Hydrazine was therefore discarded, while electric propulsion was rejected for the mothership because repeated rendezvous and transfer manoeuvres require higher thrust than the campaign timeline would allow. The selected propellant is LMP-103S, an ADN-based green monopropellant used in High Performance Green Propulsion (HPGP) systems. It offers long-term storability, lower toxicity than hydrazine, and a vacuum specific impulse close to 253 s+-, making it suitable for both the main transfer branch and the RCS/proximity-control branch [79]. The updated mothership propellant budget is 1172.2 kg, including main propulsion, RCS, and a residual margin.

For the main transfer branch, two HPGP options were compared: four 22 N HPGP thrusters and a higher-thrust 200 N to 220 N HPGP alternative. The higher-thrust option is attractive because it reduces burn duration, but the public data indicate lower maturity and lower demonstrated capability for the high-I_{sp} transfer mode. The 22 N HPGP thruster operates with LMP-103S, provides approximately 5.5 N to 22 N of thrust, has a typical vacuum specific impulse of 243 s to 255 s, and has public qualification-level data for 150 kg throughput and 38 min continuous firing at TRL 7 [1]. In contrast, the 200 N to 220 N HPGP unit is split into an RCS mode and a high-I_{sp} Δv mode. The RCS mode is reported at TRL 5, with 50 N to 200 N thrust, 150 kg target throughput and 10 min target continuous firing time, while the high-I_{sp} mode is reported at TRL 3, with 55 N to 220 N thrust, only 25 kg target throughput and 200 s target continuous firing time [2]. Since REAVER requires transfers, throughput, continuous firing capability and maturity are more critical than thrust alone.

The comparison is based on the worst-case single manoeuvre from the astrodynamics analysis, requiring $\Delta V = 368.4$ m/s and approximately 464.4 kg of LMP-103S. The burn time is estimated using equation (8.1), with $I_{sp} = 253$ s. In this equation, the propellant mass m_{prop}, specific impulse I_{sp}, standard gravity g_0, and total thrust T_{tot} are used to compute the burn time t_{burn}.

$$t_{\text{burn}} = \frac{m_{\text{prop}} I_{sp} g_0}{T_{\text{tot}}} \tag{8.1}$$

For four 22 N thrusters, the total thrust is 88 N, giving a burn time of approximately 5.0 h. This exceeds the 38 min continuous firing qualification value, so the manoeuvre would need to be split into multiple firing arcs with thermal recovery periods. However, the throughput is shared between four thrusters, resulting in approximately 130 kg per thruster for the worst-case burn, which remains within the public 150 kg qualification-level throughput.

Using two 200-220 N thrusters would reduce the same burn to approximately 0.8 h to 0.9 h. However, the required throughput would be approximately 260 kg per thruster, exceeding both the 150 kg target throughput of the RCS mode and the 25 kg target throughput of the high-I_{sp} mode. In addition, the 200 s target continuous firing time of the high-I_{sp} mode would require many short pulses, reducing the practical benefit of the higher thrust. Therefore, despite the longer burn duration, the selected main propulsion architecture uses four 22 N

[1] https://satcatalog.s3.amazonaws.com/components/863/SatCatalog_-_Bradford_Space_-_22N_HPGP_-_Datasheet.pdf [accessed 16 June 2026]

[2] https://satcatalog.s3.amazonaws.com/components/866/SatCatalog_-_Bradford_Space_-_200N_HPGP_Long_-_Datasheet.pdf [accessed 16 June 2026]

HPGP thrusters because this option has higher maturity, better demonstrated throughput and lower qualification risk.

For proximity control and trimming, the mothership uses 24×5 N HPGP thrusters operating with the same LMP-103S propellant. Lower-thrust 1 N thrusters were considered, but they provide limited control authority for the mothership wet mass and for disturbance rejection during non-cooperative debris interaction. The 5 N thrusters are arranged as a distributed 6-DOF RCS network with six sets of four thrusters. This provides translational and rotational control while maintaining robustness to centre-of-gravity shifts caused by propellant depletion and sequential tug release. [3]

Propellant Tank Sizing

The updated mothership chemical propulsion budget requires 1172.2 kg of LMP-103S, including main propulsion, RCS and residual margin. Using a propellant density of 1240 kg/m^3, the required propellant volume is given by equation (8.2) resulting in 946 L. In this equation, the propellant mass m_{prop} and the density of LMP-103S $\rho_{\text{LMP-103S}}$ are used to compute the required propellant volume V_{prop}.

$$V_{\text{prop}} = \frac{m_{\text{prop}}}{\rho_{\text{LMP-103S}}} \tag{8.2}$$

The tank selection was driven by required volume, dry mass, packaging, centre-of-gravity (CG) control and compatibility with LMP-103S. Since LMP-103S is compatible with conventional metallic propulsion-system materials but not with silica-based diaphragms, tanks using incompatible diaphragm materials are excluded [80, 16]. Propellant management device (PMD) tanks were therefore preferred, as they avoid diaphragm compatibility issues and provide propellant acquisition in microgravity.

A four-tank configuration was selected instead of one or two larger tanks. This provides a more symmetric layout around the mothership centreline, limits lateral centre-of-gravity shift during propellant depletion, and improves packaging around the central propulsion structure. It also allows opposite tanks to be drained together, reducing disturbance torques from asymmetric propellant usage. The disadvantage is a more complex feed system, but this was considered acceptable because centre-of-gravity control is important during propellant depletion and sequential tug release.

The selected tank is the Northrop Grumman 80350-1/80415-1 PMD tank. Each tank has a volume of 368 L, a dry mass of 13.1 kg, an internal diameter of 892 mm, and an operating pressure of 17.9 bar [4]. The four tanks in total provide a geometric volume of 1472 L and a dry tank mass of 52.4 kg. For the required 946 L of LMP-103S, each tank is filled with approximately 237 L, corresponding to a fill fraction of 64 %. This leaves approximately 524 L of total free volume for pressurisation, thermal expansion and operational margin, while maintaining a compact and symmetric tank layout.

Pressurant System Sizing

For the pressurisation of the monopropellant propulsion system, two feasible options are identified. The first option is a blowdown system. This option utilises one propellant tank in which both the propellant and a pressurant gas are stored under high pressure. This system is characterised by its simple design, but also by its pressure drop during operation as propellant leaves the system. For LMP-103S, the associated thruster blowdown ranges from 24 – 5.5 bar with a respective thrust of 22 – 5.5 N for the main thrusters and 5.0 – 1.5 N for the RCS thrusters [80, 81]. 5.5 and 1.5N are insufficient for transfer manoeuvres. A second option of a pressure-regulated system is thus considered. This system, although more complex and heavy, utilises a separate high-pressure gas tank, which keeps the propellant tanks under approximately constant pressure. This allows the thrusters to operate closer to their full thrust capability and exhibit more constant and predictable thrust characteristics.

From the risk assessment, RPOD is identified as one of the most critical phases in the REAVER mission. Because of this, high priority is given to the aforementioned predictable and constant thrust characteristics. The pressure-regulated system architecture is thus chosen mainly for this reason.

Based on the maximum expected operating pressure (MEOP) of the chosen propellant tanks in the previous section, and several other components, it is decided to operate the system at 250 psi ($\approx$ 17.2 bar). This means, assuming linear interpolation, that the main thrusters will deliver 16 N of thrust each, whereas the RCS thrusters will deliver 4 N of thrust each.

[3] https://satcatalog.s3.amazonaws.com/components/862/SatCatalog_-_Bradford_Space_-_5N_HPGP_-_Datasheet.pdf [accessed 16 June 2026]

[4] https://www.northropgrumman.com/what-we-do/space/mission-enabling-products/pmd-tanks [accessed 15 June 2026]

For the pressurant gas, helium is selected over nitrogen as it is inert, very light, and has a strong spacecraft propulsion heritage. For the helium tank sizing, a code is set up to calculate the required helium tank volume. The code performs a first-order isothermal helium sizing for a pressure-regulated LMP-103S propulsion system. It calculates the total propellant tank volume, loaded propellant volume, initial ullage/unoccupied tank volume, and the expelled propellant volume at depletion. It then sets a required helium pressure at depletion (P_{HDOP}) by adding a pressure margin to the regulated propellant tank pressure.

The maximum helium tank pressure at the beginning of the mission (P_{HBOM}) is limited by the lowest hardware pressure limit. Using the ideal gas law, the code estimates the helium density and calculates the required helium mass and helium tank volume. The main assumptions used in this sizing are as follows:

1. Helium behaves as an ideal gas; compressibility factor(Z) is 1.
2. Pressure losses are represented only by a simple pressure margin.
3. The helium tank temperature at depletion is constant; the process is assumed to be isothermal. [5]

Equation (8.3) [82] calculates the mass of gaseous helium in the propellant and pressure tanks once the propellant is depleted (M_{HDOP}).

$$M_{\mathrm{HDOP}} = M_{\mathrm{HPDOP}} \left(1 + \frac{F_{\mathrm{REG}} P_{\mathrm{TP}}}{Z R_{\mathrm{HE}} T_{\mathrm{THDOP}} \rho_{\mathrm{HBOM}} - F_{\mathrm{REG}} P_{\mathrm{TP}}}\right) \tag{8.3}$$

Here, F_{REG} is the ratio of inlet to outlet pressure and is set to 2.0 [82], and Z is set to 1 based on the ideal gas assumption. To be conservative, the temperature of helium at depletion of propellant (T_{HDOP}) is taken to be 253.15 K based on the temperature limits of the selected tank. The helium mass delivered to the propellant tanks at depletion of propellant (M_{HPDOP}) is given by equation (8.4) [82].

$$M_{\mathrm{HPDOP}} = \frac{P_{\mathrm{TP}} V_{\mathrm{THDOP}}}{Z R_{\mathrm{HE}} T_{\mathrm{THDOP}}} \tag{8.4}$$

The volume of expelled propellant (V_{THDOP}) is determined by the required propellant volume without any margin applied to it. P_{TP} is the propellant tank pressure and R_{HE} the Helium gas constant and ρ_{HBOM} is the Helium density at begin-of-mission. The helium propellant volume is then determined using equation (8.5).

$$V_{\mathrm{He}} = \frac{M_{\mathrm{HDOP}}}{\rho_{\mathrm{HBOM}}} \tag{8.5}$$

For this process, the helium tank is selected beforehand, after which its volume is checked to ensure it is large enough. For the full propellant loading (1472 L) it followed that 4.5 kg or equivalently 97.2 L of helium is required for the system. For the mission-specific 946 L of LMP-103S, 72.6 L of helium is required for the entire propulsion system. Based on these values a 120 L HPV helium tank from MT Aerospace is selected. [6] The pressure system architecture thus consists of four LMP-103S propellant tanks and one high-pressure helium tank.

CG Management

The mothership propulsion layout shall remain controlled throughout the campaign despite CG shifts caused by propellant depletion, tank-drain imbalance, propellant sloshing and sequential tug release. During main burns, a lateral offset between the actual CG and the thrust line produces a disturbance torque, approximated as equation (8.6), where T is the total main thrust and Δr_{CG} is the lateral CG offset from the nominal centreline. For the selected 4×22 N main-thruster cluster, the maximum nominal thrust is 64 N, as explained previously when sizing the pressurant system.

$$\tau_{\mathrm{dist}} = |\Delta \mathbf{r}_{\mathrm{CG}} \times \mathbf{T}| \approx T \Delta r_{\mathrm{CG}} \tag{8.6}$$

A reduced-order Python model is used to estimate the CG envelope over the mission. The model updates the spacecraft mass properties after each mission event, including the LMP-103S depletion, tank-drain imbalance, propellant sloshing and tug release. The CG offset is calculated from the lateral mass moment using equation (8.7), where m_i is the mass of each relevant item and r_i is its lateral distance from the spacecraft centreline. Since the

[5] The isothermal assumption is used because the helium is delivered gradually over multiple burn phases spread over multiple days

[6] `https://www.mt-aerospace.de/files/mta/tankkatalog/PVG-Family-80-120.pdf` [accessed 15 June 2026]

four LMP-103S tanks are placed symmetrically around the centreline, equal draining cancels first-order lateral CG motion. Tank-drain imbalances of 2, 5 and 10 % are included to assess sensitivity to unequal depletion.

$$\Delta r_{\mathrm{CG}} = \frac{\left|\sum_i m_i r_i\right|}{\sum_i m_i} \tag{8.7}$$

Propellant sloshing is modelled using the classical equivalent-mechanical approach, where the dominant lateral slosh mode is represented as a spring–mass–damper system [83]. Since the selected tanks use propellant management devices (PMDs), only a reduced mobile-liquid fraction was considered. Additional supplier-level anti-slosh features, such as vanes, screens or baffles, remain possible if the final AOCS margin is insufficient, although these need to be designed together with the PMD to avoid increasing residuals or disturbing propellant acquisition [84].

The largest CG driver is found to be sequential tug release (depicted in figure 8.1) rather than tank depletion. The current tug dry mass is 193.15 kg. Two tugs carry 114.54 kg of xenon each, while the other three carry approximately 33.35 kg each. This gives tug wet masses of approximately:

$$m_{\mathrm{tug}} = [307.69,\ 307.69,\ 226.50,\ 226.50,\ 226.50]\ \mathrm{kg}.$$

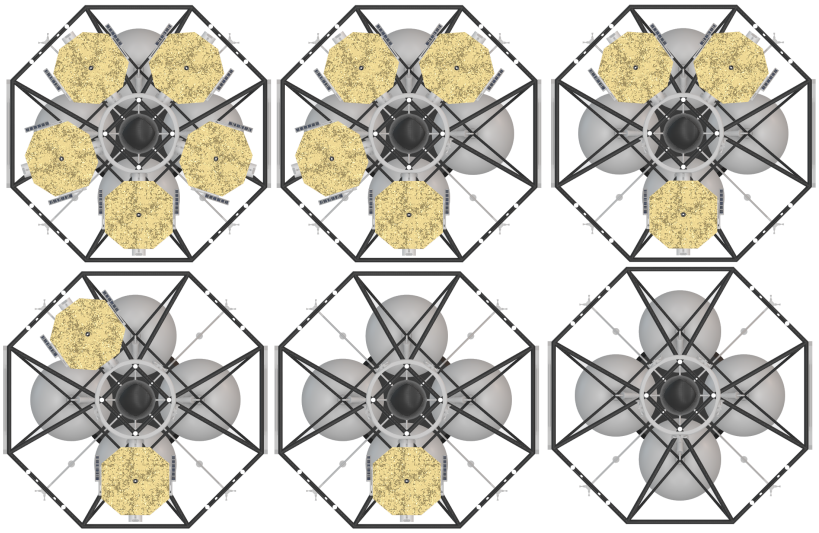

Figure 8.1: Top-view tug deployment sequence used to identify the most asymmetric CG configuration.

The tugs are initially positioned on the rail so that their lateral mass moments cancel. No continuous rail rebalancing is assumed, so each tug release creates a new post-release CG offset. As shown in figure 8.1, the worst case occurs later in the sequence, when only one off-axis tug remains attached. For one remaining 226.5 kg tug on a 1 m radius rail and a representative late-mission mass of 1296 kg, the tug-driven CG shift is 148 mm. Including tank-drain imbalance and slosh uncertainty, the updated untrimmed worst-case lateral CG shift is estimated as approximately 165 mm. From equation (8.6), this gives a conservative main-burn disturbance torque of 11.1 N m.

Propellant trim is initially assessed as a mitigation method, but is ruled out as it would deliberately bias the remaining LMP-103S toward tanks opposite the final tug to counter the tug-induced mass moment. At the critical phase, approximately 398 kg of LMP-103S remains, which could provide a trim moment of about 10.8 N m while keeping minimum propellant in the tank under the remaining tug. This, however, does not entirely eliminate the induced torque. Full elimination would require non-nominal tank-drain sequencing, increase feed-system operational complexity, and reduce flexibility for later manoeuvres. It also couples CG control to propellant availability and slosh uncertainty. Therefore, propellant trim is discarded as a feasible option.

The preferred mitigation method is thrust-vector control, supported by RCS authority. A two-axis gimballed main-thruster mechanism is selected as the primary burn-time mitigation. A representative option is the LMO Shaman-C2 / TPM-CP-22-type mechanism, intended for 5 N to 22 N chemical thrusters, with a ±10 deg steering range and approximately 0.3 deg pointing accuracy [85, 86]. The required gimbal angle is estimated with equation (8.8), where L is the distance between the thruster plane and the CG.

$$\theta = \tan^{-1}\left(\frac{\Delta r_{CG}}{L}\right) \tag{8.8}$$

For $\Delta r_{CG} = 0.165\,\text{m}$ and $L = 1\,\text{m}$, the required gimbal angle is 9.4 deg. This remains well within the representative ±10 deg gimbal range. Final use requires confirmation of LMP-103S compatibility, feedline flexibility, pressure drop, thermal environment and qualification status.

Differential throttling of the four main thrusters is retained as a backup mitigation. If two opposite thruster pairs share the correction at a distance to the mothership centre of 0.8 m, the thrust difference required per pair is approximately 9.8 N. This is compatible with the 5.5 N to 22 N thrust range of the 22 N HPGP thruster [7], but it would increase control complexity and may reduce net thrust efficiency. It is therefore kept as a secondary correction method rather than the nominal solution.

Feed System and Interface Definition

Based on the selected LMP-103S tanks and HPGP thrusters, a pressure-fed chemical feed system is defined for the mothership. The feed-system architecture is developed from conventional spacecraft monopropellant feed-system layouts and adapted to the REAVER mission needs [87, 17]. Since LMP-103S is compatible with most materials used in conventional spacecraft propulsion systems, but requires avoidance of incompatible diaphragm and seal materials, the component selection is restricted to metallic or LMP-103S-compatible wetted materials [16, 80].

The resulting feed system is shown figure 8.2. Tank isolation valves, fill/drain/test valves, filters, pressure transducers, regulators and thruster-level solenoid valves are included to provide isolation, cleanliness control, pressure monitoring and commanded flow control. For the interface definition, refer to appendix A.

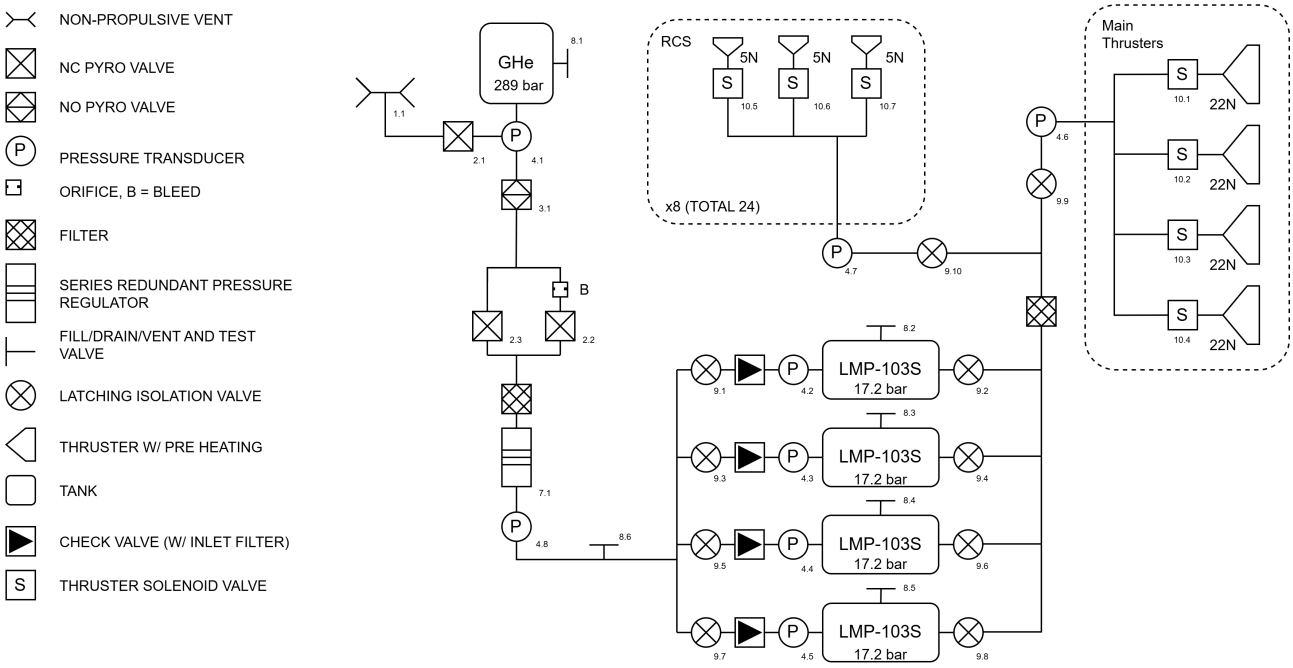

Figure 8.2: Schematic of the mothership chemical propulsion feed system

The schematic in figure 8.2 defines the functional architecture of the propulsion feed system, while figure 8.3 shows its preliminary physical implementation. The CAD layout illustrates the symmetric placement of the four LMP-103S tanks, the central helium pressurant tank, and the routing of the feed lines toward the main and RCS thruster branches.

[7] https://satcatalog.s3.amazonaws.com/components/863/SatCatalog_-_Bradford_Space_-_22N_HPGP_-_Datasheet.pdf [accessed 16 June 2026]

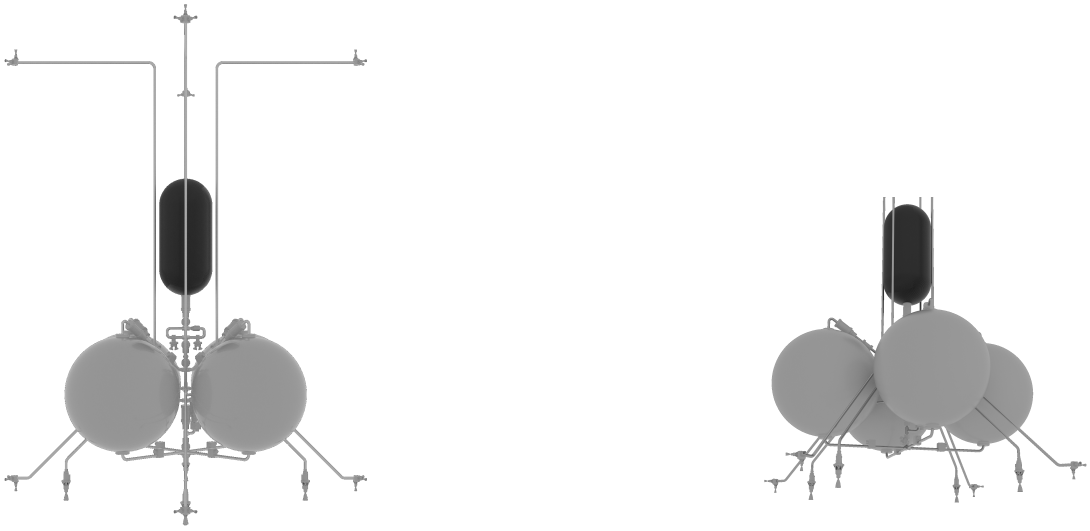

(a) Overall tank and feed-line layout

(b) Local routing near the tanks and thruster branches

Figure 8.3: Preliminary CAD layout of the mothership chemical propulsion feed system

8.2. Tug Propulsion System

The tug propulsion system is sized for low-thrust transport of the captured debris from the handover point to the recycling hub or hold point. Since these transfers are less time critical than the mothership rendezvous manoeuvres, electric propulsion is used to reduce propellant mass and improve overall mission efficiency. This section presents the tug propulsion requirements, thruster and propellant selection, tank sizing, feed-system layout and main propulsion components.

Propellant and Thruster Selection

The selected propellant is xenon, which is commonly used for Hall-effect thrusters because it is inert, non-toxic, easily ionised and has a higher storage density than lighter noble gases. Krypton can also be considered since the EPS-X00 system is compatible with it. However, xenon is selected in the end as it provides higher total impulse for the same propulsion system and reduces qualification risk for the tug mission. Safran EPS-X00 development data reports a total impulse capability of up to 1 MN s with xenon, compared with 750 kN s with krypton [88].

The selected thruster is the Safran PPS-X00 Hall-effect thruster, operated as part of the EPS-X00 low-power electric propulsion system, replacing the PPU-500-based selection from the midterm trade-off with the more integrated PPU-X00 solution. The PPS-X00 uses xenon, provides approximately 15 mN to 75 mN of thrust, has a specific impulse range of 1300 s to 1650 s, operates between 200 W to 1000 W, and has a thruster mass below 3.2 kg. [8] The EPS-X00 architecture is suitable for the compact tug because it is a sub-kilowatt single-string system in which one PPU-X00 powers one PPS-X00 thruster and one low-power flow management system. The complete EPS-X00 string, including thruster, PPU and FMS, is reported to have a mass below 11 kg, while the FMS can be connected directly to the tank and operate at tank pressures up to 300 bar [88].

The updated tug sizing uses a dry mass of 193.15 kg. The maximum loaded xenon allocation for the most demanding tug is 114.54 kg, while the total xenon allocation across all five tugs is 328.44 kg. For a representative thrust level of 60 mN, the xenon mass flow rate is approximately 3.7 mg/s to 4.7 mg/s, depending on the operating specific impulse. Public PPS-X00 data list a minimum total impulse of 1 MN s and a minimum throughput of 79 kg [4]. The maximum REAVER tug propellant allocation of 114.54 kg therefore exceeds the public baseline throughput if consumed by a single thruster. At 1300 s to 1650 s specific impulse, this corresponds to approximately 1.48 MN s to 1.87 MN s of total impulse. This does not invalidate the option; however, the final tug design shall demonstrate, through supplier qualification data or additional lifetime testing where necessary, that the selected thruster configuration can sustain the required 114.54 kg xenon throughput and up to 1.87 MN s total impulse with an appropriate margin.

A two-thruster PPS-X00 configuration was considered to reduce the required throughput per thruster and provide additional redundancy. However, this would increase propulsion system mass, power demand, PPU/FMS hardware, integration complexity and thrust-vector alignment effort. Since each tug is a small vehicle and the mission already contains multiple independent tugs, the design will continue using one centrally

[8] https://www.safran-group.com/sites/default/files/2022-11/Safran%20Spacecraft%20Propulsion%20-%20PPSX00%20-%20Datasheet.pdf [accessed 16 June 2026]

mounted PPS-X00 thruster per tug. This minimises mass and complexity while keeping the thrust vector close to the combined tug and debris centreline. A two-thruster configuration could remain a fallback option if the required single-thruster throughput doesn't suffice for the REAVER mission.

The tug also includes a small xenon cold-gas RCS branch for attitude control, thrust-vector alignment, proximity operations and reaction-wheel desaturation. This branch is fed from the same xenon tank as the PPS-X00, but is separated upstream of the EPS-X00 FMS and regulated to a lower pressure suitable for cold-gas operation. A total of 12 RCS thrusters is selected, arranged as four banks of three thrusters, providing compact 6-DOF control while avoiding a second propellant system.

Tug Xenon Tank Sizing

The tug xenon tank is sized for the maximum loaded tug propellant allocation of 114.54 kg. The sizing is based on the MT Aerospace S-XTA xenon tank family, which provides 40 L to 120 L xenon tanks with a 405 mm internal diameter, 418.4 mm outer diameter, 186 bar to 187 bar MEOP, and titanium/CFRP COPV construction. [9] From the catalogue capacities, the equivalent xenon storage density is approximately 1.83 kg/L, giving a minimum required tank volume of 63.2 L using equation (8.9).

$$V_{\mathrm{Xe,req}} = \frac{m_{\mathrm{Xe}}}{\rho_{\mathrm{Xe,storage}}} \tag{8.9}$$

A standard 90 L S-XTA tank is first considered, as it can store up to approximately 165 kg of xenon with a dry mass of 12.8 kg. However, its 418.4 mm outer diameter is too large for the tug layout. A two-tank solution is therefore selected to reduce the radial envelope and allow symmetric placement around the tug centreline, improving packaging, centre-of-gravity control and integration with the mothership.

The final design uses two custom S-XTA-based xenon tanks, each with an internal diameter of 242 mm and a length of 842 mm. Treating each tank as a first-order equivalent cylindrical volume (equation (8.10)) gives 38.7 L. In this equation, the internal diameter D_i and the length L of the tank are used to compute the equivalent cylindrical tank volume V_{tank}.

$$V_{\mathrm{tank}} = \frac{\pi D_i^2}{4} L \tag{8.10}$$

The two tanks therefore provide a total volume of approximately 77.4 L. Using the S-XTA-derived xenon capacity density, this corresponds to a maximum xenon capacity of approximately 142 kg. For the required 114.54 kg maximum tug load, this gives a capacity margin of approximately 26 kg and a used capacity fraction of about 82 %. This margin accounts for residual propellant, temperature effects, pressure uncertainty and tank-sizing uncertainty.

The dry mass is estimated by linearising the MT Aerospace S-XTA tank-family data as per equation (8.11), where $V_{\mathrm{tank,L}}$ is the tank volume in litres.

$$m_{\mathrm{dry}} \approx 1.05 + 0.131 V_{\mathrm{tank,L}} \tag{8.11}$$

For one 38.7 L custom tank, this gives a dry mass of approximately 6.1 kg, or 12.2 kg for the two-tank system. Since the selected tanks are custom S-XTA-based pressure vessels rather than catalogue items, the final design shall require supplier confirmation of the liner and overwrap sizing, proof and burst pressure margins, mounting interfaces, thermal limits, leak tightness, cyclic life and qualification status.

Feed System and Interface Definition

The main electric-propulsion branch feeds the EPS-X00 FMS through a tank isolation valve and a high-pressure filter. The FMS meters the xenon flow to the PPS-X00 anode and cathode, while the PPU-X00 provides the electrical power required for discharge, cathode operation and thruster control. [88] [4]

A secondary xenon cold-gas RCS branch is separated upstream of the EPS-X00 FMS. This branch feeds 12 small RCS thrusters arranged as 4 banks of 3 thrusters. The RCS branch includes its own isolation, filtration, pressure monitoring and local distribution manifold, since the Hall-thruster FMS is not used to meter the RCS flow. The complete tug feed-system schematic is shown in figure 8.4.

[9] `https://www.mt-aerospace.de/files/mta/tankkatalog/MT-Tankkatalog.pdf` [accessed 15 June 2026]

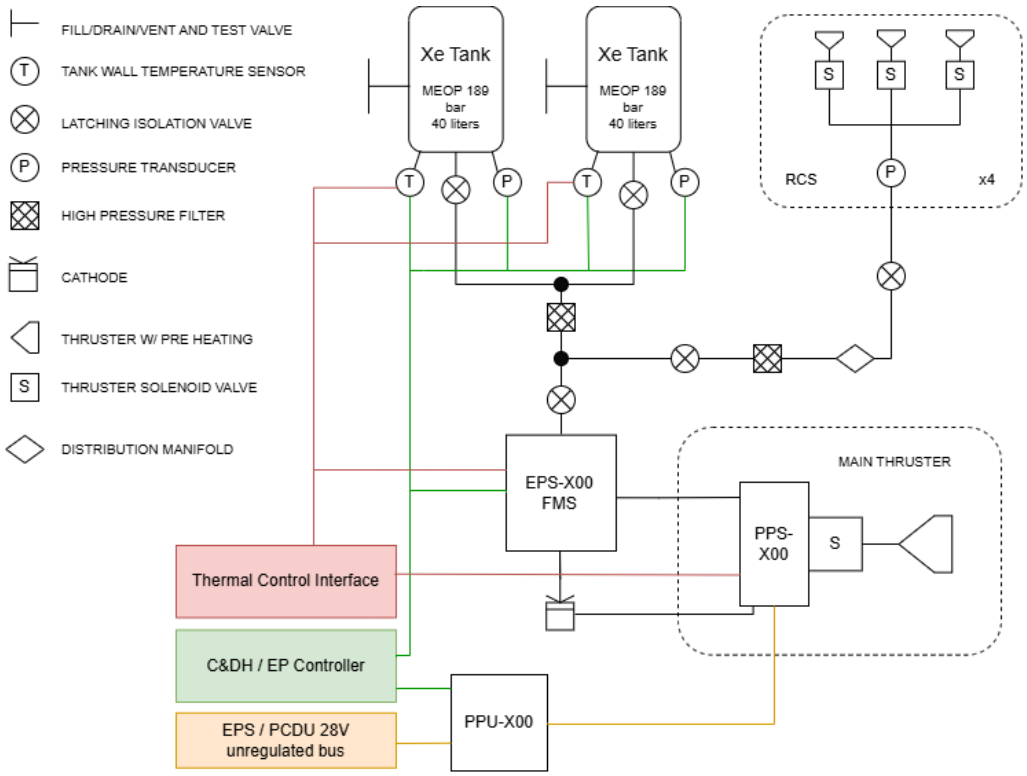

Figure 8.4: Schematic of the tug xenon feed system and electric-propulsion interfaces

Final verification shall confirm xenon tank compatibility, high-pressure leak tightness, RCS regulator stability, FMS inlet-pressure compatibility, valve cycle life, filtration rating, PPS-X00 anode/cathode flow split and electrical/thermal interfaces with the PPU, C&DH and TCS.

8.3. Verification of Propulsion Subsystem Requirements

This section will discuss all the propulsion subsystem requirements and their compliance (table 8.1). Furthermore, the verification procedures are discussed for selected requirements.

Table 8.1: Propulsion subsystem requirements and compliance

ID	Propulsion subsystem requirements	Parent Requirement	Method	Check
Mothership				
REQ-PSS-M1	The mothership propulsion system shall provide at least 1200 m/s of main-transfer ΔV for the selected worst-case campaign.	REQ-MIS-09, REQ-MIS-10	A	Yes
REQ-PSS-M2	The mothership main propulsion system shall have a nominal vacuum specific impulse of at least 250 s.	-	T	TBD
REQ-PSS-M3	The mothership main propulsion system shall provide a minimum translational acceleration of 0.050 m/s^2 in the maximum wet-mass configuration of 3750 kg across the nominal operating pressure range.	REQ-MIS-09, REQ-STK-01	T	TBD
REQ-PSS-M4	The mothership propulsion system shall include a main-transfer branch for orbit-transfer manoeuvres and an RCS/proximity branch for fine correction, docking support, wheel desaturation, retreat and abort manoeuvres.	-	I	Yes
REQ-PSS-M5	The mothership propulsion system shall be able to compensate for centre-of-gravity changes caused by propellant depletion, tank-drain imbalance and sequential tug deployment.	REQ-SYS-05	A	Yes
REQ-PSS-M6	The mothership propulsion system shall be able to perform a minimum of 50 engine start and shutdown cycles over one campaign.	-	T	TBD
REQ-PSS-M7	The mothership RCS/proximity branch shall perform commanded fine velocity corrections with an absolute residual error below 20 mm/s after trim manoeuvres.	REQ-MIS-12, REQ-MIS-13	T	TBD
REQ-PSS-M8	The mothership propulsion system shall use the non-toxic monopropellant LMP-103S and shall use propellant tanks, seals, filters, valves and feed-system materials compatible with LMP-103S.	REQ-STK-09	I	Yes

Continued on next page

Table8.1– continued from previous page

ID	Propulsion subsystem requirements	Parent Requirement	Verification	Compliance
Tugs				
REQ-PSS-T1	The tug electric propulsion system shall provide at least 600 m/s of ideal ΔV while attached to a 2000 kg debris object.	REQ-STK-15, REQ-MIS-09	A	Yes
REQ-PSS-T2	The tug electric propulsion system shall provide a minimum thrust of 0.060 N while transporting the tug–debris stack, to support completion of the worst-case campaign within one year.	REQ-STK-01, REQ-MIS-09	T	TBD
REQ-PSS-T3	The tug electric propulsion system shall have a nominal specific impulse of at least 1600 s at the selected operating point.	-	I	Yes
REQ-PSS-T4	The tug propulsion system shall be able to perform at least 10 start and shutdown cycles	REQ-MIS-09	T	TBD
REQ-PSS-T5	The tug propulsion system shall perform commanded velocity changes with an absolute residual error below 100 mm/s after correction manoeuvres.	REQ-SYS-07	T	TBD
REQ-PSS-T6	The tug propulsion system shall remain safely isolated and inactive while attached to the mothership and shall only be activated after deployment and propulsion health checks.	-	D	TBD
REQ-PSS-T7	The tug propulsion system shall use non-toxic xenon as propellant and shall use tankage, feed-system hardware, PPU interfaces and thruster components compatible with xenon operation.	REQ-STK-09	I	Yes
REQ-PSS-T8	The tug propulsion system shall provide sufficient attitude-control and reaction-wheel desaturation capability through a xenon cold-gas RCS branch.	-	T	TBD

For REQ-PSS-M2, REQ-PSS-M3, REQ-PSS-T2, and REQ-PSS-T8, compliance shall be determined by a static fire test. Compliance of REQ-PSS-M6 and REQ-PSS-T4 shall be determined by a start/shutdown cycle test. Compliance of REQ-PSS-M7 and REQ-PSS-T5 shall be determined by a closed-loop test. Finally, compliance of REQ-PSS-T6 shall be determined by a demonstration.

9. Structures

This chapter defines the structural design of the REAVER spacecraft and verifies its ability to withstand the main mechanical and environmental loads. The design follows the European Cooperation for Space Standardization (ECSS) structural standards for spacecraft structures and structural factors of safety [20, 89]. The objective is to establish a feasible baseline structure for the mothership and tugs.

The chapter first defines the launch vehicle, kick-stage interface, payload fairing constraints, and mechanical attachment assumptions. It then identifies the main load cases, selects the structural materials, and includes radiation shielding considerations for the geostationary orbit (GEO) environment. Finally, the primary truss is checked for static strength, buckling, and natural frequency requirements, before estimating the structural mass budget and verifying the subsystem requirements [71].

9.1. Launch Vehicle Characteristics and Interface

This section aims to make a selection for both the launch vehicle and kick stage, which are responsible for inserting the REAVER spacecraft into the Recycling hub orbit located on the outer edges of the GEO graveyard orbit.

Launch Vehicle

The REAVER spacecraft will be launched on a SpaceX Falcon 9 Block 5 launch vehicle. This selection is driven primarily by cost and performance considerations. With a launch price of around 74 M€ and a payload capacity to GTO of 8300 kg [90], the Falcon 9 provides a large mass margin over the REAVER launch mass of approximately 4000 kg, while remaining within the mission budget of 200 M€.

Kickstage

The Falcon 9 is only capable of delivering a payload to GTO rather than directly to GEO. For this reason, a dedicated kick stage is required to perform the GTO-to-GEO transfer, delivering the spacecraft stack to the Recycling Hub operational orbit at 36 500 km altitude, corresponding to a semi-major axis of approximately 42 800 km. To estimate the required delta-v for this transfer, the vis-viva equation is applied at the apogee of the GTO orbit, where the kick stage burn is performed. The GTO is characterised by a perigee altitude of 185 km and an apogee altitude of 35 786 km, giving a semi-major axis of $a_{\mathrm{GTO}} = 24\,371$ km. Using equation (3.1) and equation (3.3), which can be used to determine the orbital velocities at GTO apogee and GEO, the resulting delta-v required for the circularization burn at apogee can be computed using equation (9.1), where the standard gravitational parameter $\mu \approx 398\,600.44\,\mathrm{km}^3\,\mathrm{s}^{-2}$ and the apogee radius $r_{apo} \approx 42\,164$ km.

$$\Delta v_{\mathrm{req}} = v_{\mathrm{GEO}} - v_{\mathrm{GTO,apo}} \tag{9.1}$$

Plugging in the values gives $v_{\mathrm{req}} = 1478\,\mathrm{m\,s}^{-1}$. In order to account for injection dispersions and orbit raising losses it is rounded conservatively to $1500\,\mathrm{m\,s}^{-1}$.

Based on these calculations, the Northrop Grumman Star-63D kick stage is selected. It has a total propellant mass of approximately 3250 kg, total dry mass of approximately 250 kg, and a vacuum specific impulse of 314 s [91]. To confirm that it is indeed capable of inserting the REAVER spacecraft into the correct orbit, a preliminary verification is performed using the rocket equation, where 7500 kg is the total initial mass of the combined REAVER spacecraft and kick stage mass, and $m_f = m_{\mathrm{dry,stage}} + m_{\mathrm{payload}} = 4250$ kg is the final mass after burnout. Applying equation (3.11) yields a ΔV of approximately $1750\,\mathrm{m\,s}^{-1}$, exceeding the design requirement of $1500\,\mathrm{m\,s}^{-1}$ by a margin of around $250\,\mathrm{m\,s}^{-1}$. This margin is sufficient to accommodate for launch vehicle injection dispersions and insertion conditions. Additionally, the total integrated launch mass of 7500 kg complies with the Falcon 9 GTO payload capacity.

Payload Fairing and Spacecraft Integration

The payload that is integrated within the Falcon 9 needs to comply with the limiting dimensions of its fairing. It is equipped with a standard payload fairing of 5.2 m diameter which is available in both standard and extended configurations [90]. SpaceX also provides a mechanical interface between the payload and the launch vehicle through a standard payload attach fitting (PAF). The guide defines three standard diameters for these attachments: 1575 mm, 2624 mm, and 3117 mm [90]. For a proper fit, the PAF should have a diameter larger

than the kick stage in order to be able to clamp it as intended. Since, the Star-63D kick stage has a diameter of 1600 mm[91] exceeding the 1575 mm option, the 2624 mm PAF is selected as the mechanical interface.

Finally, the total height of the REAVER launch stack, including the kick stage is determined. The total mothership height is 3.5 m and the Star-63D has a length of approximately 1.8 m [91]. Therefore, the total height of the combined system is approximately 5.3 m. According to the Falcon 9 guide, the standard fairing has a length of 13.2 m which leaves a margin of over 7 m [90]. This accounts for safety factors, the fairing wall thickness and other constraints that restrict the dimensional envelope allowed for the payload.

9.2. Load Cases

Having established the general configuration of the spacecraft and its launch vehicle, the load cases are identified across the full mission timeline. The purpose of this section is to characterise the structural load environment at different mission phases and subsequently identify the limit load cases carried forward into the structural analysis.

The primary structure of the Mothership consists of the main load-bearing truss, which carries the axial and lateral launch loads from the payload adapter interface through the spacecraft. This truss structure represents the critical load path of the spacecraft and is the primary sizing case for structural analysis. The secondary structures encompasse all non-primary load-bearing components, including equipment panels and shelves, subsystem mounting brackets, tank support fittings, the tug attachment interfaces, and the mechanical joints connecting secondary panels to the primary truss. Secondary components must nonetheless withstand the launch environment and remain functional throughout the mission lifetime. The distinction between primary and secondary structure is consistent with the definitions provided in [58].

The following load cases are informed by those mentioned within the ECSS-E-ST-32C [20] guidelines:

- **Ground and transportation loads:** Prior to launch, the spacecraft experiences quasi-static loading during transportation to the launch facility. The design transportation load envelope is estimated as $-1\ g$ to $+1.5\ g$ axially and $\pm 1.5\ g$ laterally [90].
- **Launch loads:** During ascent, the spacecraft is subject to quasi-static inertial loads, sinusoidal and random vibration, acoustic loading, and shock events at fairing separation and spacecraft release, as defined in the Falcon 9 Payload User's Guide [90]. Launch loads represent the primary sizing case for the REAVER primary structure and dominate all other load cases. Similarly the kick stage imposes quasi-static loads during the GTO-to-GEO burn and a separation shock at release. However, these are expected to be substantially lower than the Falcon 9 launch loads and are not considered a sizing case.
- **Rendezvous operations**: the mothership performs impulsive orbital manoeuvres between debris targets. The quasi-static loads associated with these burns are driven by the chemical propulsion systems maximum thrust level of approximately 64 N. Considering the maximum mass of the mothership and tugs configuration of 3750 kg, the accelerations are far below 1 g and are therefore negligible compared to launch loads.
- **Proximity operations**: the spacecraft may experience localised loads arising from attitude control manoeuvres, contact events, docking interactions, and mechanism actuation. Given the low-magnitude nature of proximity operations, these loads are not expected drive the sizing of the primary structures. However, they remain an important design consideration for secondary structures.
- **Thermal loads:** Thermal loads arise from the GEO thermal environment though their quantification is deferred to the thermal control subsystem to avoid repetition.

Limit Loads

As identified, the launch loads are the main drivers for structural sizing. A major requirement to comply with for launch is the specified minimum natural frequencies of 10 Hz laterally and 25 Hz axially for the primary structure, and 35 Hz for all secondary structures. The Falcon 9 guide specifies that this will minimise coupling with launch vehicle dynamics. The following loads are taken from for a payload mass ≥ 1800 kg:

Quasi-static Loads: The limit load envelope is $+6\ g$ to $-2\ g$ axially and $\pm 2\ g$ laterally, where negative axial values indicate tension and positive values indicate compression [90]. These loads are applied at the spacecraft centre of mass and are critical for the sizing of the main load bearing structure [92].

Sinusoidal Vibration: The predicted sinusoidal vibration frequency range is from 5 to 100 Hz with peak acceleration levels between 0.5 and 1 g depending on frequency and axis. Although the associated accelerations are lower than those of the quasi-static load case, sinusoidal vibration can result in significant dynamic

amplification. Therefore, these loads are particularly important for appendages, antennas, solar array supports, and equipment mounting brackets [90].

Acoustic Loading: The payload acoustic environment ranges from approximately 31.5 Hz to 10 000 Hz and reaches an overall sound pressure level (OASPL) of approximately 131.4 to 138 dB. Acoustic loading generates distributed pressure fluctuations across external spacecraft surfaces, resulting in local panel vibrations and secondary structural responses. While acoustic loads are generally not the primary sizing case for the spacecraft, they are important for lightweight structures with low mass, such as antennas, solar arrays, and side panels [92].

Shock Loads: Shock events occur at discrete moments such as stage separation, fairing deployment and spacecraft separation. The shock environment is specified using a Shock Response Spectrum (SRS) which reaches frequencies above 10 kHz. Peak responses can reach several hundred g at those high frequencies. Despite this, these loads occur over very short durations and at frequencies significantly higher than the primary structural modes of the spacecraft [90]. Therefore, shock loading is generally not a sizing case for the primary structure, but rather a design driver for sensitive equipment, electronic assemblies, and deployable mechanisms.

Random Vibration: Unlike sine vibration, random vibration excites a wide range of frequencies simultaneously and is often the dominant design driver for spacecraft equipment. The payload is exposed to a random vibration environment extending from approximately 20 Hz to 2000 Hz with a root mean square acceleration (GRMS) of 5.13 g [90].

Table 9.1: Summary of identified limit load cases

Load Type	Direction	Limit Value
Quasi-static		
Axial compression	Longitudinal	+6.0 g
Axial tension	Longitudinal	−2.0 g
Lateral	Transverse	±2.0 g
Dynamic		
Sine vibration	All axes	0.5 to 1.0 g at 5 to 100 Hz
Random vibration	All axes	5.13 g at 20 to 2000 Hz
Acoustic	External surfaces	131.4 to 138 dB OASPL
Shock (SRS)	All axes	Several hundred g above 10 kHz although negligible for structural components
Stiffness requirements		
Primary axial mode	Longitudinal	$f \geq 25$ Hz
Primary lateral mode	Transverse	$f \geq 10$ Hz
Secondary structures	All axes	$f \geq 35$ Hz

9.3. Material Characteristics

This section defines the material basis for the REAVER structural design. It first assesses the radiation environment in geostationary orbit (GEO) and sizes the aluminium shielding required for sensitive components. It then identifies candidate materials for primary and secondary structures, comparing their strength, stiffness, density, thermal behaviour, manufacturability, and spaceflight heritage. Finally, a weighted trade-off is used to select the baseline material for the mothership primary structure.

Radiation

The REAVER mission will operate in the GEO environment, located at or near the outer edge of the Van Allen Belt, and radiation effects must therefore be accounted for. According to Becker et al. [93], the total accumulated radiation dose in GEO can reach up to 50 krad (Si) per year. Without adequate shielding, this poses a danger to the selected EPS components over time, necessitating the use of radiation shielding panels. Aluminium is the industry standard for this purpose and was selected accordingly; beyond its shielding properties, aluminium is electrically conductive, allowing it to serve a dual purpose: mitigating electrostatic charging, a known concern in the GEO plasma environment where low plasma density causes charge to bleed off slowly and differential charging between surfaces can cause arcing.

To determine the required shielding thickness, the dose-depth curve for GEO provided by Buchner [63], given in figure 9.1, was used. The most radiation-sensitive components in the mothership were identified as originating

from the Command and Data Handling subsystem: the SCFE6933 (233 mm × 160 mm × 25.4 mm) and the cOBC (300 mm × 119 mm × 239 mm). For the tugs, the most radiation-sensitive component is the Bradford Space SuperNova PCDU (60 mm × 120 mm × 135 mm), present in each tug. For each of these components, the total surface area was computed to size the radiation shielding panels, though these calculations are left out for brevity. These surface areas were then summed to determine to total area of the panels, resulting in $A = 0.681\,\mathrm{m}^2$. After applying an additional margin of 1.2 to ensure all components fit in, the area becomes $A_{rad} = 0.8172\,\mathrm{m}^2$. To determine the thickness of the panel, the critical component which is able to withstand the smallest amount of radiation is to be identified; the most sensitive of these components is the COTS CubeSat OBCs, rated to withstand 10 krad [94]. From figure 9.1, the resulting shielding thickness is approximately 200 mils (5.08mm). It should be noted that this is the expected accumulated radiation over five years, whereas the REAVER mission will be one year, hence a substantial safety margin is provided. Using the density of Al 6061-T6 given in Table table 9.2, the total mass contribution from the radiation shielding panels is 11.21 kg, rounded upwards.

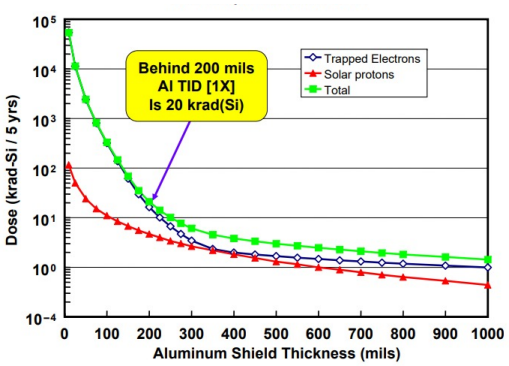

Figure 9.1: Dose-depth curve for geostationary orbit [63]

Material Identification

The selection of structural materials is a critical stage in the preliminary design of the REAVER spacecraft, as material properties directly influence structural mass, launch survivability, thermal stability, manufacturability, and long-term mission reliability. Based on the launch loads, frequency constraints, and the environmental conditions encountered in GEO, a range of candidate materials are identified for both primary and secondary structural applications. The objective of this stage is to establish a list of viable candidates possessing sufficient flight heritage and performance characteristics to satisfy the mission requirements. The candidate set was selected on the basis of established spaceflight heritage and suitability for the GEO environment.

For the primary structure, aluminium alloy Al-7075-T6 [1] is selected as the baseline candidate material due to its high strength-to-weight ratio, favourable stiffness, and extensive aerospace heritage. Its combination of mechanical performance and well-established manufacturing processes makes it well suited to carrying the launch-induced loads that dominate the structural sizing of the spacecraft [92]. Carbon fibre reinforced polymer (CFRP) in a quasi-isotropic laminate configuration is also considered as a candidate primary structural material. Compared with aluminium alloys, CFRP offers significantly higher specific stiffness and specific strength, providing the potential for structural mass reduction and improved compliance with launch vehicle frequency requirements [92]. However, its quasi-isotropic (Q-I) behaviour should be noted; by definition, CFRP is both stronger and stiffer along the fibre direction; consequently, its material properties vary depending on the axis along which the load is applied. The effective in-plane stiffness and strength used in table 9.2 is estimated via the QI approximation $E_{\mathrm{QI}} \approx \frac{3}{8}E_{11} + \frac{5}{8}E_{22}$, applied to the unidirectional lamina properties reported in [95].

For secondary structural applications, Al 6061-T6[2] is considered for equipment panels, subsystem mounting structures, and internal support members due to its favorable manufacturability, and widespread use in spacecraft structures [92]. Titanium alloy Ti-6Al-4V[3] is included for highly loaded local structures such as brackets, fittings, and interface components where high strength, fatigue resistance, and durability are required [92]. Furthermore, titanium is commonly used in conjunction with composite structures due to its favourable compatibility with CFRP interfaces. Finally, Invar 36[4] is considered for thermally sensitive secondary structures requiring exceptional dimensional stability. Its extremely low coefficient of thermal expansion makes it suitable for precision mounting applications where thermal distortions must be minimised over the GEO thermal

[1] https://www.matweb.com/search/DataSheet.aspx?MatGUID=4f19a42be94546b686bbf43f79c51b7d [accessed 10 June 2026]
[2] https://www.matweb.com/search/DataSheet.aspx?MatGUID=b8d536e0b9b54bd7b69e4124d8f1d20a [accessed 10 June 2026]
[3] https://www.matweb.com/search/DataSheet.aspx?MatGUID=a0655d261898456b958e5f825ae85390 [accessed 10 June 2026]
[4] https://www.matweb.com/search/datasheet.aspx?MatGUID=cbca9060763c4079b1b6768933881936 [accessed 10 June 2026]

environment.

For the design of the primary structure, only Al 7075-T6 and CFRP are considered for the following reasons: The titanium alloy would be significantly more expensive and harder to manufacture. Second, as discussed earlier, Invar is only considered due to its extremely low CTE, which makes it well suited for secondary structures, it is also very heavy and wouldn't be suitable for the primary structure. Lastly, Al 6061-T6 was excluded as Al 7075-T6 provides more favorable material characteristics, with the exception of a slightly larger density.

Table 9.2: Material properties used in the preliminary structural material trade study

Material	Density ($kg\,m^{-3}$)	Young's Modulus (GPa)	Ultimate Strength (MPa)	Specific Stiffness ($MN\,m\,kg^{-1}$)	Specific Strength ($kN\,m\,kg^{-1}$)	CTE ($\mu m\,m^{-1}\,°C^{-1}$)
Al 6061-T6	2700	69	310	25.6	115	23.6
Al 7075-T6	2800	72	572	25.6	180	21.6
CFRP (Q-I) [95]	1570	69	600	44.0	382	2-3
Ti-6Al-4V	4430	114	950	25.7	214	8.6
Invar 36	8055	141	490	17.5	61	1.3

Material Selection

The material trade study evaluates the primary structure candidates identified in table 9.2 against criteria derived from the structural requirements and mission environment established in the preceding sections. Four criteria are identified and weighted as follows.

Specific Stiffness (E/ρ) is assigned the highest weight of 0.35, as the launch vibration environment, particularly random vibration and the minimum natural frequency requirements, represents the primary structural design driver.
Specific Strength (σ_u/ρ) is weighted at 0.25; although both candidates exhibit high strength levels, specific strength determines the structural efficiency of the primary truss structure under axial compression and lateral loading and therefore remains a significant criterion.
Structural Compatibility is assigned a weight of 0.20. This criterion captures the complexity of integrating the material into a truss structure. The reliability of a primary truss structure is highly dependent on its joints and the interface between structural members.
Cost and Sustainability are combined into a single criterion weighted at 0.20. This criterion reflects the missions constrained budget as well as its emphasis on the possibility for end-of-life recyclability.

No formal trade study is conducted for secondary structural components, as these do not form part of the primary load path and their material selection does not influence the structural analysis at this design stage. All candidates are scored on a scale of 1 to 5, where 5 represents the most favourable performance. Weighted scores are summed to obtain a total for each candidate, with weights reflecting the mission priorities.

Table 9.3: Weighted trade matrix for primary structural material selection

Criterion	Weight	Al 7075-T6	CFRP (Q-I)
Specific stiffness (E/ρ)	0.35	3	5
Specific strength (σ_u/ρ)	0.25	4	5
Structural compatibility	0.20	5	2
Cost and sustainability	0.20	5	3
Weighted total		**4.05**	**4.00**

Al 7075-T6 achieves the highest weighted score of 4.05. Although CFRP offers superior specific stiffness and strength, its structural compatibility penalty at metallic joints is particularly significant for the REAVER truss, which has a large number of nodes which would require a bonded interface if CFRP is used. In the GEO environment, where repair is not possible, the inspectability and reliability of bonded joints is a greater design risk than the mass penalty of aluminium. Accordingly, Al 7075-T6 is selected as the primary structural material and is carried forward into the structural analysis. It is noted that a CFRP design would offer potential mass savings of 30–40% at the cost of substantially higher interface complexity and manufacturing risk.

9.4. Structural Analysis

In this section, a structural analysis will be conducted on the mothership's primary load-bearing structure. The design loads used throughout the section are derived from the limit loads established earlier by applying yield and ultimate factors of safety (FOSY and FOSU). For an unmanned satellite, ECSS-E-ST-32-10C specifies FOSY = 1.1 and FOSU = 1.25 for metallic structural parts verified by test. For buckling assessed by analysis only, $\text{FOSU}_{\text{buck}} = 2.0$ is specified [89]. The resulting design loads are summarized in table 9.4.

Table 9.4: Design yield and ultimate loads

Load Case	Limit Load [g]	FOSY	Yield factor [g]	Ultimate factor [g]
Axial compression	+6.0	1.1	+6.6	+7.5
Axial tension	−2.0	1.1	−2.2	−2.5
Lateral	±2.0	1.1	±2.2	±2.5

Load-bearing Structure

The primary structure of the mothership is an octagonal truss split into three separate bays with a total structural height $L = 3.5\,\text{m}$, illustrated in figure 9.2. The structure is composed of Al 7075-T6 truss members assumed to be cylindrical and hollow. The heights of the bays are; $L_1 = 1.5\,\text{m}$, $L_2 = 1\,\text{m}$ and $L_3 = 0.5\,\text{m}$ respectively. For this analysis, the entire structure will be considered as if it consists of eight hollow cylinders along the full 3.5 m. This is a conservative assumption, as the second bay contains twelve cylinders and thus a better structural performance.

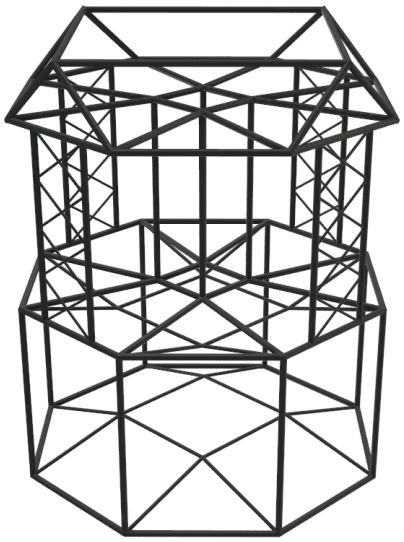

Figure 9.2: CAD model of primary load bearing structure

Moreover, the horizontal and diagonal bracing members (the webs inside the structure) are neglected. This too is a conservative assumption, as including them would increase both I_{eq} and the estimated natural frequencies. Lastly, the truss structure is simplified to a single beam (this is known as an equivalent beam-column idealisation, or substitute beam model); the equivalent cross-sectional properties are computed by applying the parallel axis theorem to the eight chord members located at the corners. The cross-sectional geometry is defined by a circumradius $R = 1.5\,\text{m}$ and an angle $\theta = (i-1)\frac{\pi}{4}^\circ$ from the neutral axis to any member of the chord i. Additionally, there are $n = 8$ chord members each with their own cross-sectional area A_m. For the idealized section, the equivalent second moment of area about any centroidal axis is computed as equation (9.2), where $y_i = R\sin\theta_i$ are the perpendicular distances of each chord from the neutral axis.

$$I_{\text{eq}} = \sum_{i=1}^{8}\left(I_m + A_m y_i^2\right) = 8I_m + A_m\sum_{i=1}^{8} y_i^2 \tag{9.2}$$

Evaluating the summation gives the following:

$$\sum_{i=1}^{8} y_i^2 = R^2 \sum_{i=1}^{8} \sin^2\left(\frac{(i-1)\pi}{4}\right) = 4R^2$$

Since I_m is naturally very small compared to the other terms in equation (9.2), it is neglected throughout the analysis ($I_{\text{eq}} \approx 4A_m R^2$). The equivalent axial stiffness area is simply $A_{\text{eq}} = 8A_m$. Finally, the individual member cross-sectional properties are given by equation (9.3).

$$A_m = \frac{\pi}{4}\left(d^2 - (d - 2t_w)^2\right), \qquad I_m = \frac{\pi}{64}\left(d^4 - (d - 2t_w)^4\right) \tag{9.3}$$

The thickness t_w and diameter d that truss members require to withstand the launch loads are be derived in the upcoming sections. This is done by first computing the minimum area A_m and the minimum second moment of inertia I_m for the static, dynamic, and buckling case. The goal is to identify the limiting case and use it to size the individual members.

Static Analysis

The worst-case structural load case is combined axial compression and lateral loading applied simultaneously at the spacecraft centre of mass, assumed at $h_{CG} = 1.5\,\text{m}$ above the mothership-kickstage interface. The spacecraft mass used for static analysis is the fully loaded mothership with five tugs. A preliminary conservative value of $m = 4000\,\text{kg}$ is selected for the analysis. The resulting applied forces follow from equation (9.4) where $g_0 = 9.81\,\text{m s}^{-2}$ and both a_z as well as a_y are axial and lateral yield loading factors from table 9.4.

$$F_{axial} = a_z \cdot m \cdot g_0 \quad F_{lat} = a_y \cdot m \cdot g_0 \tag{9.4}$$

The applied forces are therefore $F_{axial} = 258.9\,\text{kN}$ and $F_{lat} = 86.3\,\text{kN}$. The bending moment at the base of the mothership is computed using equation (9.5), which gives $M_{base} = 129.5\,\text{kN m}$.

$$M_{base} = F_{lat} \cdot h_{CG} \tag{9.5}$$

The maximum compressive stress occurs at the base of the equivalent beam-column ($z = 0$), and is given by equation (9.6).

$$\sigma_{\max} = \frac{F_{\text{axial}}}{A_{\text{eq}}} + \frac{M_{\text{base}} \cdot R}{I_{\text{eq}}} \tag{9.6}$$

Substituting the equivalent section relations $A_{\text{eq}} = 8A_m$ and $I_{\text{eq}} = 4A_m R^2$ from equation (9.2), this can be rewritten as equation (9.7). Then, setting $\sigma_{\max} = \sigma_{\text{yield}}$ allows to solve for the minimum chord member area required to satisfy the strength constraint, with $\sigma_{yield} = 503\,\text{MPa}$, a minimum individual member area of $A_{m,\min} = 1.0726 \times 10^{-4}\,\text{m}^2$ is obtained. From this, the corresponding minimum equivalent second moment of area of the entire structure is computed using equation (9.2) resulting in $I_{eq} = 9.65 \times 10^{-4}\,\text{m}^4$.

$$\sigma_{\max} = \frac{F_{\text{axial}}}{8A_m} + \frac{M_{\text{base}} \cdot R}{4A_m R^2} = \frac{1}{A_m}\left(\frac{F_{\text{axial}}}{8} + \frac{M_{\text{base}}}{4R}\right) \quad A_{m,\min} = \frac{1}{\sigma_{\text{yield}}}\left(\frac{F_{\text{axial}}}{8} + \frac{M_{\text{base}}}{4R}\right) \tag{9.7}$$

Buckling Analysis

For this analysis, instead of the simplified single beam, buckling analysis will be performed for one hollow cylinder, modelled as an Euler column under axial compression. The cross-sectional properties can then be computed using Euler's Formula for the critical buckling load (equation (9.8)), where E is the elastic modulus and $L_e = K \cdot L$ is the effective column length. The factor K is determined from the boundary condition; since the mothership is attached to the PAF through a rigid bolted interface, the lower boundary condition is assumed to be fixed. The upper end of the bay is connected to a ring frame, which is assumed to provide translational restraint while allowing rotation. Consequently, the member is modelled as a fixed-pinned column, resulting in an effective length factor of $K = 0.7$ [96]. The column length is simply the spacecraft length which is 3.5 m, giving $L_e = 0.7 \times 3.5 = 2.45\,\text{m}$.

$$P_{cr} = \frac{\pi^2 EI}{L_e^2} \tag{9.8}$$

Now, the critical buckling load is the superposition of the direct axial load and the bending-induced axial force due to lateral loading is shown in equation (9.11), where $n = 8$, since the load is divided over eight columns.

$$P_{\text{direct}} = \frac{F_{\text{axial}}}{n} \tag{9.9}$$

$$P_{\text{bending}} = \frac{2M_{\text{base}}}{n \cdot R} \tag{9.10}$$

$$P_{\text{member}} = P_{\text{direct}} + P_{\text{bending}} \tag{9.11}$$

The resulting loads are $P_{\text{direct}} = 32\,373\,\text{N}$, $P_{\text{bending}} = 21\,582\,\text{N}$ and $P_{\text{member}} = 53\,955\,\text{N}$. As Euler buckling is a limit state requirement, a FoS of 2 is applied [89], resulting in the ultimate design buckling load $P = 107\,910\,\text{N}$. The minimum second moment of area per individual cylinder required to prevent global buckling is found by rearranging equation (9.8) resulting in equation (9.12).

$$I_{\text{member, min}} = \frac{P \cdot L_e^2}{\pi^2 \cdot E} \tag{9.12}$$

This yields = $I_{\text{member, min}} \approx 9.116 \times 10^{-7}\,\text{m}^4$. This is the minimum second moment of area per cylinder required to prevent global Euler buckling under the combined load case [97].

Dynamic Analysis

Compliance with the Falcon 9 minimum natural frequency requirements (lateral $\geq 10\,\text{Hz}$, axial $\geq 25\,\text{Hz}$) is verified using simplified analytical models. The mass used for frequency estimation is the payload mass at launch conservatively rounded up to $m = 4000\,\text{kg}$, as natural frequencies are assessed for total spacecraft mass at launch.

First Lateral Natural Frequency: The primary structure is modelled as a uniform cantilever beam, fixed at the mothership's interface with the kickstage. Additionally, the full structural height $L = 3.5\,\text{m}$, including all three bays, is used as the cantilever length for frequency estimation (equation (9.13)). The equivalent section properties of the lower bay are applied conservatively across the full height.

$$f_{\text{lat}} = \frac{1}{2\pi}\sqrt{\frac{3EI_{\text{eq}}}{mL^3}} \tag{9.13}$$

Applying the required minimum natural frequencies, the corresponding minimum equivalent second moment of area for the equivalent section is found: $I_{\text{eq, min}} = 2.569\,492\,55 \times 10^{-4}\,\text{m}^4$. Using equation (9.2), a minimum required area per member of $A_m = 2.586 \times 10^{-6}\,\text{m}^2$ is found.

First Axial Natural Frequency: The primary structure is modelled as a lumped mass on an equivalent axial spring (equation (9.14)). By substituting the equivalent section relation $A_{eq} = 8A_m$, equation (9.14) can be rewritten as equation (9.15).

$$f_{ax} = \frac{1}{2\pi}\sqrt{\frac{EA_{\text{eq}}}{mL}} \tag{9.14}$$

$$A_m = \frac{(f_{ax}2\pi)^2 mL}{8E} \tag{9.15}$$

Applying the required minimum natural frequencies, the minimum area of the equivalent section is found to be $A_m \geq 6.022 \times 10^{-4}\,\text{m}^2$.

Truss Sizing

The objective is to minimize the mass of the members, while still complying with the structural determined in the previous sections. The mass can straightforwardly be computed using equation (9.16), where ρ is the density of AL 7075-T6 from table 9.2.

$$m = \rho \cdot A_m \cdot L \tag{9.16}$$

As Euler buckling was identified to be the limiting load case, the theoretical lower bound on the member properties is given by equation (9.17), yielding $I_m = 9.116 \times 10^{-7}\,\mathrm{m}^4$.

$$I_m = \frac{\pi}{64}\left(d^4 - (2t_w)^4\right) \tag{9.17}$$

The cross-sectional area increases with both diameter and wall thickness. For a fixed area, a larger diameter combined with a thinner wall provides greater bending efficiency; however, excessively thin walls increase the risk of local wall buckling. In the present configuration, bending is not the primary design driver, as the members are distributed around the perimeter of the cross-section.

The selected member dimensions are therefore $d = 90\,\mathrm{mm}$ and $t_w = 4\,\mathrm{mm}$. This combination provides a comfortable structural margin, sufficient wall thickness for fastener integration, and straightforward manufacturability. Finally, all structural checks are summarised in table 9.5.

Table 9.5: Margin of Safety summary for primary truss members ($d = 90\,\mathrm{mm}$, $t_w = 4\,\mathrm{mm}$)

Check	Applied	Allowable	FoS	MoS
Static strength	49.9 MPa	503 MPa	1.1	+8.16
Chord buckling (Euler)	54.0 kN	$P_{\mathrm{cr}} = 118.5\,\mathrm{kN}$	2.0	+0.10
Lateral frequency	17.6 Hz	$\geq 10\,\mathrm{Hz}$	—	7.6 Hz
Axial frequency	33.6 Hz	$\geq 25\,\mathrm{Hz}$	—	8.6 Hz

This confirms the successful performance of the selected dimensions for the truss members of the mothership's primary structure under the identified limit loads.

9.5. Capture Mechanism Structural Analysis

Since both the robotic arm and AEP mechanism are subjected to significant forces during the capture sequence, especially detumbling structural analysis needs to be performed to validate that the subsystem will be able to perform the capture. The main load cases that need to be considered for the robotic arm are bending and torsion while for the AEP mechanism bending and tension are key.

Since all the loads during capture are produced by either AOCS components or the motors driving the mechanism the forces can be easily calculated. The absolute maximum possible bending and torsional loads are created when 8 RCS thrusters fire to detumble the spacecraft and the total torque on the mothership from the manoeuvre can be calculated according to equation (9.18), where $n = 8$, and $d_{thruster}$ is equal to the distance between 2 opposite thrusters (3 m), resulting in 96 N m.

$$T = F_{thruster} \cdot d_{thruster} \cdot n \tag{9.18}$$

If we apply this torque on the 17.5 cm diameter CFRP robotic arm we can calculate the theoretical thickness needed to withstand the torsional load, leading to a minimum thickness of only 0.05 mm which is clearly too little to meaningfully affect the design.

$$t = \frac{T}{2\pi r^2 \tau_{allow}} \tag{9.19}$$

The bending loads for the robotic arm and AEP mechanism are calculated according to the following properties presented in table 9.6. The thicknesses for the respective segments were chosen based off of practical and manufacturing constraints. Quasi-isotropic CFRP is chosen for the robotic arm and AEP shaft because of high strength to weight and 17-4 PH Steel is chosen for the tip since it has the highest strength to volume ratio.

Table 9.6: Component specifications and loading conditions

Component	L (m)	d (mm)	t (mm)	Material	FOS	Load (Nm)
Robotic arm	4.627	175	2	CFRP (Q-I)	1.25	96 N m
AEP shaft	0.65	65	2	CFRP (Q-I)	1.25	96 N m
AEP tip	0.15	15	5	17-4 PH Steel	1.1	96 N m

The maximum bending stress and deflection of the respective segments are calculated according to equation (9.20) and equation (9.21) respectively.

$$\sigma_{max} = \frac{Td}{2I} \tag{9.20}$$

$$\delta_{max} = \frac{TL^2}{2EI} \tag{9.21}$$

The results of the calculations are summarized in table 9.7. As can be seen, the maximum stress in the worst possible case scenario is always significantly lower than the stress required for structural failure. Maximum deflection values are also very small. It should also be noted that a manoeuvre like this with the robotic arm fully extended would never be performed and these calculations are only meant to provide an absolute upper bound for the capture mechanism structural characteristics.

Table 9.7: Maximum bending stress, deflection, and material limits

Component	σ_{max} (MPa)	δ_{max} (mm)	Stress Limit (MPa)
Robotic arm	2.07	5.05	600 (Ultimate)
AEP shaft	15.87	2.06	600 (Ultimate)
AEP tip	293.35	2.25	1000 (Yield)

To calculate the axial loads on the AEP mechanism during retraction the specification of the selected lead screw can be analysed to determine the load. The axial force generated by the lead screw motor can be calculated according to equation (9.22), by plugging in values obtained from [98] a value of 12 840 N was obtained, where l is the screw lead and T is the servo motor torque.

$$F = \frac{2\pi T}{l} \tag{9.22}$$

The stress on the AEP tip and shaft can be calculated according to equation (9.23). By calculating the corresponding cross-section areas the stresses on the tip and shaft are found to be 81.74, and 27.26 MPa, respectively which are also well below the maximum allowable stresses for the components.

$$\sigma = \frac{F}{A} \tag{9.23}$$

From this analysis it is concluded that both the robotic arm and capture mechanism design are structurally sound and primarily driven by practical and manufacturing constraints and not loading.

9.6. Structures Mass Budget

This section presents the mass budget for the structures subsystem, distinguishing between the primary load-bearing structure, sized in section 9.4, and the secondary structure, which comprises all remaining structural hardware including diagonal and horizontal bracing members, node fittings, equipment mounting brackets, tank support fittings, tug attachment interfaces, solar array deployment mechanisms, and fasteners. The mass allocated to radiation shielding panels is treated separately, as it is driven by the radiation environment rather than structural loads, and is established in section 9.3.

Total Structural Mass Budget

The structural mass budget for the mothership and tugs is estimated using statistical relations derived from historical spacecraft data. Two separate relations are applied, reflecting the architectural differences between the two vehicle types. For the mothership, the statistical approach described in SMAD [71] for GEO spacecraft is applied, relating structural mass to dry mass for a spacecraft of comparable complexity. This yields an allocation of 24 % of the mothership dry mass. For the tugs, a lower structural fraction of 15 % of dry mass is applied, consistent with the statistical range of 10 to 15 % reported by [99] for smaller, simpler spacecraft with fewer secondary structural requirements. The mothership carries a complex primary truss, a larger number of secondary structural components, and substantially greater overall subsystem mass than the tugs, making the difference between the two appropriate.

Applying these fractions to the current dry mass estimates of $m_{\text{dry,MS}} = 956\,\text{kg}$ and $m_{\text{dry,tug}} = 221\,\text{kg}$ gives equation (9.24). This results in a total structural mass of $m_{\text{structures}} = 395.19\,\text{kg}$.

$$m_{\text{structures}} = (0.24 \cdot m_{\text{dry,MS}}) + 5 \cdot (0.15 \cdot m_{\text{dry,tug}}) \tag{9.24}$$

Primary Structure

The primary load-bearing structure of the mothership is an octagonal truss composed of eight hollow cylindrical chord members of Al 7075-T6, spanning a total structural height of $L_{\text{tot}} = 3.5\,\text{m}$. The member mass follows directly from equation (9.25).

$$m_{\text{prim,MS}} = 8 \cdot \rho \cdot A_m \cdot L_{\text{tot}} \tag{9.25}$$

With the selected member dimensions of $d = 90\,\text{mm}$ outer diameter and $t_w = 4\,\text{mm}$ wall thickness, giving $A_m = 1.081 \times 10^{-3}\,\text{m}^2$, and using $\rho = 2800\,\text{kg m}^{-3}$ for Al 7075-T6 from table 9.2, the mothership chord-members' mass is 84.727 kg.

The same cylindrical cross-section is adopted for the tug primary structure. Each tug has a rectangular configuration with four corner chord members spanning the full tug height of 1.2 m. Applying equation (9.25) to the five tugs combined yields a total tug primary structural mass of 72.624 kg.

The combined primary structural mass of the mothership and five tugs is therefore 157.351 kg. This figure accounts only for the chord members and explicitly excludes horizontal and diagonal bracing members, node fittings, and interface hardware. To account for these elements, a 30 % margin is applied, giving a final primary structure mass of $m_{\text{prim}} = 1.30 \cdot 157.351 = 204.556\,\text{kg}$.

Secondary Structure

The secondary structure mass is obtained by subtracting the primary structure mass and the radiation panel mass from the total structural mass budget as seen in equation (9.26), where $m_{\text{rad}} = 11.21\,\text{kg}$ is the radiation shielding panel mass derived in section 9.3. This results in a secondary structural mass of $m_{\text{sec}} = 179.424\,\text{kg}$.

$$m_{\text{sec}} = m_{\text{structures}} - m_{\text{prim}} - m_{\text{rad}} \tag{9.26}$$

9.7. Verification of Structures Subsystem Requirements

The structures subsystem requirements are listed in table 11.3.

Table 9.8: Structures subsystem requirements, and requirement IDs

ID	Structures Subsystem Requirement	Parent Requirement	Method	Check
Mothership				
REQ-STC-M1	The mothership structure shall facilitate integration of all other mothership subsystems.	-	D	YES
Tugs				
REQ-STC-T1	The tug structure shall facilitate integration of all other tug subsystems.	-	D	YES
Universal				
REQ-STC-U1	The spacecraft structure shall fit within the payload fairing volume envelope of the selected launch vehicle.	REQ-SYS-12	D	YES
REQ-STC-U2	The structures subsystem shall endure a **6 g** longitudinal load factor during launch.	REQ-SYS-12	T	YES
REQ-STC-U3	The structures subsystem shall endure a **2 g** lateral load factor during launch.	REQ-SYS-12	T	YES
REQ-STC-U4	The structures subsystem shall withstand the launch-induced vibrations	REQ-SYS-12	T	YES
REQ-STC-U5	The structures subsystem shall withstand the launch-induced acoustic loads.	REQ-SYS-12	T	TBD
REQ-STC-U6	The structures subsystem shall survive impacts from debris smaller than **TBD** m in diameter.	REQ-SYS-11, REQ-STK-22	A	TBD

Compliance of REQ-STC-U2 and REQ-STC-U3 shall be determined by a load test. REQ-STC-U5 compliance shall be determined by a vibration test. REQ-STC-U6 also remains open as the debris impact survivability has not yet been defined.

10. Thermal Control Subsystem

The Thermal Control Subsystem (TCS) for the REAVER mission maintains thermally critical components within their allowable operating and survival temperature ranges throughout the mission. Its main functions are to reject heat from avionics, AOCS, payload sensors and propulsion electronics; protect propellant and feed systems from excessive cooling or heating; maintain battery temperatures during eclipse and low-power modes; thermally isolate hot thruster interfaces; and account for thermal disturbances caused by proximity to captured debris [21].

The design follows a passive-first philosophy. Passive elements such as radiators, MLI, thermal coatings, conductive panels, thermal straps and thermal isolation are sized first [100]. Active heaters are only added where passive control cannot maintain the required lower temperature limits, mainly during eclipse, standby and safe mode. No pumped loops, cryo-coolers, louvers or deployable radiators are included at this stage to minimise mass, power and complexity [100].

This chapter presents the entire detailed design process for this subsystem, reevaluating its requirements, identifying the thermal cases and heat-load drivers, in order to size the TCS for the mothership and separately for the tugs. At the end, additional debris proximity thermal effects are discussed, along with limitations, verification, and validation procedures.

Thermal Design Cases and Heat-Load Drivers

The TCS requirements are refined from the midterm [38] to reflect the selected spacecraft architecture and the thermal limits of the chosen subsystem components. Instead of defining a separate requirement for each component, the requirements are grouped by spacecraft element and thermal function. This keeps the requirement set concise while still ensuring that the main thermal design drivers are covered. The resulting TCS requirements are listed in table 10.6. These requirements are supported by a reduced set of driving thermal design limits, shown in table 10.1.

Table 10.1: Driving thermal limits used for preliminary TCS sizing

Thermal zone / interface	Design range	Sizing relevance
Propellant and feed-system bay	10 °C to 50 °C	Drives MS LMP-103S MLI and heater sizing.
Battery and regulated equipment bay	0 °C to 45 °C	Drives battery and regulator cold-case heater sizing.
Avionics and communications bay	−20 °C to 60 °C	Used for OBC, TT&C, C&DH and general electronics.
Payload and precision sensor bay	−10 °C to 40 °C	Drives payload/sensor thermal control during capture.
Tug electric-propulsion bay	−20 °C to 75 °C	Drives tug EP radiator sizing.
Thruster interfaces	Local isolation required	Not treated as a normal equipment bay; requires stand-offs/shielding.
Passive external equipment	Survival check only	Passive antennas, passive sun sensors and external hardware have wide thermal ranges and are not expected to drive TCS sizing.

The thermal design cases are derived from the REAVER mission phases and subsystem power budgets. For spacecraft in orbit, the temperature of each component is driven by the balance between absorbed external heat, internally generated heat, stored heat and dissipated heat [1]. Therefore, the TCS must be checked in both high-dissipation hot cases and low-power cold cases. In GEO, eclipse seasons are also relevant, since geostationary spacecraft can rely on battery power for up to approximately 72 minutes per day during eclipse periods [21].

The main hot case for the mothership occurs during proximity operations and capture, because AOCS, avionics, payload sensors and propulsion support equipment are active at the same time. The main cold cases occur

[1] https://www.ospo.noaa.gov/operations/goes/eclipse.html [accessed 11 June 2026]

during safe mode, standby and eclipse, where internal heat generation may be insufficient to maintain the battery, propellant and feed-system temperatures. For the tugs, the dominant hot case occurs during electric-propulsion thrusting, while the dominant cold case occurs during safe mode or standby, analogous to the mothership. The corresponding heat-load drivers are summarised in table 10.2, these values sum up the power consumptions for all the components selected.

Table 10.2: Main heat-load drivers used for preliminary TCS sizing

Mission mode	Mothership power incl. margin	Tug power incl. margin
Safe mode	230 W	110 W
Communication	230 W	110 W
Long-range rendezvous / EP thrusting	485 W	1550 W
Proximity operations	1450 W	135 W
Capture / attachment	1315 W	210 W
Standby	235 W	110 W
Peak power	3655 W	2235 W

For most electronics, the consumed electrical power is conservatively assumed to be dissipated as heat inside the spacecraft. For electric propulsion, however, only the PPU/FMS losses and conducted heat from the propulsion system are treated as radiator loads, since part of the input power leaves the spacecraft through the thruster plume [21]. This is important for the tug, where the EP thrusting mode dominates the electrical power budget but only the waste heat is the one which sizes the radiator.

10.1. Sizing Assumptions and Equations

The preliminary TCS sizing is based on first-order steady-state heat balances, following ECSS thermal-control practice [21]. The assumptions used for the first-order sizing are summarised in table 10.3.

Table 10.3: Main assumptions used for preliminary TCS sizing

Assumption	Value used	Source / basis
Radiator heat-rejection model	Stefan–Boltzmann radiation balance	Standard spacecraft radiation balance; radiators reject heat to space through high-emissivity surfaces [100].
Reference radiator temperature	$T_{rad} = 317\,\mathrm{K}$	GEO radiator reference case [101].
Deep-space sink temperature	$T_{space} = 3\,\mathrm{K}$	GEO radiator reference case [101].
Radiator infrared emissivity	$\epsilon_{rad} = 0.8$	GEO radiator reference case [101].
Radiator solar absorptivity	$\alpha_{rad} = 0.2$	Conservative value; AZ-93 has low solar absorptance and high thermal emittance [2].
Solar flux	$S = 1371\,\mathrm{W\,m^{-2}}$	GEO radiator reference case [101].
Solar incidence correction	$\beta = 23.4°$	GEO North/South radiator illumination correction [101].
Net radiator heat rejection	$q_{net} \approx 350\,\mathrm{W\,m^{-2}}$	Derived from $q_{out} - q_{abs}$ using the values above.
Radiator areal mass	$\sigma_{rad} = 6.6\,\mathrm{kg\,m^{-2}}$	Conservative traditional radiator panel value [102].
MLI type	15-layer MLI	Selected non-cryogenic spacecraft MLI configuration [3].
MLI areal mass	$\sigma_{MLI} = 0.272\,\mathrm{kg\,m^{-2}}$	15-layer AstraWrap blanket data [3].
MLI effective emissivity	$\epsilon_{eff} = 0.0044$	AstraWrap thermal-performance data [3].
MLI installation factor, mothership	$K_{inst,MS} = 2$	Preliminary allowance for seams, penetrations and installation losses, based on MLI installation sensitivity [103].
MLI installation factor, tug	$K_{inst,T} = 3$	Conservative allowance for the smaller tug geometry and higher leakage sensitivity [103].
Heater sizing margin	$m_h = 20\%$	Preliminary design margin applied after installation losses.
Mothership external area	$\approx 50\,\mathrm{m^2}$	Derived from current REAVER octagonal-prism geometry.
Tug external area	$\approx 5\,\mathrm{m^2}$	Derived from current REAVER cuboid geometry.
Mothership radiator heat load	1200 W-1500 W	Sustained proximity/capture heat allocation from the REAVER power budget.
Tug EP efficiency	$\eta_{EP} = 48\%$	Used to estimate EP waste heat; only losses are assigned to the tug radiator [4].

Continued on next page

[2] https://www.aztechnology.com/product/1/az-93 [accessed 11 June 2026]

[3] `https://aerospacefab.com/wp-content/uploads/2023/10/DataSheet_AstraWrap_092723.pdf` [accessed 10 June 2026]

[4] https://www.safran-group.com/sites/default/files/2022-11/Safran%20Spacecraft%20Propulsion%20-%20PPSX00%20-%20Datasheet.pdf [accessed 16 June 2026]

Table 10.3 – continued from previous page

Assumption	Value used	Source / basis
Heater technology	Polyimide/Kapton flexible heaters	Standard spacecraft heater technology; GSFC specification covers all-polyimide thermofoil heaters for space applications [104] [5].
Thermal straps	Copper foil / PGS straps	Flexible conductive links for transferring heat while reducing mechanical load transfer [105].

Radiator Heat-rejection

The radiator sizing is based on the Stefan–Boltzmann radiation balance. The gross radiative heat rejection from a radiator with area A_{rad}, infrared emissivity ϵ_{rad} and radiator temperature T_{rad} to deep space is given by equation (10.1), where $\sigma = 5.67 \times 10^{-8}\,\mathrm{W\,m^{-2}\,K^{-4}}$ is the Stefan-Boltzmann constant and T_{space} is the deep-space sink temperature [100].

$$Q_{out} = \epsilon_{rad} A_{rad} \sigma \left(T_{rad}^4 - T_{space}^4 \right) \tag{10.1}$$

Dividing equation (10.1) by the radiator area gives the gross heat rejection per unit area as equation (10.2), which results in a gross heat rejection of approximately $459\,\mathrm{W\,m^{-2}}$ when using the assumptions given in table 10.3.

$$q_{out} = \epsilon_{rad} \sigma \left(T_{rad}^4 - T_{space}^4 \right) \tag{10.2}$$

For a sunlit radiator surface, part of the incident solar flux is absorbed. Following the GEO reference case, the absorbed solar heat per unit area is calculated as equation (10.3) resulting in an absorbed flux of $109\,\mathrm{W\,m^{-2}}$.

$$q_{abs} = \alpha_{rad} S \sin\beta \tag{10.3}$$

The net useful heat rejection available for first-order radiator sizing is therefore obtained by subtracting this absorbed flux from the gross radiative heat rejection (equation (10.4)) giving a net heat rejection capability of $350\,\mathrm{W\,m^{-2}}$.

$$q_{net} = q_{out} - q_{abs} \tag{10.4}$$

The required radiator area is then calculated by dividing the sustained heat load assigned to the radiator, Q_{rad}, by the net heat rejection per unit area as shown in equation (10.5).

$$A_{rad} = \frac{Q_{rad}}{q_{net}} \tag{10.5}$$

This means that the source GEO radiator geometry is not copied directly into REAVER. Only the derived per-unit-area heat rejection, q_{net}, is used for the sizing.

MLI Heat-loss and Heater-sizing

Cold-case heater sizing is based on radiative heat loss through MLI-covered zones. For each insulated zone i, the ideal radiative heat loss is approximated by equation (10.6), where $\epsilon_{eff} = 0.0044$ is the effective emissivity of the selected MLI, A_i is the insulated area of the zone and $T_{set,i}$ is the minimum controlled temperature of that zone.

$$Q_{loss,i} = \epsilon_{eff} \sigma A_i \left(T_{set,i}^4 - T_{space}^4 \right) \tag{10.6}$$

The total ideal heat loss, $Q_{loss,ideal}$, is obtained by summing $Q_{loss,i}$ over all insulated zones. The installed heater capacity must be larger than this ideal value because real MLI performance is degraded by seams, blanket edges, fasteners, harness penetrations, cut-outs and imperfect installation. This is accounted for through an installation factor K_{inst}, after which a heater size margin m_h is applied (equation (10.7)).

$$Q_{heater} = K_{inst} Q_{loss,ideal} (1 + m_h) \tag{10.7}$$

[5] https://www.minco.com/catalog/?catalogpage=product&cid=satellite-heaters&id=HAP6731 [accessed 11 June 2026]

For the mothership, $K_{inst} = 2$ is used because the main insulated zones are larger and easier to blanket. For the tug, $K_{inst} = 3$ is used because the geometry is smaller and more sensitive to local thermal leakage. These factors are preliminary design assumptions and shall be updated after detailed MLI layout and thermal testing.

Electric-propulsion Waste-heat
For most electronics, the consumed electrical power is conservatively treated as heat dissipated inside the spacecraft. Electric propulsion is treated differently, because only the inefficiency of the propulsion system and conducted heat into the spacecraft are radiator loads. The tug EP waste heat is estimated as equation (10.8), where $\eta_{EP} = 0.48$ is the EP efficiency taken from the supplier and $P_{EP,in}$ is the electric-propulsion input power.

$$Q_{EP,heat} = (1 - \eta_{EP})P_{EP,in} \tag{10.8}$$

The total tug radiator heat load during EP thrusting is then obtained by adding the EP waste heat to the relevant concurrent equipment loads as shown in equation (10.9), where Q_{other} includes any additional electronics heat that must be rejected through the tug radiator during thrusting.

$$Q_{rad,T} = Q_{EP,heat} + Q_{AOCS} + Q_{TTC} + Q_{other} \tag{10.9}$$

This avoids sizing the tug radiator for the full EP input power, which would be overly conservative because a significant part of the power leaves the spacecraft through the plume [21].

Thermal Strap Sizing
Thermal straps are not treated as heat-rejection devices. They only improve conductive heat transfer between high-dissipation equipment and the radiator or conductive equipment panel. The required strap conductance is estimated from equation (10.10), where Q_{strap} is the heat transported by the strap and ΔT_{allow} is the allowable temperature drop between the equipment and the radiator-side interface [105].

$$G_{strap} = \frac{Q_{strap}}{\Delta T_{allow}} \tag{10.10}$$

This relation is used only to justify the need for conductive links, since their geometry should be selected later once the final equipment layout and radiator positions are fixed.

10.2. Mothership TCS Sizing

The mothership TCS is sized for the sustained proximity/capture hot case and the eclipse or safe-mode cold case. From table 10.2, proximity and capture operations require approximately 1450 W including margin, while the 3655 W peak case is treated as a short transient and is not used for baseline radiator sizing.

For radiator sizing, only the sustained heat from the avionics, AOCS, C&DH, TT&C and payload thermal paths is assigned to the main radiator. Local thruster heating and propulsion heater loads are treated separately through insulation and thermal isolation. Therefore, a radiator heat load of 1200 W-1500 W is used. Using equation (10.5) and $q_{net} = 350\,\mathrm{W\,m^{-2}}$ results in $A_{rad,MS} = 3.4\text{~}4.3\,\mathrm{m^2}$.

A preliminary mothership radiator area of $5.0\,\mathrm{m^2}$ is selected to provide margin and allow distributed placement over two body-mounted panels. With an external surface area of approximately $50\,\mathrm{m^2}$, this uses around 10% of the available surface. Therefore, the radiator mass is 33.0 kg.

For cold-case control, $25\,\mathrm{m^2}$ of MLI is allocated to the LMP-103S tanks and feed lines, battery bay, regulated equipment and sensitive payload/sensor areas. This gives a mass for the MLI of 6.8 kg.

Using equation (10.6), the ideal heat loss through the MLI-covered zones is approximately 37.0 W. Applying the mothership installation factor and heater margin from table 10.3, it results on 88.8 W. A practical heater capacity of 100 W is therefore selected, with 150 W retained as peak/spare capacity. The design also includes conductive equipment panels, six copper thermal straps, 24 temperature sensors and seven thermostats for heater control and monitoring.

Table 10.4: Preliminary mothership TCS sizing summary

Item	Sizing	Mass
Radiators	5.0 m^2	33.0 kg
MLI blankets	25 m^2	6.8 kg
Thermal straps/interfaces	6 straps	2.0 kg
Heaters	100 W installed	0.2 kg
Sensors, thermostats, harness	24 sensors, 7 thermostats	1.5 kg
Thruster thermal isolation	Local shields/stand-offs	3.0 kg
Mounting/integration allowance	–	2.0 kg
Total CBE	–	48.5 kg
With 10% margin	–	54 kg

10.3. Tug TCS Sizing

The tug TCS is sized by two opposite cases: EP thrusting for hot-case radiator sizing and safe mode or standby for cold-case heater sizing. From table 10.2, the EP mode requires approximately 1550 W including margin, while safe and standby modes provide only about 110 W of internal heat.

For the tug radiator, the full EP input power is not treated as spacecraft heat. Using equation (10.8), the CBE EP input power of 962 W (chapter 11) and the efficiency η_{EP} = 48% gives $Q_{EP,heat}$ = 500 W. Adding approximately 59 W from AOCS, TT&C and support electronics gives $Q_{rad,T}$ = 559 W. Using equation (10.5) results in $A_{rad,T}$ =1.60 m^2, which is selected as the CBE radiator area for the tugs, with a 2.0 m^2 margin option retained if final EP losses or contact conductance are worse than assumed. The CBE radiator mass is therefore 10.6 kg.

For cold-case control, 2.5 m^2 of MLI is allocated to the xenon feed system, regulator bay and battery/electronics bay. Using the assumed mass relations for MLI, it ends up weighing just 0.68 kg.

Using equation (10.6), the ideal tug heat loss is 4.48 W. Applying the tug installation factor and heater margin from table 10.3, it results in $Q_{heater,T}$ = 16.1 W.

A practical installed heater capacity of 20 W is selected per tug, with 40 W retained as peak/spare capacity. The tug also includes direct PPU/FMS mounting to the radiator panel, one to two short thermal straps as contingency, 10 temperature sensors and four thermostats.

Table 10.5: Preliminary tug TCS sizing summary per tug

Item	Sizing	Mass
Radiator	1.6 m^2	10.6 kg
MLI blankets	2.5 m^2	0.7 kg
Thermal straps/interfaces	1–2 short straps	0.5 kg
Heaters	20 W installed	0.1 kg
Sensors, thermostats, harness	10 sensors, 4 thermostats	0.5 kg
Hall-thruster thermal isolation	Local shields/stand-offs	1.0 kg
Total CBE	–	13.4 kg
With 10% margin	–	14.7 kg

10.4. Verification of TCS Subsystem Requirements

The verification procedures are discussed briefly for selected requirements. At this design stage, requirements marked as compliant are satisfied by the current thermal-control architecture, sizing or component selection. Requirements marked as TBD require later verification through detailed thermal analysis, thermal-balance testing or thermal-vacuum testing.

Table 10.6: TCS subsystem requirements and compliance

ID	TCS subsystem requirements	Parent Requirement	Method	Check
Mothership				
REQ-TCS-M1	The mothership TCS shall maintain the chemical propulsion system, including propellant, pressurant and feed-system interfaces, within the allowable thermal limits.	REQ-SYS-09	T	TBD
REQ-TCS-M2	The mothership TCS shall maintain the battery, avionics, AOCS, TT&C and payload bays within their allowable operating and survival temperature limits during all mission phases.	REQ-SYS-09	T	TBD
REQ-TCS-M3	The mothership TCS shall protect critical equipment from debris-induced thermal effects, including shadowing, blocked radiator view factors and additional radiative flux during proximity, capture and transport operations.	REQ-SYS-09, REQ-STK-23	A	TBD
Tugs				
REQ-TCS-T1	The tug TCS shall maintain the electric propulsion and xenon feed-system interfaces within their allowable thermal limits during thrusting, coast and safe-mode conditions.	REQ-SYS-09	T	TBD
REQ-TCS-T2	The tug TCS shall provide sufficient radiator area and conductive heat-rejection paths for electric-propulsion operation.	-	A	Yes
REQ-TCS-T3	The tug TCS shall thermally isolate the Hall thruster and plume-facing structure from the xenon tank, battery, avionics, sensors and harness.	-	I	Yes
Universal				
REQ-TCS-U1	The TCS shall maintain all thermally critical components within their respective operating and survival temperature limits in all relevant hot, cold, eclipse and safe-mode cases.	REQ-SYS-09, REQ-STK-23	T	TBD
REQ-TCS-U2	The TCS shall use passive thermal control as the primary regulation method, with active heaters added only where passive control is insufficient.	REQ-SYS-09	I	Yes
REQ-TCS-U3	The TCS shall include temperature sensors on thermally critical equipment, with data relayed to C&DH for monitoring and heater control.	REQ-SYS-09, REQ-SYS-10	T	TBD
REQ-TCS-U4	The TCS shall maintain positive thermal margins in worst-case hot and cold thermal analyses and shall be verified by representative thermal testing.	-	T	TBD

The TCS verification approach follows ECSS thermal-control practice, where thermal models are refined and correlated using test data [21]. Thermal-vacuum testing shall include functional checks at representative hot and cold plateaux, while thermal-balance testing is used to verify the thermal design and support model correlation [28] [6] [7].

For REQ-TCS-M1, REQ-TCS-M2, REQ-TCS-T1, REQ-TCS-U1, REQ-TCS-U3 and REQ-TCS-U4, compliance shall be determined by thermal-vacuum and/or thermal-balance testing. REQ-TCS-M3 and REQ-TCS-T2 shall be verified mainly by thermal analysis, while REQ-TCS-T3 and REQ-TCS-U2 shall be verified by inspection of the implemented thermal architecture. Final compliance shall be closed after thermal-model correlation and updated hot/cold margin assessment.

[6] https://s3vi.ndc.nasa.gov/ssri-kb/topics/59/ [accessed 11 June 2026]
[7] https://s3vi.ndc.nasa.gov/ssri-kb/topics/58/ [accessed 11 June 2026]

11. Electrical Power System

The electrical power system (EPS) is responsible for generating, handling and distributing all the electrical power required for operating the spacecraft. Successfully sizing and selecting these components is crucial for ensuring the spacecraft operations can be performed as planned, especially because the tugs have significant power draw due to their electric thrusters. The power profile is first established from the component-level power budget, after which the solar array and battery are sized to meet the resulting requirements. The bus architecture, including the power conditioning and distribution unit (PCDU), voltage levels, and load distribution, is then described for both spacecraft. The beginning-of-life (BOL) power is the solar array output at the start of the mission, before radiation degradation has occurred. The end-of-life (EOL) power accounts for accumulated degradation over the design lifetime and is the governing figure for sizing.

11.1. Electrical Power Profile

To determine the power requirements for each phase of the mission, an electrical power profile was established. This profile shows the power requirements throughout the duration of the mission. Power requirements were gathered for each component, and assigned based on the spacecraft operational mode. Operational and peak power loads can be gathered from component data sheets. By assigning these to the operational modes, the electrical power profile can be accurately determined. From this power profile, the critical case necessary for sizing should be determined. The electrical power profiles for mothership and tug are presented in figure 11.1.

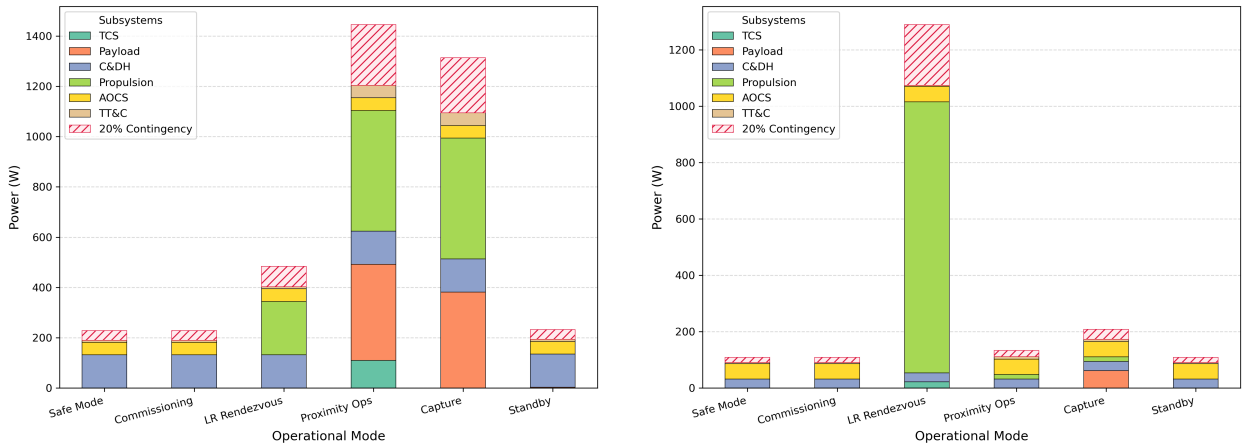

(a) Mothership electrical power profile (including 20% system-level margin)

(b) Tug electrical power profile (including 20% system-level margin)

Figure 11.1: Plots of electrical power profile for mothership and tug.

A system-level contingency of 20 % is applied to all component-level power estimates throughout the power budget, in accordance with the margin philosophy adopted for this preliminary design phase. This contingency accounts for uncertainty in component-level power draw at the current level of design maturity. The sizing cases selected for solar array and battery sizing are the worst-case sustained and worst-case peak modes respectively, as summarised in table 11.1. The solar array is sized to the mode with the highest sustained daytime load, while the battery is sized to the mode with the highest peak instantaneous demand and the eclipse survival case. As eclipse time is limited in Geostationary Orbit, power-intensive operations will be halted temporarily during this time. The operational mode during the standby phase is standby, which requires significantly less power compared to the other limiting cases.

Table 11.1: Power profile sizing cases and key values used for solar array and battery sizing

Parameter	Symbol	Mothership	Tug
Solar array sizing case			
Sizing mode	-	Proximity Ops	LR Rendezvous
Daytime load (incl. +20 % margin)	P_d	1445 W	1542 W
Battery sizing case			
Sizing mode	-	Peak load (Capture)	Eclipse (Standby)
Sizing load (incl. +20 % margin)	P_e	3656 W	109 W
Min. peak duration	T_{peak}	10 min	—
Eclipse load (incl. +20 % margin)	P_{ecl}	232 W	109 W
Max. eclipse duration	T_e	72 min	72 min

11.2. Sizing Methodology

The solar array and battery are sized using the standard spacecraft power system methodology from SMAD [71]. Both sizing methods are implemented in a Python script to allow for fast iteration across design parameters.

Solar Array Sizing

In order to determine the amount of electrical energy that can be generated by the solar panels, the complete route should be considered. The route starts at the incoming solar irradiance and ends with the power being delivered to the relevant spacecraft components. At each step of this process, losses occur that should be taken into account when sizing the solar panel.

The power density of the solar array at the beginning- and end-of-life are given by P_{BOL} and P_{EOL} in W/m^2. Solar array pointing losses are given by $\cos\theta$, which is the cosine-loss. It reflects the incidence angle of the sun and is assumed to be 23.5° as worst-case according to SMAD [71]. Cell efficiency μ_{cell} is obtained from the selected cell datasheet. The inherent degradation I_d covers the difference between the solar cells and the total solar array area, including design inefficiencies such as packing density as well as temperature and shadow losses. It is assumed to be 0.77 according to SMAD [71]. The beginning-of-life (BOL) power density is subsequently given by equation (11.1).

$$P_{BOL} = S_E \cdot \mu_{cell} \cdot I_d \cdot cos\theta \tag{11.1}$$

Solar cells degrade as they age, especially in the harsh GEO radiation environment. L_d covers this degradation, and is determined by the mission lifetime and the annual degradation rate. For GaAs solar cells this is assumed to be 2.75 % per year [71]. To allow for more missions than just the one-year minimum as required per REQ-STK-01, the design lifetime is set to 5 years, resulting in $L_d = (1 - 0.0275)^5 \approx 0.87$. Applying this results in the required end-of-life (EOL) power density of the solar array as specified by equation (11.2).

$$P_{\text{EOL}} = P_{\text{BOL}} \cdot L_d \tag{11.2}$$

The required solar array power is subsequently given by equation (11.3). It sums the total energy required, corresponding of daylight and eclipse time energy. The required energy is calculated using the power P, time T and path efficiency μ. Subscript e and d correspond to eclipse and daytime values respectively. The required values for sizing are obtained from the electrical power profile established in section 11.1.

$$P_{sa} = \frac{\frac{P_e T_e}{\mu_e} + \frac{P_d T_d}{\mu_d}}{T_d} = \frac{P_e T_e}{\mu_e T_d} + \frac{P_d}{\mu_d} \tag{11.3}$$

The path efficiencies μ_d and μ_e for the daylight and eclipse paths are given in equations (11.4) and (11.5), respectively. The daylight path runs from the solar array through the harness and PCDU directly to the loads. The eclipse path additionally passes through the battery.

$$\mu_d = \mu_{har} \cdot \mu_{pcdu} \tag{11.4}$$

$$\mu_e = \mu_{har} \cdot \mu_{pcdu} \cdot \mu_{bat} \tag{11.5}$$

The efficiency values used for both spacecraft are listed in table 11.2. Both PCDUs incorporate MPPT internally, so no separate MPPT unit is required. The harness efficiency is estimated from typical harness from heritage missions [71]. The PCDU efficiencies are taken directly from their respective datasheets and replace the generic SMAD defaults, which were derived for older, lower-efficiency hardware [71].

Table 11.2: Power path efficiency values used in solar array sizing.

Parameter	Symbol	Value	Source
Harness efficiency	μ_{har}	0.98	Typical [71]
PCDU efficiency (MS)	μ_{pcdu}	0.97	STENGG PCDU datasheet
PCDU efficiency (Tug)	μ_{pcdu}	0.95	Bradford SuperNova datasheet
Battery discharge eff.	μ_{bat}	0.90	Typical Li-ion

Lastly, the required solar array area is given by equation (11.6).

$$A_{sa} = \frac{P_{sa}}{P_{\text{EOL}}} \tag{11.6}$$

Battery Sizing

Batteries are necessary to provide electrical power when the solar panels are inadequate, primarily during an eclipse and for short-duration peak load events. The required battery energy is given by equation (11.7), where the eclipse power demand and duration are divided by the Depth-of-Discharge (DOD) and battery discharge efficiency. The DOD limit of 0.80 is applied to protect cell cycle life, and is in accordance with Lithium-Ion batteries for use in GEO [71].

$$E_{\text{bat}} = \frac{P_e \cdot T_e}{\text{DOD} \cdot \mu_{\text{bat}}} \tag{11.7}$$

11.3. Mothership Electrical Power System

The mothership EPS is sized by the proximity operations case, which combines a sustained high power demand with short capture peaks. It comprises a solar array sized for the worst-case sustained load at end-of-life, a battery sized to buffer peak capture loads and survive the maximum GEO eclipse, and a PCDU handling conditioning and distribution.

Solar Array

Applying equations (11.1) and (11.2), the BOL and EOL power densities of the selected SolAero Z4J+ cells are $P_{\text{BOL}} = 302.4\,\text{W/m}^2$ and $P_{\text{EOL}} = 263.0\,\text{W/m}^2$. The path efficiencies for the mothership are $\mu_d = 0.951$ and $\mu_e = 0.856$. Applying equation (11.3) with the proximity operations mode as the sizing case yields a solar array power requirement of $P_{sa} = 1534\,\text{W}$ at EOL. This corresponds to the worst-case sustained power demand of $P_d = 1445\,\text{W}$ (including 20% system-level margin) and a standby mode eclipse load of $P_e = 228\,\text{W}$. This corresponds to a BOL requirement of $P_{sa,\text{BOL}} = 1534/0.870 = 1764\,\text{W}$.

The selected solar array is RocketLab's Standardised Array (StarRay), providing pre-engineered customisable solar arrays with extensive flight heritage and rating for the GEO environment. The solar array deployment sequence is visualised in figure 11.2c.

A configuration with two wings in the T-Star arrangement was chosen, with 4 panels per wing each having a substrate size of 667x1198 mm. The datasheet-rated BOL output is 1818 W[1], exceeding the BOL requirement of 1764 W by a margin of 3.1 % and confirming the selected configuration is adequate at end-of-life. The 20% system-level contingency is already embedded in the power budget values used for sizing, so no additional sizing margin is applied on top.

Battery

The battery must fulfil two roles: sustaining the spacecraft through the maximum GEO eclipse duration of 72 min at standby mode power, and buffering the peak load demand during capture and control operations. Applying equation (11.7) for the eclipse case gives $E_{\text{bat}} \approx 1367\,\text{kJ} = 380\,\text{Wh}$.

[1] `https://rocketlabcorp.com/assets/Uploads/RL-SolAero-Data-Sheet-StarRay-final.pdf` [accessed 12 June 2026]

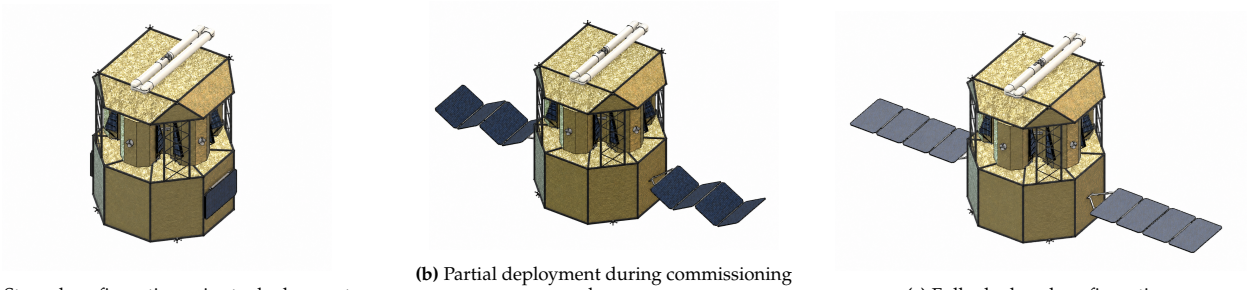

(a) Stowed configuration prior to deployment.

(b) Partial deployment during commissioning phase.

(c) Fully deployed configuration.

Figure 11.2: Deployment sequence of the mothership StarRay solar array (SolAero Z4J+ cells). The array deploys from stowed to full extension during the commissioning phase (PH-2)

For the peak load case, the solar array delivers approximately 1503 W to the bus at EOL, leaving 2153 W against the peak demand of 3656 W. The battery must sustain this for the duration of the capture sequence. With a usable battery energy of $1568 \times 0.80 \times 0.90 = 1129$ Wh, the battery can sustain the shortfall for approximately 31 min, which provides adequate headroom for the expected capture duration. The requirement for the time required has been set in accordance with the astrodynamics characteristics and is set to at minimum require the equivalent energy to perform 10 minutes of peak power operations. The 10 min minimum duration is derived from the expected capture sequence timeline as established in the mission design (see chapter 3). To provide robustness against extended capture attempts, re-grasping manoeuvres, or hold-point delays during proximity operations, a generous margin is applied as changes could rapidly increase this demand.

The selected battery is the EnerSys ABSL 8s16p, rated at 28 V, 56 Ah, and 1568 Wh [2]. This meets both the eclipse requirement (380 Wh required, 1568 Wh available) and the peak load buffering role. The battery capacity is driven by the peak load requirement rather than the eclipse survival requirement. Using the selected battery and solar panel, operations could theoretically be resumed for some time during eclipse. However, it is not the intended sequence to operate during the eclipse, rather entering standby mode temporarily as previously discussed.

Bus Architecture and PCDU Selection

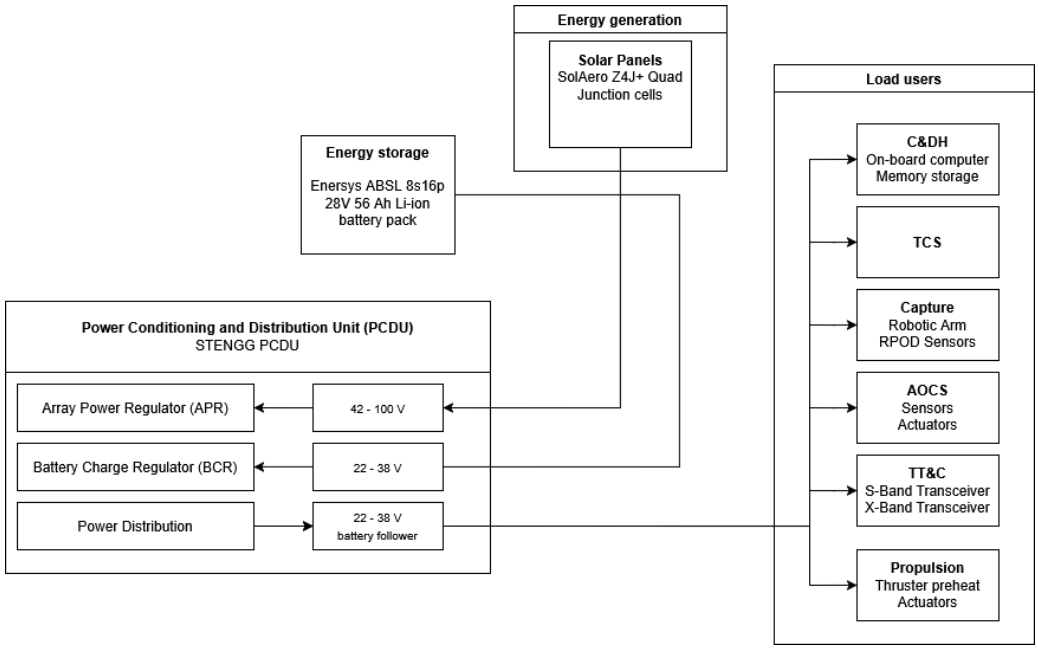

Figure 11.3: Mothership electrical power system block diagram

The power conditioning and distribution unit selected for the mothership is the ST Engineering (STENGG) PCDU[3]. It is rated for 4 kW peak output at 32 V with a conversion efficiency exceeding 97 %, enabling very high

[2] https://www.enersys.com/en/products/batteries/absl/absl-space/ [accessed 12 May 2026]

[3] https://www.stengg.com/getmedia/3b134151-cf80-4afb-9c0b-06ae919618c1/satellite-systems-pcdu-datasheet.pdf [accessed 12 May 2026]

efficiency power conversion. The unit operates a battery-follower bus architecture: the bus voltage is not fixed but follows the battery terminal voltage, ranging from 22 V to 38 V across the full charge and discharge cycle. All loads are specified to operate across this range. MPPT is integrated within the PCDU, eliminating the need for a separate MPPT unit.

Power is distributed to loads via 56 configurable Latching Current Limiters (LCLs), with four Retriggerable LCLs (RLCLs) reserved for critical lines. An additional 72 dedicated heater LCLs are provided, directly supporting TCS heater requirements without external switching hardware. The CAN bus interface connects the PCDU to the C&DH computer. The PCDU carries TRL-9 heritage with seven years of on-orbit operation without anomalies.

During proximity operations, the total bus load is 1445 W. During short peaks up to 3656 W, the solar array covers 1503 W and the ABSL 8s16p battery supplies the remaining power. The mothership electrical block diagram is presented in figure 11.3.

11.4. Tug Electrical Power System

The tug EPS is sized by the long-range rendezvous case, where the electric propulsion load dominates the sustained power demand. It comprises a solar array sized for this load at the end of life, a small battery sized only to survive an eclipse in standby mode (thrusting is halted during an eclipse), and a PCDU handling conditioning and distribution.

Solar Array

The tug solar array is a radially extending accordion-fold solar array using Northrop Grumman's UltraFlex technology. This solar array is inspired by the one flown on the Mars InSight Lander. The InSight mission used two UltraFlex wings populated with Rocket Lab SolAero ZTJ cells, with a measured flight-verified BOL output of 920 W per wing at 1 AU,AM0 (standard conditions) [22]. The tug uses the same array geometry fitted with Z4J+ quad-junction cells (31.3 % efficiency), compared to the ZTJ triple-junction cells (29.5 % efficiency) flown on InSight. These are improved versions of the same manufacturer and should thus offer great compatibility and comparable packing density. Scaling the heritage BOL output by the cell efficiency ratio gives the Z4J+ per-wing output of $P_{\text{BOL,wing}} = 976$ W per wing. With two wings, the total tug array BOL output is 1952 W, and the EOL output is $P_{\text{EOL,total}} = 1698$ W.

The tug path efficiencies are $\mu_d = 0.931$ and $\mu_e = 0.838$. The required solar array output from equation (11.3) with the long-range rendezvous mode as the sizing case is $P_{sa} = 1663$ W at EOL, corresponding to a BOL requirement of 1912 W. This corresponds to the worst-case sustained load driven by electric propulsion at $P_d = 1542$ W (including 20% system-level margin).

The two-wing UltraFlex array with Z4J+ cells provides 1952 W BOL, exceeding the requirement by a margin of 2.1 %. The 20% system-level contingency is already built into the power budget, so this positive margin confirms that the configuration is adequate. The wing area derived from the InSight array geometry is approximately 3.23 m^2 per wing, giving a total array area of 6.46 m^2. The solar array deployment sequence is provided in figure 11.4.

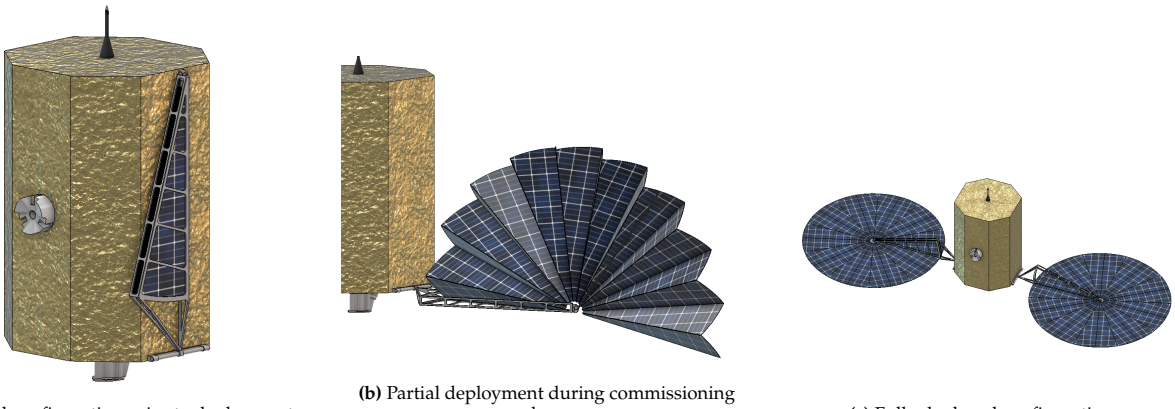

(a) Stowed configuration prior to deployment.

(b) Partial deployment during commissioning phase.

(c) Fully deployed configuration.

Figure 11.4: Deployment sequence of the tug UltraFlex solar array (SolAero Z4J+ cells). The array deploys from stowed to full extension during the commissioning phase (PH-2)

Battery

Due to the large power draw of the electric thruster, it has been decided that the tug will temporarily halt thrusting during eclipse. By entering standby mode, the power draw of the tug is limited to just 109 W and only a small battery is necessary. Applying equation (11.7) for the tug load during eclipse in standby mode yields a required battery energy of $E_{\text{bat}} = 654\,\text{kJ} = 182\,\text{Wh}$.

The selected battery is the EnerSys ABSL 8s3p with a rated capacity of 252 Wh, providing a margin of 39 % over the eclipse requirement. This is already a very small battery, and the smallest one that EnerSys provides off-the-shelf. With only a modest mass of 1.66 kg the relatively large margin is adequately justified.

Bus Architecture and PCDU Selection

The power conditioning and distribution unit selected for the tug is the Bradford Engineering SuperNova PCDU [4]. It achieves a power conversion efficiency of up to 95 % and a mass below 3 kg, making it well-suited to the tug's tight mass budget. The unit operates an unregulated battery-follower bus at 22 V to 34 V, following the battery terminal voltage. MPPT is integrated within the SuperNova, again eliminating the need for a separate unit. While the SuperNova PCDU is not necessarily designed for operations in GEO, additional shielding will be provided by structures to shield these components from radiation in order to survive in GEO chapter 9.

In addition to the main unregulated bus, the SuperNova provides two independently selectable regulated output voltages between 3.3 V and 15 V via an internal Regulated Power Distribution (RPD) module. These low-voltage rails supply the digital logic loads in C&DH and AOCS, avoiding the need for separate DC-DC converters in these components. The Hall thruster PPU (EPS-X00) is connected directly to the unregulated bus, as it contains its own internal high-voltage conversion.

During long-range rendezvous, the solar array delivers 1698 W at EOL against a total bus load of 1542 W. The array directly sustains the dominant propulsion load with margin, and the battery is not drawn upon during daytime EP thrusting. The tug electrical block diagram is presented in figure 11.5.

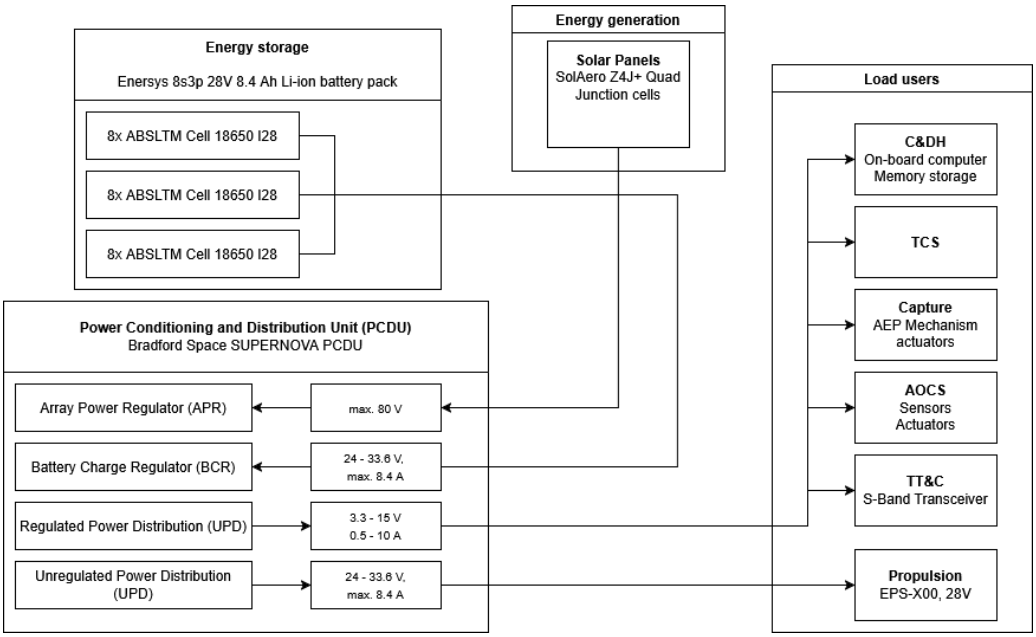

Figure 11.5: Tug electrical power system block diagram.

11.5. Verification of EPS Subsystem Requirements

The EPS subsystem requirements are derived from the sizing results presented in sections 11.2 to 11.4. Each requirement is stated with a numerical value corresponding to the sizing output, ensuring full traceability from design methodology to formal requirement.

[4] https://www.bradford-space.com/products/avionics-pcdu [accessed 12 May 2026]

Table 11.3: Electrical power subsystem requirements, and requirement IDs

ID	EPS Subsystem Requirement	Parent Requirement	Method	Check
Mothership				
REQ-EPS-M1	The mothership electrical power system shall produce 1764 W of electric power at beginning-of-life.	REQ-MIS-09	T, A	TBD
REQ-EPS-M2	The mothership electrical power system shall be able to store 847 Wh of electrical energy at beginning-of-life.	REQ-MIS-09	I	Yes
REQ-EPS-M3	The mothership electrical power system shall maintain the power bus voltage within 22-38 V across all nominal operating conditions.	REQ-MIS-09	T	TBD
REQ-EPS-M4	The mothership electrical power system shall supply peak bus loads of up to 3656 W for a minimum duration of 10 minutes using battery energy storage.	REQ-MIS-09	D	TBD
Tugs				
REQ-EPS-T1	The tugs electrical power system shall produce 1912 W of electric power at beginning-of-life.	REQ-MIS-09	T, A	TBD
REQ-EPS-T2	The tugs electrical power system shall be able to store 182 Wh of electrical energy at beginning-of-life.	REQ-MIS-09	I	Yes
REQ-EPS-T3	The tugs electrical power system shall maintain the power bus voltage within 22-34 V across all nominal operating conditions.	REQ-MIS-09	T	TBD
Universal				
REQ-EPS-U1	The electrical power system shall provide housekeeping telemetry to the C&DH subsystem, including bus voltage, load current, and battery state of charge.	REQ-MIS-09	I	Yes
REQ-EPS-U2	The electrical power system shall sustain spacecraft operations in standby mode throughout a maximum eclipse duration of 72 minutes without solar array input.	REQ-MIS-09	A	Yes

Compliance with REQ-EPS-M1 and REQ-EPS-T1 shall be verified by test, using calibrated solar simulators such as the EternalSun SpectroSun[5] to illuminate the flight-representative solar array and measure the electrical output under AM0 illumination conditions (standard measurement conditions). This test is typically performed at cell and panel level by the manufacturer, and at array level prior to integration. Compliance shall be confirmed via a test report issued against the requirement.

Bus voltage compliance with REQ-EPS-M3 and REQ-EPS-T3 shall be verified by test, using calibrated programmable electronic loads representative of each operational mode to simulate the full range of bus current draws. Bus voltage shall be measured with calibrated instrumentation across the full charge and discharge cycle of the battery, confirming that the voltage remains within the specified band under all load conditions.

REQ-EPS-M4 shall be verified by demonstration, operating the PCDU and battery at the peak bus load using electronic loads for the required minimum duration and confirming battery state of charge and voltage remain within specified limits throughout.

The EPS component mass budget is summarised in table 11.4.

Table 11.4: Electrical power system mass budget overview.

Component	**Mothership** [kg]	**Tug** [kg]
Solar array	55.55	9.90
PCDU	26.95	2.20
Battery	8.19	1.74
Total	**90.69**	**13.84**

It should be noted that EPS components do not appear as loads in the spacecraft power budget. Solar array output is a source, not a consumer, and PCDU and harness losses are embedded in the path efficiencies μ_d and μ_e used during sizing in section 11.2.

[5] `https://www.eternalsun.com/product/manufacturing-solar-simulators/` [accessed 16 May 2026]

12. Telemetry, Tracking & Command

The telemetry, tracking and command (TT&C) subsystem is responsible for maintaining bidirectional communication between the REAVER space segment and ground operators throughout all mission phases. Reliable TT&C is essential to mission success, particularly given the operational complexity of coordinating a Mothership and five independent Tugs across geosynchronous orbit, where proximity operations and rendezvous and docking manoeuvres require continuous command authority and attentive monitoring. The ground segment and communication network are established first, with the ESA Estrack stations selected as primary and secondary contact points, and the frequency band architecture for both housekeeping and payload data links defined. The communication links for each spacecraft element, covering the mothership-to-ground, tug-to-ground, and physical inter-vehicle interface, are then presented alongside the data rate allocations derived from subsystem-level telemetry budgets and payload sensor outputs. The on-board hardware selections for the Mothership and Tugs follow, after which link budgets are computed for all active radio frequency paths to verify that positive link margins are achieved at the worst-case slant range. The chapter closes with the mass, power and cost budget and the full subsystem requirements, including traceability to parent requirements and verification methods.

12.1. Ground Segment and Communication Network

The ground segment contains the infrastructure required to maintain command and control of the Mothership & Tugs throughout the entire mission phases. This section defines the selected ground station network and the communication architecture linking the space segments to ground operators.

Ground Station

The selection of a ground station is directly constrained by the top-level mission requirement, which states that the mission shall communicate with ground operators via the ESA Estrack network, as stated in section 12.8. This constraint eliminates all non-Estrack ground infrastructure from consideration and fixes the station selection to Estrack's published capabilities.

To pick the best ground station, all potential ground stations must be evaluated first. The core ESA network ground stations are: Kourou, Kiruna, Redu, Cebreros (Deep Space), New Norcia (Deep Space), Santa Maria, and Malargüe (Deep Space) [1]. Two stations fail to meet the requirements immediately: Santa Maria's due to an antenna diameter of 5.5 m, which is insufficient for reliable link closure at GEO range, and Kiruna is eliminated on geometric grounds: the maximum achievable elevation angle to any equatorial GEO satellite is approximately 13.5, derived from the standard ground station elevation formula [2], which is below the practical threshold for reliable S-band link closure at 35700-36500 km due to an excessively long atmospheric signal path and high signal attenuation. This reduces the candidate set to five stations: Redu, Kourou, New Norcia, Cebreros, and Malargüe.

Weights are assigned in multiples of 5% and ranked by their impact on mission capability.

- **Frequency Band Support (0.40):** Band compatibility is a hard constraint; a station unable to support the required S- and X-band frequencies are operationally incompatible across geometries, justifying the highest weight.
- **GEO Coverage Geometry (0.35):** Elevation angle directly governs free-space path loss and atmospheric attenuation; lower angles degrade the link budget, justifying the second-highest weight.
- **ESA GEO Mission Heritage (0.25):** Confirmed GEO TT&C heritage reduces mission risk by ensuring scheduling infrastructure and launch and early orbit phase (LEOP) procedures are in place, but cannot compensate for inadequate band support or geometry, justifying the lowest weight.

To decide between the five candidate stations, a concise trade-off is performed; table A.1 presents the scoring definitions used in table 12.1.

[1] https://www.esa.int/Enabling_Support/Operations/ESA_Ground_Stations/Estrack_ESA_s_global_ground_station_network [accessed 05 June 2026]

[2] https://rfessentials.com/rf-knowledge-base/how-do-i-calculate-the-look-angle-and-azimuth-from-a-ground-station-to-a-geostat/[accessed on 05 June 2026]

Table 12.1: Ground station trade-off table. Green - Excellent, Light Green - Good, Yellow - Acceptable, Orange - Correctable deficiencies, Red - Unacceptable

Station Criteria	GEO Coverage Geometry (0.35)	Frequency Band Support (0.40)	ESA GEO Mission Heritage (0.25)	Total
Redu	3 - acceptable Latitude 50°N; max elevation ≈33° to equatorial GEO; moderate atmospheric path loss.	5 - excellent S-band, X-band, and Ka-band all confirmed as primary operational bands.	5 - excellent Primary ESA GEO TT&C station; heritage includes Meteosat operations and GEO LEOP.	**4.30**
Kourou	5 - excellent Latitude 5°N; max elevation ≈84° to equatorial GEO; minimal atmospheric path loss.	4 - good S-band and X-band confirmed as primary operational bands; Ka-band availability not confirmed.	4 - good Standard ESA station for Ariane GEO LEOP; strong GEO operational portfolio.	**4.35**
New Norcia	4 - good Latitude 31°S; max elevation ≈54° to equatorial GEO; low atmospheric path loss.	3 - acceptable X-band and Ka-band are primary bands; S-band is present as a secondary capability only.	1 - unacceptable Deep space heritage only; no confirmed GEO TT&C operations.	**2.85**
Cebreros	3 - acceptable Latitude 40°N; max elevation ≈44° to equatorial GEO; moderate atmospheric path loss.	3 - acceptable X-band and Ka-band are primary bands; S-band present as secondary legacy capability only.	1 - unacceptable Deep space heritage only; no confirmed GEO TT&C operations.	**2.50**
Malargüe	4 - good Latitude 36°S; max elevation ≈48° to equatorial GEO; low to moderate atmospheric path loss.	3 - acceptable X-band and Ka-band are primary bands; S-band present as secondary legacy capability only.	1 - unacceptable Deep space heritage only; no confirmed GEO TT&C operations.	**2.85**

The maximum elevation angle E from a ground station to an equatorial GEO satellite at the same longitude is given by equation (12.1), where φ is the geodetic latitude, the angular distance of the station north or south of the Earth's equator. $R_E = 6371$ km is the mean Earth radius, and $h = 35786$ km is the nominal GEO altitude, giving $R_E/(R_E + h) = 0.151$. Equation (12.1) is applied to all five candidate stations, yielding the values in table 12.2.

$$E = \arctan\left(\frac{\cos\varphi - \dfrac{R_E}{R_E + h}}{\sin\varphi}\right) \tag{12.1}$$

Table 12.2: Maximum elevation angle to equatorial GEO per candidate station. Note that these values represent the geometric best case, occurring when the satellite and station share the same longitude. For targets at different longitudes, the elevation angle is lower.

Station	Latitude	$\cos\varphi$	$\sin\varphi$	E (°)
Kourou	5.3°N	0.996	0.092	84
New Norcia	31.0°S	0.857	0.515	54
Malargüe	35.8°S	0.812	0.584	48
Cebreros	40.5°N	0.760	0.650	44
Redu	50.0°N	0.643	0.766	33

Redu and Kourou are selected as the primary and secondary ground stations, respectively. Although Kourou achieves a higher trade-off score (4.35 vs 4.30), the 0.05-point difference is within the scoring process's sensitivity and is not considered a decisive margin. Redu is designated primary on the basis of its confirmed band capability (S-, X-, and Ka-band), its status as the established ESA primary GEO TT&C station, and its proximity to ESOC, which streamlines mission operations coordination. Kourou is designated secondary, providing geometric complementarity through its near-equatorial location and serving as a contingency contact station in the event of a Redu outage or malfunction.

Because a GEO spacecraft holds a fixed sub-satellite longitude, visibility from a station depends only on the station-to-target longitude separation. Applying equation (12.1) at the 5° elevation floor, Redu and Kourou jointly cover a continuous arc from roughly 129°W to 74°E, about 202° of the belt, which includes the western libration point near 105°W and the populated Atlantic and European slots. The remaining 158° arc, spanning the Pacific and Asia-Pacific longitudes, falls outside two-station visibility: a spacecraft over the Pacific would

have no contact with either station. This is a deliberate scoping constraint on the baseline operational band rather than an outage; should a later phase require that arc, the ESA Estrack station at New Norcia (116°E) closes most of the gap on secondary S-band.

Communication Network

The communication network defines the frequency band allocation and channel architecture for exchanging TT&C data between the ground station and the space segment. The selection is driven by the Estrack infrastructure constraint established in section 12.1 and the requirements defined in section 12.8.

S-band (2-4 GHz) is selected for housekeeping TT&C on both the Mothership and the Tugs. It is the ITU-designated primary band for Earth-space TT&C and the established Estrack operational standard for GEO missions, with both Redu and Kourou providing full S-band uplink and downlink capability [23]. At the GEO operating altitude, the free-space path loss is approximately 190 dB, and rain attenuation at S-band is negligible at both station latitudes, ensuring link availability across all mission modes, including Safe Mode [71]. Mature flight hardware at TRL 9 and an established GEO heritage further reduce programmatic risk. The mothership is assigned uplink 2035 MHz and downlink 2210 MHz; the tugs are assigned uplink 2065 MHz and downlink 2243 MHz, consistent with the ITU 240/221 turnaround ratio[10].

X-band (8-12 GHz) is selected for the mothership payload downlink. The sensor and LiDAR data generated during proximity operations require downlink at the HIGH data rate class (1 Mbit/s), which cannot be downlinked on the housekeeping S-band channel without conflicting with antenna, scheduling, and data rate constraints. X-band is an ITU-allocated band for spacecraft science downlinks, is supported at Estrack Redu, and provides sufficient data rate capability at GEO slant range with a high-gain antenna [71, 23]. Ka-band was not selected for this role because Estrack Kourou does not provide Ka-band coverage, and the elevated rain attenuation at low elevation angles at Redu introduces high link-margin risk.

12.2. Communication Links

This section presents the communication links utilised in REAVER. It comes with three distinct communication link types: the mothership-to-ground link, the tug-to-ground link, and the physical mothership-to-tug inter-vehicle link. All space-to-ground links interface exclusively with the ESA Estrack network, in accordance with the top-level mission requirement. Each link is designed to support the data rate class framework defined in section 12.5, which maps LOW, MEDIUM, and HIGH throughput requirements to the six spacecraft operational modes.

Mothership-to-Ground

The mothership communicates directly with the ground via ESA Estrack, with Redu as the primary station and Kourou as the secondary, providing geographic redundancy and an independent GEO elevation geometry. A relay architecture was not adopted: a GEO target lying within a ground station's longitude visibility window is continuously visible from that station, so within the mission's operational longitude band (section 12.1), the Redu-Kourou pair provides uninterrupted contact, making relay infrastructure architecturally redundant and mass-inefficient.

The mothership operates a two-band link architecture. S-band carries all telecommand uplink and housekeeping telemetry downlink across all operational modes; X-band is used exclusively for payload data downlink during Proximity Operations mode. All telecommands are issued via S-band regardless of the active downlink band. The assigned frequencies are defined in section 12.2. The mothership holds a dedicated frequency allocation and therefore requires no access scheduling with the tug fleet. Table 12.3 summarises the antenna configuration and data rate class in each operational mode.

Table 12.3: Mothership link configuration per operational mode. *Note:* LOW < 10 kbps (S-band TT&C, both vehicles); HIGH = 474.62 Mbps (X-band payload downlink, mothership only, no compression). HIGH class consistent with MEV-2 RPOD high-rate heritage [106].

Mode	Band	Antenna	Data Rate Class
Safe Mode	S-band	LGA	LOW
Commissioning	S-band	LGA/HGA	MEDIUM
Long-Range Rendezvous	S-band	HGA	MEDIUM
Proximity Operations	S-band + X-band	HGA (both)	MEDIUM (S) / HIGH (X)
Capture and Control	S-band + X-band	HGA (both)	MEDIUM (S) / HIGH (X)
Standby	S-band	HGA	MEDIUM

Tug-to-Ground
Each tug communicates directly with ESA Estrack via S-band only. X-band is not implemented; high-rate sensor data is either processed on board or transferred to the mothership via the physical link interface, eliminating the need for a dedicated high-rate downlink.

The five tugs share a single frequency allocation via scheduled TDMA, with time-slot assignments coordinated by ESOC. A tug entering Safe Mode outside its assigned slot must await the next allocation cycle, which is acceptable given the 72 min autonomous safe operations capability required.

Mothership-to-Tug (Inter-Vehicle Link)
The communication link between the mothership and the tugs is via a direct channel (physical link) used in RPOD. Table 5.1 explains this link. Therefore, a wireless communication link was not developed at this stage of the detailed design.

12.3. On-Board TT&C Hardware
This section presents the on-board TT&C hardware allocated to the Mothership and each Tug. Component selections are driven by the link budgets in section 12.5 and the coverage requirement for uninterrupted availability across all mission phases, including RPOD.

Mothership TT&C Components
The mothership is equipped with two Beyond Gravity S-band helix TTC antennas (SBA3 variant), mounted on opposing faces along the spacecraft's z-axis. The SBA3 provides an edge-of-coverage (EOC) half-angle exceeding 115°, meaning that two opposing antennas jointly cover 230° - 50° beyond the 180° threshold required for gapless spherical coverage. This ensures uninterrupted TT&C link availability regardless of mothership attitude across all mission phases. Both antennas operate in the S-band (2000-2300 MHz) and are available in LHCP and RHCP variants, allowing polarisation to be matched to ground-station conventions. At a mass of less than 235 g per unit, the two-antenna configuration adds under 470 g to the RF subsystem[3].

At the transceiver level, the mothership carries two STC-MS03 units in a prime/cold-redundant configuration, whereas each tug carries a single unit. The mothership is the primary mission-control node; loss of its TT&C link is mission-critical and unrecoverable, which justifies the added redundancy. As with the tugs, each unit integrates a diplexer and RF harness, allowing both antennas to be served from a single active transceiver[4].

For payload data downlink, the mothership carries two Anywaves high-gain X-band antennas paired with two EnduroSat X-Band Transmitters (prime and cold-redundant)[5,6]. Both transmitters operate at 8.465 GHz with an RF output of 18 W. The high-gain antenna provides the link margin required to close the X-band downlink over the 41849 km GEO slant range (formula in link budget section) at the data rates established in section 12.5. No X-band receive chain is included; the X-band subsystem is transmit-only.

Tug TT&C Components
Each tug is equipped with two Beyond Gravity SBA3 antennas (see section 12.3 for specifications), mounted on opposing faces along the spacecraft's z-axis. Spherical coverage is a hard requirement during RPOD phases, when tug attitude is unconstrained, and no preferred pointing direction toward the ground station can be guaranteed. Both antennas are available in LHCP and RHCP variants, allowing polarisation to be matched to the inter-vehicle link and ground-station conventions. At a mass of less than 235 g per unit, the two-antenna configuration adds under 470 g per tug to the RF subsystem.

Alongside the antennas, each tug carries one S-Band TT&C Transceiver STC-MS03 (with diplexer and RF harness). Unlike the mothership, no cold-redundant unit is carried; the single transceiver is sufficient given that a tug loss, while operationally significant, is not mission-critical. The diplexer enables the transceiver to operate with both antennas simultaneously. Table 12.4 summarises the link configuration per operational mode.

[3] https://satsearch.co/products/beyond-gravity-s-band-ttc-antennas#rfi [accessed 05 June 2026]
[4] https://satsearch.co/products/honeywell-aero-s-band-tt-c-transceiver-stc-ms03 [accessed 05 June 2026]
[5] https://satsearch.co/products/anywaves-high-gain-20-dbi-x-band-antenna [accessed 10 June 2026]
[6] https://satsearch.co/products/endurosat-x-band-transmitter [accessed 10 June 2026]

Table 12.4: Tug link configuration per operational mode.

Mode	Data Rate Class
Safe Mode	LOW
Commissioning	LOW
Long-Range Rendezvous	LOW
Capture and Control	LOW
Standby	LOW

Note: All modes operate on S-band via 2× SBA3 antennas. LOW < 10 kpbs (UL 2 kpbs / DL 3.8 kbps across all modes).

12.4. Data Rates

This section establishes the data rate allocations for the REAVER communication architecture. The TT&C housekeeping rates are derived for both the Mothership and Tugs, using a sensor summation approach to capture the sampling and quantisation requirements of each subsystem. The payload data rate budget is then developed from first principles for the mothership sensor suite, which includes optical, infrared, and LiDAR cameras, and drives the sizing of the X-band downlink established in section 12.5.

TT&C Data Rate Allocation

The TT&C data rates are established to guarantee robust command verification and comprehensive health and status monitoring. These data rates establish the sizing requirements for the S-band link budget margins. The data allocations are summarised in table 12.5.

Table 12.5: TT&C Data Rate Allocations for REAVER Architecture

Spacecraft Element	Link Direction	Assigned Data Rate
Mothership	Uplink (UL)	2000 bit/s
	Downlink (DL)	4000 bit/s
Tug	Uplink (UL)	2000 bit/s
	Downlink (DL)	3800 bit/s

Downlink Data Rate Derivation (Housekeeping Telemetry)

The housekeeping (HK) telemetry downlink rates are derived using a sensor summation equation to account for the real-world operational sampling requirements of individual subsystems (e.g., Thermal, Power, AOCS, and Propulsion) [71]. The baseline data rate is calculated as equation (12.2), where N_i is the number of parameters within sensor group i, f_i is the sampling frequency of group i (Hz), b_i is the quantisation bit depth of group i (bits), α_{overhead} is the protocol encapsulation overhead factor, and M_{margin} is the design engineering margin factor.

$$R_{\text{total}} = \left(\sum_{i=1}^{n} N_i \cdot f_i \cdot b_i \right) \cdot (1 + \alpha_{\text{overhead}}) \cdot (1 + M_{\text{margin}}) \tag{12.2}$$

To ensure compatibility with international ground station networks, the data stream is packetised according to the CCSDS Space Packet Protocol standard, introducing a standard packet overhead (α_{overhead}) of approximately 15% [10]. To account for early-stage design phases, a 20% engineering margin (M_{margin}) is applied to compensate for overestimating data rates in link budget calculations.

- **Mothership Downlink (4000 bit/s):** Accommodates the broader distribution of core sensors alongside the health, status, and diagnostic telemetry lines originating from the main optical and LIDAR payloads.
- **Tug Downlink (3800 bit/s):** Adjusted slightly lower to reflect a simpler architecture, focusing primarily on high-frequency AOCS and electrical propulsion parameter tracking necessary for proximity operations and capture phases.

Uplink Data Rate Derivation (Telecommand)

A uniform uplink rate of 2000 bit/s is allocated for both the Mothership and the Tug. This rate aligns with standard components of the shelf (COTS) S-band transponder capabilities to maximise the command link margin (E_b/N_0) during anomaly scenarios.

An uplink rate of 2000 bit/s provides sufficient throughput to transmit real-time critical telecommands and critical updates without inducing operational latency. Furthermore, it remains low enough to optimise the uplink

threshold and preserve high command link margins even under worst-case geometry or anomaly safe-mode attitudes.

Payload Data Rate Budget

This section presents the theoretical data-rate calculations for the mothership payload. The configuration contains six Jena-Optronik ASTROhead optical cameras[7], four Malin ECAM-IR3A infrared cameras[8], and one Jena-Optronik RVS 3000-3D LiDAR[9]. Calculations are derived from fundamental digital signal processing principles and rely on hardware specifications from the respective manufacturer's datasheets. Protocol overhead is accounted for via an applied system margin.

Optical Camera Configuration (ASTROhead)

The primary optical configuration utilises the FaintStar CMOS sensor. The uncompressed data rate (R_{cam}) for a single digital camera is the product of its spatial resolution, bit depth, number of colour channels, and frame rate given as equation (12.3), where the variables are defined by the Jena-Optronik ASTROhead datasheet: W is the horizontal resolution (1024 pixels), H is the vertical resolution (1024 pixels), D is the bit depth per pixel (12 bits), C is the number of color channels (1), and F is the frame rate (4 Hz).

$$R_{cam} = W \times H \times D \times C \times F \tag{12.3}$$

Calculating the raw rate for a single optical head yields approximately 50.33 Mbps. For the full setup of $N_{cam} = 6$ cameras, the total raw data rate is $\approx$ 302.0 Mbps.

Infrared Camera Suite (ECAM-IR3A)

REAVER utilises four Malin ECAM-IR3A cameras. Using equation (12.3), the raw data rate is calculated based on the specifications provided by the manufacturer: $W \times H = 640 \times 480$ pixels, $D = 16$ bits, $C = 1$ channel (monochromatic), and $F = 12$ Hz. The raw data rate evaluates to 58.98 Mbps per camera. For $N_{ir} = 4$ active infrared cameras operating uncompressed, the total infrared data rate is 235.92 Mbps.

Rendezvous and Docking LiDAR (RVS 3000-3D)

Unlike two-dimensional electro-optical sensors, the RVS 3000-3D utilises a 2D gimbal-mounted scanning mirror. The data rate is a function of the Pulse Repetition Frequency (PRF) and the payload size per returned 3D point (B_{point}). The data rate can be calculated by equation (12.4).

$$R_{lidar} = PRF \times B_{point} \tag{12.4}$$

According to the Jena-Optronik RVS 3000-3D technical specifications, PRF = 120,000 Hz (maximum scanning capacity) and $B_{point} = 96$ bits (standard pointing payload: range, azimuth, elevation, intensity, timestamp). This results in a raw LiDAR data rate of 11.52 Mbps. Because this data requires internal spacecraft routing within the onboard computer for real-time pose estimation, it remains uncompressed over the spacecraft bus.

Total Payload Data Rate and Margin

To account for SpaceWire packet headers, CCSDS framing, and associated housekeeping/time-sync telemetry, a protocol margin (M) of 15% (1.15) is applied to the payload data rate. Applying the margin to the sum of the active payload sensors (equation (12.5)) results in a maximum functional data generation rate for the payload suite of **631.856 Mbps**. Because the mission concept of operations requires this payload data to be downlinked directly from the mothership, this data rate serves as the driving requirement for the mothership-to-ground communication link and dictates the sizing of the mothership's onboard transmitter.

$$R_{total} = \left(R_{cam} + \sum R_{ir} + R_{lidar}\right) \times M \tag{12.5}$$

12.5. Link Budget

The link budget analysis verifies that all active radio frequency paths achieve positive link margins under worst-case operating conditions, thereby confirming that the hardware selections and frequency allocations defined in sections 12.1 and 12.3 are sufficient to support the data rate classes established in section 12.4. All

[7] https://indico.esa.int/event/321/contributions/6361/attachments/4359/6581/210922_ESA-CSID_JOP-GNC-Sensors-for-in-Orbit-Servicing.pdf [accessed on 11 June 2026]

[8] https://www.msss.com/files/ECAM-IR3A.pdf [accessed on 11 June 2026]

[9] https://www.jena-optronik.de/products/rendezvous-sensors/rvs-3000-3d.html [accessed on 11 June 2026]

budgets are evaluated at the worst-case GEO slant range, derived at the minimum admissible elevation angle of 5° over the Estrack network, corresponding to a worst-case slant range of 41 849 km. Table 12.6 lists the parameters common to all link computations. Relevant link budget calculations are provided below.

Table 12.6: Shared input parameters for the REAVER link budget.

Parameter	Symbol	Value	Unit	Note / Source
Orbit altitude (worst-case)	h	36500000	m	GEO band, worst case
Earth equatorial radius	R_E	6378100	m	
Min. elevation angle	α	5	deg	ESA Estrack worst-case [10]
Zenith atm. attenuation	L_{a0}	0.035	dB	
Boltzmann constant	k_b	$1.38064923 \times 10^{-23}$	J/K	
Speed of light	c	299792458	m/s	

Worst-case slant range: The worst-case slant range d is computed at the minimum admissible elevation angle $\alpha = 5°$ [107] by applying the law of cosines to the Earth-GS-spacecraft triangle using equation (12.6).

$$d = R_E \left(\sqrt{\left(\frac{h + R_E}{R_E} \right)^2 - \cos^2 \alpha} - \sin \alpha \right) \tag{12.6}$$

Gain: The gain of a circular parabolic dish with aperture efficiency η, physical diameter D, and frequency f in gigahertz is given by equation (12.7) [108], where $C_\eta = 10 \log_{10}(\eta \pi^2 \times 10^{18}/c^2)$. Two aperture efficiency values are applied depending on antenna type [109]:

- **Large parabolic dish antennas** (Estrack 15 m GS dishes, S-band spacecraft dish): $\eta = 0.55$.
- **Compact X-band transmit aperture** ($A_{t,X} = 0.04\ \text{m}^2$): $\eta = 0.60$, consistent with the flat-aperture geometry of a compact patch array. Gain is computed directly as $G = 10 \log_{10}[\eta(4\pi A_{t,X} f^2/c^2)]$.

$$G[\text{dBi}] = 20 \log_{10} D + 20 \log_{10} f[\text{GHz}] + C_\eta \tag{12.7}$$

Equivalent Isotropic Radiated Power (EIRP): The EIRP is given in logarithmic form by equation (12.8), where band-specific values of P_{TX}, L_{TX}, and G_{TX} are listed in Table 12.8.

$$\text{EIRP}[\text{dBW}] = P_{\text{TX}} - L_{\text{TX}} + G_{\text{TX}} \tag{12.8}$$

Free-Space Path Loss (FSPL): FSPL over slant range d is given by equation (12.9) [107]. Separate FSPL values are computed for each operating frequency; Table 12.7 lists the three wavelengths and corresponding path losses (X-band uplink is not implemented on the mothership).

$$L_{\text{FS}}[\text{dB}] = 20 \log_{10} \left(\frac{4\pi d}{\lambda} \right) \tag{12.9}$$

Table 12.7: Wavelengths and free-space path losses at worst-case slant range (d from equation (12.6)).

Link	Direction	f [GHz]	λ [m]	L_{FS} [dB]
S-Band	Uplink	2.035	0.14732	191.05
S-Band	Downlink	2.2100	0.13566	191.77
X-Band	Downlink	8.4652	0.03541	203.43

Additional Losses: A lumped additional loss term $L_x = 3$ dB is applied to all link paths, aggregating the following contributions[10]:

- Antenna pointing offset losses from TX and RX misalignment;
- Polarisation mismatch losses;

[10] `https://www.itu.int/rec/R-REC-P/en` [accessed 12 June 2026]

- Atmospheric gaseous absorption (ITU-R estimates ≈0.2-0.5 dB for S-/X-band GEO paths at 5° elevation, 99% link availability);
- Rainfall attenuation: 0 dB for S-band ($f < 5$ GHz, rain is negligible [10]); 0.5 dB for X-band, folded into L_x.

Receiver Figure of Merit (G/T): The receiver figure of merit quantifies the receive chain quality as equation (12.7), where G_{RX} is given by equation (12.7). Two distinct system noise temperatures are applied:

- **Spacecraft receiver (S-band uplink RX):** $T_{\text{sys,SC}} = 614$ K, reflecting the warm-Earth illumination of the receive antenna and uncooled receiver chain at GEO altitude.
- **Ground station receiver (downlink RX):** $T_{\text{sys,GS}} = 135$ K, consistent with the cryogenically cooled LNA of the Estrack 15 m dish.

$$\frac{G}{T}[\text{dB/K}] = G_{\text{RX}} - 10\log_{10}(T_{\text{sys}}) \tag{12.10}$$

Received Energy-per-Bit to Noise Density (E_b/N_0): Substituting EIRP (equation (12.8)), path losses, and G/T (equation (12.10)) into the Friis transmission framework gives equation (12.11) [107], where B_r is the information bit rate in bits/s.

$$\frac{E_b}{N_0}[\text{dB}] = \text{EIRP} - L_{\text{FS}} - L_x + \frac{G}{T} - 10\log_{10}(k_b) - 10\log_{10}(B_r) \tag{12.11}$$

Link Margin: The link margin is given by equation (12.12). The standard design threshold is LM $\geq$ 3 dB [109]. A required $(E_b/N_0)_{\text{req}} = 5$ dB is applied to all links, corresponding to BPSK modulation with rate-1/2 convolutional coding at BER $\leq 10^{-5}$ [107].

$$\text{LM}[\text{dB}] = \frac{E_b}{N_0} - \left(\frac{E_b}{N_0}\right)_{\text{req}} \tag{12.12}$$

Band-Specific Input Parameters

Table 12.8 lists the S-band and X-band specific parameters for the mothership.

Table 12.8: S-band and X-band input parameters (mothership).

Parameter	Symbol	Value	Unit	Note
S-Band (HK / TT&C)				
TX frequency (uplink)	$f_{\text{UL,S}}$	2.035	GHz	S-band UL
RX frequency (downlink)	$f_{\text{DL,S}}$	2.2100	GHz	Ratio 240/221 [10]
Transmitter power	P_S	18	W	
TX feed/cable efficiency	$L_{t,S}$	0.9	-	
TX antenna diameter (SC)	$D_{t,S}$	0.065	m	
GS RX antenna diameter	$D_{r,S}$	15	m	Estrack
SC system noise temp.	$T_{\text{sys,UL}}$	614	K	
GS system noise temp.	$T_{\text{sys,DL}}$	135	K	Estrack
Rain attenuation	$L_{\text{rain,S}}$	0	dB	$f < 5$ GHz [10]
Uplink TC bit rate	$B_{r,\text{UL,S}}$	2000	bps	
Downlink TM bit rate	$B_{r,\text{DL,S}}$	4000	bps	HK only
Required E_b/N_0	$(E_b/N_0)_{\text{req}}$	5	dB	BPSK $r = 1/2$ [107]
X-Band (Payload Data)				
TX frequency (downlink)	$f_{\text{DL,X}}$	8.4652	GHz	ITU-R X-band DL alloc. [10]
Transmitter power	P_X	18	W	
TX feed/cable efficiency	$L_{t,X}$	0.9	-	
SC TX antenna area	$A_{t,X}$	0.04	m^2	Compact aperture
GS RX antenna diameter	$D_{r,X}$	15	m	Estrack
GS system noise temp.	$T_{\text{sys,DL,X}}$	135	K	Estrack
Rain attenuation	$L_{\text{rain,X}}$	0.5	dB	Folded into L_x [10]
Downlink data rate	$B_{r,\text{DL,X}}$	631856000	bps	Payload data
Required E_b/N_0	$(E_b/N_0)_{\text{req}}$	5	dB	BPSK $r = 1/2$ [107]

Link Budget Results

Table 12.9 summarises the computed intermediate quantities and final link margins for all communication links, following the equation chain defined above. The tug vehicles carry only S-band HK/TT&C links; no

X-band payload data link is required. The tug budget uses identical RF parameters to the mothership S-band configuration (same transmitter power, antenna geometry, and GS interface), with the HK telemetry downlink rate reduced to $B_{r,\mathrm{DL,S}}^{\mathrm{tug}} = 3800$ bps.

Table 12.9: Link budget results - mothership and tugs (all values in dB unless noted).

	Mothership			**Tug**	
	S-Band		**X-Band**	**S-Band**	
Parameter	Uplink	Downlink	Downlink	Uplink	Downlink
P_{TX} [dBW]	12.55	12.55	12.55	12.55	12.55
L_{TX} [dB]	0.46	0.46	0.46	0.46	0.46
G_{TX} [dBi]	0.23	0.95	23.81	0.23	0.95
EIRP [dBW]	**12.32**	**13.04**	**35.91**	**12.32**	**13.04**
L_{FS} [dB]	191.05	191.77	203.43	191.05	191.77
L_x [dB]	3.00	3.00	3.00	3.00	3.00
G_{RX} [dBi]	47.49	48.21	59.87	47.49	48.21
T_{sys} [K]	614	135	135	614	135
G/T [dB/K]	19.61	26.91	38.57	19.61	26.91
B_r [bps]	2000	4000	631856000	2000	3800
$10\log_{10}(k_b B_r)$ [dBW/K]	−195.57	−192.57	−137.96	−195.57	-
E_b/N_0 **[dB]**	**33.47**	**37.76**	**8.64**	**33.47**	**37.98**
$(E_b/N_0)_{\mathrm{req}}$ [dB]	5.00	5.00	5.00	5.00	5.00
Link Margin [dB]	**28.47**	**32.76**	**3.64**	**28.47**	**32.98**
Status	✓	✓	✓	✓	✓

All five links close; the mothership X-band downlink is the most constrained at 3.64 dB, just above the 3 dB design threshold, driven by the 631.856 Mbps payload data rate and compact transmit aperture ($A_{t,X} = 0.04$ m^2, $\eta = 0.60$).

Summary of Design Drivers

The link budget analysis leads to the following design conclusions:

1. **Sizing case - X-band downlink.** With a margin of 3.64 dB, this link is the critical design constraint, computed at the worst-case GEO slant range ($h = 36500$ km, $\alpha = 5°$); operations at higher elevation angles improve all margins. Any increase in payload data rate, reduction in transmit power, or pointing degradation risks the 3 threshold; increasing the X-band transmit aperture or applying onboard data compression are the primary mitigation paths.
2. **S-band links are well-margined.** All S-band links (Mothership and Tugs) achieve margins above 28 dB, providing robust HK/TC connectivity with substantial margin for contingency operations.

12.6. Communications Block Diagram

Figure 12.1 shows the communication block diagram for the TT&C subsystem.

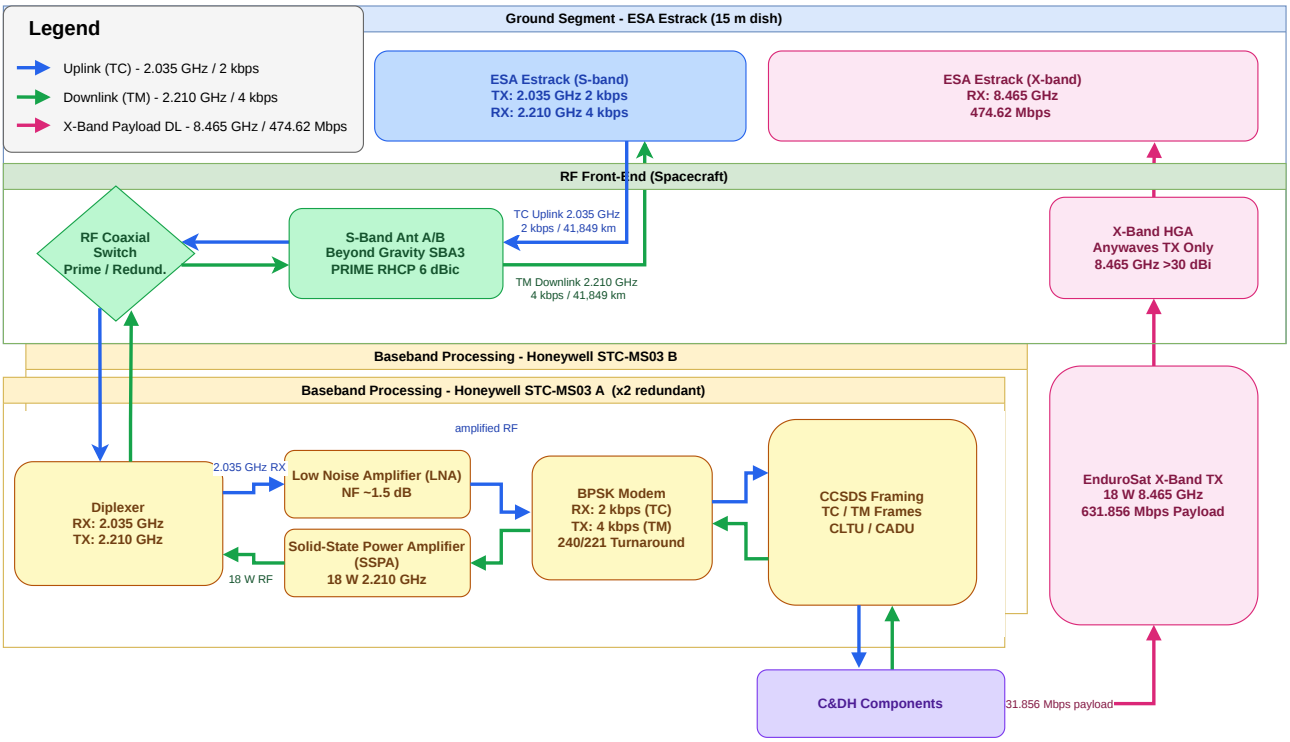

Figure 12.1: Communication Block Diagram

12.7. TT&C Mass and Power Budget

Table 12.10 presents the mass budget, and table 12.11 presents the power budget.

Table 12.10: TT&C Mass Budget

Component Name	S/C	Qty	Unit Mass (kg)	CBE (kg)	AEP (kg)
Beyond Gravity S-band helix TTC antennas - SBA3	MS	2	0.235	0.47	0.49
S-Band TT&C Transceiver STC-MS03 *(Includes diplexer & local RF harness)*	MS	2	1.250	2.50	2.63
Anywaves High-Gain X-Band Antenna	MS	2	0.605	1.21	1.27
EnduroSat X-Band Transmitter	MS	2	0.270	0.54	0.57
Beyond Gravity S-band helix TTC antennas - SBA3	Tug	2	0.235	0.47	0.49
S-Band TT&C Transceiver STC-MS03 *(Includes diplexer & local RF harness)*	Tug	1	1.250	1.25	1.31

Table 12.11: TT&C Power Budget (Prioritizing Critical Ops)

Component Name	S/C	Prox Ops (W)	Capture (W)	Peak (W)	Background (W)
Beyond Gravity S-band helix TTC antennas - SBA3	MS	0	0	0	0
S-Band TT&C Transceiver STC-MS03 *(Includes diplexer & local RF harness)*	MS	8	8	18	4
Anywaves High-Gain X-Band Antenna	MS	0	0	0	0
EnduroSat X-Band Transmitter	MS	16	16	18	0
Beyond Gravity S-band helix TTC antennas - SBA3	Tug	0	0	0	0
S-Band TT&C Transceiver STC-MS03 *(Includes diplexer & local RF harness)*	Tug	8	8	18	4

*Background Ops summarises average power draw during Safe, Commissioning, Long range rendezvous, and Standby.

12.8. Verification of TT&C Subsystem Requirements

Section 12.8 presents the final version of the TT&C requirements, including the direct link to their parent requirements, the verification method and whether compliance is met.

Table 12.12: TT&C subsystem requirements, and requirement IDs

ID	TT&C Subsystem Requirement	Parent Requirement	Method	Check
Mothership				
REQ-TTC-M1	The mothership TT&C system shall transmit all telemetry and receive all telecommands using frequency bands exclusively licensed to the mission operator under International Telecommunication Union (ITU) Radio Regulations.	REQ-SYS-13, REQ-STK-10	I	Yes
REQ-TTC-M2	The mothership TT&C system shall support a minimum housekeeping downlink data rate of 4 kbps during nominal operations.	REQ-SYS-14, REQ-STK-10	T	TBD
REQ-TTC-M3	The mothership TT&C system shall support a minimum payload downlink data rate of 474.62 Mbps during nominal operations.	REQ-SYS-14, REQ-STK-10	T	TBD
REQ-TTC-M4	The mothership TT&C system shall support a minimum housekeeping uplink data rate of 2 kbps during nominal operations.	REQ-SYS-15, REQ-STK-10	T	TBD
REQ-TTC-M5	The mothership TT&C system shall comply with the ITU and European Telecommunications Standards Institute (ETSI) frequency coordination regulations and shall not cause harmful interference to other GEO operators.	-	I	Yes
REQ-TTC-M6	The mothership shall maintain safe autonomous operations during any unplanned communication outage of up to 72 minutes without ground intervention.	-	A	Yes
Tugs				
REQ-TTC-T1	The tug TT&C system shall maintain direct S-band RF communications with the ESA Estrack ground segment at a worst-case slant range of up to 41 849 km.	REQ-SYS-13	A	Yes
REQ-TTC-T2	The tug TT&C system shall support a minimum housekeeping uplink data rate of 2 kbps during nominal operations.	REQ-SYS-13	T	TBD
REQ-TTC-T3	The tug TT&C system shall support a minimum housekeeping downlink data rate of 3.8 kbps during nominal operations.	REQ-SYS-13	T	TBD
REQ-TTC-T4	The tug TT&C system shall transmit housekeeping (HK) telemetry and mission data directly to Ground Operations independently of the mothership.	REQ-SYS-13, REQ-SYS-14	T	TBD
REQ-TTC-T5	The tug TT&C system shall maintain a bidirectional communication link with the mothership during RPOD.	REQ-SYS-13, REQ-SYS-18	T	TBD
Universal				
REQ-TTC-U1	The TT&C subsystem shall transmit housekeeping (HK) telemetry and mission data to Ground Operations.	REQ-SYS-13, REQ-SYS-14	T	TBD
REQ-TTC-U2	The TT&C subsystem shall interface with all mission-critical subsystems.	REQ-SYS-13	D	Yes

Requirements verified by test (T) will be validated through RF link performance testing conducted during the spacecraft integration and test (I&T) phase. Data rate requirements (REQ-TTC-M2, REQ-TTC-M3, REQ-TTC-M4, REQ-TTC-T2, REQ-TTC-T3) will be verified via end-to-end communication tests using a ground support equipment (GSE) RF chain, confirming that the measured downlink and uplink throughputs meet or exceed the specified minimums under worst-case link-margin conditions. REQ-TTC-T4 and REQ-TTC-U1 will be verified through functional tests in which each vehicle autonomously downlinks a complete housekeeping telemetry frame to a simulated Estrack ground station without routing through the mothership. REQ-TTC-T5 will be verified by a proximity operations communications test, exercising the inter-spacecraft link at representative RPOD ranges and confirming bidirectional data exchange at the required rates.

13. Consolidated System Budgets and Performance Analysis

This chapter consolidates the subsystem budgets developed in the previous chapters and checks whether the integrated REAVER design closes at the system level. The purpose is to show that the mass, power, cost, ΔV, pointing, link, memory and structural margins are mutually consistent. In case of a **TBD** value within a subsystem, the item is left open.

13.1. Budget and Margin Philosophy

The consolidated budgets use the current best estimate values. For mass and power, design margins are included at the subsystem level. The consolidated budget checks whether the integrated system still satisfies the launch, power-generation, communication and mission-duration constraints. The margin philosophy is summarised in table 13.1.

Table 13.1: Budget margin philosophy used in the consolidated performance analysis

Budget	Margin treatment	Closure criterion
Mass	Subsystem contingencies are retained in the subsystem budgets. The launch check uses the integrated launch mass including kick stage.	Integrated launch mass shall remain below Falcon 9 GTO capability.
Power	The operational power values used for EPS sizing already include a 20% system-level margin. No additional margin is applied here.	Solar array and battery shall meet the EOL sizing cases.
Cost	The current programme estimate is compared both to the original 200 MEUR target and to the expected base-case revenue.	Cost shall remain commercially recoverable over the base mission.
ΔV	Propellant budgets are taken from the astrodynamics and propulsion sizing.	Mothership and tugs shall meet their required manoeuvre budgets.
Link	Link margins are checked against a minimum 3 dB design margin.	All command, telemetry and payload links shall close.
Memory	Storage is sized for the maximum payload data generated during a ground-contact outage.	On-board storage shall cover at least one 72 min outage with 20% margin.
Structure	Structural margins are taken from the limiting primary-truss checks.	Static strength, buckling and first-mode frequency requirements shall be positive.

13.2. Mass Budget

The mass budget is consolidated using the Current Best Estimate (CBE), Maximum Expected Value (MEV), and the system-level contingency applied to the mothership and tug dry masses. The subsystem-level mass is summarised in table 13.2.

Table 13.2: Current Best Estimate, Maximum Expected Value, and allocated mass budgets for the mothership and tug

Subsystem	MS CBE [kg]	MS MEV [kg]	Tug CBE [kg]	Tug MEV [kg]
TCS	48.5	53.35	13.3	14.63
Payload	133.2	154.86	17.4	20.52
C&DH	14.8	16.28	8.6	9.46
Propulsion	122	132	32.7	35.0
AOCS	42.178	44.2869	17.538	18.4149
Structures	229.44	252.384	33.15	36.465
EPS	82.8	90.69	21.66	24.643
TT&C	4.72	4.956	1.72	1.806
Total dry subsystem mass	**677.91**	**748.77**	**146.14**	**160.96**

A 20 % system-level contingency is applied to the MEV dry mass. This gives a mothership dry mass of 898.52 kg and a single-tug dry mass of 193.15 kg. The mothership propellant mass is 1019.3 kg before the RCS and residual margin, and 1172.20 kg after. The resulting mothership wet mass is therefore 2070.71 kg. For the tug system,

the propellant allocation is not uniform between tugs, since the individual tug transport duties differ. The tug propellant allocation is summarised in table 13.3. All five tugs combined including the same system-level contingency as for the mothership gives a total tug fleet wet mass of 1294.87 kg.

Table 13.3: Tug propellant mass budget

Item	Required [kg]	Required with margins [kg]	Optimal load [kg]
Tug 1 propellant mass	99.6	114.54	114.54
Tug 2 propellant mass	29.0	33.35	114.54
Tug 3 propellant mass	28.7	33.01	33.35
Tug 4 propellant mass	10.9	12.54	33.35
Tug 5 propellant mass	17.8	20.47	33.35
Total tug propellant mass	–	–	**328.44**

The integrated mass budget is summarised in table 13.4. The reusable dry mass consists of one mothership and five tugs. The total tug wet contribution includes the dry mass of all five tugs and the total campaign tug propellant load of 328.4 kg. The resulting total system mass is 3365 kg.

Table 13.4: Integrated REAVER spacecraft mass budget

Mass item	Mass [kg]	Comment
Mothership dry mass	898.52	Mothership MEV dry mass including 20 % system-level contingency.
Five tug dry masses	965.74	Five tugs at 193.15 kg.each.
Mothership propellant mass	1172.20	Propellant mass including RCS and residual margin.
Total tug propellant mass	328.4	Total optimal tug propellant load across all five tugs.
Total REAVER spacecraft system mass	**3364.9**	Integrated spacecraft mass excluding kick stage.

The launch vehicle check includes the Star-63D kick stage, since Falcon 9 inserts the stack into GTO, and the kick stage performs the GTO-to-GEO insertion. The integrated launch mass remains below the Falcon 9 GTO capability, as shown in table 13.5.

Table 13.5: Launch mass closure

Item	Mass [kg]	Status
REAVER spacecraft stack	3364.9	Current integrated design value.
Star-63D kick stage wet mass	3250	Selected kick stage.
Integrated launch mass	**6615**	Spacecraft plus kick stage.
Falcon 9 GTO payload capability	8300	Launch vehicle capability.
Launch mass margin	**1685.1**	Pass, 20.3% margin relative to Falcon 9 GTO capability.

13.3. Power Budget

The EPS sizing is driven by nominal operating modes and short peak loads. The mothership solar array is sized by proximity operations, while the tug solar array is sized by electric-propulsion long-range rendezvous. The values in table 13.6 already include the 20% system-level power margin used in the EPS subsystem.

Table 13.6: Electrical power budget closure (consistent with EPS sizing cases)

System	Sizing case	Required	Available	Status
Mothership solar array	Proximity operations (EOL, sustained load)	1764 W (BOL req.)	1818 W (BOL)	Pass. Array meets BOL requirement with 3.1% margin; EOL requirement is 1534 W as derived from sizing.

System	Sizing case	Required	Available	Status
Mothership battery energy	Eclipse survival (72 min standby)	380 Wh	1568 Wh	Pass. Eclipse energy requirement is comfortably met with significant margin.
Mothership peak power support	Capture peak load buffering (10 min minimum)	3656 W peak (deficit = 2153 W)	1129 Wh usable battery energy	Pass. Battery can sustain peak deficit for ≈31 min, exceeding 10 min requirement.
Mothership PCDU peak bus capability	Peak bus operation	3656 W	4000 W	Pass. PCDU provides sufficient peak power handling margin (344 W).
Tug solar array	Long-range rendezvous (EP thrusting, EOL)	1912 W (BOL req.)	1952 W (BOL) / 1698 W (EOL)	Pass. Positive margin at both BOL and EOL; EOL requirement is 1663 W.
Tug battery energy	Eclipse survival (standby mode)	182 Wh	252 Wh	Pass. Battery exceeds eclipse requirement with 39% margin.
Tug power during eclipse	Standby load (no thrusting)	109 W (72 min)	109 W supported (battery only)	Pass. Eclipse mode is fully supported without solar input.

13.4. Cost Budget

The current one-year campaign cost estimate is 249.5 M€. This is higher than the original 200 M€ target, refer to section 15.3 and section 15.4

Table 13.7: Cost and revenue closure for the base mission

Item	Value [M]€	Interpretation
Original programme cost target	200	Initial target used in the business
Current one-year campaign estimate	249.5	Updated integrated cost estimate.
Base mission revenue	300	Five removals at 60 M€per removal.
Margin relative to original target	50.5	Not closed if 200 M€remains a hard requirement.
Margin relative to base revenue	+0.5	Only 0.4% revenue margin.

The cost result implies that the base mission is near break-even rather than strongly profitable. The extended mission case remains much stronger, since the same reusable mothership and tug architecture can perform additional captures after hub refuelling. Nevertheless, supplier quotations, test costs, insurance, operations staffing and contingency should be refined before claiming a robust positive return on investment.

13.5. ΔV Budget

The ΔV budget is split between the kick stage, the mothership and the tugs. The kick stage performs the GTO-to-GEO insertion, the mothership performs the inter-target transfer and phasing campaign, and the tugs perform low-thrust transport of captured debris to the recycling hub.

Table 13.8: Consolidated ΔV and propellant budget

Vehicle / function	Requirement	Current design value	Status
Kick stage GTO-to-GEO insertion	1500 m/s	1830 m/s capability	Pass; approximately 330 m/s insertion margin.
Mothership main campaign transfers	1200 m/s	1172.2 kg LMP-103S allocated	Pass
Mothership fine control and RCS	-	20% margin included in propellant mass allocation	Pass at budget level; closed-loop residual velocity tests remain required.
Tug debris transport	≥ 600 m/s attached to 2000 kg debris	328.4 kg xenon campaign allocation	Pass
Mission duration	5 captures in 365 d	291.4 d nominal	Pass; 74 d schedule margin.

The ΔV budget therefore closes at the system level. The two remaining sensitivities are the final target sequence and the tug electric-propulsion throughput. These should remain tied to the astrodynamics sensitivity analysis, since target mass and orbital plane selection directly affect the tug transport time and xenon consumption.

13.6. Pointing Accuracy Budget

The pointing budget combines AOCS state-estimation performance, relative navigation performance, thrust-vector pointing and capture-interface alignment. The current AOCS and capture chapters define several requirements that still require final numerical closure. Therefore, this section distinguishes between closed values and open interface values.

Table 13.9: Pointing and navigation performance budget

Function	Current value	Driver	Status
Mothership absolute state determination	100 m, 1 m/s, 5°, 0.5°/s	Long-range rendezvous and orbit control manoeuvres	Defined; verification by test is still TBD.
Mothership absolute state control	0.3 m/s, 1°, 0.1°/s	Long-range rendezvous and orbit control manoeuvres	Defined; verification by test is still TBD.
Mothership relative state determination	0.05 m, 0.01 m/s, 2°, 0.5°/s	Proximity operations, capture, and control	Defined; verification by test is still TBD.
Mothership relative state control	0.05 m, 0.01 m/s, 2°, 0.5°/s	Proximity operations, hold operations, and capture alignment	Defined; verification by test is still TBD.
Mothership thrust-vector pointing	$< 1°$	Orbit-control manoeuvre execution	Defined; verification by analysis is still TBD.
Mothership orbit-control execution	< 0.3 m/s ΔV execution error	Orbit-control manoeuvre execution	Defined; verification by analysis is still TBD.
Capture-interface alignment	$< 2°$ angular error	Capture operations	Defined; verification by demonstration is still TBD.
Tug absolute state determination	100 m, 1 m/s, 5°, 0.5°/s	Debris transport and thrust-vector pointing	Defined; verification by test is still TBD.
Tug absolute state control	0.1 m/s, 2°, 0.5°/s	Debris transport and orbit-control manoeuvres	Defined; verification by test is still TBD.
Tug thrust-vector pointing	$< 2°$	Orbit-control manoeuvre execution	Defined; verification by analysis is still TBD.
Tug orbit-control execution	< 0.1 m/s ΔV execution error	Tug transport correction	Defined; verification by analysis is still TBD.

The largest open item is not the thrust-vector authority, but the capture-interface alignment budget. The final report should therefore avoid claiming full pointing-budget closure until the capture positional and angular tolerances are defined. At system level, the current design is feasible because the relative navigation sensor suite is sized for centimetre-level position knowledge and the main-thruster gimbal has sufficient authority to compensate the worst-case CG offset.

13.7. Link Budget

The communication architecture uses S-band for housekeeping telemetry and telecommand, and X-band for the high-rate mothership payload downlink during proximity and capture operations. The link budgets are computed at the worst-case GEO slant range and checked against a 3 dB minimum link-margin criterion.

Table 13.10: Consolidated link budget summary

Link	Data rate	E_b/N_0 [dB]	Margin [dB]	Status
Mothership S-band uplink	2 kbps	33.47	28.47	Pass; large telecommand margin.
Mothership S-band downlink	4 kbps	37.76	32.76	Pass; large housekeeping margin.
Mothership X-band downlink	631.856 Mbps	8.64	3.64	Pass, but critical; only 0.64 dB above 3 dB design margin.
Tug S-band uplink	2 kbps	33.47	28.47	Pass; same S-band uplink sizing as mothership.
Tug S-band downlink	3.8 kbps	37.98	32.98	Pass; large housekeeping margin.

The link budget closes, but the X-band payload downlink is the critical communication margin. Any increase in payload data rate, antenna pointing loss or atmospheric attenuation may remove the remaining margin. The main mitigation options are on-board payload compression, downlink duty-cycle management, a larger X-band aperture or reducing the number of simultaneously downlinked raw sensor streams.

13.8. Memory Sizing

The on-board memory requirement is driven by RPOD sensor data rather than housekeeping telemetry. The C&DH chapter identifies the need for an external solid-state recorder, since internal processor memory is not adequate for mission data logs. The minimum storage requirement is therefore derived from the maximum payload data rate and the maximum unplanned communication outage.

For a data rate R, outage duration t and storage margin m_s, the required memory is given by equation (13.1). Using the conservative payload generation rate of 631.856 Mbps, a 72 min outage and a 20% storage margin gives 409GB.

$$D_{\text{req}} = \frac{Rt}{8}(1 + m_s) \tag{13.1}$$

Table 13.11: On-board memory sizing summary

Data source	Rate	72 min storage	Sizing relevance
Mothership payload data	631.856 Mbps	341 GB	Dominant storage driver.
Mothership housekeeping	4 kbps	2.2 MB	Negligible compared with payload data.
Tug housekeeping	3.8 kbps per tug	2.1 MB per tug	Negligible; can be stored locally or relayed after contact.
Telecommand queue	2 kbps	1.1 MB	Negligible; important for autonomy but not for storage capacity.
Minimum mothership SSR	–	**409 GB incl. 20% margin**	A 0.5 TB SSR is the minimum practical selection; 1 TB is recommended for operations margin, with current design value at 1.25 TB.

The recommended mothership storage requirement is therefore set to at least 0.5 TB, with 1 TB preferred to allow multiple contact gaps, packet retransmission, metadata, compression buffers and fault-tolerant file handling. The tug storage requirement is much smaller and is not a sizing driver unless future tug autonomy requires local storage of raw docking-camera footage.

13.9. Structural Characteristics Summary

The primary structure is an octagonal truss sized for the Falcon 9 launch environment. The limiting structural case is the axial natural frequency requirement, not static strength. The selected truss member dimensions are 65 mm outer diameter with 4 mm wall thickness. The consolidated structural characteristics are summarised in table 13.12.

Table 13.12: Structural characteristics and margin summary

Characteristic	Current design value	Requirement / allowable	Status
Primary material	Al 7075-T6	High specific strength and manufacturability	Selected.
Primary truss geometry	Octagonal truss, $L = 3.5$ m, $R = 1.5$ m	Fits within spacecraft configuration	Pass.
Chord member size	$d = 90$ mm, $t_w = 4$ mm	Sized by Euler buckling	Pass.
Mothership chord-member mass	84.727 kg	Primary truss chord members only	Defined; horizontal and diagonal bracing members, node fittings, and interface hardware are excluded.
Total primary structure mass	204.556 kg	Includes 30% margin on combined mothership and tug primary chord-member mass	Defined.
Total structural mass budget	395.19 kg	24% of mothership dry mass and 15% of tug dry mass	Defined.
Secondary structure mass	179.424 kg	Remaining structural mass after primary structure and radiation shielding	Defined.
Static strength	28.6 MPa	572 MPa ultimate strength	Pass; MoS = +14.99.

Characteristic	Current design value	Requirement / allowable	Status
Chord buckling	32.4 kN	P_{cr} = 131.8 kN	Pass; MoS = +1.04.
First lateral frequency	36.1 Hz	≥ 10 Hz	Pass; +26.1 Hz margin.
First axial frequency	33.9 Hz	≥ 25 Hz	Pass; +8.9 Hz margin.
Launch stack height	5.3 m	13.2 m fairing length	Pass; margin over 7 m.
Launch stack mass	7500 kg	8300 kg Falcon 9 GTO capability	Pass.

The structural design is therefore feasible at preliminary level. The main remaining structural work is to include the horizontal and diagonal truss members, secondary structures, tug attachment interfaces, local bracket sizing and coupled launch-load verification in a higher-fidelity finite-element model.

13.10. Closing Margin Health-check

The final system-level health check is shown in table 13.13. The design closes in mass, power, ΔV, communication and primary-structure performance. The main weak margins are the X-band payload link and the cost budget. The main open technical margins are the capture-interface pointing tolerance and several requirements that depend on later closed-loop testing.

Table 13.13: Closing system margin health-check

Requirement / driver	Limit	Current value	Margin	Status
Mission duration	≤ 365 d	297 d	+68 d	Pass.
Objects removed	5 per campaign	5 per campaign	Meets target	Pass.
Removed debris mass	–	10050.6 kg per campaign	–	Information only.
Falcon 9 launch mass	≤ 8300 kg	7500 kg incl. kick stage	+800 kg	Pass.
Kick-stage insertion ΔV	1500 m/s	1830 m/s	+330 m/s	Pass.
Mothership main ΔV	≥ 1200 m/s	1380 kg LMP-103S sized	Embedded	Pass at budget level.
Tug transport ΔV	≥ 600 m/s	Xenon budget sized	Embedded	Pass at budget level.
Mothership solar array	1534 W required	1818 W available	+284 W	Pass.
Tug solar array	1663 W required	1698 W available	+35 W	Pass, small margin.
Mothership battery eclipse	380 Wh required	1568 Wh rated	+1188 Wh	Pass.
Tug battery eclipse	182 Wh required	252 Wh rated	+70 Wh	Pass.
Mothership peak bus power	3656 W	4000 W PCDU	+344 W	Pass.
X-band payload link	≥ 3 dB margin	3.64 dB margin	+0.64 dB	Thin pass.
S-band TT&C links	≥ 3 dB margin	> 28 dB margin	> 25 dB	Pass.
Mothership SSR storage	409 GB required	1.25TB proposed	~0.841 GB	Pass if selected.
Primary truss static strength	MoS > 0	MoS = +14.99	Positive	Pass.
Primary truss buckling	MoS > 0	MoS = +1.04	Positive	Pass.
Primary truss frequencies	10 Hz lateral, 25 Hz axial	36.1 Hz, 33.9 Hz	+26.1 Hz, +8.9 Hz	Pass.
Cost against original target	≤ 200 MEUR	249 MEUR	-49 MEUR	Not closed if target is strict.
Cost against base revenue	250 MEUR revenue	249.5 MEUR cost	+0.5 MEUR	Commercially close, but low margin.
Capture-interface alignment	< 2° angular error	Verification TBD	–	Open.
Closed-loop orbit-control execution	< 0.3 m/s MS, < 0.1 m/s tug	Verification TBD	–	Open.

Overall, the REAVER design is buildable at the preliminary system level. However, several design areas still require improvement or further closure. The tug solar array margin remains small, with only 35 W excess EOL power, making the tug EPS sensitive to future power growth. The X-band payload link also has a thin margin of only 0.64 dB above the required 3 dB, and should therefore be improved or verified with a more detailed communications analysis. In addition, the cost remains a major concern, as the current cost estimate exceeds the original €200 M target, while the margin against the base revenue case is only €3 M. Finally, the capture-interface alignment and closed-loop orbit-control execution remain open verification items, meaning that the AOCS, C&DH, and capture subsystem must further close these performance tolerances during detailed design.

14. Design Assessment

This chapter evaluates the final REAVER design at the system level. First, the sustainability assessment quantifies the environmental, economic and social impact of the Mothership and Tugs architecture. The RAMS analysis then assesses the reliability, availability, maintainability and safety of the mission, identifying the main dependability and safety drivers. This is followed by the verification, validation and requirements-compliance assessment, which links subsystem-level design evidence to the mission, system, and stakeholder requirements. Finally, sensitivity analyses are used to evaluate the design's robustness to key technical and cost uncertainties before the integrated system architecture is presented.

14.1. Sustainability

At the midterm, the sustainability strategy defined the functional unit, system boundaries and main performance indicators for REAVER. In this design phase, this framework is updated to reflect the latest mass, propellant, and cost budgets, along with the reuse assumptions. The objective is to quantify whether the final Mothership and Tugs architecture provides a net sustainability benefit by removing more long-term orbital risk than it introduces through manufacturing, launch, operations and possible failure modes.

The assessment is performed as a design-level Life Cycle Sustainability Analysis (LCSA), considering environmental, economic and social dimensions. This approach follows the ESA space-system LCA logic, while the Space Sustainability Rating (SSR) is used as a qualitative benchmark for responsible mission behaviour [26].[1] [2]

The functional unit remains:

> *The recovery and delivery of five non-cooperative, defunct GEO graveyard satellites to the recycling hub per yearly campaign, using a reusable mothership and reusable tugs.*

This is more representative than assessing the spacecraft alone, since REAVER's value is measured by the amount of uncontrolled GEO debris removed. The recycling hub is treated as a shared infrastructure and is excluded from the spacecraft LCA. However, docking, debris handover, refuelling, inspection and preparation for reuse are included as operational interfaces.

Sustainability Indicators

The first indicator is the mass efficiency, defined as the amount of debris removed per kilogram launched:

$$K_{\text{mass},1} = \frac{m_{\text{debris,removed}}}{m_{\text{launched}}} \tag{14.1}$$

Using the updated mass budget, the first-campaign value is: $K_{\text{mass},1} = 2.52\,\text{kg debris/kg launched}$. This means that REAVER removes more mass from the GEO graveyard environment than it launches. Since the mothership and tugs are designed for five campaigns, the ideal reusable mass efficiency is:

$$K_{\text{mass,reuse,ideal}} = \frac{5 \times m_{\text{debris,removed}}}{m_{\text{launched}}} = 12.58\,\text{kg debris/kg launched} \tag{14.2}$$

This value is an upper bound because it excludes propellant replenishment after the first campaign and overestimates the mass of recovered defunct satellites. A more representative reuse-adjusted value includes propellant for campaigns two to five:

$$K_{\text{mass,reuse,prop}} = \frac{5 \times m_{\text{debris,removed}}}{m_{\text{launched}} + 4 \times m_{\text{prop,total}}} = 4.63\,\text{kg debris/kg supplied to orbit} \tag{14.3}$$

Even with refuelling included, the reuse value is significantly higher than the first-campaign value. Therefore, the sustainability of REAVER depends strongly on achieving the five-object removal campaign, with the impact increasing as more campaigns are completed. This value is excluded from the kick-stage because a detailed capture sequence for the kick-stage has not yet been developed. Moreover, the propellant intensity is defined as:

[1] ESA Clean Space Ecodesign, `https://www.esa.int/Space_Safety/Clean_Space/Ecodesign` [15 June 2026

[2] Space Sustainability Rating, `https://spacesustainabilityrating.org/the-rating/` [accessed 15 June 2026]

$$K_{\text{prop}} = \frac{m_{\text{prop,total}}}{N_{\text{debris}}} \tag{14.4}$$

For the updated design $K_{\text{prop}} = 342.38\,\text{kg/object}$. The chemical propulsion system dominates the value, contributing to $K_{\text{prop,chem}} = 276.0\,\text{kg/object}$, while the tug propellant contribution is $K_{\text{prop,tug}} = 66.38\,\text{kg/object}$. The total propellant consumed per kilogram of debris removed is:

$$K_{\text{prop,mass}} = \frac{m_{\text{prop,total}}}{m_{\text{debris,removed}}} = 0.170\,\text{kg propellant/kg debris} \tag{14.5}$$

The high chemical propellant use is due to the mothership performing several rendezvous and capture operations within one year, along with long transfers between orbits. The tugs still reduce the overall mission burden by avoiding the need to duplicate a full mothership-class servicing spacecraft for each target. The economic indicators are based on the updated one-year campaign cost of €247 M, further explained in chapter 15. The cost intensity per kilogram of debris removed is:

$$K_{\text{cost,1}} = \frac{C_{\text{camp}}}{m_{\text{debris,removed}}} = 24\,576\,€/\text{kg} \tag{14.6}$$

The corresponding cost per object is:

$$K_{\text{cost,obj}} = \frac{C_{\text{camp}}}{N_{\text{debris}}} = €49.4\,\text{M/object} \tag{14.7}$$

For the full five-campaign design lifetime, the cost intensity becomes:

$$K_{\text{cost,reuse}} = \frac{C_{\text{camp}} + 4 \times C_{\text{recur}}}{5 \times m_{\text{debris,removed}}} \tag{14.8}$$

where C_{recur} is the recurring cost of each additional campaign. This includes propellant replenishment, inspection, minor refurbishment, operations and target-specific planning. Since the mothership and tugs are reused, C_{recur} is expected to be much lower than the cost of the first campaign. If recurring costs are neglected, the lower-bound reuse-amortised cost intensity is $K_{\text{cost,reuse,ideal}} = 4915\,€/\text{kg}$. This value is not a final business-case cost, but it shows the economic importance of reusing the main hardware over several campaigns. Finally, the orbital sustainability benefit is quantified using the avoided uncontrolled debris mass-time:

$$K_{\text{orbital}} = m_{\text{debris,removed}} \cdot t_{\text{risk,reduced}} \tag{14.9}$$

A 100 yr assessment horizon is used to provide a finite comparison period. This does not imply that the targets would collide within 100 yr; it simply specifies the time span during which they receive credit for avoiding an uncontrolled presence. For one campaign, the five removals are assumed to occur sequentially during the year, giving an average removal time of 0.5 yr. Therefore, $t_{\text{risk,reduced,1}} = 99.5\,\text{yr}$, and $K_{\text{orbital,1}} = 1.00 \times 10^6\,\text{kg yr}$. Over five yearly campaigns, removals are assumed to occur around years 0.5, 1.5, 2.5, 3.5 and 4.5. This gives $K_{\text{orbital,5}} = 4.90 \times 10^6\,\text{kg yr}$. This value does not replace a full collision-probability model, but it gives a clear measure of the amount of uncontrolled mass removed from the GEO graveyard environment over time.

Environmental Burden

The main environmental benefit of REAVER is the removal of large, long-lived GEO debris. One campaign removes 10 051 kg of uncontrolled mass, as shown in section 3.5 for the worst-case campaign we are designing for, while the full five-campaign lifetime could be estimated to remove up to 50 253 kg. Thus, it directly supports the need for active debris removal since mitigation alone is not sufficient to stabilise the long-term debris environment [110, 111, 112, 113].

The main environmental burdens are the launch mass, spacecraft manufacturing, testing, propulsion hardware, electronics, solar arrays, batteries, robotic systems, propellant production and ground operations. The final architecture reduces all of these by avoiding the launch of a separate full-capability spacecraft for each target. Instead, the five smaller tugs, which remain as smaller transport modules, reduce subsystem duplication and distribute the manufacturing and launch burden over five campaigns.

The propulsion campaign system is also part of the sustainable trade-off. Chemical propulsion is used for the campaigns because they require high-thrust manoeuvres and repeated rendezvous operations, while electric propulsion is used for the tugs because their debris-transport transfers can tolerate longer durations. Although electric propulsion introduces power-processing hardware, solar-array area and noble-gas propellant demand, it reduces the need for high chemical propellant mass on each transport element. Therefore, this hybrid system balances operational feasibility and propellant efficiency.

Additionally, orbital sustainability is the mission's strongest positive contribution. The avoided mass-time indicator gives 1.00×10^6 kg yr for one campaign and 4.90×10^6 kg yr over the five-campaign design lifetime. In addition, the mission-generated collision risk is assessed separately using ARES/DRAMA. The midterm analysis estimated an annual collision probability of 2.373×10^{-7}, which is below the 1×10^{-4} threshold used in the collision-avoidance assessment. This value has been re-assessed using the final spacecraft mass, geometry, deployed area and trajectory assumptions. Since the final values have not changed by orders of magnitude, the updated ACP is expected to remain in the same range. However, GEO flux-based estimates can underestimate collision risk by several orders of magnitude, so the final design should retain collision-avoidance capability and should not rely only on the nominal ARES/DRAMA value [47]. The highest mission-specific collision and debris-generation risks occur during rendezvous, proximity operations, capture, tug release, debris transport and hub docking. Therefore, controlled RPOD corridors, autonomous abort modes, safe hold points, fault-tolerant capture-and-release mechanisms, trackable configurations, and decommissioning capability are required.

The mission will also remain compatible with the GEO debris mitigation practice. The GEO protected region extends approximately 200 km around the nominal GEO altitude, and IADC disposal guidance defines a minimum perigee increase using the term $235\,\text{km} + 1000 C_R A/m$ [2]. Any failed REAVER element should therefore remain trackable and outside the protected GEO region.

Economic Burden

The first-campaign cost intensity is 24 576 €/kg, corresponding to €49.4 M per removed object. This value is high because the first campaign includes the initial mothership, tugs, launch, commissioning and first year of operations. REAVER's economic argument depends on reuse. If recurring costs are kept low, the cost per kilogram removed decreases substantially over the five-campaign lifetime. In the ideal case where recurring costs are neglected, the cost intensity decreases to 4915 €/kg. In practice, the true value will lie between the first-campaign value and this lower bound. The mission also provides indirect economic value by protecting the long-term usability of GEO, as it supports high-value communication, broadcasting, meteorological, and governmental services. Removing large inactive objects reduces long-term risk to operators, insurers and institutional stakeholders.

Social Burden

The social benefit of REAVER is linked to the protection of critical space infrastructure and the responsible use of the GEO environment. As stated in the previous subsection, GEO services support many public services, and reducing the risk in this region therefore has value beyond the direct mission customer.

There are also governance challenges, as the targets require clear ownership, consent and liability agreements. In addition, rendezvous, proximity operations and robotic capture are dual-use capabilities. That is why REAVER should operate under transparent civil objectives, with documented target selection, operator authorisation, shared ephemerides [3], manoeuvre coordination and clear communication with relevant space surveillance and tracking actors.

These measures also support the Space Sustainability Rating (SSR). A formal SSR score cannot be claimed without submitting the mission to the rating process, but REAVER is expected to perform strongly in the external services and mission-index categories because its primary function is active debris removal. Additionally, it is expected that REAVER will comfortably meet the detectability and trackability category requirements, as the mission captures debris of significant size. The main remaining SSR improvement areas are final collision-risk verification, data-sharing procedures and proof of compliance with debris mitigation standards.[4][5]

14.2. RAMS Analysis

The reliability, availability, maintainability, and safety (RAMS) characteristics are used to model and quantify REAVER's dependability throughout its lifecycle.

[3] Ephemerides are tables or datasets that give the predicted positions, and sometimes velocities, of astronomical objects at specific times

[4] Space Sustainability Rating, Data Sharing Module, `https://spacesustainabilityrating.org/the-rating/modules-data-sharing/` [accessed 12 June 2026]

[5] Space Sustainability Rating, The Rating, `https://spacesustainabilityrating.org/the-rating/` [accessed 12 June 2026]

Reliability

Reliability is the likelihood that a system performs its required function without failure over a specified period of time. Evaluating the exact reliability of the entire system is complex, considering the number of COTS components used in the design, since manufacturers rarely publish such data. Performing a reliability analysis is nonetheless critical for understanding component and system failure mechanisms, and where exact numbers are missing, a qualitative analysis is performed.

To quantify reliability, the mission success criterion is defined as the capture and delivery of 5 debris in 1 year with no debris creation. The REAVER mission can then be decomposed into a series of subsystem blocks that must all work for successful mission execution. This structure is distinctive: the mothership is the dominant single-point of failure with each capture dependent on the robotic arm. The five tugs can be described as a k-out-of-5 set tolerating one tug loss as per TR-T-04. The reliability block diagram is provided in figure 14.1 where the singular mothership block flows into the parallel tug blocks. Despite the mothership as a whole constituting a singular point of failure, built-in subsystem-level redundancy can mitigate this risk.

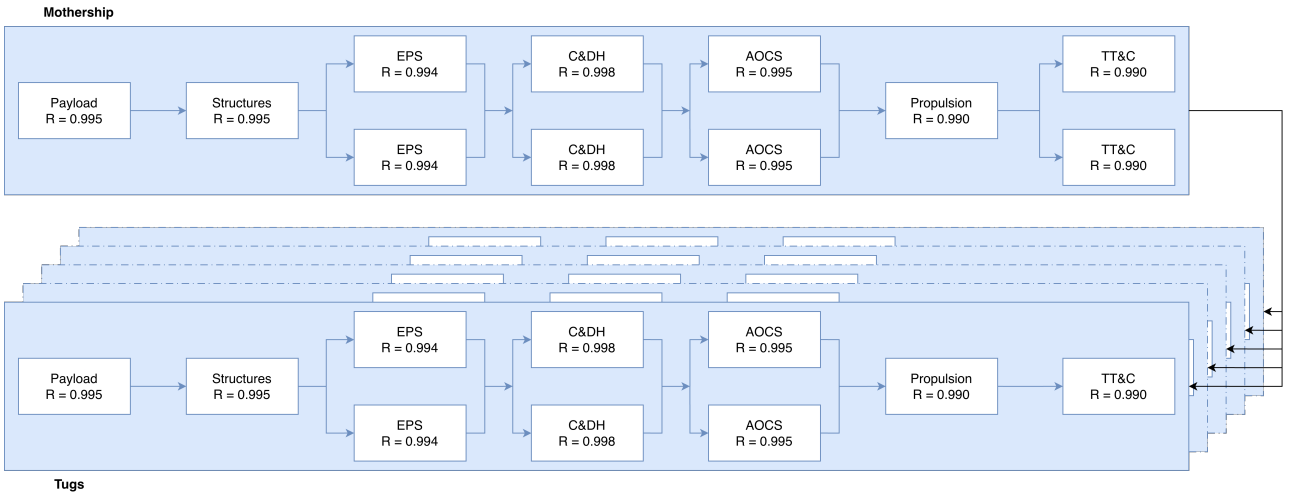

Figure 14.1: Reliability block diagram

Within each spacecraft, the dependency between subsystems means that the failure of a single subsystem has a flow-down effect on the rest. The reliability block diagram in figure 14.1 depicts this failure propagation chain: failure of a single subsystem results in the loss of all downstream subsystems that depend on it. The critical failure point of the mission is the inability to capture the debris, hence loss of the capture mechanism leads to mission failure. Following this, the complete loss of the spacecraft structure leads to a complete failure of the spacecraft system, making it the next point of failure. The chain of failure follows from the failure of the power supply, followed by command & data handling, AOCS, propulsion, and lastly communication.

Quantitatively, reliability can be estimated using equation (14.10), where t is the operational time (in hours) and λ is the failure rate. Series, and parallel reliabilities are computed using equation (14.11), and equation (14.12), respectively. The failure rate λ can be computed as the failures in time (FIT) $\times 10^{-9}$, or as inversely proportional to mean time between failures (MTBF). FIT and MTBF values are sometimes published by manufacturers and can thus be used to estimate the reliability of specific components. A table of published reliability values of COTS components is provided in table 14.1.

$$R(t) = e^{-\lambda t} \tag{14.10}$$

$$R_{series} = \Pi_i^n R_i \tag{14.11}$$

$$R_{parallel} = 1 - \Pi_i^n (1 - R_i) \tag{14.12}$$

An important note is that the software / autonomy has no λ. Autonomy is mission critical and a residual high risk even post mitigation (TR-U-10). This can be handled qualitatively. The FDIR coverage and fault tolerance of the chosen C&DH components should provide adequate redundancy for the processors running autonomous operations. Ensuring rigour in the V&V procedures is another way to assure reliability.

Subsystem	Component	FIT	MTBF	Reliability [R]	Time period [yrs]	TRL
C&DH	cOBC	-	-	0.990	10	9
C&DH	TMS570-SEP	2.41	4.153×10^8	0.999	5	-
C&DH	Total	-	-	0.998	5	-
Payload	ASTROhead cameras	215	-	0.990	5	-
Payload	Mechanisms	-	-	0.995	5	-
Payload	Total	-	-	0.998	5	-
AOCS	ASTRIX 120	-	-	0.995	5	9
AOCS	Redwire space sun sensor (fine)	-	-	-	-	9
AOCS	Bradford sun sensor (coarse)	-	-	-	-	9
AOCS	AURIGA-CP	230	-	0.989	5	9
AOCS	AMU	-	-	-	-	9
AOCS	Bradford sun sensor (fine)	70	-	0.997	5	9
AOCS	Bradford sun sensor (coarse)	6	-	0.999	5	9
AOCS	Total	-	-	0.995	5	-
TT&C	X-Band Transmitter	-	-	-	-	9
TT&C	Total	-	-	0.990	5	-
PSS	Valves	0	-	1	10	9
PSS	Pressure transducer	0	-	1	18	9
PSS	5N HPGP Thruster	-	-	-	-	5
PSS	22N HPGP Thruster	-	-	-	-	6
PSS	Total	-	-	0.990	5	-
EPS	Solar array deployment	-	-	0.9985	5	-
EPS	Solar array operating	-	-	0.996	5	-
EPS	Electrical distribution	-	-	0.994	5	-
EPS	Battery / cell	-	-	0.995	5	-
EPS	Total	-	-	0.994	5	-
Structures	Total	-	-	0.995	5	-
Thermal	Total	-	-	0.995	5	-

Table 14.1: Components with published reliability and TRL values (sourced from manufacturer data sheets)

For subsystems whose COTS components do not have published reliability values, another approach using literature values from statistical analyses is used [114] . These are also included in table 14.1. The reliability of the mothership and tugs are thus calculated as 0.980 and 0.970, respectively (purely on the basis of subsystem reliabilities). The system thus has a total reliability of 0.980.

Availability

Availability assessment is conducted as per ECSS-Q-ST-30-09C[6] outlining the standards defining the requirements regarding the availability of systems and subsystems. This can be assessed using component lead times, and the likelihood of increase in technology readiness level for components at lower technological maturity. Analysis of lead-times of the main COTS companies results in a maximum delivery time of 18 months. TRL development is much harder to estimate, with non-aerospace technologies advancing through 1-2 TRL levels during 3-4 year implementation periods. [7] For aerospace components, however, these times are assumed to be longer. The LMP-103S filter Mott at TRL7 is less of a concern than the HPGP thrusters at TRL5 and TRL6, and the high gain X-band antennas at TRL5. TRL7 signifies that the prototype operates in the real world, proving it can perform as intended under actual mission conditions. TRL5 and TRL6 entail testing in a simulated operational environment, and rigorous testing in conditions approximating the target environment. ESA missions typically require a technology to reach TRL 5 or 6 (system validation in a relevant environment) before project adoption, and TRL 8 (flight-qualified) prior to launch [115]. As long as this criteria is met at the end of development, availability is satisfied. Another mission-relevant metric for availability is schedule-completion probability P(5 captures in 365 days). This is assessed within the sensitivity analysis outlining the volatility of the schedule to technical parameters.

[6] https://ecss.nl/standard/ecss-q-st-30-09c-availability-analysis/ [accessed 17 June 2026]
[7] https://www.swisscore.org/climbing-the-trl-ladder-from-idea-to-impact/ [accessed 15 June 2026]

Maintainability

Maintainability assesses the probability that a product can be restored to operational status following a failure. Geostationary spacecraft are usually not maintainable once launched but REAVER has a unique maintainability dimension with the RH outside of the 1 year mission duration. During flight no physical repairs are possible so maintainability depends on the fraction of ground / autonomously recoverable faults. Ground can ensure maintainability through diagnostics, software updates, periodic checks of equipment performance (housekeeping data), as well as reboots and overrides of autonomous system capabilities. No maintenance exists for hardware during operations. After the mission, maintainability depends solely on the refurbishing capabilities of the RH.

Safety

Safety consists of ensuring the safety of manufacturing processes / on-ground operations, launch, use of non-toxic propellants, and the safety of the GEO environment and other operator's assets. These safety concerns are split into two domains: ground/launch, and on-orbit. The ground segment consists of handling, AIT, and component selection while on-orbit safety consists of target fragmentation during capture (debris creation), collision with an operational GEO satellite, and stored energy rupture / leak (TR-M-04). A fault tree analysis (ECSS-Q-ST-40-12C) [8] is performed for the worst catastrophic safety event (identified here as debris generation in GEO, see REQ-STK-04, REQ-STK-05, REQ-STK-06, and REQ-STK-08), with events linked to the technical risks. Similar analyses can be performed for all identified safety risks to identify and mitigate relevant safety-critical risks.

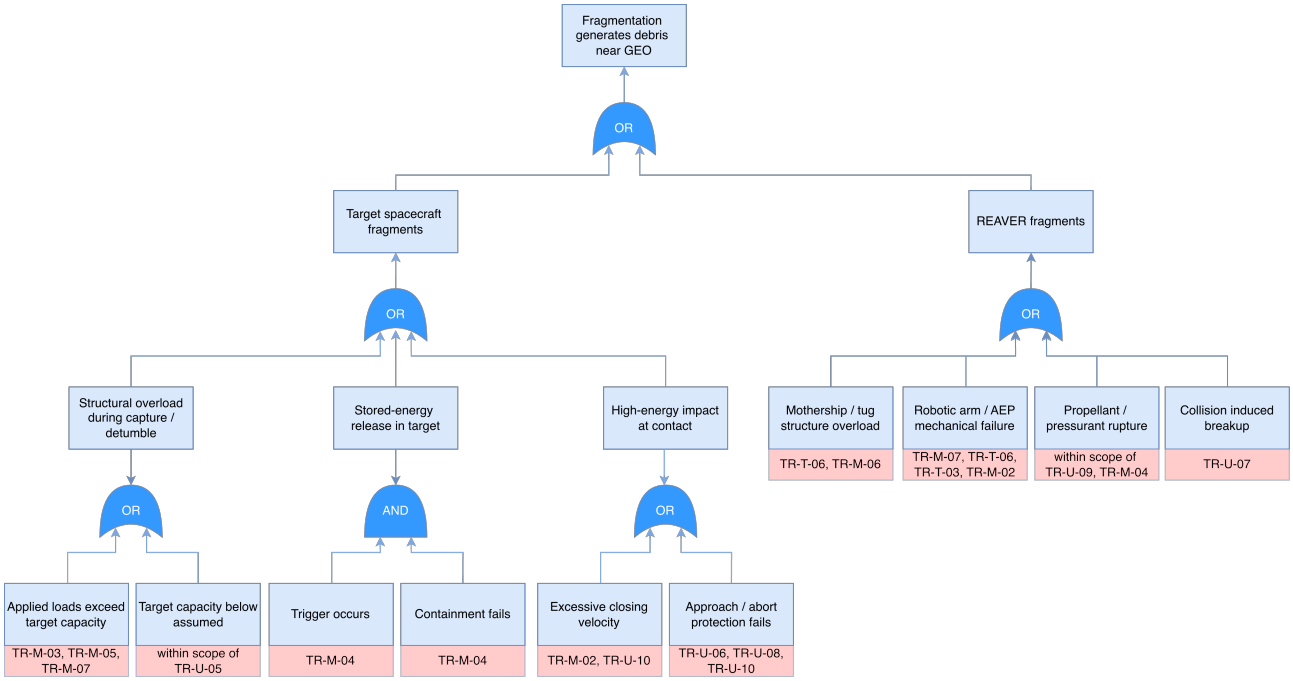

Figure 14.2: Fault tree analysis of the worst-case safety event due to relevant technical risks

14.3. Verification, Validation, and Requirements Compliance

The verification and validation build upon the framework established in the Midterm report [38]. Validation is divided into system (requirement) and software validation.

Subsystem requirement verification is conducted and discussed in each dedicated subsystem chapter. Requirements are given a verification method, which can be either demonstration, analysis, test, or inspection. Their compliance is checked and the requirement can either be compliant, non-compliant, or to be determined in case of a test or demonstration method for which the set-up is there, but the actual verification is to be conducted. These compliances will directly influence the validation framework assessing whether the mission concept satisfies the stakeholder needs defined in the baseline report [116]. This is done through a traceability matrix, in which each stakeholder requirement is linked to one or more mission or system requirements, and each mission or system requirement is linked to one or more subsystem requirements. In this way, subsystem-level verification results can be used as supporting evidence for system-level validation.

[8] https://ecss.nl/standard/ecss-q-st-40-12c-fault-tree-analysis-adoption-notice-ecssiec-61025/ [accessed 17 June 2026]

A requirement is considered validated when all child requirements have been verified and when the resulting evidence demonstrates that the original stakeholder need is satisfied. Some requirement values remain marked as **TBD**. These values are not filled in where no lower-level subsystem requirement, mission analysis, environmental analysis, or interface definition currently provides a justified numerical value.

The validation traceability matrix not only checks if stakeholder requirements are supported by lower-level mission, system, and subsystem requirements but also identifies areas and requirements needing improvement, as shown in the status/action column.

Table 14.2: Validation traceability matrix linking stakeholder, mission, system, and subsystem requirements

ID	Description	Child requirement(s)	Status/Action	Check
Stakeholder requirements				
REQ-STK-01	The mission shall be able to capture 5 target objects from the near-GEO orbit regime in one year.	REQ-MIS-17, REQ-MIS-09	-	TBD
REQ-STK-02	The spacecraft shall be capable of capturing debris with mass from 1000 to 2000 kg.	REQ-MIS-08	-	TBD
REQ-STK-03	The mission shall be able to capture an uncooperative satellite or rocket body tumbling at a rate of 1 rpm about an arbitrary axis.	REQ-MIS-06	-	TBD
REQ-STK-04	The mission shall have a cumulative probability of collision < **TBD** with objects in geostationary orbit for at least 200 years in case of failure.	REQ-SYS-19	-	TBD
REQ-STK-05	The mission shall maintain an accepted collision probability level (ACPL) with trackable debris less than 1.0×10^{-4} during its operational phase.	REQ-SYS-22	-	Yes
REQ-STK-06	The mission shall not create any additional debris during its operation.	REQ-SYS-23, REQ-SYS-24	-	TBD
REQ-STK-08	The mission shall have a cumulative probability of collision < **TBD** with objects in geostationary orbit for at least 200 years after the end of its operational phase.	REQ- SYS-20	-	TBD
REQ-STK-09	The mission shall use non-toxic propellants.	REQ-SYS-25	-	Yes
REQ-STK-10	The mission shall communicate with ground operators via the ESA Estrack network.	REQ-SYS-13, REQ-MIS-15, REQ-SYS-14, REQ-SYS-15	-	TBD
REQ-STK-11	The total mission cost shall be less than €200 million, including manufacturing, testing, launch, and operations.	REQ-SYS-27	-	No
REQ-STK-12	The mission shall launch before January 1, 2035.	REQ-MIS-18, REQ-SYS-12	-	Yes
REQ-STK-13	The mission shall be conducted in compliance with regulations.	REQ-SYS-28, REQ-SYS-29	-	TBD
REQ-STK-14	The General Public shall be able to witness and track the progression of key mission milestones to encourage public engagement and promote sustainable reusability.	REQ-MIS-16	-	TBD
REQ-STK-15	The mission shall transport the debris from its original orbit to the recycling hub.	REQ-SYS-06	-	TBD
REQ-STK-16	The mission shall have the capability to dock with the recycling hub.	REQ-SYS-01	-	TBD
REQ-STK-17	The mission shall have the capability to transfer the debris to the recycling hub.	REQ-SYS-17	-	TBD
REQ-STK-18	The mission shall be able to control its attitude sufficiently to enable capture of tumbling debris.	REQ-MIS-01, REQ-MIS-06	-	TBD
REQ-STK-20[9]	The spacecraft shall autonomously estimate target debris physical and orbital parameters.	REQ-MIS-01	-	TBD
REQ-STK-21	The mission shall be able to navigate to and match the orbital trajectory of the target debris.	REQ-MIS-04, REQ-MIS-11	-	TBD
REQ-STK-22	The mission shall be able to withstand impacts from debris < **TBD** m diameter in GEO.	REQ-SYS-11	-	TBD
REQ-STK-23	The mission shall be able to withstand the temperature extremes and thermal eclipse cycling present in GEO.	REQ-SYS-09, REQ-SYS-10	-	TBD
REQ-STK-24	The mission shall be able to withstand the total ionising radiation dose and single-event effects present in GEO.	REQ-SYS-08	-	Yes
REQ-STK-25	The mission shall utilise a launch vehicle that is currently operational or expected to be operational by 2035.	REQ-SYS-12	-	Yes
REQ-STK-27	The spacecraft shall capture debris in GEO at an altitude of 35 700 to 36 500 km.	REQ-MIS-10	-	Yes

Continued on next page

[9] REQ-STK-19 is not included in this requirement table to maintain consistency with the requirement numbering used in the baseline report. The requirement itself was not omitted, but the numbering sequence in the baseline report simply did not assign an entry to REQ-STK-19 by mistake.

Table 14.2 – continued from previous page

ID	Description	Child requirement(s)	Status/Action	Check
REQ-STK-28	The spacecraft shall be able to capture debris with an orbital inclination within 0-20°.	REQ-MIS-07	-	Yes
Mission requirements				
REQ-MIS-01	The spacecraft shall estimate target debris size, shape, rotational axis, and tumbling rate with sufficient accuracy for capture, detumbling, and transport control.	REQ-CDH-M1	Changed: additional parameters and accuracy defined	TBD
REQ-MIS-04	The spacecraft shall be able to autonomously approach the target object from the hold point.	REQ-PSS-M7, REQ-CAP-M1, REQ-ACS-M7, REQ-ACS-M8, REQ-ACS-M9	-	TBD
REQ-MIS-05	The spacecraft shall be able to autonomously abort a capture attempt and retreat to a stand-off distance ≥ 20 m from the target debris.	REQ-CAP-U1, REQ-ACS-M12, REQ-ACS-M13	-	TBD
REQ-MIS-06	The spacecraft shall be capable of capturing a non-cooperative target tumbling at up to 1 RPM about an arbitrary axis.	REQ-CAP-T2, REQ-CAP-T1, REQ-ACS-M7, REQ-ACS-M8, REQ-ACS-M11	-	TBD
REQ-MIS-07	The spacecraft shall be able to capture debris with an orbital inclination within 0-15°.	-	Changed: before 20°	Yes
REQ-MIS-08	The spacecraft shall be capable of capturing debris from 1000 to 2000 kg.	REQ-PSS-T1, REQ-PSS-T2, REQ-CAP-T1, REQ-ACS-M11	-	TBD
REQ-MIS-09	The spacecraft shall capture and return ≥ 5 pieces of uncooperative debris to the recycling hub within 1 year.	REQ-PSS-M1, REQ-PSS-T1, REQ-EPS-T1, REQ-PSS-M3, REQ-PSS-T2	-	TBD
REQ-MIS-10	The spacecraft shall capture debris in GEO at an altitude of 35 700 to 36 500 km.	REQ-PSS-M1	-	Yes
REQ-MIS-11	The spacecraft shall navigate to a hold point within 5 m from the target debris.	REQ-CAP-M1, REQ-ACS-M1, REQ-ACS-M2, REQ-ACS-M4, REQ-ACS-M5, REQ-ACS-M6	-	TBD
REQ-MIS-15	The spacecraft shall communicate with ground operators via the ESA Estrack network.	REQ-TTC-M1, REQ-TTC-T1, REQ-CDH-U1, REQ-TTC-U1	-	TBD
REQ-MIS-16	The General Public shall be able to witness and track the progression of key mission milestones.	REQ-TTC-M3, REQ-TTC-T4	-	TBD
REQ-MIS-17	The mission shall achieve a mission success probability of > **95** %.	-	-	Yes
REQ-MIS-18	The mission shall launch before January 1, 2035.	-	-	Yes
System requirements				
REQ-SYS-01	The spacecraft shall be able to autonomously dock with the recycling hub.	REQ-CDH-U3, REQ-PSS-M7, REQ-ACS-M7, REQ-ACS-M8, REQ-ACS-M9, REQ-ACS-M10	-	TBD
REQ-SYS-06	The spacecraft shall transport the debris to a hold point at **TBD**m from the recycling hub.	REQ-PSS-T1, REQ-ACS-T1, REQ-ACS-T2, REQ-ACS-T4, REQ-ACS-T5, REQ-ACS-T6	Action: define TBD	TBD
REQ-SYS-08	All spacecraft components shall be qualified to withstand a total ionising dose of at least 30 krad and the single-event effects encountered in GEO for the full mission lifetime.	-	Status: selected components comply	Yes
REQ-SYS-09	The spacecraft shall operate within the temperature ranges of both eclipse and full sunlight encountered in GEO.	-	-	TBD
REQ-SYS-10	The spacecraft shall limit temperature variations of **TBD** K/hour of critical components.	-	Action: assess relevance	TBD
REQ-SYS-11	The spacecraft shall survive impacts from small debris/micrometeorites with a kinetic energy < **TBD** kJ.	REQ-STC-U5	Action: quantify TBD	TBD
REQ-SYS-12	The spacecraft shall be compatible with launch vehicles expected to be operational by the planned launch date.	REQ-STC-U1	-	Yes
REQ-SYS-13	The spacecraft shall transmit telemetry and receive telecommands using frequency bands licensed exclusively to the mission operator under ITU Radio Regulations.	REQ-TTC-M1	-	Yes
REQ-SYS-14	The spacecraft shall support a minimum housekeeping downlink data rate of 4 kbit s^{-1} for the mothership and 3.8 kbit s^{-1} for each tug, and a minimum mothership payload downlink data rate of 474.62 Mbit s^{-1}.	REQ-TTC-M2, REQ-TTC-M3, REQ-TTC-T3, REQ-TTC-T4	Changed: rates filled and separated	TBD

Continued on next page

Table 14.2 – continued from previous page

ID	Description	Child requirement(s)	Status/Action	Check
REQ-SYS-15	The spacecraft shall support a minimum uplink telecommand data rate of 2 kbit s^{-1}.	REQ-CDH-M2, REQ-CDH-T1, REQ-TTC-M4	-	TBD
REQ-SYS-17	The spacecraft shall maintain control of the captured debris until positive handover to the recycling hub has been confirmed.	REQ-CAP-T1	-	TBD
REQ-SYS-19	The mission shall have a cumulative probability of collision < **TBD**% with objects in geostationary orbit for at least 200 years in case of failure.	-	Action: collision-risk analysis	TBD
REQ-SYS-20	The mission shall have a cumulative probability of collision < **TBD**% with objects in geostationary orbit for at least 200 years after the end of its operational phase.	-	Action: post-mission collision analysis	TBD
REQ-SYS-22	The mission shall maintain an accepted collision probability level (ACPL) with trackable debris less than 1.0×10^{-4} during its operational phase.	-	Assessed in Midterm	Yes
REQ-SYS-23	The spacecraft shall not cause any structural or other damage to components intended for reuse.	REQ-CAP-U2, REQ-ACS-M3, REQ-ACS-T3	-	TBD
REQ-SYS-24	The mission shall not create any additional debris during its operation.	REQ-CAP-U3	-	TBD
REQ-SYS-25	The mission shall use non-toxic propellants.	REQ-PSS-M8, REQ-PSS-T7	-	Yes
REQ-SYS-26	Total equivalent CO_2 emissions shall not exceed **TBD** kg throughout the development, operation, and end-of-life of the mission.	-	Action: detailed LCA required	TBD
REQ-SYS-27	The total mission cost shall be less than €200 million, including manufacturing, testing, launch, and operations.	-	See section 15.3	No
REQ-SYS-28	The mission shall comply with applicable international space treaties, including the Liability Convention (1972), Outer Space Treaty (1967), Registration Convention (1976), and Artemis Accords (2020).	-	Action: assess compliance	TBD
REQ-SYS-29	The spacecraft shall maintain safe autonomous operation during unplanned communication outages of up to 72 min without ground intervention.	REQ-TTC-M6, REQ-CDH-U3	Added: replaces REQ-SYS-18	TBD

Table 14.3: Deleted requirements and reasoning

ID	Description	Reason
Mission requirements		
REQ-MIS-02	The spacecraft shall estimate debris mass, centre of mass, and moment of inertia with sufficient accuracy for capture, detumbling, and transport control.	Omitted: similar to REQ-MIS-01, subsystem-level specificity
REQ-MIS-03	The spacecraft shall be able to autonomously estimate the relative target position at a distance of < **0.05**m.	Omitted: encompassed by REQ-MIS-04, subsystem-level specificity
REQ-MIS-12	The spacecraft shall achieve a relative-velocity residual error < 20 mm s^{-1} with respect to the target debris at hold point.	Omitted: encompassed by REQ-MIS-04, subsystem-level specificity
REQ-MIS-13	The spacecraft shall have a relative closing-velocity residual error < 20 mm s^{-1} during the close approach phase.	Omitted: encompassed by REQ-MIS-04, subsystem-level specificity
REQ-MIS-14	The mission shall use a target-screening process to confirm that each selected target is within the spacecraft's mass, orbit, tumbling rate, and capture interface limitations.	Omitted: redundant
REQ-MIS-19	The mission shall designate debris targets that consist of > **TBD** % recyclable and or reusable material.	Omitted: insufficient data
System requirements		
REQ-SYS-02	The spacecraft shall have a relative closing velocity of **TBD** m s^{-1} ± **TBD** mm s^{-1} during the docking sequence.	Omitted: encompassed by REQ-SYS-01, subsystem-level specificity
REQ-SYS-03	The spacecraft shall autonomously align its docking axis with the recycling hub interface with an accuracy of ± **TBD**° in attitude prior to initiating docking.	Omitted: encompassed by REQ-SYS-01, subsystem-level specificity
REQ-SYS-04	The spacecraft shall autonomously align its docking axis with the recycling hub interface with a positional error < **TBD**m prior to initiating docking.	Omitted: encompassed by REQ-SYS-01, subsystem-level specificity
REQ-SYS-05	The captured debris shall stay within acceleration limits of **TBD**m s^{-2} during transportation.	Omitted: encompassed by REQ-SYS-23, subsystem-level specificity
REQ-SYS-07	The spacecraft shall ensure that the relative velocity between the debris and recycling hub is < 20 mm s^{-1}.	Omitted: encompassed by REQ-SYS-01, subsystem-level specificity

Continued on next page

Table 14.3 – continued from previous page

ID	Description	Reason
REQ-SYS-16	The spacecraft shall maintain a minimum communication contact window of **TBD** minutes per 24-hour period via the ESA Estrack network throughout its operational lifetime.	Omitted: LEO requirement
REQ-SYS-18	The spacecraft shall maintain continuous ground communications during close approach, debris capture, and docking phases.	Replaced by REQ-SYS-29
REQ-SYS-21	During any proximity operation or capture attempt, the spacecraft shall not approach an active GEO satellite within a keep-out zone of **TBD**km in-track and **TBD**km cross-track without ground authorisation.	Omitted: redundant

Software V&V covers verification, which confirms that the code does what it is intended to do, and validation, which confirms that it accurately represents the physical system. Both are applied to the REAVER codebase.

Verifying the code ensures that each part of the code does what it is intended to, regardless of whether it accurately reflects the physical reality. Three methods for code verification are considered: unit checks, hand calculations, and peer review. Unit checks are applied to individual functions, confirming that isolated components produce correct outputs for known inputs before integration with the rest of the code. Hand calculations are performed for selected key outputs. Peer review is conducted by a team member independent of the original author, who checks the code's consistency, logic, and implementation errors.

Code validation confirms that the software accurately represents the physical system it models, rather than merely verifying that it does what it's supposed to do. Three validation procedures are introduced: comparison, benchmarking, and expert review. Comparison with trusted reference tools is performed by running similar scenarios under the same conditions in both the code and astrodynamics tools, such as GMAT. If both are consistent across a range of input values, this provides confidence that the code is correctly implemented. Benchmarking against known analytical solutions is performed on closed-form solutions such as Hohmann transfers and plane change manoeuvres. Reference values are taken from established literature [6]. Finally, stakeholder consultation is used as a qualitative validation step to assess whether the model assumptions and outputs are reasonable for the GEO context, given their greater expertise and experience in the area. The feedback obtained is used to identify unrealistic assumptions and guide model refinements where necessary.

14.4. Sensitivity Analysis

A sensitivity analysis is performed to establish the degree of feasibility of the final design. The driving design constraints to consider the mission successful are the mission duration and cost. Mission duration is driving because it encompasses the stakeholder requirements of capturing five debris within one year, and cost is driving because it is an external constraint imposed by the stakeholder requirements.

Mission Duration Sensitivity Analysis

The mission duration is a high-level constraint that encompasses both the direct and indirect effects of the design on mission success. To conduct a robust sensitivity analysis, parameters that either directly define the trajectory and transfer time, or represent higher-level effects of subsystem design changes are considered: the ΔV, dry mass, thruster specific impulse I_{sp}, and target debris mass. These parameters are considered sufficient for a system-level analysis because subsystem changes ultimately propagate through one of these quantities. For example, a change in the power consumption directly changes the solar array size, increasing the dry mass. Hence, the effect of power consumption on mission duration stems from the increase in dry mass, thereby extending the burn duration. For each variation, a complete astrodynamic analysis of the system is conducted using the methodology described in section 3.5. While only one parameter is directly varied in each analysis, all variables that are subsequently affected are accounted for to determine the mission duration.

The variation ranges are based on the dominant source of uncertainty for each parameter. For the ΔV, the variations are the optimised trajectories for each combination of debris, which inherently vary the target RAAN, inclination, and altitude. For the dry mass, a ±20% range is applied to the maximum estimated value, given the design maturity level. The range used for the specific impulse is defined by the uncertainty from the manufacturer specifications. For the mothership, the propellant LMP-103S reports a 243–256 s range, while the tug Xenon Hall-effect thrusters report a 1400–1650 s range. Finally, the debris mass is varied for every permutation of the target 1000–2000 kg range in 200 kg increments. For example, the best case is where all debris are the minimum mass of 1000 kg, and the worst case is where all debris are 2000 kg.

For each sensitivity analysis, the mission duration is calculated across the specified parameter range. The results are presented as box plots, which summarise the distribution of mission-duration values by showing the median,

interquartile range, and the minimum and maximum values. The median indicates the typical mission duration expected over the investigated parameter range, while the spread reflects the sensitivity of mission duration to the parameter variation. Since all parameter box plots are shown on one graph, the relative influence of each parameter can be compared directly.

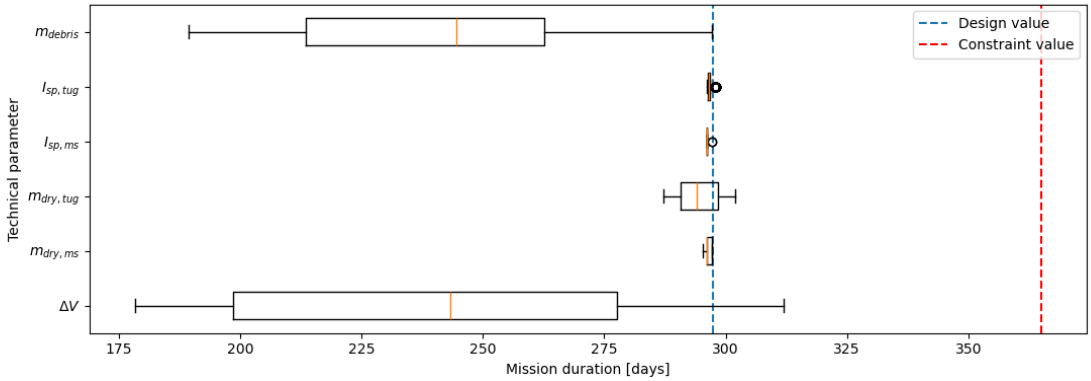

Figure 14.3: Sensitivity analysis for technical parameter variations on mission duration

This sensitivity analysis reveals how variations in each technical parameter affect the overall mission duration, identifying critical parameters that must be considered for the design margins. The nominal design estimates a mission duration of 298 days, with a critical duration of 365 days for mission success. Parameter variations that result in larger mission duration ranges imply that the duration is more sensitive to that parameter. From figure 14.3, it is evident that the driving mission duration parameters are the ΔV, debris mass, and, to a lesser extent, the tug dry mass as well. On the other hand, changes in the tug and mothership-specific impulses and mothership dry mass do not have a significant effect on the mission duration. In particular, the specific impulse primarily affects propellant consumption; hence, its effect on mission duration is only indirect, through the resulting change in wet mass and, consequently, acceleration. Since the manufacturer's range is quite small, the resulting change in wet mass is too small to significantly alter the mothership burn time or the tug spiral time.

Since the mission is designed for the worst-case potential target combinations, it is logical that most technical parameter variations result in a mission duration shorter than the design value. Most critically, the mission duration never exceeds the constraint value of 365 days for all variations analysed as shown in figure 14.3. Furthermore, the median mission duration for all parameter variations is at or below the design value, and the interquartile ranges of the parameters producing the largest variations, namely debris mass and ΔV, also fall below the design value. This indicates that the mission is expected to be completed in less time than the design value in most cases, while remaining compliant with the schedule constraint in all analysed cases, demonstrating the robustness of the mission architecture with respect to mission duration.

However, figure 14.3 reveals that the upper ends of the mission duration ranges for the tug dry mass and ΔV variations exceed the design value. This occurs because both parameters affect the mission's time-critical components. An increase in tug dry mass reduces the tug acceleration for the given thrust, thereby increasing the low-thrust spiral time back to the recycling hub. Similarly, larger ΔV trajectories require the propulsion system to deliver a greater velocity change, increasing the required thrusting time. This increases the mothership's finite burn duration and the tug's spiral time, delaying the tug's release, arrival, and final handover. Nonetheless, all analysed durations remain below the 365 day mission constraint; hence, these parameters are not constraint-critical. Therefore, the design case was selected based on the worst-case propellant requirement, which represents the sizing-critical case. Uncertainty in tug dry mass and trajectory ΔV can reduce the schedule margin, but does not violate mission feasibility.

Interestingly, figure 14.3 shows that the mission duration is more sensitive to changes in the tug dry mass than the mothership dry mass. Since the tugs use electric propulsion, the thrust-to-mass ratio is significantly lower than the mothership's chemical propulsion system. This means that changes in the tug's mass have a larger effect on its burn time during the spiral transfer. This is the same reason the mission duration is so sensitive to changes in the debris mass. Since the debris mass is an order of magnitude larger than the tug's dry mass, the debris forms the dominant part of the tug-debris system mass. Consequently, variations in debris mass have an even more pronounced effect on tug spiral time. In addition, tug dry mass also has a secondary effect on the mothership since the heavier tugs must be carried before release, thereby also increasing the mothership transfer time. This supports the astrodynamic analysis, where the tug transfer time is the limiting factor for mission duration.

Cost Sensitivity Analysis

The mission's cost is a driving constraint on the design's feasibility. To quantify the associated uncertainty, a sensitivity analysis is performed based on the cost-estimation methodology described in section 13.4. The cost breakdown has two sources of uncertainty: the input design parameters and the outputs of the cost-estimating relationships. Since the cost breakdown is conducted by means of empirical equations, the output of each relation carries a certain level of uncertainty, which is documented as the standard error of the estimate [71]. Furthermore, the inputs are design parameters that remain uncertain due to the current design maturity.

A comprehensive sensitivity analysis is conducted by running two separate Monte Carlo simulations: one for the uncertainty in design inputs and another for the uncertainty in the empirical relations. Since the cost estimation is composed of many uncertain contributions that vary simultaneously, investigating each parameter in isolation would not capture the accumulation of uncertainty across the full cost breakdown. A Monte Carlo approach propagates multiple uncertainties through the cost model at the same time, providing a probabilistic cost range. This gives a more realistic representation of the expected spread in total mission cost. 20 000 iterations are performed to sufficiently identify trends without increasing computational cost excessively.

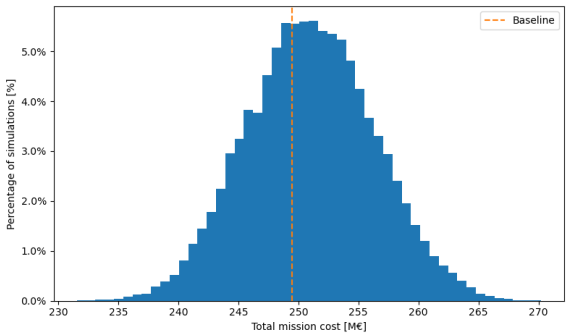

(a) Sensitivity analysis varying input design parameter uncertainty

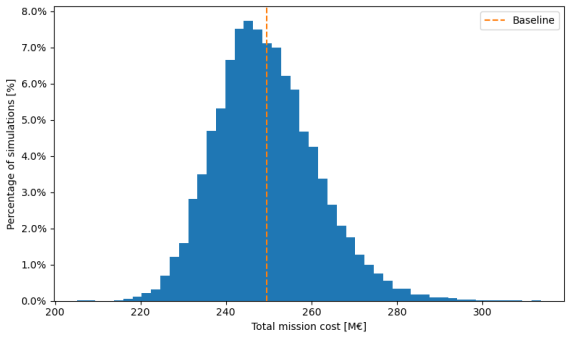

(b) Sensitivity analysis varying output mission cost uncertainty

Figure 14.4: Sensitivity analyses on mission cost

This sensitivity analysis, shown in figure 14.4, highlights the driving source of uncertainty in the cost. Both analyses show that the baseline computed cost coincides with the median, indicating the baseline estimate is representative of the central tendency of costs. However, figure 14.4b demonstrates a very large spread of data, spanning 120M€, especially when compared to the figure 14.4a. Hence, the largest source of uncertainty in the cost breakdown is the estimation methods, rather than the design maturity. This can be problematic if a more precise method for estimating costs is not developed as the design matures. The spread of the design parameter uncertainty in cost will continue to decrease as development progresses; however, unless a different cost breakdown methodology is used, the cost uncertainty will remain fixed. Furthermore, figure 14.4b is skewed slightly right, showing a longer high-cost tail. This indicates a higher risk that the cost will exceed the baseline, rather than be lower.

14.5. Design Integration

Figure 14.5 shows the hardware block diagrams for the mothership and tugs identifying the physical components across each subsystem and the connections between them. Primarily, it shows the main hardware components that exist within each spacecraft and which subsystem they belong to. Subsequently, it defines how those components interact, which processor commands which actuator, which sensor feeds which computer, and how power flows to each subsystem. This forms the physical foundation on which the software architecture of the design is built. Additionally, a key architectural distinction between the two vehicles becomes apparent: the mothership uses three separate processors to handle mission management, attitude control, and payload processing independently, while the tug has a much simpler architecture that requires only one. Lastly, the required amount of lines of code was estimated using the approach outlined in the SMAD textbook [71], resulting in table 14.4.

Table 14.4: Estimated lines of code per subsystem using statistical relations from SMAD

System	Single lines of code (SLOC)
Mothership flight software	7608
Tug flight software (common)	2838
Ground software	4080

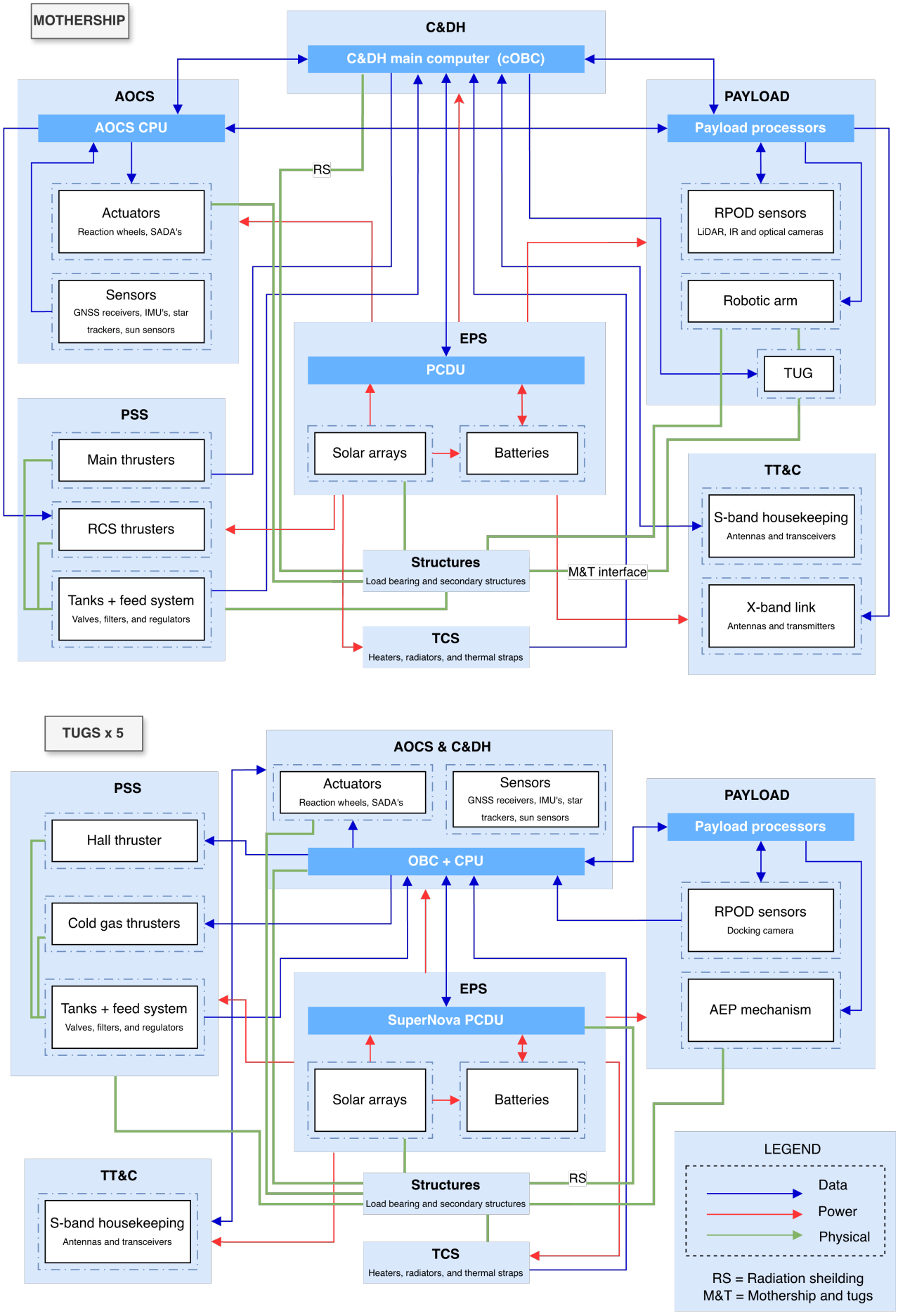

Figure 14.5: Hardware diagram of the mothership and tugs

15. Future Development

This chapter outlines the main steps required to mature REAVER from the current DSE design into an implementable mission. It first defines the manufacturing, assembly and integration logic, including production, integration and qualification activities. The chapter then presents the post-DSE development logic and schedule, followed by the cost breakdown and return-on-investment assessment needed to evaluate the mission's future feasibility.

15.1. Manufacturing, Assembly and Integration (MAI) Plan

The Manufacturing, Assembly and Integration (MAI) plan defines how the REAVER flight system shall be produced, integrated and accepted after the DSE. The plan follows a make-buy logic: mature spacecraft units are considered as qualified or qualification-compatible components, while specific hardware designed for REAVER is manufactured and qualified separately. This reduces development risk by limiting custom production to the primary structure, tug interfaces, capture hardware, propulsion integration and mission-specific harnessing. The MAI process shall follow ECSS product-assurance, configuration-management and test-planning practices [117, 118, 28].

Production Plan

The REAVER production plan is organised into production work packages rather than part-level process sheets. A detailed manufacturing-process plan, such as the one presented by Subramanya et al. for aerospace component production, requires approved drawings, defined operations, work centres, tooling, machining parameters and stage inspections, which are not yet available at this system-design stage [119]. Therefore, the REAVER plan remains traceable to the spacecraft product tree while avoiding excessive detail. The baseline production set consists of one flight mothership, five flight tugs, one qualification/engineering tug (model used to produce the five flight tugs), representative target-nozzle mock-ups, and the required subsystem qualification hardware.

Table 15.1: REAVER production plan organised by production work package

Work package	Produced hardware	Production logic	Acceptance evidence
Mothership structure and interfaces	Primary truss, equipment panels, tank supports, launch-adapter interface, robotic-arm interface and tug rail.	Custom manufacture from space-qualified aluminium alloy. Interface machining and dimensional control are critical because this structure defines the launch load path, tank locations, robotic-arm alignment and tug deployment geometry.	Material certificates, dimensional inspection, non-destructive inspection where needed, mass-property measurement and structural/frequency verification [20, 120].
Tug production batch	Five flight tugs and one qualification/engineering tug, including frames, tank brackets, PPS-X00 mounting interface, AEP mounting plate and mothership rail interfaces.	One qualification tug is produced first to verify the repeated tug design. The five flight tugs are then batch-produced using common tooling and the same interface-control documents to maximise repeatability.	Rail-fit check, tug deployment clearance check, mechanical interface test, electrical interface test and qualification-tug environmental test.

Continued on next page

Table 15.1 - continued from previous page

Work package	Produced hardware	Production logic	Acceptance evidence
Propulsion modules	Mothership LMP-103S module with four propellant tanks, helium pressurisation, 22 N main thrusters, 5 N RCS thrusters and gimbals; tug xenon modules with tank pairs, PPS-X00, PPU-X00, FMS and cold-gas RCS.	Supplier-supported integration is preferred for tanks, thrusters, valves, regulators and high-pressure lines. The mothership module is produced once, while the tug xenon module is repeated for each tug after qualification.	Cleanliness inspection, material-compatibility review, proof-pressure test, leak test, valve-cycle test, regulator/FMS test, static-fire test and PPS-X00 throughput qualification.
Capture and robotic hardware	Five AEP mechanisms, one qualification AEP, robotic manipulator, REAVER-specific end-effector and representative LAE nozzle mock-ups.	The AEP is custom-manufactured because it is specific to the tug capture concept. The robotic manipulator should use heritage hardware where possible, with only the tug end-effector and mission-specific interfaces customised.	AEP insertion test, locking-force test, retraction test, repeated cycling, nozzle compatibility test, robotic-arm calibration, torque-margin test and hardware-in-the-loop capture rehearsal.
Avionics, sensors, EPS, TT&C and TCS	OBCs, AOCS sensors and actuators, RPOD cameras, IR sensors, LiDAR, payload processors, transceivers, PCDUs, batteries, solar-array equipment, heaters, radiators, MLI and thermal straps.	Qualified or qualification-compatible units are procured where possible. Integration focuses on electrical, data, thermal and mechanical interfaces rather than custom unit development.	Incoming inspection, functional test, data-bus test, power-interface test, optical calibration, EMC test, heater-continuity test and thermal-vacuum verification.
Harness, brackets and ground-support equipment	Electrical harnesses, fluid-line supports, handling fixtures, lifting interfaces, alignment tools and target/nozzle ground-test equipment.	These items are manufactured after the mechanical and electrical interface-control documents are frozen to avoid late rework during system integration.	Continuity test, insulation-resistance test, connector inspection, routing inspection, fit check and ground-support-equipment validation.

The production order depends mainly on how mature the interfaces are. Long-lead components, such as tanks, thrusters, avionics, batteries, reaction wheels, solar-array hardware and TT&C units, are ordered after PDR. Custom structures, harnesses and brackets are only manufactured once the main interface-control documents are frozen, to avoid late redesign. The qualification tug and AEP test articles are built before the flight tugs, so that deployment, xenon propulsion, AEP capture and rail-interface issues can be found and corrected before producing the final tug batch.

Assembly and Integration Plan

The assembly and integration plan follows a bottom-up approach. First, all procured units are inspected on arrival to verify documentation, dimensions, electrical interfaces and handling constraints [117, 118]. Subsystem-level integration is then completed before system-level integration, so that faults such as harness errors, valve-interface issues or software communication problems are detected before the complete spacecraft is assembled [**?**].

The tug integration line starts with the qualification tug. Its structure is assembled first, followed by the xenon tanks, PPS-X00 propulsion module, cold-gas RCS branch, AEP mechanism, AOCS hardware, C&DH electronics, EPS components, harnessing and thermal hardware. After functional and environmental testing of this unit, the five flight tugs are integrated using the same tooling, assembly sequence and interface-control documents. This

improves repeatability, reduces integration time and keeps the flight tugs traceable to the qualified configuration [28, 118].

In parallel, the mothership is assembled around its primary structure. The tank supports, LMP-103S propulsion module, helium pressurisation system, avionics panels, EPS units, TT&C hardware, AOCS hardware, RPOD sensors and thermal-control hardware are installed before final close-out. Propulsion hardware is installed early because feed lines, valves and pressure sensors require physical access for inspection and leak testing. The robotic manipulator and tug rail are installed after the main spacecraft bus has passed electrical and mechanical fit checks, since these mechanisms require accurate alignment with the tug mounting points.

After the mothership and tugs have been accepted separately, the five flight tugs are mounted on the rail and connected through their mechanical, electrical and data interfaces. The integrated spacecraft then undergoes an end-to-end functional test to verify that ground commands can be received by the mothership, routed through the C&DH system, used to command tug interfaces and confirmed through telemetry. A dry-run tug deployment test is also performed with ground-support equipment to check release clearances, connector separation, robotic-arm reachability and safe-mode recovery [28].

Qualification and Acceptance Testing

The MAI test campaign is split into qualification testing and flight acceptance testing. Qualification testing demonstrates that the design can survive the expected launch and space environments with margin. Acceptance testing confirms that the specific flight hardware has been manufactured and integrated correctly [28, 121].

Standard spacecraft acceptance tests include alignment surveys, mass-property measurements, electrical continuity tests, data-bus tests, EMC testing, propulsion proof-pressure and leak tests, vibration, acoustic, shock and thermal-vacuum testing. These tests are required because the integrated REAVER stack must survive Falcon 9 launch loads, kick-stage transfer operations and the GEO thermal environment. The environmental test results also provide final evidence that the structural, thermal, electrical and mechanical interfaces are compatible at system level [28, 121].

The mission-specific tests focus on the functions that cannot be fully verified by standard spacecraft testing. The most important test is a hardware-in-the-loop (HIL) RPOD and capture rehearsal. This test combines the RPOD sensors, C&DH processing, AOCS control logic, robotic manipulator and AEP mechanism with a representative tumbling-target mock-up. It shall demonstrate target characterisation, tug positioning, AEP alignment, capture confirmation, abort logic and safe retreat. The tug qualification unit shall also demonstrate xenon propulsion activation, PPS-X00 thrusting, cold-gas RCS control, reaction-wheel desaturation and safe isolation while attached to the mothership [28].

The final MAI output is therefore both the accepted flight hardware and the evidence package proving that it is ready for launch and operations. This package includes the accepted mothership and five flight tugs, as-built configuration records, mass and CG report, electrical and fluid-interface records, propulsion and environmental test reports, software and command-database versions, non-conformance/waiver log, and launch-site handling procedures; once accepted at AR/FRR, the spacecraft can be shipped for Star-63D and Falcon 9 integration, with any remaining open items limited to launch-site operations to avoid post-acceptance redesign risk [122, 118].

15.2. Project Design and Development (PD&D) Logic

The PD&D logic follows a V-model approach, where mission needs are decomposed into system, subsystem and interface requirements, and then verified back up to mission level through analysis, inspection, test and demonstration [29]. Since the current design is still a preliminary system baseline, post-DSE development must first close open assumptions, freeze requirements and mature the highest-risk interfaces before detailed design release. This follows ECSS project-planning practice, where phased reviews are used to control technical, cost and schedule maturity [89, 122].

The main REAVER development drivers are the mission-specific functions that cannot be accepted from heritage alone: uncooperative GEO RPOD, computer-vision target characterisation, robotic-arm tug positioning, AEP capture, tug–debris coupled dynamics, PPS-X00 lifetime, LMP-103S propulsion integration and recycling-hub handover.

Table 15.2: Simplified post-DSE project design and development logic

Phase / gate	Development activity
Post-DSE consolidation	Remaining TBDs are closed, the target list is updated, ownership and recycling-hub assumptions are confirmed, and the mass, power, thermal, link, ΔV, cost and risk budgets are made consistent [89, 29].
System Requirements Review (SRR)	The mission need and system requirements are checked before further design work. For REAVER, this includes the five-target-per-year requirement, GEO operating envelope, target compatibility, launch-before-2035 constraint, stakeholder needs and requirement traceability [122, 29].
Preliminary Design Review (PDR)	The preliminary design is matured until the main architecture and budgets are credible. The mission layout, subsystem sizing, interface-control documents, make-buy logic, mission timeline and propellant budget are updated before detailed design starts [89, 122].
Technology maturation	The mission-specific technologies are tested before the design is frozen. The key items are RPOD and computer vision, robotic-arm tug positioning, AEP capture with representative LAE nozzles, tug deployment, PPS-X00 throughput, LMP-103S feed-system compatibility and gimbal authority. This is needed because these functions drive several spacecraft interfaces and cannot be accepted from heritage alone [28, 29].
Critical Design Review (CDR)	The detailed flight design is frozen. Mechanical, electrical, thermal, software, data, propulsion and recycling-hub interfaces are closed, along with the major TBDs, and the safety, reliability and verification plans are updated before procurement and manufacturing [122, 118].
Phase D: Manufacturing, AIT and qualification	The flight system is produced, integrated and tested. This includes the mothership protoflight unit, one qualification/engineering tug, five flight tugs, propulsion tests, AEP and robotic-arm tests, environmental tests and hardware-in-the-loop RPOD/capture tests [28, 121].
Flight Readiness Review (FRR)	Launch and early-operation readiness are confirmed. Falcon 9 and Star-63D interfaces, launch-site procedures, commissioning logic, safe-mode behaviour, abort procedures and first-target operations are checked before launch approval [122, 29].
Phase E: Operations	The spacecraft is commissioned and the debris-removal campaign is executed. The mothership performs sequential rendezvous and tug deployment, while the tugs transport captured debris to the recycling hub for handover. Campaign replanning is performed if vehicle health, propellant or schedule margins change [89, 29].
Phase F: Reuse or disposal	After the base campaign, the spacecraft state is assessed at the recycling hub. Remaining propellant, tug condition, degraded components and ROI are reviewed to decide whether REAVER is refurbished for further removals or safely passivated/disposed [89, 29].

The critical path is therefore expected to run through RPOD/autonomy maturation, capture-system qualification, propulsion-interface verification, system-level AIT and launch readiness. Schedule margin should be placed before CDR and before environmental acceptance testing, where late design changes would have the highest cost and schedule impact. The Post-DSE Gantt chart in figure 15.1 shows this schedule implementation. It translates the PD&D logic into a scheduled overview, showing also the main review gates and dependencies between activities, making it clear which later tasks would be affected by delays in critical activities.

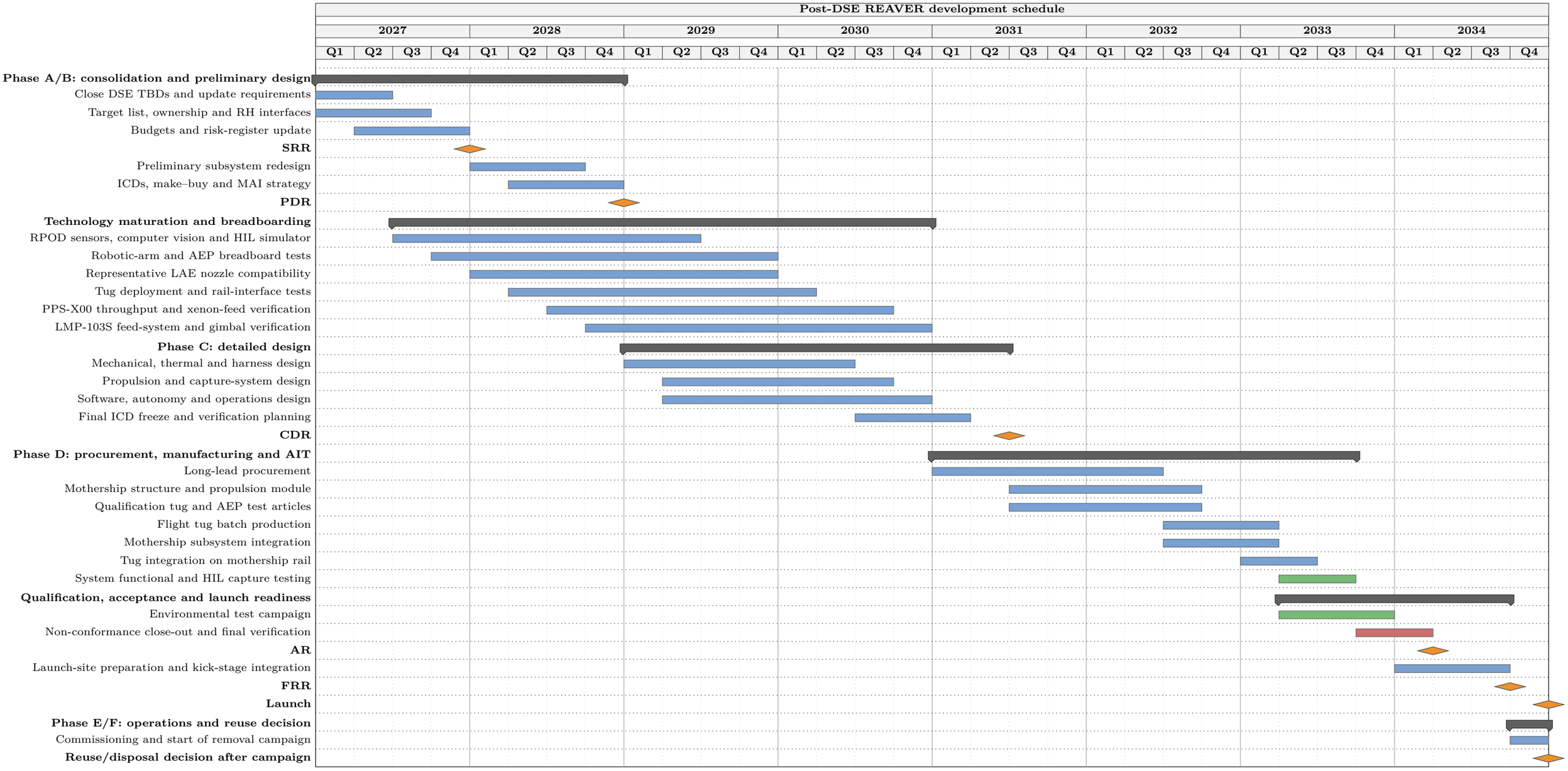

Figure 1: Indicative Post-DSE Gantt chart for REAVER. The schedule is shown at quarterly resolution and assumes launch readiness before 2035.

Figure 15.1: Post-DSE Gantt chart

15.3. Cost Breakdown Structure (CBS)

In this section, an estimate of the life-cycle cost (LCC) for one operational year of the REAVER mission is provided. At this level of the design, the 2026 fiscal year (FY2026) estimate gives a total LCC of **€249.5 M** . This exceeds the budget cap of 200 M€by about 25 %. It is also important to note that the RH is treated as an existing space station and is therefore excluded from the cost breakdown. The cost estimation methodology is reverse-engineered in the next subsection. The cost distribution is presented, and finally, the discussions are reported.

Cost Estimation Methodology

For cost estimation, a top-down approach based on cost-estimating relationships (CERs) is adopted as per Wertz et al. [71]. The work-breakdown structure (WBS) described in this book is used for cost estimation. Additionally, the CERs are first evaluated in FY2010 US dollars and then converted to FY2026 euros using an inflation factor of 1.382 and a €/USD exchange rate of 0.86.

From the cost estimation tool [71], each WBS element has its own CER, usually based on its mass class. Since REAVER system consists of two types of spacecraft, two cost models are used. The Unmanned Spacecraft Cost Model (USCM8) is applied to the mothership, in which the subsystems' costs are estimated using a power-law function of their own mass. The five tugs instead use the Small Satellite Cost Model (SSCM) as they have a total wet mass below 500 kg and take into account a fleet production cost reduction by a 95 % cumulative average learning curve applied on all five units. The capture subsystem of both spacecraft types has no existing validated CER; therefore, a mass-based estimation is used: 50 000 USD/kg (FY2010 USD). Next, flight and ground software costs are estimated on a source line of code basis, operations on a level-of-effort model over a one-year campaign, and launch cost is considered a fixed-price service when including the kick-off stage Star 63D.

For this estimation, assumptions are made. All spacecraft components are assumed to be available and procured as off-the-shelf items. Hence, non-recurring (development) costs are set to zero for all subsystems for both mothership and tugs. Only recurring manufacture and procurement, integration and test (AI&T), program-level management, launch, operations and a programme reserve are included in this cost breakdown. It is important to note that a 5 % reserve is considered and added to the acquisition cost, while the contractor fee is excluded.

This cost estimation tool by Wertz et al. is appropriate at the conceptual design level, as the CERs provide statistically reliable estimates based on mass and performance [71].

Cost Breakdown

The cost breakdown is summarised in table 15.3 and figure 15.2. There are three elements that account for almost 90 % of the total cost: launch services, the tug fleet and the mothership.

Launch services are the most costly with a 32.6 % share. This is due to the large mass needed to be launched, the mothership and the Star-63D kick stage, which when stacked together weigh approximately 7250 kg. This mass lies near the performance limit of the Falcon 9, so the launch price is then interpolated within the vehicle's published price to ≈90M USD [90].

The cost of the five tugs represents 29.6 %, which is the second most costly element of the breakdown. Although the 95 % learning curve makes the unit cost of the tugs much cheaper, having five of them plus their IA&T, program-management and ground-support still keeps the cost at a higher bound. It is important to note that the AOCS and EPS of the tugs are the most expensive subsystems.

Finally, the mothership cost represents 28.2 % of the total mission cost. This one is driven mostly by the bus production and the capture subsystem.

The three other types of costs shown in figure 15.2 are minor compared to the three main elements. Software cost is related to source lines of code and the effort required for proper software maintenance, both for flight and ground systems. Operations, on the other hand, are related to labour; for this mission, eight mission operations engineers and four technicians are assumed to be working for REAVER on a one-year campaign.

It is important to note that the cost breakdown estimate is highly sensitive to the no-development assumption. If none of the components is developed and the non-recurring costs are introduced, the total life-cycle cost would be ≈ 460M €.

Table 15.3: REAVER life-cycle cost breakdown (FY2026).

WBS element	Cost (M €)	Share (%)
1.1 Mothership (procurement, IA&T, program)	70.3	28.2
1.2 Tug fleet ×5 (procurement)	49.4	19.8
1.2 Tug fleet (IA&T, program, GSE)	24.4	9.8
1.4 Software (flight + ground)	7.5	3.0
2.0 Launch services (Falcon 9 + kick stage)	81.4	32.6
7.0 Operations (1-year campaign)	4.7	1.9
Programme reserve (5%)	11.7	4.7
Total life-cycle cost	**249.5**	**100.0**
Budget cap	200.0	-
Overrun	**49.5**	**24.7**

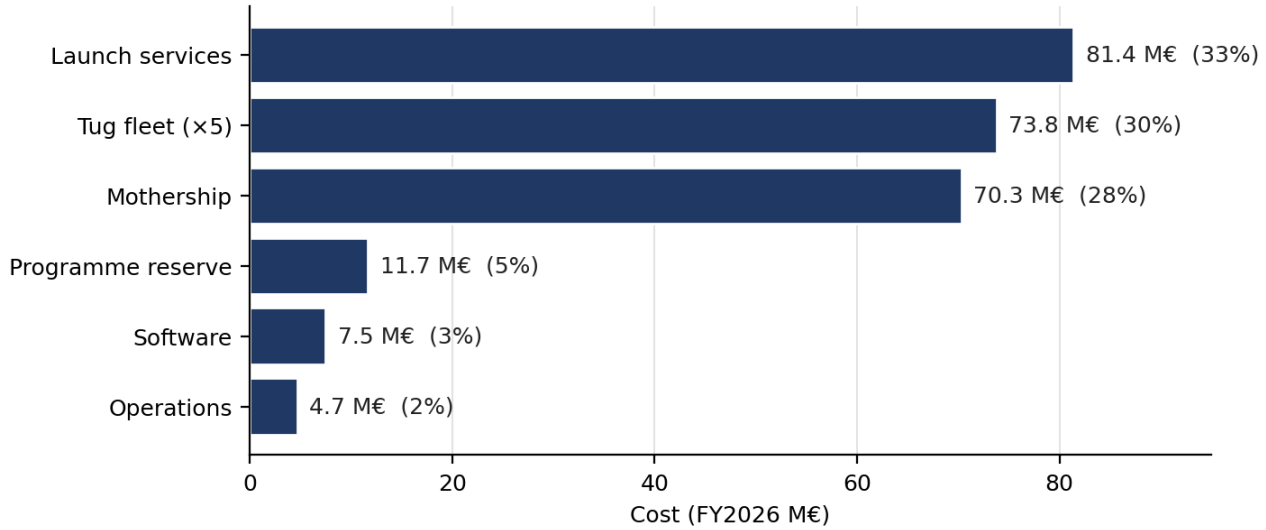

Figure 15.2: REAVER life-cycle cost by element

Discussion

The cost breakdown reported above shows that REAVER is currently considered a procurement- and launch-driven architecture, not a development-driven one. This off-the-shelf strategy, which excludes subsystem non-recurring CERs, has a direct impact on mission cost, as explained earlier. This assumption shall be considered optimistic rather than conservative and must be verified before relying on this estimate.

On another level, several cost-reduction strategies can be addressed. For example, reducing the launch mass below the reusable Falcon 9 limit by using a lighter kick stage and a low-thrust transfer from GTO to RH orbit would bring the launch cost to the baseline price and save approximately €14M. Another strategy is to maximise commonality across the five tugs by steepening the learning curve. Also, minimising the program level cost, which consists of "contractor and subcontractor costs for system engineering, program management, systems integration and test, and product assurance" [71].

However, the estimate still has an important limitation. In fact, the CERs for each element have standard errors in the range of 13 and 39 %. When propagated to the final mission budget, the lower bound becomes €187 M and the higher bound €349 M. As can be seen, the lower bound is below the €200 M cap; therefore, the overrun cannot be considered conclusive yet. Even so, it is decided to consider this cost breakdown of ≈ €250 M the re-iterated budget. The return-on-investment details how this budget update is planned.

15.4. Return-on-Investment (ROI)

Following the CBS, this section evaluates REAVER's financial return. This analysis covers the perspective of a prospective investor and the view of a co-funding agency (such as ESA, in REAVER´s case). Tools such as the net present value (NPV) and internal rate of return (IRR) framework [71]. Revenue projections draw directly on the market model established in chapter 2.

Cost Basis

The total re-iterated REAVER cost totals to €250 M (Section 15.3). This represents the entire investment required to reach first revenue (the first stage where the product/service can generate revenue): development, launch, and first-year operations are fully funded by the initial investment. For simplicity purposes, the total budget is distributed uniformly across the nine-year pre-operational development period 2026-2034 is given as equation (15.1).

$$C_{\text{dev}} = \frac{250\,\text{M}}{9\,\text{yr}} = 27.78\,\text{M}\,\text{yr}^{-1}. \tag{15.1}$$

This uniform spread is a conservative assumption: a heavier spread in the final integration and test years would increase the NPV by reducing early-discounted outflows (i) in the NPV equation. Each extension year beyond the mission incurs only operation and re-fuelling costs, totalling €10 M; the detailed breakdown can be found in chapter 2.

Revenue Model

Revenue can be divided into the operating revenue from a company's core business and non-operating revenue derived from secondary sources [1]. REAVER earns revenue through a fixed-price debris removal service contract. The primary service price is **€60M per removal**, set below the only comparable contracted precedent (ESA ClearSpace-1 at ≈ €86M for a single LEO cooperative target; Chapter 2) and above the break-even cost of €50 M (= €250 M / 5 base mission debris captures). Customers are commercial satellite operators, space agencies, and, as a secondary revenue stream, the recycling hub operator through material offtake (selling) section 2.2. Recycling hub revenue is excluded from the base case and treated as upside. Table 15.4 presents the full annual revenue projection across the modelled 14-year mission horizon.

Table 15.4: REAVER annual revenue projection (2026-2039). Development years carry no revenue; all removals are priced at €60 M per target.

Year t	Calendar	Targets	Price / Target (M€)	Revenue (M€)	Phase
1	2026	0	-	0	Development
2	2027	0	-	0	Development
3	2028	0	-	0	Development
4	2029	0	-	0	Development
5	2030	0	-	0	Development
6	2031	0	-	0	Development
7	2032	0	-	0	Development
8	2033	0	-	0	Development
9	2034	0	-	0	Development / launch
10	2035	5	60	300	Base mission
11	2036	5	60	300	Extension year 1
12	2037	5	60	300	Extension year 2
13	2038	5	60	300	Extension year 3
14	2039	5	60	300	Extension year 4
Gross revenue - base mission only (Years 1-10)				**300**	
Gross revenue - extended mission (Years 1-14)				**1500**	

Cash Flow

Table 15.6 combines cost outflows and revenue inflows into a net annual cash flow stream. Development years (Years 1-9) carry a uniform outflow of €27.78M and zero revenue. The base-mission year (Year 10) is cost-free on the operations side; first-year operations are included in the €250M sunk budget and deliver €300M in service revenue. Each extension year (Years 11-14) incurs €10M incremental operations cost against €300M gross revenue, yielding a net annual contribution of €290M.

[1] `https://www.investopedia.com/terms/r/revenue.asp` [accessed on 16 June 2026]

Table 15.6: REAVER annual cash flow (CF) table (2026–2039). All figures in M€. Extension-year operations cost is €10 M yr^{-1}.

t	Calendar	Phase	Cost outflow (M€)	Revenue inflow (M€)	Net CF (M€)
1–8	2026–2033	Development, each year	−27.78	–	−27.78
9	2034	Development / launch	−27.78	–	−27.78
10	2035	Base mission (5 targets)	0.00	+300.00	+300.00
11–14	2036–2039	Extension year 1–4 (5 targets), each year	−10.00	+300.00	+290.00
Nominal total – base mission (Years 1–10)			−250.00	+300.00	**+50.00**
Nominal total – extended mission (Years 1–14)			−290.00	+1 500.00	**+1 210.00**

Net Present Value

The net present value is computed using equation (15.2) [71], where R_t is the net cash flow in year t from Table 15.6 (M€, negative during development), i is the annual discount rate, and t is the number of years between now and each specified future year.

$$\mathrm{NPV} = \sum_{t=1}^{T} \frac{R_t}{(1+i)^t} \tag{15.2}$$

Following SMAD [71], high-risk space investments are evaluated at $i = 18\,\%$ (minimum acceptable return) and $i = 25\,\%$ (preferred return for high-risk ventures); $i = 20\,\%$ is included as the primary analysis rate, consistent with an anticipated ESA co-funding arrangement that partially de-risks the development phase.

Table 15.8: Year-by-year discounted cash flow using equation (15.2) at $i = 18\,\%$, $20\,\%$, and $25\,\%$. Net CF from Table 15.6. All monetary values in M€.

			Discount factor $(1+i)^{-t}$			Present value PV (M€)		
t	Cal.	Net CF	i=18%	i=20%	i=25%	i=18%	i=20%	i=25%
1	2026	−27.78	0.8475	0.8333	0.8000	−23.54	−23.15	−22.22
2	2027	−27.78	0.7182	0.6944	0.6400	−19.95	−19.29	−17.78
3	2028	−27.78	0.6086	0.5787	0.5120	−16.91	−16.08	−14.22
4	2029	−27.78	0.5158	0.4823	0.4096	−14.33	−13.40	−11.38
5	2030	−27.78	0.4371	0.4019	0.3277	−12.14	−11.16	− 9.10
6	2031	−27.78	0.3704	0.3349	0.2621	−10.29	− 9.30	− 7.28
7	2032	−27.78	0.3139	0.2791	0.2097	− 8.72	− 7.75	− 5.83
8	2033	−27.78	0.2660	0.2326	0.1678	− 7.39	− 6.46	− 4.66
9	2034	−27.78	0.2255	0.1938	0.1342	− 6.26	− 5.38	− 3.73
10	2035	+300.00	0.1911	0.1615	0.1074	+57.32	+48.44	+32.21
11	2036	+290.00	0.1619	0.1346	0.0859	+46.96	+39.03	+24.91
12	2037	+290.00	0.1372	0.1122	0.0687	+39.79	+32.53	+19.93
13	2038	+290.00	0.1163	0.0935	0.0550	+33.72	+27.10	+15.94
14	2039	+290.00	0.0985	0.0779	0.0440	+28.58	+22.59	+12.75
	Σ PV dev costs (Years 1-9)		−119.53	−111.97	−96.20			
	Σ PV revenues (Years 10-14)		+206.37	+169.69	+105.74			
		NPV - base mission only (Years 1-10)				−62.21	−63.52	−64.00
		NPV - extended mission (Years 1-14)				**+86.84**	**+57.73**	**+9.55**

Each PV entry is computed directly from equation (15.2): or example, at $i = 20\,\%$ and $t = 10$, PV $= 300.00/(1.20)^{10} = 300.00 \times 0.1615 = +48.44$ M. Summing all 14 PV entries at $i = 20\,\%$ gives the extended-mission NPV of +57.73 M€. The base-mission NPV is negative at all three rates (−€62 to −64 M€). This is not an operational loss; the base mission nominally generates +50 M€ in revenue, but the 300 M€ revenue event occurs nine years after programme initiation. The extended mission converts this into a positive risk-adjusted return at

every rate. At the most demanding rate of $i = 25\,\%$, the extended-mission margin is slim (+9.55 M€), confirming that the investment case is sensitive to the discount rate in the upper range.

Internal Rate of Return

The IRR is the discount rate i^* satisfying equation (15.2) with NPV = 0. No closed-form solution exists for $T > 4$; i^* is found numerically for $T > 4$. Table 15.10 shows the IRR results vesus SMAD guidelines.

$$\sum_{t=1}^{T} \frac{R_t}{(1+i^*)^t} = 0. \tag{15.3}$$

Table 15.10: IRR results versus SMAD guidelines [71]

Mission state	IRR (%)	≥ 18 %?	≥ 25 %?	Verdict
Base mission only (Years 1-10)	3.63	No	No	Not investable on a discounted basis
Extended mission (Years 1-14)	26.49	Yes	Yes	Exceeds both SMAD thresholds

The base-mission IRR of 3.63 % lies far below the 18 % minimum, confirming what the NPV analysis shows: a single operational year is insufficient to justify the nine-year development investment on a risk-adjusted basis. The extended-mission IRR of **26.49 %** exceeds the preferred 25 % high-risk threshold. Mission extension is, therefore, not only financially beneficial but also the mechanism by which the investment becomes viable in the first place.

RAAN Filter Sensitivity and Mission Extension

The number of accessible debris objects directly governs how many operational years REAVER can sustain, and therefore how much of the 290 M€ yr^{-1} net cash flow stream is realisable. Two independent ways are available: widening the RAAN filter around the current hub at no cost, and relocating the hub to access an entirely new debris cluster at a one-time propellant charge. Both are analysed below against the baseline of 21 objects and 5 operational years.

Analysis 1: Hold the RH at 64° and widening the debris RAAN range

For this first analysis, the RH is kept in the same orbital plane, and therefore no extra costs are added; with the hub kept at 64°, the list of debris is increased from the original 21 spacecraft to 33 when widening the RAAN range to 50°-100°).

From the $\binom{33}{5} = 237\,336$ combinations available from this new list, all are time-feasible: the 365 d limit is never reached. Therefore, propellant becomes the only limiting factor for a campaign to be feasible. Figure 15.3 displays the resulting distribution of the mothership orbital propellant for all possible campaigns. As shown, the majority of the 237 336 campaigns are located to the left of the design cap. Out of all combinations, 214 181 (90.24 %) have a propellant mass below the design cap of 1019.3 kg (green line) and 234 987 (99.01 %) below the margin cap (orange line).

With 33 debris added to the list, another two years of operation can be added if the sequence chosen by the customer doesn't fall in the 9.76 % above the propellant design cap.

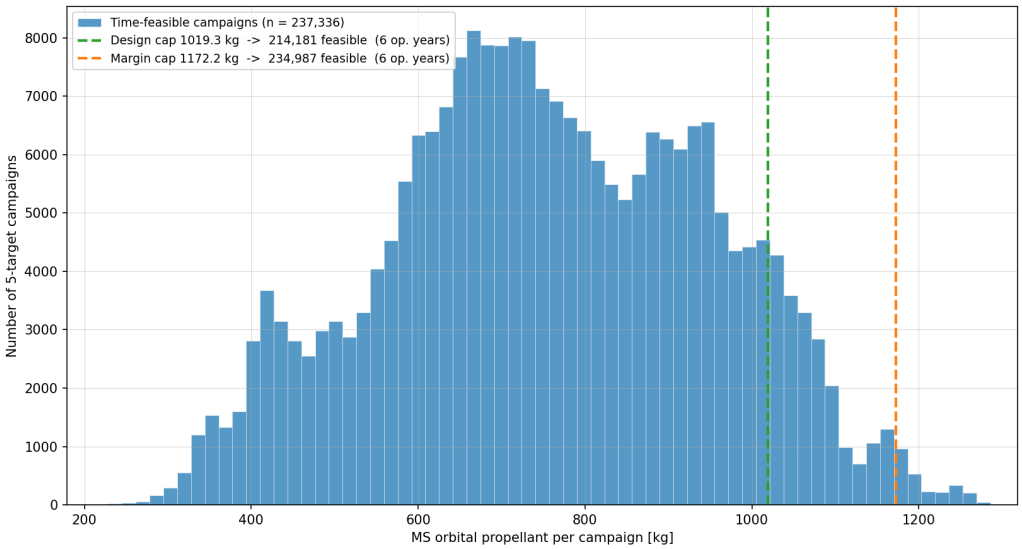

Figure 15.3: Distribution of per-campaign MS orbital propellant for all 237 336 time-feasible 5-target campaign, $\Omega^*_{RH} = 64°$.

The 9.8 % of combinations that are not feasible are driven by RAAN extremes of the objects: those that are furthest from the 64° RH position. Figure 15.4 shows a ranking of every object based on the share of its campaigns that are above the design cap. This is assessed against the 9.8 % fleet baseline. The single worst object is the 804/COMSATBW-1 ($\Omega = 89.7°$), which shares over the design cap at 42 % of its combinations. It can also be seen that most of the new 12 debris are at or below the baseline. It is important to note that the fleet baseline helps analyse how difficult it is to include an object within a feasible sequence. Debris with bars higher than the fleet baseline makes campaigns harder than average. As can be seen, because COMSATBW-1 is part of the design sequence, it can still be included. In fact, the RAAN distance between objects makes missions not feasible as high ΔV are required.

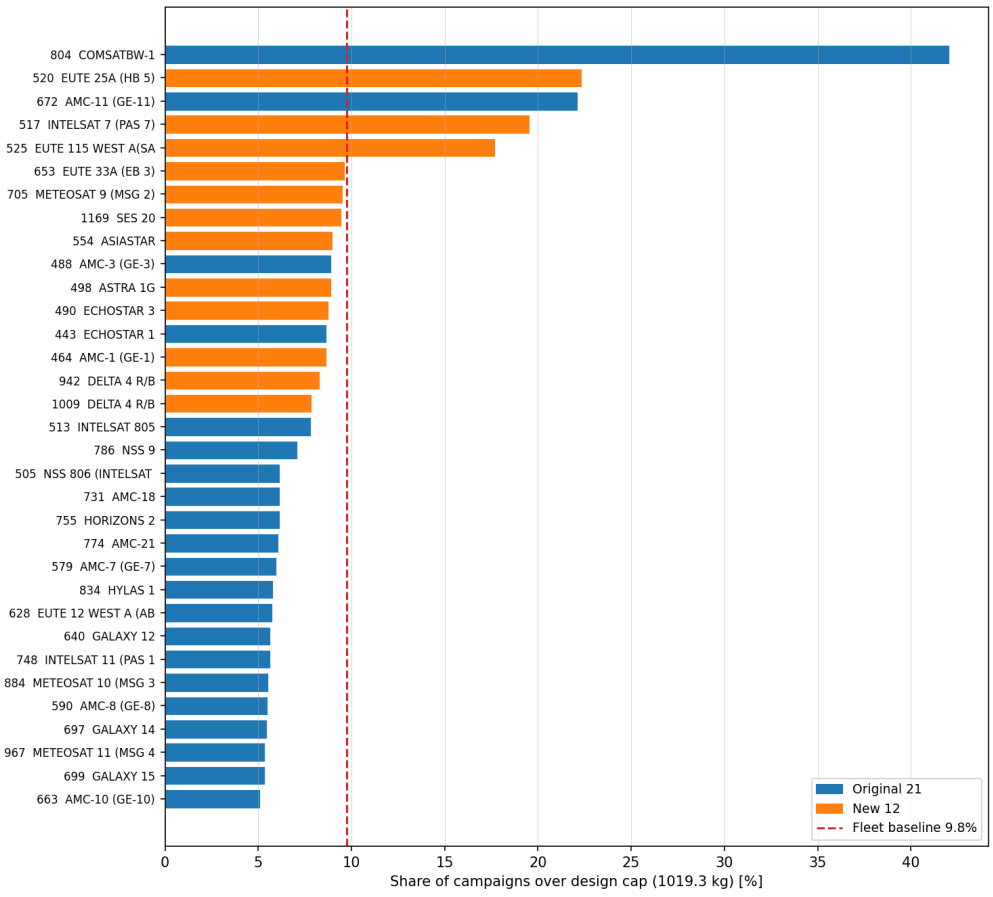

Figure 15.4: Debris share of 5-target campaigns exceeding the design cap against the 9.8 % fleet baseline.

Analysis 2: Relocate the RH to a new RAAN band

Now, the second analysis assumes an operational RAAN band 0°-30° giving a new list of 23 debris. From the current 64° hub, this RAAN band is completely unreachable with the mothership and the tugs: only 193 out of 33 649 possible sequences are feasible. This amount is marked by the lower (red) reference line in figure 15.5. By applying the RAAN RH optimisation explained in section 3.5 across the new range, the in-band optimum line in figure 15.5 sets at 14°. At the 14° optimum, the design cap allows 27 845 campaigns out of 33 649 possible representing 82.75 %. Again, all debris can be chosen at least once but it must be compatible with the four other debris to have the sequence feasible. The non-feasible constraint is therefore relying on the RAAN difference between debris of one sequence.

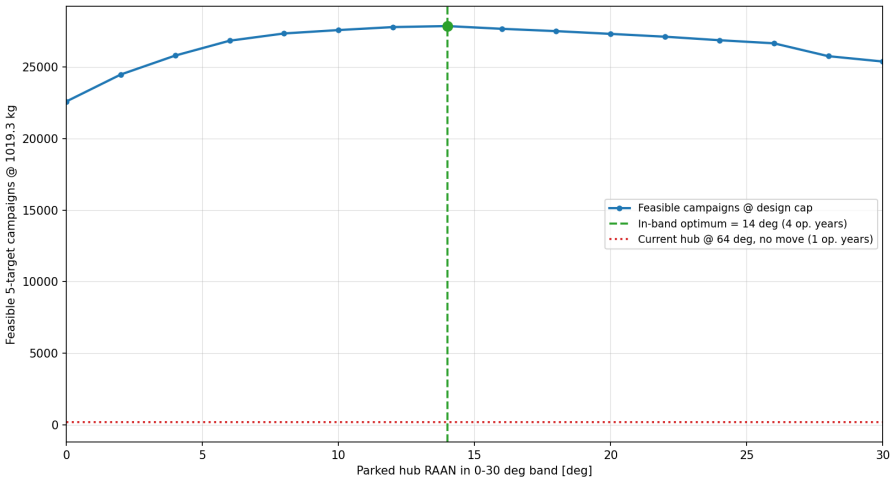

Figure 15.5: Feasible 5-target campaigns at the design cap for a 0 ° to 30 °

Figure 15.6 shows the mothership propellant distribution at the 14° optimum Ω^*_{RH}. As can be seen, it is bimodal: a major low-propellant lobe of easily feasible campaigns, followed by a smaller high-propellant lobe. The interesting part is that the design cap separates the two. This is the reason why 27 845 out of the 33 648 campaigns (83 %) are inside the design cap, while the margin cap captures all but 16 campaigns.

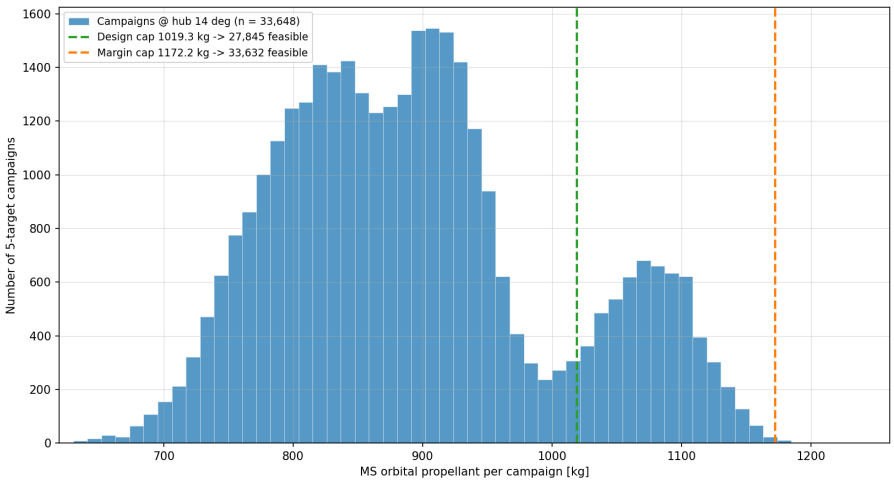

Figure 15.6: Per-campaign mothership orbital propellant at $\Omega^*_{RH} = 14°$

Now moving the RH from 64° to 14° RAAN comes at a cost. The relocation is a one-time 314 m s^{-1} single-burn plane change. Sizing the burn propellant mass with a recycling hub wet mass taken as 104 931 kg (one-fourth of an ISS-class structure, 419 725 kg) at an assumed I_{sp} = 250 s requires 12 614 kg of propellant. At an assumed propellant cost of €5000/kg, this is a one-time charge of **€63.07 M**, incurred once in 2041 (an assumption of 6 operational years before moving to another RH RAAN).

Note that in this table, the operational years are combined. Once all debris in the initial RAAN range is captured, the two other mission-extension strategies are sequentially added in operational years.

ROI Conclusion

ROI is positive under the following joint conditions:

Table 15.12: Mission-extension strategies and their NPV impact (discount rate $i = 20\,\%$).

Extension strategy	Hub RAAN	Accessible objects	Op. years	One-time cost	NPV @ 20 % (€M)
Initial RAAN range	64°	21	4	-	+35.14
Hold + increase RAAN filter range (Analysis 1)	64°	33	6	-	+76.5
Relocate recycling hub (Analysis 2)	14°	+23	+4 (→ 10)	€63 M	+121.9

1. **Service price ≥ €50 M per removal.** Any contract below the break-even floor (€250 M ÷ 5) converts the base mission from a nominal surplus to a nominal loss.
2. **At least two extension years are completed.** The extended-mission cumulative PV first crosses zero in Year 12 (2037) at $i = 20\,\%$ and in Year 11 (2036) at $i = 18\,\%$ (see Table 15.8). A single operational year yields a negative NPV at any realistic investor discount rate.
3. **Discount rate** $< 26.49\,\%$ **(the extended-mission IRR).** At rates above the IRR, the project yields a negative NPV even with full extension. ESA co-funding or agency anchor contracts reduce the effective cost of capital below this ceiling.
4. **RAAN filter is widened (Analysis 1).** The initial 4-year extension yields IRR = 24.44 %, below the preferred 25 % threshold. Widening at zero cost raises IRR to 27.85 %, clearing both SMAD hurdle rates.
5. **Mission extension cost ≤ 10 M€ yr^{-1}.** Recycling hub relocation (Analysis 2) adds four further years at a one-time 63 M€ charge, raising the full-programme IRR to 30.08 % and NPV at $i = 20\,\%$ to 121.9 M€.

The investment case is unsuccessful if the following scenarios occur:

- **Mission confined to one operational year.** IRR = 3.63 %; NPV negative at all rates > 4 %. If the hub is unavailable or extension contracts cannot be signed, the nominal +€50 M surplus does not compensate investors on a time-value basis.
- **Discount rate** > 26.49 %**.** Unlikely under a co-funded programme structure, but possible in a pure private-equity scenario with no government off-take agreement (not REAVER's case).
- **Mission failure.** A total loss eliminates all revenue while €250 M in costs are already sunk. Partial risk mitigation is available through launch insurance and an anchor contract that commits revenue before the first flight.

For an investor, REAVER offers an IRR of 27.85 % to 30.08 % depending on extension strategy, exceeding the SMAD preferred 25 % high-risk threshold [71], in a market growing at 29.9 % CAGR with no commercial GEO competitor. ESA co-funding lowers the effective cost of capital, recycling hub offtake provides uncaptured upside, and the hub-based architecture creates structural barriers to entry (for competitors).

16. Conclusions & Recommendations

The increasing accumulation of non-operational spacecraft in geostationary Earth orbit (GEO) represents one of the most significant long-term challenges facing the sustainability of the space environment. Unlike debris in low Earth orbit, objects located in GEO experience negligible atmospheric drag and therefore remain in orbit for centuries or longer unless actively removed. As the number of inactive spacecraft continues to grow, so does the probability of collision events, fragmentation cascades, interference with operational satellites, and the degradation of one of humanity's most valuable orbital resources. Addressing this challenge requires solutions that are not only technically feasible but also economically sustainable and operationally scalable. To extract economic value from these objects, an orbital recycling hub has been developed; however, a critical challenge remains: transporting this debris to the facility.

The Resource Extraction Autonomous Vehicle for Environmental Recovery (REAVER) mission proposes an ambitious and complex multi-vehicle architecture to retrieve five uncooperative, defunct geostationary satellites in one year, launching before 2035. The system consists of six spacecraft: a central mothership carrying five tugs, each assigned to a single target. By utilizing a distributed architecture, demanding functions such as rendezvous, sensing, and synchronization are performed by the mothership, allowing the tugs to maintain an ultralight, simple design. Multiple tugs allow for fast, parallel operations, enabling the use of highly efficient, low-thrust electric propulsion. Conversely, the mothership utilizes high-thrust LMP-103S green monopropellant to ensure it can attach a tug to each debris object within the strict mission timeline. This report details the complete conceptual design of the REAVER mission, establishing both its technical and economic viability.

Because the exact locations of target debris in 2035 are unknown, a statistical analysis was performed on the current debris catalogue to select a worst-case ΔV-mission profile. By sizing REAVER for this worst-case scenario, the system is guaranteed to possess the capability to capture and retrieve any five geostationary targets that meet the mission criteria. A detailed trajectory optimization was performed, and analytic calculations were validated with high-fidelity GMAT simulations. The resulting campaign returns five debris objects with a combined mass of approximately 10 050 kg to the recycling hub, while maintaining a total mission duration of approximately 291 days.

Detailed design was conducted across all mission subsystems, proving the architecture's technical viability. Most innovation efforts were directed toward developing the Apogee Engine Probe (AEP) mechanism, the robotic arm, and the various sensors and AOCS components required to execute the complex capture sequence. Conversely, subsystems such as the EPS, TCS, and primary structures utilize mostly standard commercial components and were designed with simplicity and availability in mind. The total launch mass of the REAVER stack is approximately 7245 kg, remaining well below the 8300 kg limit of the Falcon 9 launch vehicle for geostationary transfer orbits.

Beyond satisfying the immediate mission requirements, REAVER demonstrates a fundamentally different approach to active debris removal. Rather than treating debris removal as a single-use cleanup operation, the mission has been designed around reusability and long-term infrastructure development. The reusable tug fleet, autonomous rendezvous capability, robotic manipulation system, and planned integration with a recycling hub collectively transform the mission from a standalone debris-removal campaign into the foundation of a broader orbital logistics network. This distinction is critical, as the long-term sustainability of space operations will likely depend on reusable infrastructure rather than one-off missions.

The commercial assessment indicates that a viable market opportunity exists for GEO active debris removal services. Regulatory trends, increasing concern regarding orbital sustainability, and growing operator liability collectively suggest that demand for debris-removal services will continue to rise over the coming decades. The project identified a target service price of approximately €50M per removal and demonstrated that the selected architecture occupies a market position that is not currently served by existing commercial systems. In particular, REAVER's ability to capture uncooperative legacy spacecraft without requiring pre-installed servicing interfaces represents a significant competitive advantage.

At the same time, the project revealed several important limitations that must be acknowledged. The final life-cycle cost estimate of approximately €250M exceeds the original programme target of €200M, indicating that further cost optimization will be required prior to implementation. More importantly, the economic analysis shows that the base mission alone provides only a limited financial return. The strongest business case emerges when the architecture is operated as reusable infrastructure over an extended period. Under the extended mission scenario, where hub refuelling enables up to 20 additional debris removals over four years, the project

achieves a positive net present value and an internal rate of return of approximately 26.5%. This result proves that reusability is not simply an attractive design feature, but a fundamental requirement for long-term economic success.

In conclusion, REAVER demonstrates that a reusable GEO active debris removal mission is technically feasible, operationally practical, and strategically valuable. The final design achieves the removal of five non-cooperative GEO spacecraft with a combined mass exceeding 10 tonnes within a single operational year, all while maintaining positive system margins and a significant schedule reserve. Although challenges remain in technology maturation, economic optimization, and regulatory implementation, the project establishes a credible pathway toward the sustainable management of the GEO environment. More importantly, it proves that the future of orbital sustainability extends far beyond debris mitigation alone. By combining debris removal, reusability, and resource recovery within a single architecture, REAVER provides the foundation for a future in which space infrastructure is maintained, reused, and ultimately integrated into a circular orbital economy.

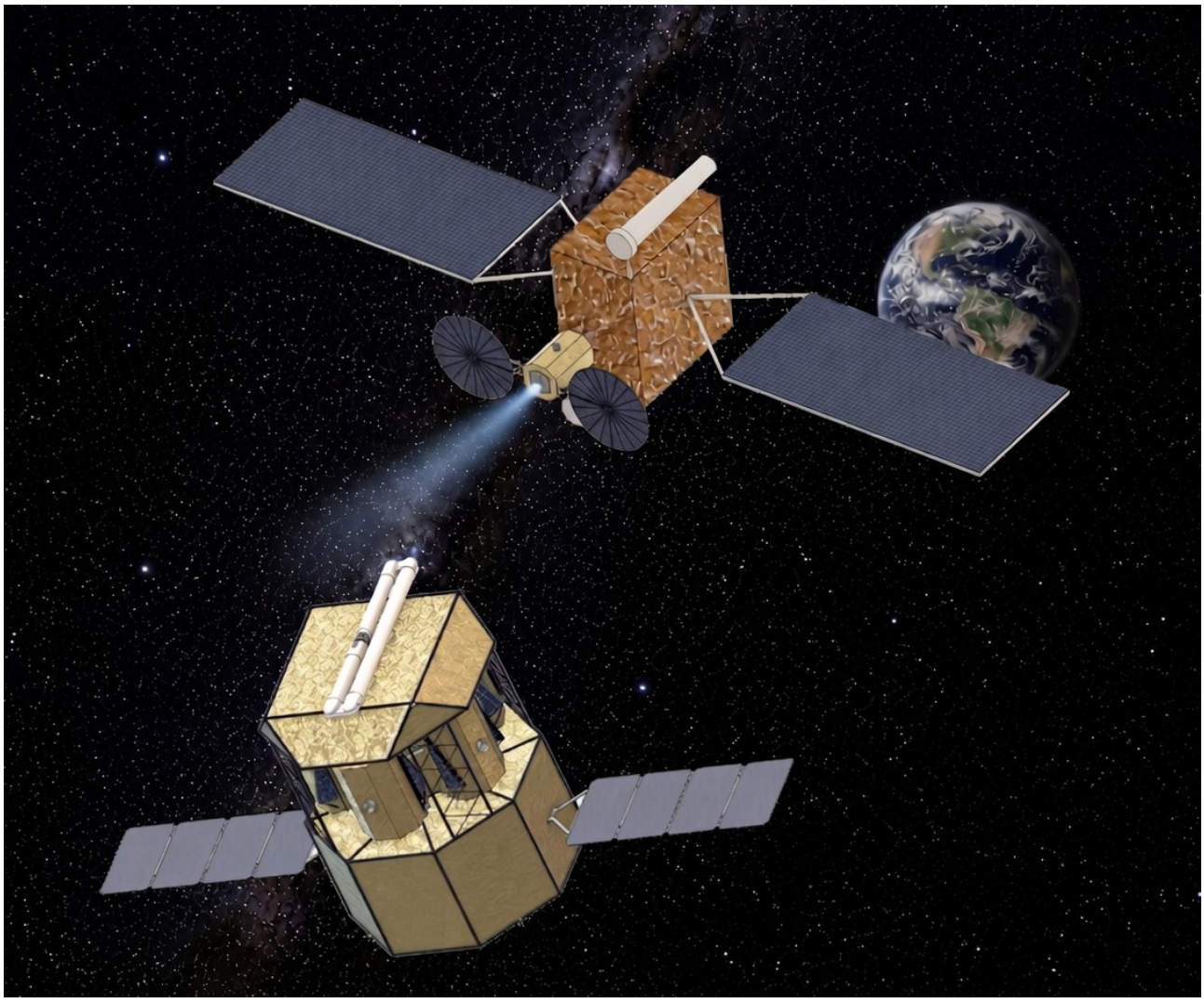

Figure 16.1: Mission visualization created with 3DEXPERIENCE Catia (background and plume generated by ChatGPT)

16.1. Recommendations & Next Steps

From a technical perspective, the greatest remaining challenges are associated with the rendezvous, proximity operations, and capture of non-cooperative targets. While the propulsion systems and many spacecraft technologies used by REAVER possess significant flight heritage, the integrated autonomous capture sequence remains the primary source of programme risk. Successful mission execution depends entirely on the reliable interaction of computer vision systems, relative navigation sensors, robotic manipulation hardware, guidance algorithms, and capture mechanisms operating in close proximity to uncontrolled spacecraft. As a result, the overall feasibility of the mission is driven less by any individual subsystem and more by the successful integration of these technologies into a robust operational framework. Furthermore, it must be noted that many critical analyses and tests still need to be conducted at both the subsystem and system levels. Detailed structural,

modal, and thermal simulations are required to refine the subsystems, alongside lower-level component design for secondary and tertiary structural elements, detailed electronic hardware, and propulsion sensors. The specifics of the recommended next steps for the REAVER project are as follows:

Capture System Development The high-level design of the capture system has been successfully completed, but many steps still have to be taken to ensure a robust design. While the architecture of the control software has been outlined, the software itself still needs to be created and validated. Specifically, computer vision algorithms to analyze the debris during proximity operations, AOCS robotic arm control algorithms, and the autonomy logic need to be finalized. Furthermore, extensive ground integration testing is recommended for all the capture system elements, especially the AEP mechanism, robotic arm, and all the sensors used to analyze the debris. Particularly, ground capture tests of the AEP mechanism should be performed during the start of the AIT mission phase on the exact hardware that is expected to be present on the target debris. Interface testing between the robotic manipulator and tugs should also be performed at this time.

Detailed Structural Design and Analysis This report presented the design of the primary structure of the mothership. However, secondary and tertiary structural design still needs to be performed. Structural interfaces between all the subsystem components and the spacecraft structure should be fully designed while making sure all components can be assembled and manufactured. Since the sizing and analysis was performed mostly with hand calculations, detailed simulations should be performed using the finite element method and modal analysis to optimize the structure weight and design. If the structure is significantly optimized, another design iteration is recommended to update the spacecraft propellant mass and tank sizing. Alongside the structural simulations, modal and thermal analysis should be carried out with the specific vibration and acoustic profile present during a Falcon 9 launch to validate the structure. It is highly suggested that this analysis is completed before the critical design review (CDR).

Attitude & Orbit Control Development While this report presents a preliminary approach to a comprehensive attitude and orbit control system design, many aspects remain to be developed for a functional spacecraft. Since all hardware components of the AOCS have been selected, the next step is to develop a detailed numerical spacecraft model that captures the spacecraft dynamics, actuator behaviour, sensor characteristics, and time-varying mass properties. This model forms the basis for developing the control and navigation algorithms, as well as for analysing the spacecraft's robustness to executing commanded manoeuvres and rejecting disturbances. Since the AOCS regulates how the spacecraft perceives and interacts with its environment, algorithms must be developed to interpret sensor measurements, estimate the spacecraft state, and command the actuator responses. The challenges of active debris removal present the need for highly complex and precise control and navigation systems provided by the AOCS. As with the structural design and analysis, it is recommended that these actions are performed before the REAVER CDR.

Propulsion Development & Analysis Subsequent phases of propulsion system development must finalize the detailed fluidic architecture, including the precise layout of tanks, valves, propellant lines, and the pressure-control system. Furthermore, the transient effects of propellant depletion and sequential tug deployment on the spacecraft's center of gravity require comprehensive dynamic analysis. The cumulative propellant throughput for each thruster must be rigorously verified against operational design limits. This is particularly critical for the tug's electric propulsion system, as the extended duration of debris-transfer spirals and potential mission extension campaigns risk exceeding thruster lifetime and accelerating component erosion. Regarding the mothership, the total throughput of the LMP-103S monopropellant across both the primary and reaction-control thrusters must be evaluated in conjunction with maximum continuous firing durations, thermal constraints, and propellant slosh dynamics. Finally, the reliability of the tug's xenon feed system and cold-gas control branch, alongside the operational lifespan of the PPS-X00 thruster, must be validated through rigorous component-level testing and manufacturer qualification data.

From an economic perspective, several analyses and opportunities need to be explored. As it stands, REAVER's economic viability is questionable if further actions are not taken. The most economically enticing prospect is increasing the mission duration and number of target debris. Several modifications would be required to enable this, such as refuelling capability for the mothership and tugs at the recycling hub. Particularly, REAVER's economic outlook could be improved by establishing a firm service price strictly above the €50M break-even floor per removal; executing binding contracts for at least two operational extension years prior to launch (as the investment's cumulative present value only transitions to positive between the years 2036 and 2037); and securing co-funding agreements with agencies like ESA to artificially lower the cost of capital and insulate the investment against total mission failure.

Bibliography

[1] Klinkrad, H., *Space Debris: Models and Risk Analysis*, Springer-Praxis, Chichester, UK, 2006.

[2] Inter-Agency Space Debris Coordination Committee, "IADC Space Debris Mitigation Guidelines," Tech. Rep. IADC-02-01 Rev. 4, Inter-Agency Space Debris Coordination Committee, Jan. 2025, Issued by IADC Steering Group and Working Group 4.

[3] United Nations, "Treaty on Principles Governing the Activities of States in the Exploration and Use of Outer Space, including the Moon and Other Celestial Bodies," 1967, United Nations Treaty Series, Vol. 610, No. 8843. Entered into force 10 October 1967.

[4] United Nations, "Convention on International Liability for Damage Caused by Space Objects," 1972, United Nations Treaty Series, Vol. 961, No. 13810. Entered into force 1 September 1972.

[5] Sellmaier, F., Uhlig, T., and Schmidhuber, M., editors, *Spacecraft Operations*, Springer, Cham, Switzerland, 2nd ed., 2022.

[6] Curtis, H. D., *Orbital Mechanics for Engineering Students*, Butterworth-Heinemann, 3rd ed., 2014.

[7] Edelbaum, T. N., "Propulsion Requirements for Controllable Satellites," *ARS Journal*, Vol. 31, No. 8, 1961, pp. 1079–1089.

[8] Juillard, M., Richard-Noca, M., and Kneib, J.-P., "Dedicated On-Board Computer for Active Debris Removal Mission," *Proceedings of the 34th Annual AIAA/USU Conference on Small Satellites*, SSC20-P2-17, Utah State University, Logan, Utah, USA, Aug. 2020, Technical Poster Session II.

[9] Parkes, S. and Rosello, J., "SpaceWire ECSS-E50-12A," *International SpaceWire Seminar (ISWS 2003)*, ESTEC, Noordwijk, The Netherlands, Nov. 2003.

[10] Consultative Committee for Space Data Systems, "Space Packet Protocol," Recommendation for Space Data System Standards CCSDS 133.0-B-2, CCSDS, Washington, D.C., June 2020.

[11] Consultative Committee for Space Data Systems, "Space Data Link Security Protocol," CCSDS 355.0-B-2, Blue Book, 2022.

[12] European Cooperation for Space Standardization, "Space Engineering: Satellite Attitude and Orbit Control System (AOCS) Requirements," Standard ECSS-E-ST-60-30C, ECSS Secretariat, ESA-ESTEC Requirements & Standards Division, Noordwijk, The Netherlands, aug 2013.

[13] Flores-Abad, A., Ma, O., Pham, K., and Ulrich, S., "A Review of Space Robotics Technologies for On-Orbit Servicing," *Progress in Aerospace Sciences*, Vol. 68, 2014, pp. 1–26.

[14] Space Logistics, LLC, "MEV-2 Technical Appendix," Tech. Rep. SAT-LOA-20191210-00144, Federal Communications Commission, Dec. 2019.

[15] Faure, M., Henry, D., Cieslak, J., Colmenarejo, P., and Ankersen, F., "A H control solution for space debris removal missions using robotic arms: the ESA e.Deorbit case," *International Conference on Control*, 2022.

[16] Persson, M., Anflo, K., and Friedhoff, P., "Flight Heritage of Ammonium Dinitramide (ADN) Based High Performance Green Propulsion (HPGP) Systems," *Propellants, Explosives, Pyrotechnics*, Vol. 44, No. 9, 2019, pp. 1073–1079.

[17] Huzel, D. K. and Huang, D. H., *Design of Liquid Propellant Rocket Engines*, No. NASA-SP-125 in NASA Special Publication, National Aeronautics and Space Administration, Washington, DC, 1967.

[18] Goebel, D. M. and Katz, I., *Fundamentals of Electric Propulsion: Ion and Hall Thrusters*, JPL Space Science and Technology Series, Wiley, 2008.

[19] Safran Spacecraft Propulsion, "PPS®X00 Stationary Plasma Thruster Datasheet," Datasheet, 2022, Accessed: 2026-05-19.

[20] European Cooperation for Space Standardization, "ECSS-E-ST-32C: Structural General Requirements," Ecss standard, ESA-ESTEC, 11 2008.

[21] European Cooperation for Space Standardization, "ECSS-E-ST-31C: Space Engineering – Thermal Control General Requirements," Standard ECSS-E-ST-31C, ECSS Secretariat, ESA-ESTEC Requirements & Standards Division, Nov. 2008, Accessed: 2026-06-11.

[22] Lam, G. Q., Billets, S. A., Norick, T. A., and Warwick, R. W., "Solar Array Design for the Mars InSight Lander Mission," Tech. rep., Salt Lake City, UT, July 2016, AIAA 2016-4520.

[23] European Cooperation for Space Standardization, "Space Engineering: Radio Frequency and Modulation," Tech. Rep. ECSS-E-ST-50-05C, ESA-ESTEC, Noordwijk, The Netherlands, Oct. 2011.

[24] European Cooperation for Space Standardization, "Space Project Management: Risk Management," Standard ECSS-M-ST-80C, ECSS Secretariat, ESA-ESTEC Requirements & Standards Division, Noordwijk, The Netherlands, jul 2008.

[25] ECSS Secretariat, "Technology Readiness Level (TRL) Guidelines," Tech. Rep. ECSS-E-HB-11A, European Space Agency – ESA-ESTEC, Requirements & Standards Division, Noordwijk, The Netherlands, March 2017.

[26] European Space Agency, "Space System Life Cycle Assessment (LCA) Handbook," Tech. Rep. ESSB-HB-U-005, Issue 2, European Space Agency, 2026, Accessed: 18 May 2026.

[27] ECSS Working Group E-10-02, "Space Engineering – Verification," ECSS Standard ECSS-E-10-02A, European Space Agency / ESTEC, Noordwijk, The Netherlands, November 1998.

[28] European Cooperation for Space Standardization, "ECSS-E-ST-10-03C Rev.1: Space Engineering – Testing," Standard, European Cooperation for Space Standardization, May 2022, Accessed: 2026-05-22.

[29] National Aeronautics and Space Administration, "NASA Systems Engineering Handbook," Handbook NASA/SP-2016-6105 Rev 2, NASA, Washington, D.C., jan 2020.

[30] National Aeronautics and Space Administration, "NASA Schedule Management Handbook," Tech. Rep. NASA/SP-2010-3403, NASA, 2010, Revision 1, effective date: 30 October 2020. Accessed: 2026-05-01.

[31] Federal Communications Commission, "Report and Order: Mitigation of Orbital Debris in the New Space Age," Report and Order FCC-22-74, Federal Communications Commission, Washington, D.C., USA, 2024.

[32] Inter-Agency Space Debris Coordination Committee, "IADC Space Debris Mitigation Guidelines," Technical Guideline IADC-02-01 Rev. 1, IADC, 2007.

[33] Lenkart, M. and Biller, S., "Space debris material sourcing for in-space manufacturing: a quantitative evaluation framework," *Frontiers in Space Technologies*, Vol. 6, 2026, pp. 1690460.

[34] European Space Agency, "ClearSpace-1: First Active Debris Removal Mission," ESA Press Release, 2020.

[35] Defense Advanced Research Projects Agency, "Robotic Servicing of Geosynchronous Satellites (RSGS) Programme," Programme Information Page, 2026.

[36] Conings, V. and Mooij, E., "Integrated Guidance, Navigation, and Control System Design for Active Debris Removal," *AIAA Guidance, Navigation, and Control Conference*, American Institute of Aeronautics and Astronautics (AIAA), Orlando, Florida, USA, Jan. 2025, AIAA Paper 2025-0085.

[37] Weiss, A., Kalabić, U. V., and Di Cairano, S., "Station keeping and momentum management of low-thrust satellites using MPC," *Aerospace Science and Technology*, Vol. 76, 2018, pp. 229–241.

[38] REAVER Group 7, "Midterm Report: REAVER Mission Design," Design Synthesis Exercise Report Group 7, TU Delft, Faculty of Aerospace Engineering, 2026, AE3200 Design Synthesis Exercise.

[39] European Cooperation for Space Standardization, "ECSS-E-TM-10-21A: Space Engineering – System Modelling and Simulation," Tech. rep., ECSS Secretariat, April 2010, Accessed: 2026-05-21.

[40] Guarro, S., "Launch Vehicle Reliability and Risk Metrics: Definition and Estimation in Relation to Requirements," *Proceedings of the 14th International Probabilistic Safety Assessment and Management Conference*, Los Angeles, CA, USA, 2018, Accessed: 2026-05-21.

[41] National Aeronautics and Space Administration, "NASA-HDBK-1002: Fault Management Handbook," Tech. rep., NASA, April 2012, Draft 2. Accessed: 2026-05-21.

[42] European Space Agency, "Margin Philosophy for Science Assessment Studies," Technical memorandum, European Space Agency, 2012.

[43] European Space Agency, "Guidelines for Delta-V and Propellant Budget Computation," Tech. rep., European Space Agency, 2020.

[44] Tian, Z., "Legal Aspects of Active Debris Removal (ADR): Regulation of ADR Under International Space Law and the Way Forward for Legal Development," *Meijers-reeks*, 2024.

[45] European Cooperation for Space Standardization, "Space Engineering: Space Segment Space Link Extension Protocols," Standard ECSS-E-ST-70-11C, ECSS Secretariat, ESA-ESTEC Requirements & Standards Division, Noordwijk, The Netherlands, jul 2008.

[46] Inter-Agency Space Debris Coordination Committee, *IADC Space Debris Mitigation Guidelines*, June 2021.

[47] Oltrogge, D. L., Alfano, S., Law, C., Cacioni, A., and Kelso, T. S., "A Comprehensive Assessment of Collision Likelihood in Geosynchronous Earth Orbit," *Acta Astronautica*, Vol. 147, 2018, pp. 316–345.

[48] National Aeronautics and Space Administration, "NASA-HDBK-4002B: Mitigating In-Space Charging Effects – A Guideline," Tech. rep., NASA, June 2022, Accessed: 2026-05-21.

[49] Shan, M., Guo, J., and Gill, E., "Review and Comparison of Active Space Debris Capturing and Removal Methods," *Progress in Aerospace Sciences*, Vol. 80, 2016, pp. 18–32.

[50] Opromolla, R., Fasano, G., Rufino, G., and Grassi, M., "A Review of Cooperative and Uncooperative Spacecraft Pose Determination Techniques for Close-Proximity Operations," *Progress in Aerospace Sciences*, Vol. 93, 2017, pp. 53–72.

[51] Ledkov, A. and Aslanov, V., "Review of Contact and Contactless Active Space Debris Removal Approaches," *Progress in Aerospace Sciences*, Vol. 134, 2022, pp. 100858.

[52] Estable, S., Telaar, J., Lange, M., Ahrns, I., Pegg, K., Jacobsen, D., Gerrits, D., Theybers, M., Dayers, L., Vanden Bussche, S., Ilsen, S., Debraekeleer, T., Lampariello, R., Wygachiewicz, M., Santos, N., Canetri, M., Serra, P., Soto Santiago, L., Łukasik, A., Ratti, J., Puddephatt, D., Rembala, R., Evans Brito, L., Bondy, M., Biesbroek, R., and Wolahan, A., "Definition of an Automated Vehicle with Autonomous Fail-Safe Reaction Behavior to Capture and Deorbit ENVISAT," *Proceedings of the 7th European Conference on Space Debris*, edited by T. Flohrer and F. Schmitz, ESA Space Debris Office, Darmstadt, Germany, April 2017.

[53] National Aeronautics and Space Administration, "On-Orbit Satellite Servicing Study: Project Report," Tech. rep., NASA Goddard Space Flight Center, Oct. 2010.

[54] National Aeronautics and Space Administration, "NASA-STD-5001B: Structural Design and Test Factors of Safety for Spaceflight Hardware," Tech. rep., NASA, 2014, With changes. Accessed: 2026-05-21.

[55] Larson, W. J., Kirkpatrick, D., Sellers, J. J., Thomas, L. D., and Verma, D., *Applied Space Systems Engineering*, Space Technology Series, McGraw-Hill, New York, NY, 2009.

[56] Poivey, C., "Radiation Hardness Assurance for Space Systems," Tech. rep., NASA Goddard Space Flight Center / SGT-Inc., 2002.

[57] Global Satellite Operators Association (GSOA), "Latency in Communications Networks," Tech. rep., 2017.

[58] Zandbergen, B. T. C., "Spacecraft Bus Design and Sizing," Tech. Rep. Reader 1222, Delft University of Technology, 2020, Version 2.3-1, including errata.

[59] Lacombe, D. and Farhat, L., "Harness Reduction: Future Trends and Prospects," *ADCSS 2017*, European Space Agency (ESA), 2017.

[60] Rostan, M. et al., "How Space Robotics Benefits from the World Standard for Motion Communication," Tech. rep., EtherCAT Technology Group, 2022.

[61] Landzettel, K., Preusche, C., Albu-Schäffer, A., Reintsema, D., Rebele, B., and Hirzinger, G., "Robotic On-Orbit Servicing – DLR's Experience and Perspective," *Proceedings of the IEEE/RSJ International Conference on Intelligent Robots and Systems (IROS)*, IEEE, 2006.

[62] Mahadeo, D. M., Rohwer, L., Martinez, M., and Nowlin, N., "Assessment of Commercial-Off-The-Shelf Electronics for use in Short-Term Geostationary Satellites," Tech. rep., Sandia National Laboratories, 2018.

[63] Buchner, S., "Radiation Hardness Assurance (RHA) for Space Systems," Dec. 2008, Presented at the 4th International School on the Effects of Radiation on Embedded Systems for Space Applications (SERESSA), West Palm Beach, FL.

[64] Wu, A., Zuo, J., Zhao, Z., Luo, X., Wang, R., and Wan, X., "SpaceSense-Bench: A Large-Scale Multi-Modal Benchmark for Spacecraft Perception and Pose Estimation," *arXiv*, 2026.

[65] Schneider, S. and Steindorfer, M., "Spin axis and inertial spin period determination of satellites utilizing dual-station simultaneous Satellite Laser Ranging: a simulation study," *Advances in Space Research*, 2026.

[66] Perez, R., "Command Data Handling Subsystem," *Wireless Communications Design Handbook*, Vol. 1, 1998, pp. 141–201.

[67] Delépaut, A., Giordano, P., Ventura-Traveset, J., Blonski, D., Schönfeldt, M., Schoonejans, P., Aziz, S., and Walker, R., "Use of GNSS for lunar missions and plans for Lunar In-Orbit Development," *Advances in Space Research*, Vol. 66, 05 2020.

[68] Agency, E. S., "Guidance, Navigation Control building blocks for Space Servicing Vehicles Active Debris Removal missions," Tech. rep., European Space Agency, 2018.

[69] Cherd, V. T., Hamzah, N. H., and Ali, S. S., "Analysis on the Configuration of Four Reaction Wheels on the Attitude Manoeuvring of the Satellite," *International Communication in Computational Mechanics*, 2025.

[70] Derman, H. O., *3-Axis Attitude Control of a Geostationary Satellite*, Master's thesis, The Middle East Technical University, 1999.

[71] Wertz, J. R., Everett, D. F., and Puschell, J. J., editors, *Space Mission Engineering: The New SMAD*, Microcosm Press, Hawthorne, CA, USA, 2011, Second printing, 2015.

[72] Mulder, J., van Staveren, W., van der Vaart, J., de Weerdt, E., de Visser, C., in 't Veld, A., and Mooij, E., *Flight Dynamics Lecture Notes*, Faculty of Aerospace Engineering, 2013.

[73] Telaar, J., Ahrns, I., Estable, S., Rackl, W., De Stefano, M., Lampariello, R., Santos, N., Serra, P., Canetri, M., Ankersen, F., and Gil-Fernande, J., "GNC architecture for the e.Deorbit mission," *European Conference for Aeronautics and Space Sciences*, 2017.

[74] Pyrak, M. and Anderson, J., "Performance of Northrop Grumman's Mission Extension Vehicle (MEV) RPO imagers at GEO," *Autonomous Systems: Sensors, Processing and Security for Ground, Air, Sea and Space Vehicles and Infrastructure 2022*, 2022, pp. 28.

[75] Jena-Optronik GmbH, "ASTROhead Cam: Optical Head for Visible Range Space Imaging Applications," April 2024, Product datasheet.

[76] Malin Space Science Systems, "ECAM-IR3A: LWIR (8–14 µm) Uncooled Microbolometer, 640×480, 17 µm Pitch," Product datasheet.

[77] Jena-Optronik GmbH, "RVS 3000 Product Family: Ready for the Next Rendezvous," 2025, Product datasheet.

[78] European Space Agency, "RVS3000," May 2016, Presentation at Clean Space Industrial Days, ESTEC, Noordwijk, The Netherlands.

[79] Ciezki, H. K., "Short Overview on the Development of Advanced Green Monopropellants for Satellite Propulsion Applications, Status Summer 2025," *Aerospace*, Vol. 12, No. 12, 2025, pp. 1093.

[80] Mulkey, H. W. and Cardiff, E. H., "Green Propulsion: A NASA GSFC Assessment," *9th Edition of the 3AF International Conference on Space Propulsion*, Glasgow, Scotland, May 2024.

[81] Cavender, D. P., "Emerging Low Toxicity "Green" Chemical Propulsion Technologies for SmallSats," S3VI webinar presentation, NASA Small Spacecraft Community of Practice, Sept. 2020.

[82] Benfield, M. P. J. and Belcher, J. A., "Modeling of Spacecraft Advanced Chemical Propulsion Systems," NASA Technical Reports Server, Document ID 20050000113, Oct. 2004.

[83] "The Dynamic Behavior of Liquids in Moving Containers, with Applications to Space Vehicle Technology," Tech. Rep. NASA-SP-106, National Aeronautics and Space Administration, 1966.

[84] Scholl, H. F., "Ring-Baffle Pressure Distribution and Slosh Damping in a Cylindrical Tank," Tech. rep., National Aeronautics and Space Administration, 1972.

[85] LMO Space, "EP & CP Thruster Pointing Mechanisms," Datasheet, 2021, Accessed 2026-06-12.

[86] Poucet, A. et al., "Development of Thruster Pointing Mechanisms for Electric and Chemical Propulsion," *Proceedings of the 19th European Space Mechanisms and Tribology Symposium*, 2021.

[87] Mayer, N. L., "Advanced X-ray Astrophysics Facility-Imaging (AXAF-I) Propulsion Subsystem," *32nd Joint Propulsion Conference and Exhibit*, No. AIAA Paper 96-2869, American Institute of Aeronautics and Astronautics, Lake Buena Vista, FL, July 1996.

[88] Piragino, A., Le Mehaute, D., Gerard, T., Briges, A., Bobon, P., Guyon, V., Krzymuski, T., Lecervoisier, A., Lo Basso, A., Richard, A.-M., Pouleau, E., Vial, V., Duchemin, O., Lemoine, G., Prost, J. F., Kuiper, J., and Koopmans, R.-J., "Safran's EPS-X00 Low Power System: Latest Development and Qualification Tests," *Proceedings of the 39th International Electric Propulsion Conference*, No. IEPC-2025-526, London, United Kingdom, 2025, Available via ResearchGate and referenced by NASA Small Spacecraft Technology State of the Art.

[89] European Cooperation for Space Standardization, "ECSS-E-ST-32-10C Rev.2: Space Engineering – Structural Factors of Safety for Spaceflight Hardware," Tech. Rep. ECSS-E-ST-32-10C Rev.2, European Cooperation for Space Standardization (ECSS), May 2019.

[90] Space Exploration Technologies Corp. (SpaceX), *Falcon Payload User's Guide*, SpaceX, Hawthorne, CA, 5 2025, Rev. May 2025.

[91] Northrop Grumman Corporation, *Propulsion Products Catalog*, Northrop Grumman Space Systems, 2023.

[92] Fortescue, P., Swinerd, G., and Stark, J., *Spacecraft Systems Engineering*, Wiley, 4th ed., 2011.

[93] Bhat, B. R., Upadhyaya, N., and Kulkarni, R., "Total Radiation Dose at Geostationary Orbit," *IEEE Transactions on Nuclear Science*, Vol. 52, No. 2, 2005, pp. 530–534.

[94] "On-Board Computer for CubeSats: State-of-the-Art and Future Trends," *IEEE Access*, 2023, Reports COTS CubeSat electronics TID tolerance typically 3–30 krad(Si), with radiation-tolerant variants up to 20–50 krad(Si).

[95] Hexcel Corporation, "HexPly® 8552 Epoxy Matrix (180°C/356°F Curing Matrix) Product Data Sheet," Tech. rep., Hexcel Corporation, 2023, Accessed: June 2026.

[96] Fang, S., Liu, C., and Zhang, C., "Automatic Calculation Method for Effective Length Factor of Bridge Piers Considering Shear Deformation," *Buildings*, Vol. 15, 2024, pp. 46.

[97] Megson, T. H. G., *Aircraft Structures for Engineering Students*, Butterworth-Heinemann, 7th ed., 2021.

[98] Ewellix, "3D CAD Models: SRC, SRF, SRP, BRC, BRF, BRP, PRU, PRK, HRC, HRF, HRP - Ultra power planetary roller screw," 2026.

[99] Guerra, A. G. C., Francisco, F., Villate, J., Aguado Agelet, F., Bertolami, O., and Rajan, K., "On Small Satellites for Oceanography: A Survey," *arXiv preprint*, 2016.

[100] NASA Small Spacecraft Systems Virtual Institute, "Small Spacecraft Technology State of the Art: Thermal Systems," Tech. rep., National Aeronautics and Space Administration, 2026.

[101] European Commission, "Study of the State of the Art of Space Thermal Control Systems," Tech. rep., European Commission, 2019.

[102] van Gerner, H. J., "A Heat Pump for Space Applications," Tech. rep., National Aerospace Laboratory NLR, 2007, Accessed: 2026-06-11.

[103] Finckenor, M. M. and Dooling, D., "Multilayer Insulation Material Guidelines," Tech. Rep. NASA/TP-1999-209263, NASA Marshall Space Flight Center, 1999, Accessed: 2026-06-11.

[104] NASA Goddard Space Flight Center, "General Specification for Thermofoil Heater, All-Polyimide, Space Applications," Tech. Rep. S-311-P-841, NASA Goddard Space Flight Center, 2016, Accessed: 2026-06-11.

[105] Space Dynamics Laboratory, "PGS Thermal Solutions: Thermal Straps and Conductor Bars," Product brochure, 2024, Accessed: 2026-06-11.

[106] Space Logistics LLC, "Technical Appendix: Application for Authority to Launch and Operate the MEV-2 Spacecraft," Tech. rep., Federal Communications Commission, December 2019, FCC Part 25 Application, §25.114(d). Certified by R. Capozzi, Program Director, Space Logistics LLC, 10 December 2019.

[107] Roddy, D., *Satellite Communications*, McGraw-Hill, New York, 4th ed., 2006.

[108] Balanis, C. A., *Antenna Theory: Analysis and Design*, Wiley, Hoboken, NJ, 4th ed., 2016.

[109] Pratt, T. and Allnutt, J. E., *Satellite Communications*, Wiley, Hoboken, NJ, 3rd ed., 2019.

[110] ESA Space Debris Office, "ESA's Annual Space Environment Report," Tech. Rep. GEN-DB-LOG-00288-OPS-SD, Issue/Revision 9.1, European Space Agency, Oct. 2025, Accessed: 18 May 2026.

[111] Liou, J.-C., Johnson, N. L., and Hill, N. M., "Controlling the growth of future LEO debris populations with active debris removal," *Acta Astronautica*, Vol. 66, No. 5–6, 2010, pp. 648–653.

[112] Liou, J.-C., "An active debris removal parametric study for LEO environment remediation," *Advances in Space Research*, Vol. 47, No. 11, 2011, pp. 1865–1876.

[113] Bonnal, C., Ruault, J.-M., and Desjean, M.-C., "Active debris removal: Recent progress and current trends," *Acta Astronautica*, Vol. 85, 2013, pp. 51–60.

[114] Castet, J.-F. and Saleh, J. H., "Satellite and satellite subsystems reliability: Statistical data analysis and modeling," *Reliability Engineering & System Safety*, Vol. 94, No. 11, 2009, pp. 1718–1728.

[115] European Space Agency (ESA) TRL Working Group, *Guidelines for the Use of TRLs in ESA Programmes*, European Space Agency, issue 1, revision 0 ed., 2013, Approved/Applicable, 21 August 2013.

[116] REAVER Group 7, "Baseline Report: REAVER Mission Design," Design Synthesis Exercise Report Group 7, TU Delft, Faculty of Aerospace Engineering, 2026, AE3200 Design Synthesis Exercise.

[117] European Cooperation for Space Standardization, "ECSS-Q-ST-20C Rev.2: Space Product Assurance – Quality Assurance," Tech. rep., ECSS Secretariat, ESA-ESTEC, Noordwijk, The Netherlands, Feb. 2018.

[118] European Cooperation for Space Standardization, "ECSS-M-ST-40C Rev.1: Space Project Management – Configuration and Information Management," Tech. rep., ECSS Secretariat, ESA-ESTEC, Noordwijk, The Netherlands, March 2009.

[119] Subramanya, N., Satheesh Kumar, A. R., Yadav, V., and Venkatesh, R. K., "Manufacturing Process Planning in Aerospace Systems," *IOP Conference Series: Materials Science and Engineering*, Vol. 1258, No. 1, 2022, pp. 012027.

[120] European Cooperation for Space Standardization, *Space Engineering: Structural Factors of Safety for Spaceflight Hardware*, European Cooperation for Space Standardization (ECSS), Noordwijk, Netherlands, May 2019.

[121] National Aeronautics and Space Administration, "GSFC-STD-7000B: General Environmental Verification Standard (GEVS) for GSFC Flight Programs and Projects," Tech. rep., NASA Goddard Space Flight Center, Greenbelt, MD, USA, April 2021.

[122] European Cooperation for Space Standardization, "ECSS-M-ST-10-01C: Space Project Management – Organization and Conduct of Reviews," Tech. rep., ECSS Secretariat, ESA-ESTEC, Noordwijk, The Netherlands, Nov. 2008.

A. Appendix A

Ground Station Trade-off Scoring Levels

Table A.1: Ground station trade-off scoring levels

Score	GEO Coverage Geometry	Frequency Band Support	ESA GEO Mission Heritage
5	Near-equatorial; elevation >60°; minimal atmospheric path loss.	S-band, X-band, and Ka-band all confirmed as primary operational bands.	Primary function is routine GEO TT&C; direct heritage with GEO operational missions.
4	Moderate latitude; elevation 45–60°; low atmospheric loss.	S-band and X-band confirmed as primary bands; Ka-band available but not primary.	Regular GEO support forms a major part of the operational portfolio.
3	Mid-latitude; elevation 30–45°; moderate atmospheric path loss.	S-band confirmed; X-band or Ka-band present as a secondary capability only.	GEO contact demonstrated but not the primary operational focus.
2	High latitude; elevation 15–30°; significant atmospheric path loss.	S-band confirmed; X-band and Ka-band unavailable or unconfirmed.	Primarily non-GEO operations; GEO contact is not routine.
1	Very high latitude; elevation <15°; near-horizon; unacceptable atmospheric loss.	S-band not confirmed as a primary operational band; frequency requirement unmet.	No confirmed GEO TT&C heritage.

Chemical Propulsion System Interface Definition

```
-------- Pre-Launch --------
COMMAND CLOSED:
    V-2.1 to V-2.4
    V-9.1 to V-9.10
    SV-10.1 to SV-10.29

-------- Startup --------
STEP 1:
    OPEN V-2.2
STEP 2:
    IF PT-4.16 approx. P_SET:
        OPEN V-2.3
STATE = SYSTEM PRESSURISED

-------- RCS initialisation --------
STEP 1:
    OPEN V-9.10
STEP 2:
    OPEN one selected tank outlet valve:
        V-9.2 OR V-9.4 OR V-9.6 OR V-9.8
STEP 3:
    IF required RCS sensors PT-4.7 to PT-4.15
    approx. P_SET:
        STATE = RCS READY

-------- RCS activation --------
WHEN RCS firing is commanded:
    OPEN required RCS solenoid valve:
        SV-10.5 to SV-10.29

IF any required RCS pressure sensor < P_SET:
    OPEN one selected tank outlet valve:
        V-9.2 OR V-9.4 OR V-9.6 OR V-9.8

IF any required RCS pressure sensor > P_SET:
    CLOSE selected tank outlet valve:
        V-9.2 OR V-9.4 OR V-9.6 OR V-9.8

-------- Thruster initialisation --------
STEP 1:
    OPEN V-9.9
STEP 2:
    OPEN one selected tank outlet valve:
        V-9.2 OR V-9.4 OR V-9.6 OR V-9.8
STEP 3:
    IF PT-4.6 approx. P_SET:
        STATE = MAIN THRUSTER READY

-------- Thruster activation --------
WHEN main-thruster firing is commanded:
    OPEN required main-thruster solenoid valve:
        SV-10.1 to SV-10.4

IF PT-4.6 < P_SET:
    OPEN one selected tank outlet valve:
        V-9.2 OR V-9.4 OR V-9.6 OR V-9.8

IF PT-4.6 > P_SET:
    CLOSE selected tank outlet valve:
        V-9.2 OR V-9.4 OR V-9.6 OR V-9.8

-------- LMP-103S Tanks --------
IF PT-4.2 < P_SET:
    OPEN V-9.1
IF PT-4.3 < P_SET:
    OPEN V-9.3
IF PT-4.4 < P_SET:
    OPEN V-9.5
IF PT-4.5 < P_SET:
    OPEN V-9.7

-------- Fault detection --------
IF any pressure sensor PT-4.2 to PT-4.8
reports abnormal pressure:
    CLOSE V-9.1 to V-9.10
    INHIBIT SV-10.1 to SV-10.29
    STATE = FAULT

IF PT-4.1 > P_PROOF:
    OPEN V-2.1
    OPEN V-1.1
    STATE = HELIUM TANK OVERPRESSURE FAULT

IF PT-4.1 > P_BURST:
    CLOSE V-3.1
    OPEN V-2.1
    OPEN V-1.1
    STATE = SYSTEM SHUTDOWN

IF PT-4.8 > P_PROOF:
    OPEN VENT-8.6
    STATE = REGULATED HELIUM REGULATOR
            OVERPRESSURE FAULT

IF PT-4.2 > P_PROOF:
    OPEN VENT-8.2
    STATE = PROPELLANT TANK 1
            OVERPRESSURE FAULT

IF PT-4.3 > P_PROOF:
    OPEN VENT-8.3
    STATE = PROPELLANT TANK 2
            OVERPRESSURE FAULT

IF PT-4.4 > P_PROOF:
    OPEN VENT-8.4
    STATE = PROPELLANT TANK 3
            OVERPRESSURE FAULT

IF PT-4.5 > P_PROOF:
    OPEN VENT-8.5
    STATE = PROPELLANT TANK 4
            OVERPRESSURE FAULT
```

Listing A.1: Chemical propulsion system interface definition